UNIVERSITÀ DEGLI STUDI DI PADOVA

Dipartimento di Fisica e Astronomia "Galileo Galilei"
Scuola di dottorato di ricerca in Astronomia
Ciclo XXV

GAMMA-RAY BURSTS AND THEIR X-RAY AND OPTICAL AFTERGLOW

Direttore della scuola: Ch.mo Prof. Giampaolo Piotto
Supervisori: Ch.mo Prof. Alberto Franceschini
Ch.mo Prof. Guido Chincarini
Dott.ssa Maria Grazia Bernardini

Dottoranda: Elena Zaninoni

Abstract

The aim of this PhD thesis is to study and characterize the optical and X-ray emission of the afterglows of gamma-ray bursts (GRBs).

GRBs are the most powerful sources of electromagnetic radiation in the universe, with an isotropic luminosity that can reach values of 10^{54} erg s^{-1}. The *Swift* satellite, launched in November 2004, opened a new era for the study and understanding of the phenomenon of GRBs, thanks to the rapid response of its narrow FOV instruments that allows the accurate localization of most GRBs and the more complete coverage of the GRB evolution.

In the first part of my PhD I was involved in a comprehensive statistical analysis of the *Swift* X-ray light-curves (LCs) of GRBs, carried out in a model-independent way. Our sample is composed of the X-ray LCs of more than 650 GRBs observed by *Swift* from December 2004 to December 2010. For 437 GRBs the statistics were good enough to allow us to extract a spectrum to convert their count-rate LCs into flux LCs. For GRBs with a known redshift, also rest-frame luminosity LCs in the 0.3-30 keV band were computed. From the fit of these LCs, we obtained the values of the temporal slopes and break times of the continuum of the X-ray emission, since the used fitting procedure automatically discards the positive fluctuations (i.e. flares). Then, we computed the total fluences and energies, those of flares and differentiating between the components of the X-ray LCs. Thanks to this large sample of LCs, we could carry out a homogeneous analysis of GRBs in a common rest frame energy band (0.3-30 keV), investigating the intrinsic time scales and energetics of the different LC phases. In addition, we studied the properties of flares superimposed to the smooth X-ray decay. GRBs are classified as long and short, depending on the duration of the prompt emission ($T_{90} > 2$ s and $T_{90} < 2$ s, respectively); our sample of GRBs allowed us to investigate the possible differencies and similarities between these two classes, for example the nature of long and short GRBs and the emission mechanisms involved. Finally, we examined the possible relation between the X-ray and gamma-ray emission and we found the existence of a universal scaling involving two parameters of the prompt emission and one of the X-ray emission: the isotropic prompt emission energy ($E_{\gamma,\mathrm{iso}}$), the peak energy (E_{pk}) and the isotropic X-ray energy ($E_{\mathrm{X,iso}}$).

The main idea of the project presented above is to study all quantities that characterize the X-ray data and to look for a link between prompt and afterglow emission. During this work, we realized that the optical data were very

important for our understanding, adding information to investigate the GRB emission mechanisms and to study the environment properties. Therefore, in the second part of my PhD we carried out a systematic analysis of the optical data available in literature, collecting data from all the available sources. From the collected optical data, we determine the shapes of the optical LCs. Then, we modeled the optical/X-ray spectral energy distribution (SED), we studied the SED parameter distributions and we compared the optical and X-ray LC slopes and shapes. For 20% of GRBs the difference between the optical and X-ray slopes is consistent with 0 or 1/4 within uncertainties (we do not consider here the steep decay phase), but in the majority of cases (80%) the optical and X-ray afterglows show significantly different temporal behaviors. Interestingly, we found an indication that the onset of the forward shock in the optical LCs (initial peaks or shallow phases) could be linked to the presence of the X-ray flares. Indeed when there are X-ray flares the optical LC initial peak or plateau end occurs during the steep decay, instead if there are no X-ray flares or if they occur during the plateau, the optical initial peak or plateau end takes place during the X-ray plateau. This could link the prompt emission with the optical emission. The forward shock model cannot explain all the features of the optical (e.g. bumps, late re-brightenings) and X-ray (e.g. flares, plateaus) LCs. However, the synchrotron model is a viable mechanism for GRBs afterglow emission at late times. Further to the intrinsic spectrum of the afterglow, the SED analysis allows to study the properties of the GRB environment, by quantifying the amount of absorption at optical and X-ray wavelengths. The first is due to dust while the latter is mostly due to metals. Our analysis shows that the gas-to-dust ratios of GRBs are larger than the values calculated for the Milky Way, the Large Magellanic Cloud, and the Small Magellanic Cloud assuming solar abundances.

Riassunto

Lo scopo di questa tesi è lo studio e la caratterizzazione dell'emissione X e ottica dei *gamma-ray burst* (GRB).

I GRB sono la sorgente più potente di radiazione elettromagnetica dell'universo, la cui luminosità può raggiungere valori di 10^{54} erg s^{-1}. Il satellite *Swift*, lanciato nel novembre del 2004, ha aperto una nuova era per lo studio e la comprensione dei GRB, grazie alla rapida risposta dei suoi strumenti che ha permesso localizzare in modo accurato la maggior parte dei GRB e di ottenere una visione più completa della loro evoluzione.

Nella prima parte del mio Dottorato sono stata coinvolta nell'analisi statistica delle curve di luce (CL) osservate nella banda energetica corrispondente ai raggi X del telescopio per i raggi X a bordo del satellite *Swift*. Questo studio non ha assunto alcun modello teorico per spiegare le osservazioni, ma è stato finalizzato alla raccolta di tutte le possibili informazioni osservative. Il nostro campione è composto dalle CL di più di 650 GRB osservati da *Swift* tra Dicembre 2004 e Dicembre 2010. Per 437 GRB, grazie alla bontà statistica dei dati, è stato possibile estrarre uno spettro per convertire le loro CL da conteggi a flusso. Per i GRB per cui è stato misurato il *redshift*, sono state calcolate anche le CL in luminosità nella banda energetica 0.3-30 keV nel sistema di riferimento della sorgente, in modo da approssimare la luminosità bolometrica. Dall'interpolazione dei dati delle CL, abbiamo ottenuto i valori delle pendenze temporali e dei *break time*, cioè dei tempi in cui la CL cambia la sua pendenza, e abbiamo caratterizzato l'andamento temporale dell'emissione duratura in banda X, escludendo le fluttuazioni (*flares*) che sono probabilmente dipendenti da meccanismi diversi. Per ogni GRB, sono state calcolate le densità di flusso e le energie corrispondenti all'emissione X totale, dei *flares* e delle diverse componenti della CL. È stata realizzata un'analisi omogenea dei GRB in una banda energetica comune (0.3-30 keV) nel sistema a riposo della sorgente. I GRB sono classificati come lunghi e corti, in base alla durata dell'emissione iniziale, detta *prompt emission* ($T_{90} > 2$ s and $T_{90} < 2$ s, rispettivamente); il nostro campione di GRB ci ha permesso di studiare le differenze e le somiglianze di queste queste due classi di GRB. Infine abbiamo identificato una nuova relazione tra l'emissione X e gamma trovando una legge universale che coinvolge due parametri che si riferiscono alla *prompt emission* e uno che si riferisce all'emissione X: l'energia totale della *promp emission* ($E_{\gamma,\mathrm{iso}}$), l'energia di picco dello spettro integrato nel tempo della *prompt emission* (E_{pk}) e l'energia X ($E_{\mathrm{X,iso}}$).

L'idea principale del progetto appena discusso è lo studio di tutte le quantità che caratterizzano i dati X e la ricerca di un legame tra l'emissione *prompt* nei raggi gamma e quella nelle altre bande energetiche, X, ottico e radio, detta *afterglow*. Durante questo lavoro, ci siamo resi conto della necessità di aggiungere le informazioni che provengono dai dati ottici dei GRB, in modo da studiare in modo più dettagliato i meccanismi di emissione dei GRB e le proprietà dell'ambiente che li circonda. Quindi, nella seconda parte del mio Dottorato ho condotto un mio personale progetto di ricerca, analizzando in modo sistematico i dati ottici disponibili in letteratura. Il primo passo è stato quello di interpolare le CL ottiche, in modo da caratterizzare il loro andamento temporale. Poi abbiamo modellato le distribuzioni di energia spettrale ottica e X (SED) e abbiamo studiato le distribuzioni dei parametri ottenuti da questo studio. Infine abbiamo confrontato l'andamento temporale delle CL ottiche.

Per il 20% dei GRB la differenza tra la pendenza ottica e X è consistente con i valori attesi dal modello standard per l'afterglow dei GRB, mentre nella maggior parte dei casi le CL ottiche e X mostrano un andamento temporale diverso. Inoltre, abbiamo trovato un'indicazione che l'inizio della fase di *afterglow* nelle CL ottiche (che corrisponde nelle CL a picchi iniziali o fasi quasi-costanti) potrebbe essere collegato alla presenza dei *flare* nei raggi X. Quindi, quando ci sono *flares* X, il picco iniziale o la fine della fase quasi-costante della curva di luce ottica avvengono durante la fase iniziale della CL X, detta *steep decay*, invece se non ci sono *flare* X o se avvengono successivamente allo *steep decay*, il picco iniziale o la fase quasi-costante della CL ottica si manifestano durante la fase quasi-costante della curva di luce X. Questo potrebbe legare l'emissione *prompt* con l'ottico. In generale, troviamo che il modello del standard per l'*afterglow* non può spiegare tutte le caratteristiche delle CL ottiche e X. Comunque, l'emissione di sincrotrone può essere un meccanismo plausibile per spiegare l'emissione dell'*afterglow* a tempi tardi.

L'analisi delle SED ci ha permesso di studiare le proprietà dell'ambiente dei GRB, quantificando la quantità di assorbimento alle lunghezze d'onda ottiche e X. Il primo è dovuto alla polvere invece l'ultimo è dovuto principalmente ai metalli. La nostra analisi ha mostrato che il rapporto tra il gas e la polvere per i GRB è maggiore rispetto ai valori calcolati per la Via Lattea, la Grande Nube di Magellano e la Piccola Nube di Magellano, assumendo abbondanze solari.

Plan of the thesis and publications

During my PhD I was involved in the study and characterization of the optical and X-ray emission of the afterglows of gamma-ray bursts (GRBs).

The first Chapter of this thesis summarizes the observational properties and theoretical models about GRBs. I will present the observational characteristics of the gamma-ray prompt emission and of their X-ray, optical and radio counterparts (i.e. afterglows). Then I will focus on the sub-classes of GRBs, short and long, examining their energetics, environments, and the possible correlations involving both the prompt and afterglow quantities. Finally, I will introduce some theoretical models: the standard fireball model and the scenarios for the progenitors.

In the second Chapter I will focus on the statistical analysis of a large sample of X-ray light-curves of the *Swift* satellite. I will explain the data selection and data analysis. For a sample of 437 GRBs we fitted their LCs and we calculated the temporal properties of their light-curves and we calculate the energetics of the X-ray continuum and flares. We investigate all the possible relations between the X-ray and prompt emission properties, finding an interesting 3-parameter correlation between the X-ray isotropic energy, the prompt gamma-ray emission and the peak energy. This Chapter is based on the articles:

- "The prompt-afterglow connection in gamma-ray bursts: a comprehensive statistical analysis of Swift X-ray light curves". Margutti, R., **Zaninoni, E.**, Bernardini, M.G; Chincarini, G.; Pasotti, F.; Guidorzi, C.; Angelini, L.; Burrows, D. N.; Capalbi, M.; Evans, P. A.; Gehrels, N.; Kennea, J.; Mangano, V.; Moretti, A.; Nousek, J.; Osborne, J. P.; Page, K. L.; Perri, M.; Racusin, J.; Romano, P.; Sbarufatti, B.; Stafford, S.; Stamatikos, M. (2013, MNRAS, 428-729)

- "A universal scaling for short and long gamma-ray bursts: $E_{\rm X,iso}$-$E_{\gamma,\rm iso}$-$E_{\rm pk}$". Bernardini, M. G.; Margutti, R.; **Zaninoni, E.**; Chincarini, G. (2012, MNRAS, 425, 1199)

- "The X-ray light curve of gamma-ray bursts: clues to the central engine". Bernardini, M. G.; Margutti, R.; Mao, J.; **Zaninoni, E.**; Chincarini, G. (2012, A&A, 539, 3)

In the third Chapter I present the analysis of optical data of a sample of 68 GRBs with known redshift. I present the data selection and analysis: the fitting of the optical light-curves, the fitting of the optical/X-ray spectral energy distributions (SEDs), the distributions of the parameters obtained from the SED fit and the comparison within the optical and the X-ray LCs. Interestingly we found a possible relation between the presence of X-ray flares and the shape of the optical light curve X-ray flares and optical light-curve shape. This Chapter is based on:

- "The gamma-ray burst optical light-curve zoo: comparison with the X-ray observations". **Zaninoni, E.**, Bernardini, M. G., Margutti, R., Oates, S., and Chincarini, G. (2013, under submission).

Finally, in the fourth Chapter I will summarize the results of the previous chapters.

Other articles:

Published articles:

- "*X-ray flare candidates in short gamma-ray bursts*", R. Margutti, G. Chincarini, J. Granot, C. Guidorzi, E. Berger, M.G. Bernardini, N. Gehrels, A.M. Soderberg, M. Stamatikos, **E. Zaninoni** (2011, MNRAS, 417, 2144)

Conference proceedings:

- "*Highlights From The Comprehensive Analysis Of 650 Gamma Ray Bursts (Nov 2004 - Dic 2010)*", Chincarini, G.; Margutti, R.; Bernardini, M.; **Zaninoni, E.** (2012, American Astronomical Society Meeting Abstracts #220, 220, #524.05)

- "*The prompt-afterglow connection in Gamma-Ray Bursts: a comprehensive statistical analysis of Swift X-ray light-curves*", Margutti, R.; **Zaninoni, E.**; Bernardini, M. G.; Chincarini, G. (2012, Proceedings of the Gamma-Ray Bursts 2012 Conference (GRB 2012). May 7-11, 2012. Munich, Germany; 2012grb..confE..61M)

- "*A universal scaling for short and long gamma-ray bursts:* $E_{X,iso} - E_{\gamma,iso} - E_{pk}$", Bernardini, M. G.; Margutti, R.; **Zaninoni, E.**; Chincarini, G. (2012, Proceedings of the Gamma-Ray Bursts 2012 Conference (GRB 2012). May 7-11, 2012. Munich, Germany; 2012grb..confE..70B)

- "*X-ray emission of GRBs: what is the light curve morphology telling us?*", Bernardini, M. G.; Margutti, R.; **Zaninoni, E.**; Chincarini, G. (2012, Memorie della Società Astronomica Italiana Supplementi, 21, 226)

- "*X-ray light curves of Gamma-ray bursts without flares*", Bernardini M.G.; Margutti R.; Mao, J.; **Zaninoni, E.**; Chincarini, G. (The X-ray Universe 2011, 35)

- "*The Complete Study of GRB X-Ray Afterglow: energetics, time-scales and Luminosity*", **Zaninoni E.**; Margutti R.; Bernardini M. G.; Chincarini G. (The X-ray Universe 2011, 306)
- "*The Swift/XRT Catalogue of GRBs*", **Zaninoni, E.**; Margutti, R.; Bernardini, M.G.; Chincarini, G. (2011, arXiv:1107.2870v1)

Contents

Abstract **i**

Riassunto **iii**

Plan of the thesis and publications **v**

1 Gamma-Ray Bursts **1**
1.1 Gamma-ray bursts: a brief history 1
1.2 Observations 3
1.2.1 The prompt emission 3
1.2.2 The afterglow 4
1.2.3 Subclasses of gamma-ray bursts 7
1.2.4 The environments 8
1.2.5 The correlations 9
1.3 Models and Theory 12
1.3.1 The standard fireball model 14
1.3.2 The progenitors 21

2 GRB XRT light-curves **25**
2.1 Sample selection, LC and spectra extraction 26
2.2 *XCURVE* and *ENERGY* programs 27
2.3 Classification 29
2.4 Results and Discussion 30
2.4.1 Dispersion of X-ray LCs 32
2.4.2 Energetics 35
2.4.3 The luminosity 40
2.4.4 The plateau phase 40
2.4.5 LC temporal slopes 43
2.4.6 The intrinsic hydrogen-equivalent absorption 46
2.4.7 The 3-parameter correlation: $E_{\gamma,\mathrm{iso}}$ - E_{pk} - $E_{\mathrm{X,iso}}$ 46
2.4.8 Observational biases 52
2.5 Conclusions 52

3 The gamma-ray burst optical light-curve zoo **55**
3.1 Sample selection and data analysis 56
3.1.1 Optical data 57

3.1.2 X-ray data 58
3.1.3 Optical/X-ray SEDs 58
3.2 Results 61
3.2.1 Spectral parameter distributions 61
3.2.2 Luminosity and energetics 67
3.2.3 The optical LCs 70
3.2.4 Comparison between the optical and X-ray LCs 72
3.3 Discussion 78
3.3.1 The LC phases 78
3.3.2 The closure relations 82
3.3.3 The broad band SEDs 85
3.3.4 The 3-parameter correlation 86
3.4 Conclusions 86

4 Conclusions **89**

Appendix **93**

A Principal component analysis **93**

B The synchrotron emission **95**

C The efficiency **101**

D GRB XRT light-curves: glossary **105**

E The optical light-curves: tables and figures **107**

Bibliografy **151**

1

Gamma-Ray Bursts

1.1 Gamma-ray bursts: a brief history

Gamma-ray bursts (GRBs) are the most powerful sources of electromagnetic emission in the universe with isotropic luminosities that can reach values of 10^{54} erg s^{-1}.

They were discovered by chance at the end of '60s by the ***Vela* satellites**, built to monitor nuclear experiments in and out the terrestrial atmosphere. The first GRB was detected on 1967, but this discovery was announced to the scientific community only in 1973 by Klebesadel et al. (1973). Until the launch of the ***Compton Gamma Ray Observatory*** (CGRO) by NASA (5 April 1991), with on board the *Burst And Transient Source Experiment* (BATSE), scientists did not know if GRBs were Galactic or extragalactic objects. Thanks to the BATSE data, which detected and observed more than 2700 GRBs during 9 years of activity, it was established that GRBs have a cosmological origin, because they are distributed isotropically in the sky. This was confirmed also by the X-ray data obtained with the italian-dutch satellite ***Beppo*SAX**[1] launched in 1997. There were three instruments on board of *Beppo*SAX : the *Gamma-Ray Burst Monitor* (GRBM) and two X-ray instruments (*Wide Field Cameras* (WFCs) and *Narrow Field Instruments* (NFIs)). On February 28, 1997 the first X-ray counter part of a GRB (Costa et al. 1997) was observed: this long lasting emission gave the possibility to establish the GRB position accurately and thus enabling optical observations in order to measure the redshift (van Paradijs et al. 1997). After these first successful results, several satellites were designed to study these mysterious objects.

***Konus*[2] (1994).** The Russian *Konus* experiment, on board of the USA *Wind* mission, provides the omnidirectional and continuous observation of the sky in the hard X- and gamma-ray bands, from 10 to 770 keV, with 64 millisecond time resolution. It reaches 2 millisecond resolution during high intensity portions of events, making possible to study accurately the temporal structures

[1] *Beppo* in honor of Giuseppe Occhialini; SAX means "*Satellite per l' Astronomia X*" (X-ray astronomy satellite).

[2] http://heasarc.gsfc.nasa.gov/docs/heasarc/missions/wind.html

of GRBs.

Chandra[3] **(1999).** The *Advanced X-ray Astrophysics Facility* (AXAF), renamed "Chandra" in honor of Chandrasekhar, is one of the most sophisticated X-ray observatories. It was designed to observe X-rays from high-energy regions of the universe, such as GRBs. It can study extremely faint sources thank to the combination of high resolution, large collecting area and sensitivity to higher energy X-rays. *Chandra* was the first instrument to observe the X-ray emission lines associated to a GRB (GRB 991216, Piro et al. 2000). This allowed to measure unambiguously the redshift of a GRB.

XMM-*Newton*[4] **(1999).** The main characteristic of the *X-ray Multi-Mirror* mission (XMM-*Newton*) is the unprecedent effective area of the X-ray detector. Because of the large collecting area and ability to make long uninterrupted exposures, it provides highly sensitive observations. XMM data presented for the first time the presence of the emission lines of light elements (GRB 011211, Reeves et al. 2002), associated to the explosion of a SN shortly before the GRB. Moreover, it detected the variable X-ray halos around GRBs, which give rise form the scattering because of the dust in our Galaxy (Vaughan et al. 2004; Watson et al. 2004, 2006b), providing information about the dust and the GRB X-ray emission.

HETE-2[5] **(2000).** HETE-2 was designed to detect and localize GRBs. The suite of instruments on board (FREGATE - wide-field gamma-ray spectrometers; WXM - wide-field X-ray monitor; SXC - soft X-ray cameras) allows simultaneous observations in soft and medium X-ray and gamma-ray energies. HETE-2 was the first mission to transmit arcminute positions of GRBs to the scientific community in few seconds from the GRB trigger, allowing detailed studies of the initial phases of GRBs.

INTEGRAL[6] **(2002).** The *International Gamma-Ray Astrophysics Laboratory* (INTEGRAL) was the first space observatory that could simultaneously observe objects in gamma rays, X-rays and visible light. It can produce a complete map of the sky in the soft gamma-ray band and it is capable of performing high spectral and spatial observations in gamma-rays. On board of the INTEGRAL observatory there are two gamma-ray instruments, a spectrometer (SPI) and an imager (IBIS), a X-ray detector (JEM-X) and an optical detector (OMC).

Swift[7] **(2004).** This satellite was specifically designed for the detection and observation of GRBs. It has three instruments that work together to observe GRBs in the gamma, X and optical bands: the *Burst Alert Telescope* (BAT),

[3] http://chandra.harvard.edu/
[4] http://xmm.esac.esa.int/
[5] http://space.mit.edu/HETE/
[6] http://www.esa.int/esaMI/Integral/index.html
[7] http://heasarc.gsfc.nasa.gov/docs/swift/swiftsc.html

the *X-Ray Telescope* (XRT) and the *Ultraviolet/Optical Telescope* (UVOT). BAT constantly monitors a wide area of the sky and when it detects a GRB it calculates its position within about 10 seconds. Therefore *Swift* rapidly repoints XRT and UVOT towards the source and the observations begin. The GRB coordinates are immediately transmitted to ground observers and other satellites. The important features of the *Swift* satellite are the rapid localization of GRBs and the rapid follow-up of the afterglows in different wavelengths. This allowed to obtain a large number of GRBs with redshift measurements, discovering GRBs with high redshift (GRB 090423 with $z \sim 8.2$, Salvaterra et al. 2009; Tanvir et al. 2009; GRB 090429B with $z \sim 9.4$ Cucchiara et al. 2011b), and to study the early-time X-ray emission.

***Fermi* satellite[8] (2008).** The aim of this mission is the observation of the sky at very high energies. On board there are two instruments: the *Gamma-ray Burst Monitor* (GBM, 8 keV-40 MeV), and the *Large Area Telescope* (LAT, 20 MeV-300 GeV). GBM observes more or less 250 GRBs per year, while LAT observes only ∼10 GRBs yr^{-1}. An higher fraction of the GRBs detected by LAT are short compared to the GBM GRBs. *Fermi* revealed that long and short GRBs have common spectral properties at high energies.

1.2 Observations

1.2.1 The prompt emission

Usually we observe a *prompt* high-energy emission (gamma-rays), followed by a long lasting multiwavelength emission called *afterglow*. The prompt emission is operationally defined as the time period when the gamma-ray detector detects a signal above background (Piran 2004). The prompt gamma-ray emission has a non-thermal spectrum which varies from a GRB to another. Prompt GRB spectra are well fitted by a phenomenological broken power-law function introduced by Band et al. (1993):

$$N_{\mathrm{E}}(E) = \begin{cases} A \left(\frac{E}{100\ \mathrm{keV}}\right)^{\alpha} \exp\left(-\frac{E}{E_0}\right) & (\alpha-\beta)E_0 \geq E \\ A \left(\frac{(\alpha-\beta)E_0}{100\ \mathrm{keV}}\right)^{-\alpha-\beta} \exp(\beta-\alpha) \left(\frac{E}{100\ \mathrm{keV}}\right)^{\beta} & (\alpha-\beta)E_0 \leq E. \end{cases} \quad (1.1)$$

α is the low-energy spectral index, β the high-energy spectral index, E_0 the break energy and A the normalization. This function is not linked to a theoretical model, but reflects only the informations given by observations. If $\beta < -2$ we define the peak energy as $E_{pk} = E_0(2+\alpha)$, which represents the typical energy of the observed radiation (see Sec. 2.4).

The duration of gamma-ray emission ranges from less than 0.01 s to more than 100 s. The characteristic time is T_{90} (T_{50}) defined as the time in which 90% (50%) of GRB counts arrive. Based on the T_{90} distribution, Kouveliotou et al. (1993) divided the GRBs into two groups: long GRBs with $T_{90} > 2$ s and short GRBs with $T_{90} < 2$ s. Moreover, these two classes have also a different

[8] http://www.nasa.gov/mission_pages/GLAST/main/index.html

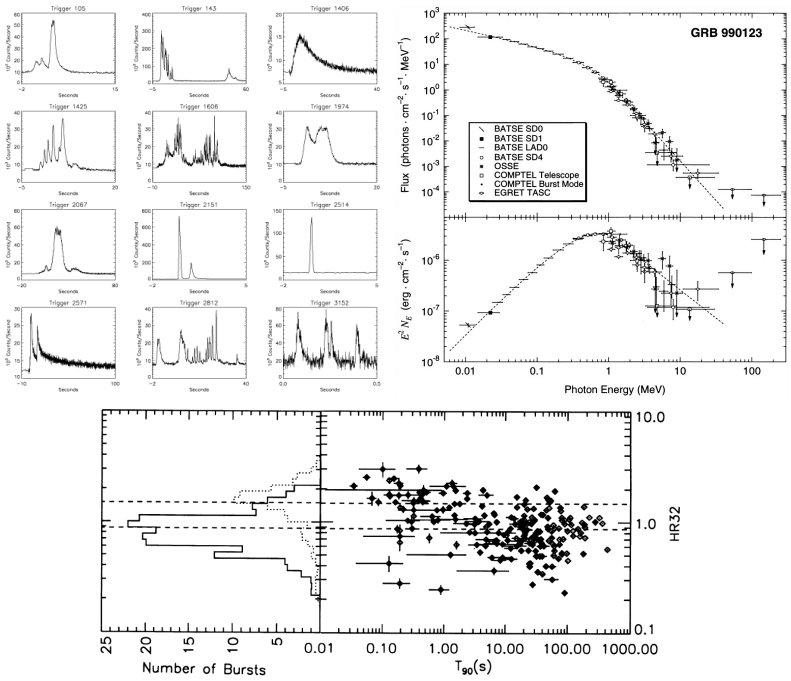

Figure 1.1: Prompt emission properties. *Top left*: a selection of the large variety of gamma ray burst time profiles, as detected from the Compton Gamma Ray Observatory (http://imagine.gsfc.nasa.gov/docs/science/know_l1/grb_profiles.html). *Top right*: example of a deconvolved spectrum from the CGRO detectors, shown both as photon flux $N_{\rm E}$ and in $E^2 N_{\rm E} \propto \nu f_\nu$ units (Briggs et al. 1999). *Bottom*: GRB classification in short and long depending on their T_{90} and BATSE HR (Kouveliotou et al. 1993). The solid line shows long GRBs (T_{90} >2 s) and the dotted line the short GRBs (T_{90} <2 s). The dashed lines corresponded to the mean HR of the two classes of GRBs.

spectral hardness ratio (HR), that is the ratio between the photons observed in the hard and soft energy band. It depends on the considered instrument, for example the BATSE HR is conventionally defined as the ratio of photons observed in channel 3 (100-300 keV) and those observed in channel 2 (50-100 keV) (HR32, Fig. 1.1). Short GRBs are harder than long GRBs.

The prompt emission light curves (LCs) are highly variable and show a great variety of temporal profiles, ranging from the most simple single-peaked structures to the most complex one, with a time variability down to 1 ms (Piran 2004) (Fig. 1.1).

1.2.2 The afterglow

The afterglow shows a different behavior than the prompt one, softening from X-rays to optical to radio. For the X-ray and the optical LCs, we can define the temporal slope as the slope of the LC.

The X-ray emission[9]**.** $\sim$ 30% of X-ray LCs show a canonical behavior (Nousek et al. 2006; Zhang et al. 2006) (Fig. 1.2):

1. *Steep decay phase.* The temporal slope of this phase is $\sim$3 (or steeper) and lasts until 100-1000 s after the trigger. Sometimes this segment has a softer spectrum than the other parts of the LC (e.g., $\beta_{\rm X} \sim 1.5$).

2. *Shallow decay phase or plateau.* Its temporal slope is $\sim$0.5, with a spectral slope $\beta_{\rm X} \sim 1$. This phase begin at $\sim$100-1000 s after the trigger, lasting until 10^4 s.

3. *Normal decay.* The normal decay has a typical slope of $\sim$1.5 and $\beta_{\rm X} \sim 1$.

4. *Post jet break phase.* Some times, at late time ($\sim 10^6$ s) the X-ray LC steepens. The break to this phase is a signature of non-spherical emission (see below).

5. *Flares.* They are in $\sim$30% of XRT LCs (Chincarini et al. 2010a; Margutti et al. 2013). Flares are in the LCs of both long and short LCs (Margutti et al. 2011a), and also late time flares (e.g $t_{pk} \gtrsim 1000$ s) have been observed (Bernardini et al. 2011).

The optical emission[10]**.** Many facilities in the past have been designed to detect and observe the optical counterpart of GRBs. Some examples are UVOT, the Robotic Optical Transient Search Experiment (ROTSE-III, Akerlof et al. 2003), the Rapid Eye Mount telescope (REM, Zerbi et al. 2001; Chincarini et al. 2003), the Gamma-Ray Burst Optical/Near-Infrared detector (GROND, Greiner et al. 2008), the Liverpool (LT) and Faulkes telescopes (Gomboc et al. 2006), the Télescopes à Action Rapide pour les Objets Transitoires (TAROT, Klotz et al. 2008b), etc. The main characteristics of the optical counterparts revealed with these facilities are:

- Optical and X-ray LCs are different at early times in the majority of the cases (Melandri et al. 2008b; Rykoff et al. 2009; Oates et al. 2009, 2011). In particular, Oates et al. (2009, 2011) noted that before 500 s after the trigger the optical LCs can decay or rise, instead they only decay after this time. Panaitescu & Vestrand (2008, 2011) subdivided optical LCs depending of their initial behavior (peak or plateau phase). Peaks were associated to impulsive ejecta releases, instead plateau phases to the energy released by a long-lived central engine.

- There are achromatic and chromatic breaks in the optical and X-ray LCs (Melandri et al. 2008b; Rykoff et al. 2009; Oates et al. 2009, 2011; Panaitescu & Vestrand 2011), that is the breaks occur at the same time or not, respectively, in the optical and X-ray LCs.

- The brightest optical LCs decay fastest (Oates et al. 2009, 2011, 2012).

[9] For more details see Margutti et al. (2013) and Chap. 2

[10] For more details See Chap. 3.

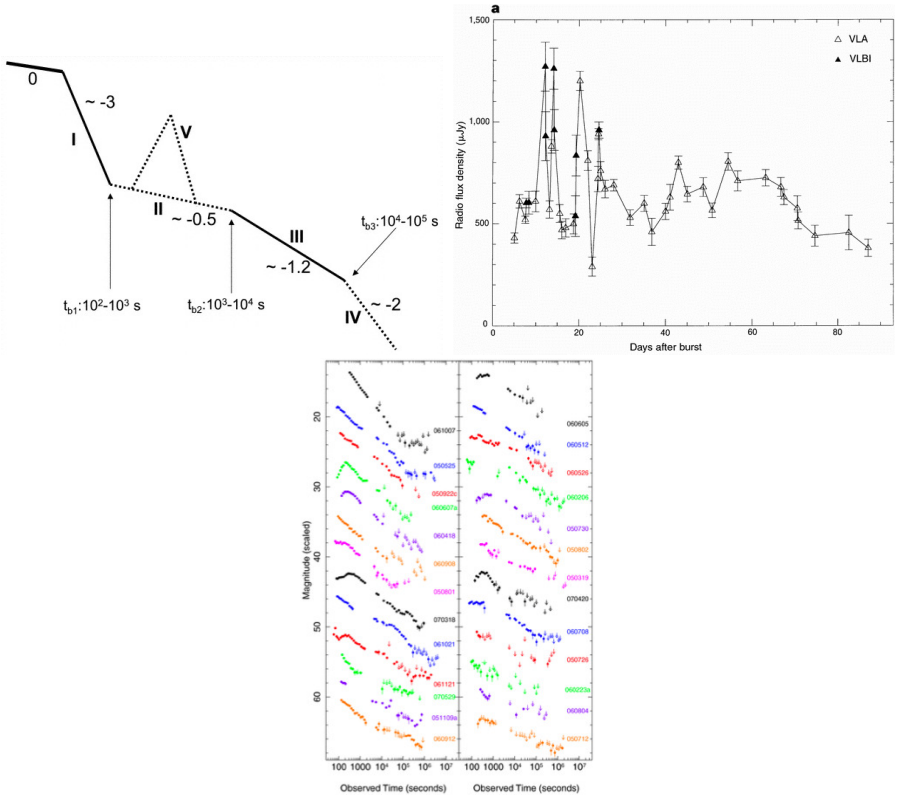

Figure 1.2: Afterglow properties. *Top left*: synthetic cartoon of the X-ray light curve based on the observational data from the *Swift*/XRT (Zhang et al. 2006). The phase "0" denotes the prompt emission, "I" is the steep decay phase, "II" the shallow decay phase or plateau, "III" the normal decay, "IV" the post jet-break phase and "5" the flaring phase. Typical temporal indices in the four segments are indicated in the figure. *Top right*: radio LC of GRB970508 (Frail et al. 1997). *Bottom*: some examples of optical LCs (Oates et al. 2009).

- When the optical and X-ray LCs do not have the same slopes, X-ray LCs decay faster then the optical ones (Oates et al. 2009, 2011; Panaitescu & Vestrand 2011).

- In some cases, the X-ray LC shallow phase corresponds to the optical shallow phase (Rykoff et al. 2009; Li et al. 2012).

- Optical LCs sometimes show flares (Li et al. 2012).

- Some authors claimed a bimodal distribution of the luminosities at one day after the trigger (Liang & Zhang 2006; Nardini et al. 2006; Kann et al. 2006). Recent studies rule out this possibility (Melandri et al. 2008b; Oates et al. 2009, 2011; Kann et al. 2010b, 2011).

- A class of dark GRBs exists: they are characterized by a low optical flux compared to the X-ray value. They are defined as GRBs with a optical/X-ray spectral index $\beta_{\rm op,X} < 0.5$ (Jakobsson et al. 2004) or $\beta_{\rm X} -$

$0.5 < \beta_{\rm op,X} < \beta_{\rm X}$ (van der Horst et al. 2009). These GRBs are dark mainly because of the host galaxy extinction (Melandri et al. 2008b, 2012; Cenko et al. 2009a; Greiner et al. 2011a).

Some examples of the optical LCs are shown in Figure 1.2.

The radio emission. The radio observations first allow to prove that the region emitting the GRB radiation must be expanding relativistically (Figure 1.2, Frail et al. 1997) and to follow the evolution of the relativistic wave for a longer time than for other bands (e.g. GRB 030329, van der Horst et al. 2007). In addition we can constrain the evolution of the peak flux of the synchrotron spectrum, and its self-absorption and peak frequencies (e.g. Staley et al. 2012).Recently, Chandra & Frail (2012) collected a sample of 304 radio afterglows observed from 1997 until 2011, the majority of which in the cm-band. They found that for long GRBs the canonical radio LC at 8.56 GHz (∼3.5 cm) has a peak between three and six days in the rest frame, where the afterglow has a median luminosity of 10^{31} erg s^{-1} Hz^{-1}. After ∼10-20 days the LC decays with a slope ∼1. The detectability of the radio observations is related to the X-ray and optical fluxes: the GRBs with detected radio emission have, on average, brighter X-ray and optical fluxes (Chandra & Frail 2012). Detailed information about radio afterglows will be provided by the ALMA observations in the mm- and submm-band (e.g. de Ugarte Postigo et al. 2012) and EVLA (e.g. Chandra & Frail 2012).

1.2.3 Subclasses of gamma-ray bursts

As shown in Sec. 1.2.1, GRBs are usually subdivided into two groups, long and short, depending on the duration of the prompt emission ($T_{90} > 2$ s for long GRBs and $T_{90} < 2$ s for short GRBs) and the hardness of their γ-ray spectrum (short GRBs are harder than long GRBs).

Short GRBs are less energetic than long GRBs both in the γ-rays ($E^{\rm short}_{\gamma,\rm iso} \sim 10^{50}$ erg, $E^{\rm long}_{\gamma,\rm iso} \sim 10^{52}$ erg) and the X-rays ($E^{\rm short}_{\rm X,iso} \sim 10^{50}$ erg, $E^{\rm long}_{\rm X,iso} \sim 10^{52}$ erg) and less luminous (of a factor two)[11]. Both show flares in their X-ray LCs, with short GRB flares two order of magnitude less energetic than long GRB flares. The prompt emission and the X-ray flares of short and long GRBs seem to originate from a similar dissipation and/or emission mechanism (e.g. Chincarini et al. 2010a; Margutti et al. 2011b).

Short GRBs explode in every kind of galaxies, instead long GRBs only in late type galaxies and they are associated with supernovae (SNe)[12] . From these observational facts, short GRBs are thought to originate from the merger of compact objects, as neutron stars (NS) or black holes (BH), while long GRBs from the collapse of a massive stars[13].

Another class of GRBs are the X-ray flashes (XRF), which are bursts with a temporal behavior similar to long GRBs, but are less energetic. Their X-ray

[11] For details about short and long GRB energetic and luminosity See Sec. 2.4.1-C.10

[12] For details about the GRB environment, see Sec. 1.2.4

[13] For details about GRB progenitors, see Sec. 1.3.2.

fluxes are in the same range of long GRBs ($\sim 10^{-7} - 10^{-8}$ erg s^{-1} cm^{-2}), but their peak energy is less than 40 keV.

1.2.4 The environments

Short GRBs. Short GRBs can explode in every kind of galaxy, early- or late- type, field or cluster galaxies, with a star formation rate (SFR) lower than that of long GRBs ($\mathrm{SFR_{short}} < 1\ M_\odot\ \mathrm{yr}^{-1}\ (L/L_*)^{-1}$, with L_* the characteristic luminosity of the galaxy) (Nakar 2007). The principal properties of the host galaxies of the short GRBs are (Fong et al. 2010; Berger 2011): *a)* the majority of the short GRB hosts are star forming galaxies, even if different from long GRB hosts and they resemble the general field galaxy population; *b)* some short GRB host galaxies are elliptical; *c)* the physical offsets are five times larger than those for long GRBs and the distribution of the observed offsets supports the predictions for NS-NS binary mergers; *d)* short GRBs occur in parts of the host galaxies less luminous than those for long GRBs and they are more correlated to the rest-frame optical light (old stars) than the UV light (young massive stars). Therefore, the short GRB progenitors may belong to old stellar population with a large interval of ages and generally track the stellar mass. These findings support the NS-NS binary merger scenario and exclude a dominant population of prompt magnetars, even if the data cannot exclude a partial contribution from delayed magnetar formation or accretion-induced collapse (Fong et al. 2010; Berger 2011).

Long GRBs. Long GRBs occur in star forming, blue, generally faint, small and irregular galaxies (Fruchter et al. 1999, 2006; Bloom et al. 2002; Le Floc'h et al. 2003; Christensen et al. 2004; Castro Cerón et al. 2006, 2010; Savaglio et al. 2009), in particular GRBs explode within the UV-bright parts of the host galaxies (Bloom et al. 2002; Fruchter et al. 2006). Therefore GRBs take place in similar regions of the type-Ic SNe (Kelly et al. 2008), consistent with the connection between long GRBs and SNe. In addition, the GRB hosts typically are fainter and with lower metallicities than Lyman-break galaxies in a determined redshift interval (Jakobsson et al. 2005; Savaglio 2006; Fynbo et al. 2008). The study of the host galaxies improved with the study of the host of the *dark GRBs*, which have very obscured afterglows due to the strongly absorbing regions along the line of sight (Fynbo et al. 2001; Cenko et al. 2009a; Fynbo et al. 2009; Jakobsson et al. 2004, 2006c; Perley et al. 2009a; Krühler et al. 2011; Greiner et al. 2011b; Svensson et al. 2012). To minimize the problem of optically biased samples, the TOUGH program (Hjorth et al. 2012) was developed. They selected 69 host galaxies, using the selection criteria introduced by Jakobsson et al. (2006c) and Fynbo et al. (2009)[14]. The mean

[14]Selection criteria (Hjorth et al. 2012): *(a)* Long GRBs ($T_{90} > 2$ s, Sakamoto et al. 2011) triggered by *Swift*-BAT, with a detected X-ray afterglow and position location avaible less than 12 hr after the trigger. *(b)* The Galactic foreground optical extinction must be $A_V \leq 0.5$ mag (Schlegel et al. 1998), the distance on the sky, between the GRB and the Sun at the time of explosion, must be more than 55° and the host galaxies are not contaminated by nearby stars or bright objects. *(c)* The GRBs triggered between March 1, 2005 and

redshift of this sample is $\langle z \rangle = 2.3$ (Krühler et al. 2012) (lower than early *Swift* results, Jakobsson et al. 2006c) and the star-formation rate (SFR) calculated by Milvang-Jensen et al. (2012) is $\sim 0.6-2.3\ M_\odot\ \mathrm{yr}^{-1}$. The GRB rate at redshift $z \gtrsim 3$ seems greater than that predicted assuming that it should follow conventional determinations of the star formation history of the universe, combined with an estimate of its likely metallicity dependence (Kistler et al. 2009; Virgili et al. 2011; Robertson & Ellis 2012; Jakobsson et al. 2012). This suggests that either star formation at high redshifts has been significantly underestimated, for example due to a dominant contribution from faint, undetected galaxies, or that GRB production is enhanced in the conditions of early star formation, beyond that usually ascribed to lower metallicity (Jakobsson et al. 2012). From the radio observation ($z \lesssim 1$) (Michałowski et al. 2012) the SFR is $< 100\ M_\odot\ \mathrm{yr}^{-1}$ for the 63% of the cases, $> 500\ M_\odot\ \mathrm{yr}^{-1}$ for the 8% of the hosts and $< 15\ M_\odot\ \mathrm{yr}^{-1}$ for the radio undetected hosts. Moreover, the TOUGH galaxies are fainter (Milvang-Jensen et al. 2012) than Lyman-break galaxies of previous studies (Shapley et al. 2003) and the Lyα emission is not obiquitous (Milvang-Jensen et al. 2012), in contrast with previous works (Fynbo et al. 2003; Jakobsson et al. 2005); this could be connected to the presence of dust and the weakness of the Lyα line. Finally, because the GRB population is similar to other star-forming galaxies, GRBs (at least at $z \lesssim 1$) can trace a large fraction of all star-formation, being less biased indicators than once though (Michałowski et al. 2012).

Dark GRBs. In general *dark* GRBs are object wothout an optical or infrared afterglow, because of different factors (Perley et al. 2009a; Greiner et al. 2011a; Melandri et al. 2012): *a)* the GRBs have a high redshift ($\gtrsim 5$) (Greiner et al. 2009a; Tanvir et al. 2009; Salvaterra et al. 2009; Cucchiara et al. 2011a); *b)* they have large dust column densities (Klose et al. 2000, 2003; Tanvir et al. 2008; Perley et al. 2011); *c)* they are intrinsically faint (Panaitescu et al. 2006; Ghisellini et al. 2009; Nardini et al. 2010). The first studies of dark GRB hosts indicated that these galaxies are similar to the hosts of the other optically bright GRBs (Berger et al. 2003; Le Floc'h et al. 2003; Perley et al. 2009a). Recent works (Perley et al. 2010; Rossi et al. 2012; Krühler et al. 2011) claim that dark GRB hosts are on average redder, more luminous and massive than the hosts of optically bright GRBs. In particular, Krühler et al. (2011) suggest that previous host samples miss of the massive and metal rich galaxies.

1.2.5 The correlations

GRBs are extragalactic objects (Metzger et al. 1997) and they are observed also at very high redshifts (Salvaterra et al. 2009; Tanvir et al. 2009; Cucchiara et al. 2011b). GRBs can be used as cosmological probes of the star formation rate (Totani 1997; Paczynski 1998; Bromm & Loeb 2002) and they can be

August 10, 2007, the declination range must be $-70^\circ < \delta < +27^\circ$ (J2000.0) and the X-ray localization uncertainty must be better than or equal to 2 arcsec (90% error radius).

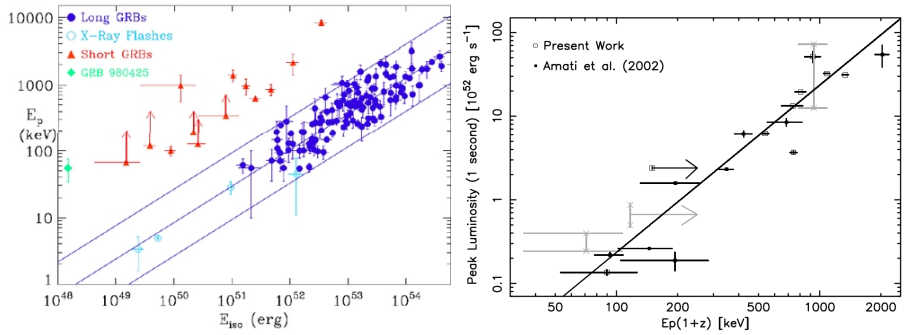

Figure 1.3: *Left*: correlation between the peak energy ($E_{\rm pk}$) and the isotropic prompt emission energy ($E_{\rm p}$) (Amati et al. 2009). *Blue dots*: long GRBs. *Red triangles*: short GRBs. *Light blue empty dots*: X-ray flashes. *Green diamond*: GRB 980425. *Blue line*: best fit for long GRBs. *Right*: correlation between the rest frame peak energy ($E_{\rm p}(1+z)$) and the peak luminosity (Yonetoku et al. 2004). *Black open squares*: BATSE data. *Black filled squares*: results of *Beppo*SAX (Amati et al. 2002). *Gray crossed*: results of GRBs with ambiguous redshifts (GRB 980326, GRB 980326, and GRB 000214). *Solid line*: the best-fit power-law model.

used to constrain the cosmological parameters (Liang & Zhang 2005, 2006; Amati et al. 2008). A way to investigate these problems and to analyze the reliability of proposed GRB models is to identify different correlations which involve prompt and afterglow emission parameters.

γ-ray correlations. Various authors have investigated the prompt emission properties to looking for some reliable correlations (Amati et al. 2002; Yonetoku et al. 2004; Ghirlanda et al. 2004; Firmani et al. 2006). The first attempt to relate the temporal and spectral properties of the prompt emission were done by Norris et al. (2000), who proposed the anticorrelation between the peak luminosity and the spectral lag, and by Fenimore & Ramirez-Ruiz (2000) and Reichart & Lamb (2001), who suggested the existence of a correlation between the peak luminosity and the temporal variability. The first and "stable" in time correlation found was the "Amati relation" (Amati et al. 2002; Amati 2006; Amati et al. 2009) which correlates the isotropic prompt energy ($\rm E_{\gamma,iso}$) and the rest-frame νF_ν spectrum peak energy ($E_{\rm pk}$). This relation is followed by long GRBs observed by different instruments (from the *Beppo*SAX sample to *Fermi* GRBs); short and sub-energetic[15] GRBs are outliers of this relation. This property could be used to distinguish GRBs from different classes and progenitors and to constrain the cosmological parameters (Amati et al. 2008). Yonetoku et al. (2004) discussed the connection between the peak energy ($E_{\rm pk}$) with the peak luminosity ($L_{\rm pk}$) and used this relation to estimate GRB redshifts and GRB formation rate. Ghirlanda et al. (2004) considered the GRB jet opening angle and calculated the collimated-corrected energy ($E_\gamma = E_{\gamma,iso}(1-\cos\theta)$). This quantity correlates tightly with $E_{\rm pk}$; to calculate the opening angle they used the relation found for the standard

[15] In particular, GRB 980425 and 031203.

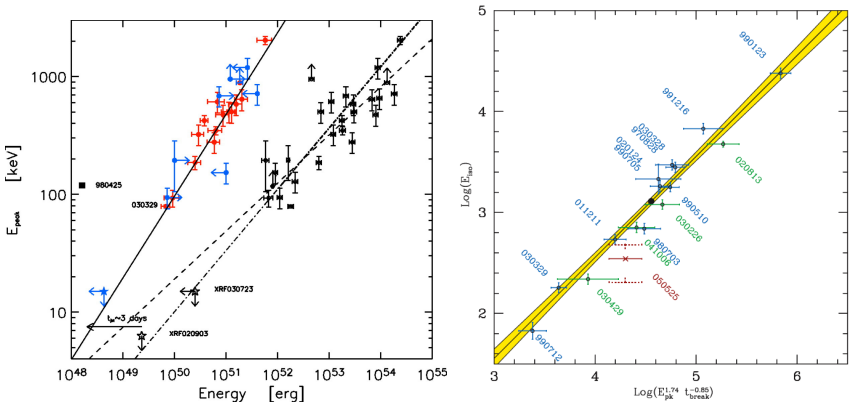

Figure 1.4: *Left*: correlation between the rest frame peak energy ($E_{\rm peak} = E^{\rm obs}_{\rm peak}(1+z)$) and the bolometric energy (Ghirlanda et al. 2004). *Red filled circles*: isotropic energy corrected by the collimation angle by the factor $(1-\cos\theta)$. *Blue filled circles*: lower/upper limits. *Solid line*: best fit to the correlation. *Open circles*: isotropic equivalent energy ($E_{\gamma,\rm iso}$). *Dashed line*: best fit to the open circles. *Dot-dashed line*: Amati relation (Amati et al. 2002). *Right*: relation between the peak luminosity ($L_{\rm iso}$), the peak energy ($E_{\rm pr}$) and the "high-signal" time scale ($T_{0.45}$) (Firmani et al. 2006). *Blue crosses*: GRBs with a good determination of the bolometric correction. *Green crosses*: GRBs with uncertain bolometric correction. *Solid line*: best fit. *Yellow area*: 1σ uncertainty of the fit.

model (Sari et al. 1999). Firmani et al. (2006) studied the links between different prompt emission parameters: the bolometric corrected luminosity ($L_{\rm pk}$), the "high signal" time-scale ($T_{0.45}$), the variability of the γ-ray light-curves (V), $E_{\gamma,\rm iso}$ and $E_{\rm pk}$. Fig. 1.3-1.4-1.5 portraits some correlations published in the literature.

X-rays correlations. The only recognized correlation involving only afterglow properties is the "Dainotti relation" (Dainotti et al. 2008, 2010) that links together the luminosity at the end of the plateau phase of the X-ray light curves ($L_{\rm f}$) and the plateau rest-frame end time ($t^{\rm RF}_{\rm f}$) (Fig. 1.5). This relation is predicted by some models, such as Cannizzo & Gehrels (2009); Ghisellini et al. (2009); Dall'Osso et al. (2011); Bernardini et al. (2012a). In the magnetar scenario (Dall'Osso et al. 2011) this anti-correlation reflects the spin-down of the magnetic dipole. In fact, NSs with greater spin-down luminosity will have a shorter spin-down time-scale. The more luminous afterglows would not have the plateau phase and, for a given $t_{\rm f}$, smaller initial rotational energy (so larger magnetic fields) favours the lack of the plateau phase.

From the comprehensive statistical analysis of all the X-ray light curves observed by the *Swift*/XRT made by Margutti et al. (2013) other correlations were found. For a detailed discussion See Chap. 2.

Prompt vs. afterglow emission. The prompt-afterglow parameter correlations are very useful to know if the afterglow emission is influenced by the prompt phase. An attempt to throw light on this question has been made by various authors (Nysewander et al. 2009a; Gehrels et al. 2008; Dainotti

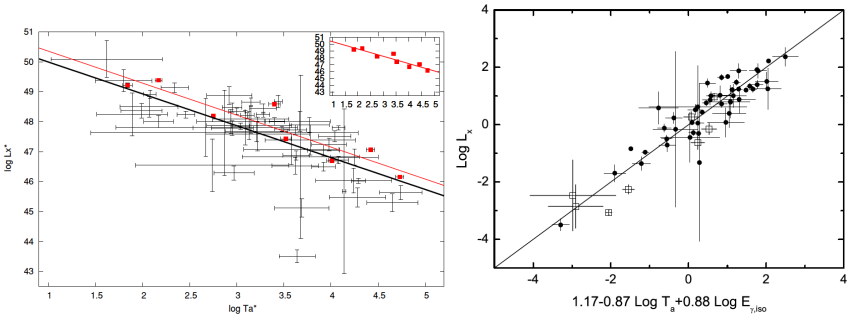

Figure 1.5: *Left*: correlation between the X-ray end plateau luminosity (L_{X*}) and time (T_a^*) (Dainotti et al. 2010). *Black points*: long GRBs. *Black line*: best fit of the data. *Red squares*: eight lower error points. *Red line*: fit of the red squares, which forms approximately an upper envelope of the full distribution. *Inset*: the upper envelope points with the fitted line. *Right*: relation between the X-ray end plateau luminosity (L_X, 10^{47} erg s^{-1}), time (T_a, 10^3 s), and isotropic prompt emission energy ($E_{\gamma,iso}$, 10^{53} erg) (Xu & Huang 2012). *Solid line*: best fit function. *Filled points*: long GRBs. *Empty squares*: intermediate class of GRBs.

et al. 2011; Xu & Huang 2012; Bernardini et al. 2012b; Margutti et al. 2013). Xu & Huang (2012) found a relation between the end plateau luminosity and time and the isotropic prompt emission energy (L_f, t_f, $E_{\gamma,iso}$) (Fig. 1.5). Dainotti et al. (2011) searched correlations between different prompt and afterglow timescales, luminosities and energies to find useful quantities to select a standard sample to constrain the cosmology and the astrophysical models. Bernardini et al. (2012b) and Margutti et al. (2013) found a new correlation between the X-ray energy ($E_{X,iso}$), E_{pk} and $E_{\gamma,iso}$; for details See Chap. 2.

1.3 Models and Theory

The mechanisms behind GRB production is still largely unknown, although these are several ingredients which are common to most models (e.g. Piran 2004):

- the emitting source expands with relativistic velocity;
- the afterglow emission is produced by synchrotron radiation of relativistic electrons accelerated in the shocks;
- the necessary energy for the GRB and its afterglow is acquired by the dissipation of the energy of the relativistic flow: the burst is powered by internal shock energy (e.g. Sari & Piran 1997), that is shocks within the jet itself, while the afterglow by the external shocks with the circumburst medium (e.g. Sari et al. 1998).
- the energy source is likely related to a compact object (central engine) (e.g. Paczynski 1986; Woosley 1993) and long GRBs are associated with supernovae (e.g. Woosley & Bloom 2006).

- in some afterglow LCs, there are monochromatic breaks followed by a steeper decline, interpreted as "jet breaks", that is the beaming angle of the jet exceeds the physical collimation angle (e.g. Rhoads 1999; Sari et al. 1999).

Critical points on the description of the GRB phenomenon are (e.g. Lyutikov 2009; Zhang 2011):

- the outflow energy density may be distributed among electron-positron pairs, photons, protons and the electromagnetic field. The standard fireball model (Sari et al. 1998; Piran 1999) assumes that the major contribution comes from an opaque photon-lepton plasma loaded with baryons (a"fireball"). In this case, photons decouple from the fireball when it becomes transparent, and the remaining protons continue their expansion arranged in shells characterized by different Lorentz factors. When the faster shells reach the slower shells, internal shocks within the flow occur, producing he prompt emission. If the outflow is poynting flux dominated, the internal energy is released in episodes of magnetic reconnection. Then the jet expands and collides with the external medium, creating the afterglow emission. The emission mechanism involved for the prompt and the afterglow is the synchrotron, since the accelerated electrons interact with the local magnetic field. On the other hand, if the dominant component is the magnetic field, the GRB radiation is powered by the rotational kinetic energy of the central source and the energy is not dissipated in the shocks but through current-driven instabilities (Lyutikov & Blackman 2001; Lyutikov 2006). Zhang & Yan (2011) proposed the Internal Collision-induced MAgnetic Reconnection and Turbulece (ICMART) model, which consider a high magnetized flow, with variable Lorentz factors; other models consider the emission from the photosphere, which is quasi-thermal and influence the prompt emission (e.g. Rees & Mészáros 2005; Ryde et al. 2006);

- the internal-external shock model is not efficient in the conversion of the initial kinetic energy into the observed radiation: if the efficiency is too low, an initial energy greater than 10^{53} erg is needed to explain the observations (Piran 2004). This can be solved by considering that the emission is beamed. Moreover, a high efficiency is necessary to form the plateau phases observed in the X-ray LCs .

- it is debated how to classify the GRBs. For example the subdivision between long and short GRBs could be influenced by the definition of the t_{90}, which relies on the detector: GRB pulses are typically broader at lower energies (Zhang 2011). Otherwise this classification is well established by the observation of the host galaxies (Sec. 1.2.4) and their afterglow (Sec. 1.2.2). T_{90} classification does not seem sufficient to capture the complexity of the long/short GRB division, and that new classification schemes has been proposed attempting to focus on the progenitor rather than on the mere duration. The classification scheme by Bloom et al. (2008) is basically not applicable to most GRBs.

1.3.1 The standard fireball model

In the standard fireball model (Rees & Meszaros 1992; Sari et al. 1998; Mészáros 2006) a relativistic fireball expands in the circum-burst medium and the prompt emission is generated by internal shocks in the baryon-dominated ejecta (Rees & Meszaros 1994), while the afterglow emission rises in the forward shock (Sari et al. 1998) (internal-external shock scenario). The mechanism that produces the observed multi-wavelengh non-thermal spectrum is the synchrotron process.

The GRB spectrum is non-thermal and indicates than the source must be optically thin. The **compactness problem** rises when we compute the optical depth of the GRB source and we find that it is optically thick. If we have a gas of photons with high energy, $\epsilon > m_e c^2$, if the density is large enough we have pair production of type $\gamma + \gamma \rightarrow e^+ + e^-$. The optical depth, $\tau = k\rho\ s$ can be written in this case as

$$\tau_{\gamma\gamma} = f_{2\mathrm{m_e c^2}} n_\gamma \sigma_{\mathrm{Th}} R, \tag{1.2}$$

where $f_{2\mathrm{m_e c^2}}$ is the fraction of photons at very high energies greater than $2m_e c^2$, n_γ the numerical density of the energetic photons and R the source size. The photon energy density is $\approx 4\pi d^2 F/(E_\gamma c^2 \delta t)$, with d the object distance, F the observed fluence, E_γ the typical photon energy and δt the variability timescale. The source size R is estimated by the variability timescale, $R < c\delta t$. If the variability is smaller than the diameter of the source then the coherence is lost. Therefore, using the typical values for GRBs ($\delta t \sim 10$ ms, $R \sim 3000$ km, $F \sim 10^{-7}$ erg cm^{-2}), we obtain

$$\tau_{\gamma\gamma} = \frac{f_{2\mathrm{m_e c^2}} \sigma_{\mathrm{Th}} D^2}{R^2 m_e c^2} \tag{1.3}$$

$$= 10^{13} f_{2m_e c^2} \left(\frac{F}{10^{-7}\ \mathrm{erg\ cm^{-2}}}\right) \left(\frac{D}{3000\ \mathrm{Mpc}}\right) \left(\frac{\delta t}{10\ \mathrm{ms}}\right). \tag{1.4}$$

This very large optical depth is inconsistent with observations and we would not detect any emission from the source. This problem is solved if we require a relativistic expansion. In fact, the observed photons are blue-shifted, so their energy is $\approx h\nu_{\mathrm{obs}}/\Gamma$; also the source size must be corrected and it is $\approx c\delta t \Gamma^2$. Introducing this correction in Eq. 1.4, we have an optical thin source ($\tau < 1$), if $\Gamma > 100$.

In the internal-external shock scenario, multiple shells at different speeds are ejected from the central engine. The **internal shocks** originate when the faster shells catch up the slower shells (Rees & Meszaros 1994) and produce the prompt emission. This occurs at $r_{\mathrm{dis}} \sim c t_{\mathrm{v}} \eta^2 \sim 3 \times 10^{14} t_{\mathrm{v},0} \eta^2$ cm, with $c t_{\mathrm{v}}$ the initial separation of two shells and $\eta = L_0/M_0 c^2$ the entropy for an outflow rate L_0 and mass loss rate $\dot{M}_0 = \mathrm{dM_0/dt}$ (Mészáros 2006). The internal shocks can explain the fast temporal variability of prompt emission LCs.

When the outflow interacts with the interstellar medium (**external shocks**), the afterglow is emitted as synchrotron radiation (Granot et al. 1999; Wijers

& Galama 1999; Panaitescu & Kumar 2001) because of the synchrotron mechanism (for details See Appendix B). For the simple case in which the the external medium has a constant density, the expected spectra and light curves are (Fig. 1.3.1):

- For the spectra, Sari et al. (1998) obtained:
  Fast cooling regime ($\gamma_{e,\min} > \gamma_{e,c}$)

$$F_\nu = \begin{cases} (\nu/\nu_c)^{(1/3)} F_{\nu,\max}, & \nu_c > \nu \quad \text{(B)} \\ (\nu/\nu_c)^{(-1/2)} F_{\nu,\max}, & \nu_m > \nu > \nu_c \quad \text{(C)} \\ (\nu_m/\nu_c)^{(-1/2)} (\nu/\nu_m)^{(-p/2)} F_{\nu,\max}, & \nu > \nu_m \quad \text{(D)} \end{cases} \tag{1.5}$$

  Slow cooling ($\gamma_{e,\min} > \gamma_{e,c}$)

$$F_\nu = \begin{cases} (\nu/\nu_m)^{(1/3)} F_{\nu,\max}, & \nu_m > \nu \quad \text{(F)} \\ (\nu/\nu_m)^{(-(p-1)/2} F_{\nu,\max}, & \nu_c > \nu > \nu_m \quad \text{(G)} \\ (\nu_c/\nu_m)^{(-(p-1)/2)} (\nu/\nu_c)^{(-p/2)} F_{\nu,\max}, & \nu > \nu_c \quad \text{(H)} \end{cases} \tag{1.6}$$

- For the light curve:
  High frequency ($\nu > \nu_0$, $t_0 > t_m > t_c$)

$$F_\nu \propto \begin{cases} t^{1/6}, & t < t_c \quad \text{(B)} \\ t^{-1/4}, & t_c < t < t_m \quad \text{(C)} \\ t^{(2-3p)/4}, & t_m < t < t_0 \quad \text{(D)} \\ t^{(2-3p)/4}, & t > t_0 \quad \text{(D).} \end{cases} \tag{1.7}$$

  Low frequency ($\nu < \nu_0$, $t_0 < t_m < t_c$)

$$F_\nu \propto \begin{cases} t^{1/6}, & t < t_0 \quad \text{(B)} \\ t^{1/2}, & t_0 < t < t_m \quad \text{(F)} \\ t^{3(1-p)/4}, & t_m < t < t_c \quad \text{(G)} \\ t^{(2-3p)/4}, & t > t_c \quad \text{(D).} \end{cases} \tag{1.8}$$

The letter refers to the corresponding segments in the spectrum (Fig. 1.3.1). Comparing the relations that refer to a determined spectral phase (indicated by a letter) we can find the relations between the spectral index (β) and the relative temporal index (α) ($F_\nu \propto t^{-\alpha}\nu^{-\beta}$), that are the **closure relations** for the two regimes (fast and slow cooling) in the case that the medium around the burst is the interstellar medium (ISM) and that there is no energy injection (Zhang et al. 2006). The relations are listed in Tab. 1.1. This relations are useful to determine whether the afterglow can be explained with the standard model (Sari et al. 1998) or not.

Since GRBs may originate from the core collapse of a massive star (long GRBs), the circumburst medium is expected to be shaped by the effect of the stellar wind from the progenitor (Chevalier & Li 2000). In this case the medium has not a constant density, but $\rho = Ar^{-s}$, where $A = \dot{M}_w/4\pi V_w = 5 \times 10^{11} A_*$ g cm^{-2} is a constant, with $\dot{M}_w$ the mass-loss rate, V_w the wind velocity and A_* the wind parameter; the reference values for these parameters

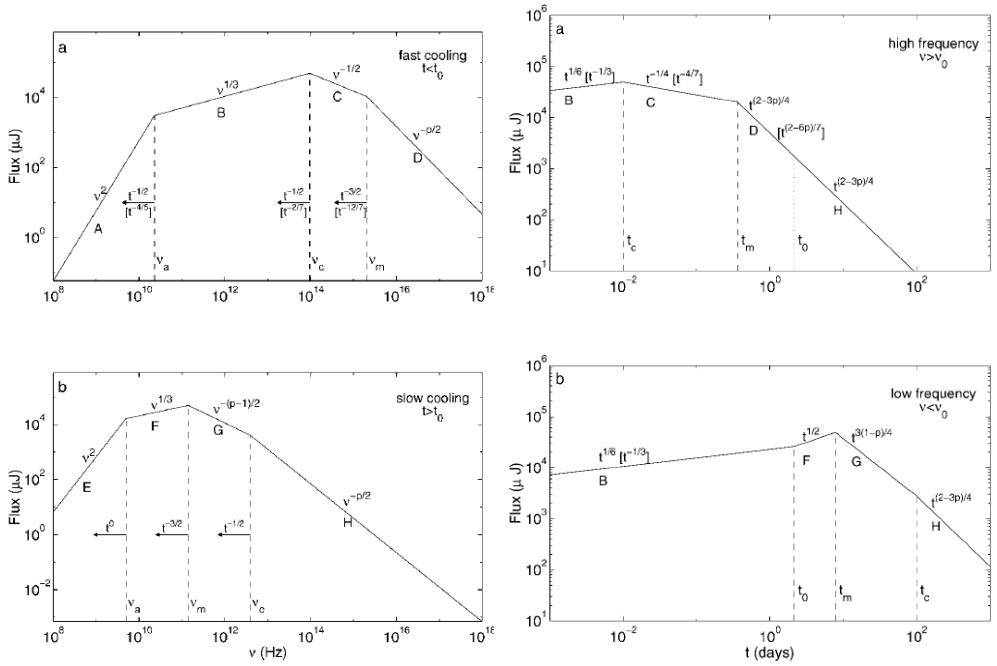

Figure 1.6: Uniform interstellar medium (Sari et al. 1998). Left: Synchrotron spectrum of a relativistic shock with a power-law electron distribution. (a) Fast cooling, which is expected at early times ($t < t_0$). The spectrum consists of four segments, identified as A, B, C, and D. Self-absorption is important below $\nu_{\rm a}$. The frequencies, $\nu_{\rm m}$, $\nu_{\rm c}$, and $\nu_{\rm a}$, decrease with time as indicated; the scalings above the arrows correspond to an adiabatic evolution, and the scalings below, in square brackets, correspond to a fully radiative evolution. (b) Slow cooling, which is expected at late times ($t > t_0$). The evolution is always adiabatic. The four segments are identified as E, F, G, and H. Right: Synchrotron light curve (ignoring self-absorption). (a) High-frequency case ($\nu > \nu_0$). The four segments that are separated by the critical times, $t_{\rm c}$, $t_{\rm m}$, and t_0 , correspond to the spectral segments in the left panel with the same labels (B, C, D, and H). The observed flux varies with time as indicated; the scalings within square brackets are for radiative evolution (which is restricted to $t < t_0$), and the other scalings are for adiabatic evolution. (b) Low-frequency case ($\nu < \nu_0$).

are $\dot{M}_{\rm w} = 1 \times 10^{-5} M_\odot$ yr^{-1} and $V_{\rm w} = 1000$ km s^{-1} (this values are for a Wolf-Rayet star, see Chevalier & Li 1999). For this model, the representative equations are:

- For the spectra:
  Fast cooling

$$F_\nu \propto \begin{cases} \nu^{-1/3}, & \nu < \nu_{\rm c} \quad \text{(a)} \\ \nu^{-1/2}, & \nu_{\rm c} < \nu < \nu_{\rm m} \quad \text{(b)} \\ \nu^{p/2}, & \nu > \nu_{\rm m} \quad \text{(c)}. \end{cases} \tag{1.9}$$

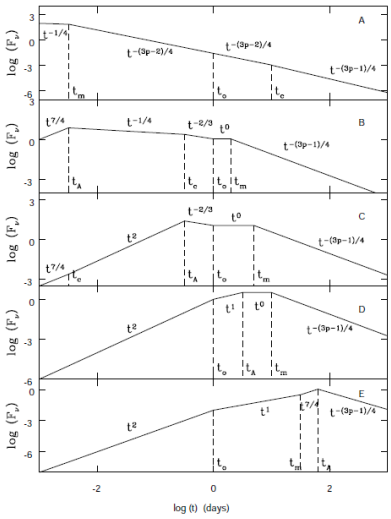

Figure 1.7: Light curves for the wind model (Chevalier & Li 2000). From (A) to (E) the frequency increases.

Slow cooling

$$F_\nu \propto \begin{cases} \nu^{-1/3}, & \nu < \nu_{\rm m} & \text{(d)} \\ \nu^{(p-1)/2}, & \nu_m < \nu < \nu_{\rm c} & \text{(e)} \\ \nu^{p/2}, & \nu > \nu_{\rm c} & \text{(f).} \end{cases} \tag{1.10}$$

- For the lightcurves:
  High frequency (X-ray and optical light curves)

$$F_\nu \propto \begin{cases} t^{-1/4}, & t < t_{\rm m} & \text{(b)} \\ t^{-(3p-2)/4}, & t_{\rm m} < t < t_{\rm c} & \text{(c, f)} \\ t^{-(3p-1)/4}, & t > t_{\rm c} & \text{(e).} \end{cases} \tag{1.11}$$

  Low frequency (radio light curve)

$$F_\nu \propto \begin{cases} t^2, & t < t_0 & \\ t^1, & t_0 < t < t_{\rm a} & \\ t^0, & t_{\rm a} < t < t_m & \text{(a)} \\ t^{-(3p-1)/4}, & t > t_{\rm m} & \text{(b).} \end{cases} \tag{1.12}$$

The letter refers to the corresponding segments in the spectrum. In Fig. 1.3.1 there are the light curves for the wind model from the high energy (type A) to the low frequency (type E). The optical and X-ray light curves usually correspond to type A, instead the radio light curve to type D. In Tab. 1.1 there are the closure relations also for the wind model.

If the central engine continues to emit energy, this is injected into the fireball during the deceleration phase, the fireball keeps being "refreshed", and then it decelerates less rapidly than in the standard phase (Zhang et al. 2006). The energy injection can be caused by the long lasting activity of the

central source, which behaves as $L(t) - L + 0(t/t_{\rm b})^{(} - q)$. In general, for an adiabatic fireball, the injection would influence the blastwave as long as $q < 1$. If the energy injection is caused by the spin-down of a millisecond pulsar (Dai & Lu 1998), $q = 0$, while assumes values between 0 and 1 if the injection is caused by the continued infall onto the central engine BH (Zhang et al. 2006). A gradual energy injection can be achieve if the central engine activity is brief and there is a range of Lorentz factors, since the lower shells arrive much later to the fast shell. In this case the q parameter depends on the amount of ejected mass (see Zhang et al. 2006 for details). In the case of the energy injection, the relations become:

- ISM case:
  Fast cooling

$$F_\nu \propto \begin{cases} \nu_{\rm c}^{-1/3} F_{\nu,\max} \propto (t^{(q-2)/2})^{-1/3} t^{1-q}, & \alpha = \frac{7q-8}{6} \qquad \nu_{\rm c} > \nu \\ \nu_{\rm c}^{1/2} F_{\nu,\max} \propto (t^{(q-2)/2})^{1/2} t^{1-q}, & \alpha = \frac{2-3q}{4} \\ & \nu_{\rm m} > \nu > \nu_{\rm c} \\ (\nu_{\rm m}/\nu_{\rm c})^{(-1/2)} \nu_{\rm m}^{p/2} F_{\nu,\max} & \propto \left(\frac{t^{-(2+q)/2}}{t^{(q-2)/2}}\right)^{-1/2} \\ & \times (t^{-(2+q)/2})^{p/2} t^{1-q}, \\ & \alpha = \frac{(2p-4)+q(p+2)}{4} \qquad \nu > \nu_{\rm m}. \end{cases} \tag{1.13}$$

  Slow cooling

$$F_\nu \propto \begin{cases} \nu_{\rm m}^{-1/3} F_{\nu,\max} \propto & (t^{-(2+q)/2})^{-1/3} t^{1-q}, \\ & \alpha = \frac{5q-8}{6} \qquad \nu_{\rm m} > \nu \\ (\nu_{\rm m})^{(p-1)/2} F_{\nu,\max} \propto (t^{-(2+q)/2})^{1-q}, & \alpha = \frac{q(3+p)+(2p-6)}{4} \\ & \nu_{\rm c} > \nu > \nu_{\rm m} \\ (\nu_{\rm c}/\nu_{\rm m})^{(-(p-1)/2)} \nu_{\rm c}^{p/2} F_{\nu,\max} & \propto \left(\frac{t^{(q-2)/2}}{t^{-(2+q)/2}}\right)^{-(p-1)/2} \\ & \times (t^{(q-2)/2})^{p/2} t^{1-q}, \\ & \alpha = \frac{q(p+2)+(2p-4)}{4} \qquad \nu > \nu_{\rm c} \end{cases} \tag{1.14}$$

- Wind case:
  Fast cooling

$$F_\nu \propto \begin{cases} \nu^{-1/3} F_{\nu,\max}, & \nu < \nu_{\rm c} & \text{(a)} \\ \nu^{1/2} F_{\nu,\max}, & \nu_{\rm c} < \nu < \nu_{\rm m} & \text{(b)} \\ \nu^{p/2} F_{\nu,\max}, & \nu > \nu_{\rm m} & \text{(c).} \end{cases} \tag{1.15}$$

  Slow cooling

$$F_\nu \propto \begin{cases} \nu^{-1/3} F_{\nu,\max}, & \nu < \nu_{\rm m} & \text{(d)} \\ \nu^{(p-1)/2} F_{\nu,\max}, & \nu_{\rm m} < \nu < \nu_{\rm c} & \text{(e)} \\ \nu^{p/2} F_{\nu,\max}, & \nu > \nu_{\rm c} & \text{(f).} \end{cases} \tag{1.16}$$

The closure relations in the case of energy injection are in Tab. 1.2.

GRB Models	β	β ($p = 2.3$)	α	α ($p = 2.3$)	$\alpha(\beta)$
		ISM,	Slow Cooling		
$\nu < \nu_{\rm m}$	$-\frac{1}{3}$		$-\frac{1}{2}$		$\alpha = \frac{3\beta}{2}$
$\nu_{\rm m} < \nu < \nu_{\rm c}$	$\frac{p-1}{2}$	0.65	$\frac{3(p-1)}{4}$	1.0	$\alpha = \frac{3\beta}{2}$
$\nu > \nu_{\rm c}$	$\frac{p}{2}$	1.15	$\frac{3p-2}{4}$	1.2	$\frac{3\beta-1}{2}$
		ISM,	Fast Cooling		
$\nu < \nu_{\rm c}$	$-\frac{1}{3}$		$-\frac{1}{6}$		$\alpha = \frac{\beta}{2}$
$\nu_{\rm c} < \nu < \nu_{\rm m}$	$\frac{1}{2}$		$\frac{1}{4}$		$\alpha = \frac{\beta}{2}$
$\nu > \nu_{\rm m}$	$\frac{p}{2}$	1.15	$\frac{3p-2}{4}$	1.2	$\frac{3\beta-1}{2}$
		Wind,	Slow Cooling		
$\nu < \nu_{\rm m}$	$-\frac{1}{3}$		0		$\frac{3\beta+1}{2}$
$\nu_{\rm m} < \nu < \nu_{\rm c}$	$\frac{p-1}{2}$	0.65	$\frac{3p-1)}{4}$	1.5	$\alpha = \frac{3\beta+1}{2}$
$\nu > \nu_{\rm c}$	$\frac{p}{2}$	1.15	$\frac{3p-2}{4}$	1.2	$\frac{3\beta-1}{2}$
		Wind,	Fast Cooling		
$\nu < \nu_{\rm c}$	$-\frac{1}{3}$		$\frac{2}{3}$		$\alpha = \frac{1-\beta}{2}$
$\nu_{\rm c} < \nu < \nu_{\rm m}$	$\frac{1}{2}$		$\frac{1}{4}$		$\alpha = \frac{1-\beta}{2}$
$\nu > \nu_{\rm m}$	$\frac{p}{2}$	1.15	$\frac{3p-2}{4}$	1.2	$\frac{3\beta-1}{2}$

Table 1.1: The closure relations Zhang et al. (2006) with $F_\nu \propto t^{-\alpha}\nu^{-\beta}$ for the no energy injection case.

Plausible emission mechanisms are the synchrotron self Compton (Waxman 1997; Ghisellini & Celotti 1999) and the inverse Compton (Brainerd 1994; Shemi 1994; Lazzati & Perna 2003).

To describe the **inverse Compton** mechanism we consider the Comptonization parameter $Y = \gamma^2\tau_e$: if $Y < 1$ the inverse Compton is not important, instead for $Y > 1$ this is relevant (Piran 2004). Now we consider the fast cooling regime

$$Y = \frac{\epsilon}{U_B} \quad \text{if} \quad U_e \ll U_B \tag{1.17}$$

$$Y = \sqrt{\frac{U_e}{U_B}} \quad \text{if} \quad U_e \gg U_B \tag{1.18}$$

with U_e and U_B the energy densities of the electrons and magnetic field, respectively. $Y > 1$ when $U_e > U_B$: a large fraction of the low-energy synchrotron photons will be scattered by the inverse Compton and the energy will be re-

GRB Models	β	β ($p = 2.3$)	α	α ($p = 2.3$) ($q = 0.5$)	$\alpha(\beta)$
ISM, Slow Cooling					
$\nu < \nu_{\rm m}$	$-\frac{1}{3}$		$\frac{5q-8}{6}$	-0.9	$\alpha = (q-1) + \frac{(2+q)\beta}{2}$
$\nu_{\rm m} < \nu < \nu_{\rm c}$	$\frac{p-1}{2}$	0.65	$\frac{(2p-6)+(p+3)q}{4}$	0.3	$\alpha = (q-1) + \frac{(2+q)\beta}{2}$
$\nu > \nu_{\rm c}$	$\frac{p}{2}$	1.15	$\frac{(2p-4)+(p+2)q}{4}$	0.7	$\alpha = \frac{q-2}{2} + \frac{(2+q)\beta}{2}$
ISM, Fast Cooling					
$\nu < \nu_{\rm c}$	$-\frac{1}{3}$		$\frac{7q-8}{6}$	-0.8	$\alpha = (q-1) + \frac{(2-q)\beta}{2}$
$\nu_{\rm c} < \nu < \nu_{\rm m}$	$\frac{1}{2}$		$\frac{3q-2}{4}$	-0.1	$\alpha = (q-1) + \frac{(2-q)\beta}{2}$
$\nu > \nu_{\rm m}$	$\frac{p}{2}$	1.15	$\frac{(2p-4)+(p+2)q}{4}$	0.7	$\alpha = \frac{q-2}{2} + \frac{(2+q)\beta}{2}$
Wind, Slow Cooling					
$\nu < \nu_{\rm m}$	$-\frac{1}{3}$		$\frac{q-1}{3}$	-0.2	$\alpha = \frac{q}{2} + \frac{(2+q)\beta}{2}$
$\nu_{\rm m} < \nu < \nu_{\rm c}$	$\frac{p-1}{2}$	0.65	$\frac{(2p-2)+(p+1)q}{4}$	1.1	$\alpha = \frac{q}{2} + \frac{(2+q)\beta}{2}$
$\nu > \nu_{\rm c}$	$\frac{p}{2}$	1.15	$\frac{(2p-4)+(p+2)q}{4}$	0.7	$\alpha = \frac{q-2}{2} + \frac{(2+q)\beta}{2}$
Wind, Fast Cooling					
$\nu < \nu_{\rm c}$	$-\frac{1}{3}$		$\frac{1+q}{3}$	0.5	$\alpha = \frac{q}{2} - \frac{(2-q)\beta}{2}$
$\nu_{\rm c} < \nu < \nu_{\rm m}$	$\frac{1}{2}$		$\frac{3q-2}{4}$	-0.1	$\alpha = \frac{q}{2} - \frac{(2-q)\beta}{2}$
$\nu > \nu_{\rm m}$	$\frac{p}{2}$	1.15	$\frac{(2p-4)+(p+2)q}{4}$	0.7	$\alpha = \frac{q-2}{2} + \frac{(2+q)\beta}{2}$

Table 1.2: The closure relations (Zhang et al. (2006)) with $F_\nu \propto t^{-\alpha}\nu^{-\beta}$ for the energy injection case.

leased via the inverse Compton process. If the electrons are too energetic, they will not influence the observed spectra[16]. On the other hand, a significant fraction of energy of the cooling electrons can influence the observations. In fact, the emitted electrons will be cooled both by the synchrotron and the inverse Compton mechanism and so the cooling time will be shorter. Moreover, the inverse Compton scattering will reduce the efficiency of the observed radiation if the observed gamma-ray photons result from the synchrotron emission. The

[16]They can influence the GeV emission.

inverse Compton scattering will rise the energy of the synchrotron photons by a factor γ^2

$$(h\nu_{\rm IC})_{\rm obs} = \frac{\hbar q_e B}{m_e c}\gamma_e^4\Gamma. \tag{1.19}$$

Therefore the cooling time is

$$t_{\rm IC} = \frac{6\pi c^{3/4}\sqrt{U_B/U_e}\hbar^{1/4}m_e^{3/4}q_e^{1/4}}{B^{7/4}(h\nu)^{1/4}\Gamma^{3/4}\sigma_T}. \tag{1.20}$$

If $Y > 1$, the scattering will influence the process even if it does not produce the observed gamma-ray photons. In fact, it will add an ultrahigh energy component to the GRB spectrum, at frequencies of about γ_e^2 times the observed photons, that is ∼100 keV, so in the GeV-TeV range. In addition, the inverse Compton scattering will also increase the rate of the electrons cooling and consequently both the synchrotron cooling time and the process efficiency will be decreased by a factor Y.

1.3.2 The progenitors

The standard fireball model presented above does not depend on the central engine and the progenitor of the GRBs. The energetics and time scales involved in the GRB phenomenon show that the possible central engine is a compact object. Hosts and afterglows, together with the GRB properties (energetic, rates, timescales) support the progenitor models. It is supposed that the BH-accretion disk system is formed by a merger of two compact objects for short GRBs (Paczynski 1986; Goodman 1986; Eichler et al. 1989; Fryer et al. 1999; Nakar 2007; Narayan et al. 1992) and by the collapse of a massive star for long GRBs (Woosley 1993; MacFadyen & Woosley 1999).

Short GRBs. Short GRBs are supposed to originate by the merger of two compact objects, which can be two NS, a NS and a BH, or a white dwarf (WD) and a BH (Paczynski 1986; Goodman 1986; Eichler et al. 1989; Fryer et al. 1999; Nakar 2007; Narayan et al. 1992). As shown in Sec. 1.2.4, the environmental properties of short GRBs strongly support this scenario. The timescales and energies involved in this scenario are consistent with those of short GRBs (e.g. Eichler et al. 1989; Narayan et al. 1992, Nakar 2007).

There are different hypotheses about the formation of the binary system from which short GRBs originate. The system can evolve from a primordial binary system (e.g. Narayan et al. 1992): before the merger, the binary system can be drift outside the star-forming region in a low-density environment (e.g. Belczynski et al. 2006), unless the evolution is fast and the system does not travel far enough from the birth ste (e.g. Belczyński & Kalogera 2001). On the other hand, the system can evolve dynamically in a globular cluster, where a NS exchanges its light star companion with an isolated NS (e.g. Grindlay et al. 2006; Salvaterra et al. 2008).

The merging of two compact objects creates a region with a low quantity of baryons along the rotational axis because of its gravitational energy and

Table 1.3: Black hole vs. proto-magnetar long-duration GRB models (Metzger 2010).

Property	Collapsar (BH)	Proto-magnetar
Total energy	$E_{\rm max} \sim 0.1 M_\star c^2 \sim 10^{54}$ erg	$E_{\rm max} \sim 3 \times 10^{52}$ erg
Duration	Stellar envelope infall time	Spin-down time or until proto-NS ν-optically thin
Lorentz factor	Neutron diffusion? (Levinson & Eichler 2003)	$\Gamma_{\rm max} \sim 10^2 - 10^3$ @ $t \sim 10 - 100$ s higher $L_\gamma \leftrightarrow$ higher $\Gamma_{\rm max}$
Time-averaged light-curve shape	Track accretion rate?	Single envelope if: (1) internal shocks; (2) minimal jet-envelope interaction
Collimation	Accretion disks produce jets	Jet formation via stellar confinement
SN association	Accretion disk winds or delayed BH formation	Neutron stars power SN
Late-time X-ray flaring	Late-time fall back accretion	Magnetar remains
Particle composition	e^--e^+ pairs or baryons (?)	Barions for $t \lesssim 100$ s Pairs for $t \gtrsim 100$ s

the energy is released by a radiation-dominated plasma (e.g. Paczynski 1986; Goodman 1986). The duration of the mergeing is $\sim 10^8 - 10^9$ yr, characterized by hight accretion rates (>1-10 $M_\odot$ s^{-1}) and short time-scales (<200 ms): in this way a big quantity of energy ($\sim 10^{48}$ erg) is emitted in a short time (Narayan et al. 1992). A massive BH surrounded by a torus forms after the mergeing. In the case of the NS-NS merger, the torus is very dense (10^9 g cm^{-3} $< \rho <$ 10^{12}g cm^{-3}) and hot ($10^{10} < T < 10^{11}$ K) (Rosswog et al. 1999; Lee & Ramirez-Ruiz 2002). The thermal and kinetic energies that can be released by the central BH are 2×10^{52} erg and 8×10^{52} erg, respectively, while the kinetic energy of the debris is $\sim 10^{52}$ erg (Rosswog et al. 2003).

Long GRBs. Long GRBs are thought to derive from the core collapse of a massive star, which forms a rapidly spinning BH with an accretion disc producing an ultra-relativistic jet (**the collapsar model**, Woosley 1993; MacFadyen & Woosley 1999). The disc is hot, with a temperature of about 10^{10} K, and dense, $\rho \sim 10^{10}$ g cm^{-3}. This scenario requires a very high angular momentum, with a minimum $j_{\rm min} \simeq 1.5 \times 10^{16}$ $(M^3/3M_\odot)$ cm^2 s^{-1} for disc formation at the innermost stable circular orbit (ISCO) of a maximally-rotating BH or $j_{\rm min} \simeq 10^{17}$ cm^2 s^{-1} in the case in which a strong "Ni wind" powered the associated Ibc SN (Thompson 2008). Along the rotation axis, the $\nu\bar{\nu}$ annihilation and the $e^-\nu$ scattering form a pair fireball that deposits $\sim 10^{50}$ erg s^{-1} (Woosley 1993). If strong magnetic fields are present, the BH rotational energy could be removed thanks to the Blanford-Znajek process[17]: the energy involved is roughly 10^{54} erg. In spite of that, it is not clear the mechanism

[17]The energy and the angular momentum of a rotating BH can be extracted electromagnetically, when an electric potential difference is established because of the magnetic filed lines supported by external currents flowing an equatorial disc (Blandford & Znajek 1977).

that creates the highly relativistic jet ($100 \lesssim \Gamma \lesssim 1000$): the neutrino energy deposition, the magnetic stresses, or both. Therefore, it is not known if this model can produce a highly relativistic jet and $\dot{E} \sim 10^{50}$, at the same time (Thompson 2008).

There are three different type of collapsar scenarios (Woosley et al. 2003), depending on the initial core/star involved:

1. MacFadyen & Woosley (1999): the BH forms in a He-core of roughly 15-40 $M_{\odot}$.

2. MacFadyen et al. (2001): the BH forms after a minute or hours and involves a massive He-core.

3. Fryer et al. (2001): the collapse of a massive metal-poor star ($> 300\ M_{\odot}$), maybe existed in the early universe.

Between the three scenarios, the most probable is the MacFadyen & Woosley (1999) model because of the time scales involved, in fact it cannot reproduce an event shorter than 5 s (MacFadyen & Woosley 1999).

Other authors claim that the long GRB central engine is a new born **magnetar** (Usov 1992; Duncan & Thompson 1992; Dai & Lu 1998; Wheeler et al. 2000; Lyutikov & Blackman 2001; Zhang & Mészáros 2001; Drenkhahn & Spruit 2002; Thompson et al. 2004; Zhang et al. 2006; Metzger et al. 2011). A magnetar is a NS with very high superficial magnetic fields, of about $10^{14}-10^{15}$ G and fast rotating (Duncan & Thompson 1992). This scenario is supported by two fatcs (Usov 1992; Metzger 2010):

1. the rotational energy of a fast rotating NS is $E_{\rm rot} \sim 10^{52}(P/1\ {\rm ms})^{-2}(R/10{\rm km})^2$ erg, with P and R the rotational period and the radius of the NS; this quantity is of the order of the energy emitted by a GRB;

2. the electromagnetic power of the NS spin-down is $\dot{E} \sim 4\pi^2 B_{\rm dip}^2 R^6 c^{-3} P^{-4}$ $\sim 10^{49}(P/1\ {\rm ms})^{-4}(B_{\rm dip}/10^{15}\ {\rm G})^2(R/10\ {\rm km})^6$ erg, with B the magnetic field and c the speed of light; this power is in agreement with the observed luminosities of GRBs.

In the first hours after the NS formation, the very high spin-down luminosity caused by the losses of the dipole magnetic radiation represents a natural mechanism for a prolonged energy injection in the external shock. For Usov (1992) the NS involved in the long GRB explosion has magnetic fields of order about 10^{15} G. These fields could be created by the gravitational collapse of an accreting white dwarf (WD) in (cataclysmic) binaries with anomalous magnetic fields. In this way an ultra-magnetized and fast rotating magnetar is formed and loses its rotational kinetic energy in a time scale of about seconds or less: the rotation of the magnetic field creates strong electric fields and an optically thick e^-e^+ plasma in quasi-thermal equilibrium. This plasma is expelled from the NS with relativistic speed and the X-ray and γ-ray emission on the photosphere of the relativistic wind would produce the GRB emission. When the fireball slows, if there is continuos energy injection, the shock is refreshed,

the deceleration becomes less fast and the fireball bulk Lorentz factor decays less fast than[18] $\Gamma \propto R^{-3/2}$ (Zhang et al. 2006): this can explain the "plateau" phase in the X-ray light curve (Chap. 2). Instead of a fireball expanding in a homogeneous medium, the ambient medium can be the relativistic wind created by the proto-magnetar (e.g. Metzger et al. 2011). As shown in Sec. 1.3.1, the refreshed shock may be caused by different phenomena. One of these is the long duration of the central engine, that behaves as $L(t) = L_0(t/t_b)^{-q}$. In this case, the energy injection comes from the initial spin-down of milli-second pulsar, preferably a magnetar (Dai & Lu 1998; Zhang et al. 2006). At a certain time the injection stops (Zhang et al. 2006): the plateau phase will last while the energy injection is sufficient to equal the radiative losses (Dall'Osso et al. 2011; Bernardini et al. 2012a). Thus, new born and highly magnetized magnetars, with rotational periods of milliseconds, are formed in the events that cause long GRBs.

The main characteristics of the two scenarios are compared in Table 1.3 (for details see Metzger 2010).

[18] $\Gamma \propto R^{-3/2}$ corresponds to a fireball expanding in a homogeneous medium.

2

GRB XRT light-curves

The *Swift* satellite (Gehrels et al. 2004), launched on November 2004, opened a new era for the study and comprehension of the GRB phenomenon. The *Swift*/X-Ray Telescope (XRT, Burrows et al. 2005) LCs showed many features that were not predicted by the standard afterglow model and its variations (Meszaros & Rees 1997; Sari et al. 1998; Sec. 1.3.1). In particular, 50% of the XRT LCs have a canonical behavior (Nousek et al. 2006; Zhang et al. 2006; Panaitescu et al. 2006, Sec. 1.2.2), with the LC composed by three power-law segments (steep, shallow and normal decay), different from the predicted simple power-law decay, and sometimes there are flares superimposed to the continuum emission (Chincarini et al. 2007; Falcone et al. 2007), both at early (Chincarini et al. 2010a) and at late time (Bernardini et al. 2011). Therefore, many alternative models have been proposed (i.e. Kumar et al. 2008; Metzger et al. 2011).

There are still many open questions about GRBs, in particular the energy release in the X-ray band, the possible relation among the different XRT LC phases and flare emission, the connection among the prompt and afterglow emission, the properties that differentiate GRBs into long and short GRBs and those in common between them. Therefore, to try to answer to these questions, we analyzed a sample of more than 650 GRBs observed by *Swift*/XRT. Previous works concentrated on the observer frame GRB properties, examining the data considering the standard forward shock model (e.g. O'Brien et al. 2006; Butler & Kocevski 2007a; Willingale et al. 2007; Liang et al. 2007, 2008; Evans et al. 2009; Racusin et al. 2009, 2011). From these studies it was shown that it is difficult to identify the observations with the standard picture. Indeed, we decided to look for correlations between X-ray and gamma-ray properties independently from a theoretical model, and respect to previous works:

- we performed a homogeneous analysis of GRBs in a common rest frame energy band (0.3-30 keV);
- we considered the properties of the temporal variability superimposed on the smooth X-ray decay;
- we compared long and short GRBs afterglows;

- we investigated the connection between the prompt gamma-ray and X-ray properties, finding a universal scaling involving prompt and X-ray parameters.

From the X-ray LC, we can study various aspects of GRBs physics and behavior. In Sec. 2.1 and 2.2 I discuss the sample selection and the data analysis. The classification of the XRT LCs is presented in Sec. 2.3. The results and discussion are in Sec. 2.4.

2.1 Sample selection, LC and spectra extraction

We considered all GRBs observed by XRT from December 2004 to December 2010. This initial sample is composed by 658 GRBs, of which 36 are short. The procedure used to extract the data is described in Margutti (2009) and Margutti et al. (2013). XRT data were extracted and analyzed using the HAESOFT package (v6.10), the XRTDAS software package and the event lists and sky images downloaded from the HEASARC archive. The principal steps of the data analysis are:

- Extraction of the LC in count-rate in the XRT 0.3-10 keV band and in four sub-bands (0.3-1, 1-2, 2-3, 3-10 keV).

- For GRBs with enough X-ray counts (minimum 1000 photons), time resolved spectral analysis was performed. In this way, the sample reduces to 437 GRBs (23 short GRBs). The spectra were fitted with a power law model, considering the intrinsic and Galactic absorption.

- Using the time resolved spectra, hence taking into account the spectral evolution of the GRB with time (when present), the LCs were calibrated in flux and luminosity. We propagated the spectral analysis uncertainties to compute the flux and, when possible, luminosity LCs (this is mandatory to discriminate between the continuum LC and the positive fluctuations). The data were corrected from Galactic[1] and intrinsic absorption, so the final data are unabsorbed in the observer frame (0.3-10 keV). GRBs with known redshift[2] are 165, 12 of which are short; for these GRBs, from the spectrum model, the data were converted from the observed energy band into a common rest frame band (0.3-30 keV), considering their redshift z and photon index Γ:

$$f_{\rm X,RF}(0.3-30\ {\rm keV}) = f_{\rm X}(0.3-10\ {\rm keV})\frac{\left(\frac{30}{1+z}\right)^{2-\Gamma}-\left(\frac{0.3}{1+z}\right)^{2-\Gamma}}{10^{2-\Gamma}-0.3^{2-\Gamma}}. \quad (2.1)$$

[1] For the Galactic absorption, the values calculated by Kalberla et al. (2005) were used.

[2] We use only secure redshifts, derived from optical spectroscopy and photometric redshifts for which potential sources of degeneracy (e.g. dust extinction) can be ruled out with high confidence. We do not consider "tentative" redshifts or those coming from uncertain host associations with a uncertain host galaxy.

The data extraction is similar (but not identical because of the points explained above) to the procedure followed by Evans et al. (2007) and Evans et al. (2009), indeed the LCs extracted with the two methods are equivalent.

2.2 *XCURVE* and *ENERGY* programs

We developed a semi-authomatic software (*XCURVE*) in IDL[3] language, in order to fit the X-ray LCs. This procedure automatically fits the continuum part of the LC and discards the positive fluctuations that are above the noise of 1σ (Margutti et al. 2011a).

The fitting routine used is *MPFIT*[4] (Markwardt 2009), based on the non-linear least squares fitting and derived by *MINPACK-1* algorithm (Moré 1977; Moré & Wright 1993). This algorithm solves the problem by linearizing it around the trial parameter set, p_0, and solving for an improved parameter set, $p = p_0 + \delta p$ via the least squares equation $(J^T J)\delta p = -J^T$ (Markwardt 2009). The solution is obtained by QR factorization of J, that decomposes the matrix J in $J = QR$, with Q an orthogonal matrix and R an upper triangular matrix. This procedure improves the numerical accuracy over the normal equation form. The fast convergence of the algorithm is provided by the Levenberg-Marquardt algorithm, which replaces $(J^T J)$ with $(J^T J + \lambda D^T D)$, with D a diagonal scaling matrix. *MPFIT* iterates until reaching user-selected convergence criteria. These criteria are based on the minimization of χ^2 and residuals[5].

We have chosen this algorithm because of: 1) its fast convergence to the solution; 2) the possibility to use an user-defined fit function; 3) the fit function parameters can be easily frozen; 4) the output includes the covariance matrix, the parameter errors, χ^2, the number of degree of freedom (DOF) and the Jacobian matrix; 6) *MPFITPROPERROR* propagates fitted model uncertainties to measured data points and it is useful to evaluate the residual errors.

XCURVE input parameters are:

- The LC data, in our case times (s), time errors, fluxes (erg cm^{-2} s^{-1}) and flux errors.
- A file with a list of general useful information: GRB name, redshift, T_{90} (s), luminosity distance (Gpc), code identifying the fit function. For each parameter of the fit function we can choose to fix it or not. The fit functions used are:
  - Single power-law:

$$F(t) = N\, t^{-\alpha}. \tag{2.2}$$

[3]Interactive Data Language, http://www.exelisvis.com/language/en-US/ProductsServices/IDL.aspx

[4]http://purl.com/net/mpfit

[5]$\chi^2 = \frac{1}{\mathrm{DOF}} \sum_{x=1}^{N} \sum_{y=1}^{N} \frac{[I_m(x,y) - I_d(x,y)]^2}{\sigma^2}$, with I_m the model, I_d the data and DOF the number of degrees of freedom.

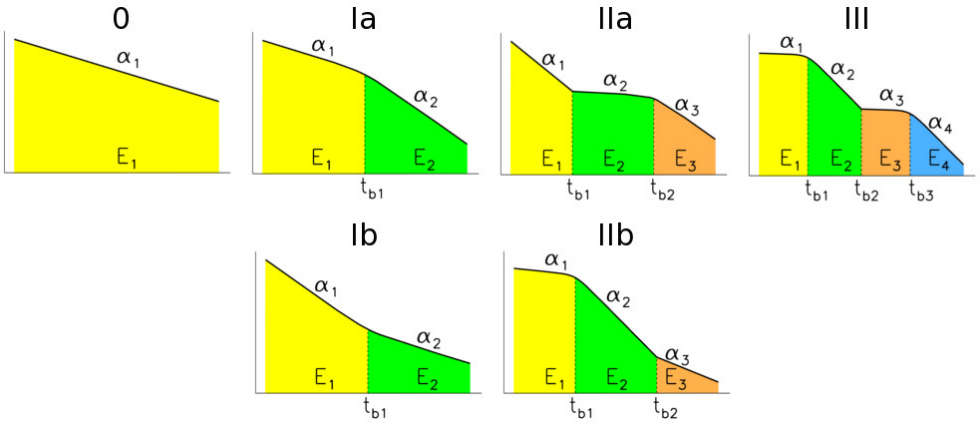

Figure 2.1: Cartoon representing the LC models used to fit our data. 0: single power-law; I: smoothed broken power-law (a if $s < 0$ and b if $s > 0$); II: single power-law plus a smoothed broken power-law (a is the canonical LC, b shows an initial plateau); III: sum of two broken power-laws. The name of the parameters we calculated are written on the cartoon: α is the LC slope, $t_{\rm br}$ the break time, and E the energy.

- Smoothly broken power-law:

$$F(t) = N \left(\left(\frac{t}{t_{\rm b}} \right)^{-\frac{\alpha_1}{s}} + \left(\frac{t}{t_{\rm b}} \right)^{-\frac{\alpha_2}{s}} \right)^{s} . \tag{2.3}$$

- Sum of power-law and smoothed broken power-law:

$$F(t) = N_1 \, t^{-\alpha_1} + N_2 \left(\left(\frac{t}{t_{\rm b}} \right)^{-\frac{\alpha_2}{s}} + \left(\frac{t}{t_{\rm b}} \right)^{-\frac{\alpha_3}{s}} \right)^{s} . \tag{2.4}$$

- Sum of two smoothed broken power-laws:

$$\begin{aligned} F(t) = \; & N_1 \left(\left(\frac{t}{t_{\rm b1}} \right)^{-\frac{\alpha_1}{s_1}} + \left(\frac{t}{t_{\rm b1}} \right)^{-\frac{\alpha_2}{s_1}} \right)^{s_1} + \\ & + N_2 \left(\left(\frac{t}{t_{\rm b3}} \right)^{-\frac{\alpha_3}{s_2}} + \left(\frac{t}{t_{\rm b3}} \right)^{-\frac{\alpha_4}{s_2}} \right)^{s_2} . \end{aligned} \tag{2.5}$$

  N is the normalization, $t_{\rm b}$ the break time, α the slope, s the smoothness parameter. Eq. 2.4 and 2.5 are the sum of two functions: a power law plus a broken smoothed power law in the first case and two smoothly broken power laws in the second case. The break time between the two parts of the LC is calculated as the time when the first component outshines the second component. In Figure 2.1 there is a representation of the LC models used.

- A file with the initial parameter guesses. At the end of the fit these guesses will be automatically replaced with the fit results.

Some features of the program:

- The program fits the data with an iterative process: for every passage the data point with the largest scatter from the fit is discarded, and this procedure is repeated until a p-value[6] is found greater then 0.3 (Margutti et al. 2011a). We identified as positive fluctuations the points that are not single fluctuations, by imposing the condition that the flare width is roughly 0.2 times the flare peak time (Chincarini et al. 2010a). Hereafter, for simplicity, we will indicate all the positive fluctuations with the word "flare". In this way all the flares are eliminated, and the "true" behavior of the X-ray continuum is identified.

- For each LC, we also considered a temporal shift, since the steep decay slope is sensitive to chosen zero time for the power-law. We used $t_0 = 0$ and $t_0 = T_{90}$. T_{90} depends both on the instrumental threshold and on the considered energy band.

- We calculated the residual values, that is the difference between the X-ray data and the LC model.

We also developed a software (*ENERGY*) that calculates the fluences and energies for: the total LC, the different parts of the LC (considering as bounderies the break times and the start and end of the observations), and flares. The fluence (energy) of the X-ray continuum is calculated by integrating the best-fitting function as found by *XCURVE*. The flare fluence (energy) is calculated by integrating the flux of each LC bin over the bin duration.
Therefore, using these two programs we extracted the following information:

- The shape of the X-ray continuum.

- The slopes, break times and normalization of the LC.

- If there are or not flares.

- The residuals between the model and the data.

- The fluence (energy) for the total LC, for parts of the LC and for the excesses.

2.3 Classification

For each GRB we assign a LC identifier that briefly explains the main characteristics of the X-ray LC. This classification is based on three features:

- The shape: depending on the number of break times there are type **0** (Eq. 2.2), **I** (Eq. 2.3, **a** if $s < 0$ and **b** if $s > 0$), **II** (Eq. 2.4, **a** is the canonical LC and **b** has an initial palteau) and **III** (Eq. 2.5) LCs (Fig. 2.1).

[6]The p-value is a number between zero and one and it is the probability of obtaining a test statistic at least as extreme as the one that was actually observed, assuming that the null hypothesis is true.

Table 2.1: List of the GRB X-ray LC types subdivided in the different groups: the total sample (first line), the complete LCs (second line), LCs with flares (third line) and LCs of GRBs with known redshift (forth line).

	0	Ia	Ib	IIa	IIb	III	Total
Total	114	89	61	133	18	22	437
Complete LCs	42	61	53	121	17	22	316
LCs with flares	23	16	24	48	8	10	129
GRBs with known z	38	36	24	52	5	10	165

Table 2.2: Short GRBs. GRBs with detected temporally extended emission are reported in bold face (Norris et al. 2011). In *italic* C-GRBs.

Short GRBs					
050724	051210	*051221A*	***051227***	*060313*	060801
061006	*061201*	***070714B***	*070724A*	*070809*	***071227***
080123	***080503***	080905A	*080919*	*090510*	*090515*
090607	*100117A*	100702A	*100816A*	*101219A*	

- The "completeness": this depends on the time coverage of the LC. GRBs with complete ("**C**") LC are those GRBs re-pointed by XRT at $t_{rep} <$ 300 s and for which we were able to follow the fading of the XRT flux down to a factor 5-10 from the background limit. If this criterium is not followed the LC is marked as **U**.

- The presence of flares: **F** (**N**) if there are (no) flares.

For example, GRB 060312 (Figure 2.2) was classified as type **IICF** for the presence of two breaks (*gray dashed lines*), flares (*red dots*), and for its X-ray coverage from ∼50 s until 3×10^5 s after the trigger. In Table 2.1 we list the GRBs in our sample in the different groups. The sample is composed of 437 LCs, of which ∼26% are type 0 LCs and ∼30% are type IIa. In the sample there are 316 C-LCs, of which ∼38% are of type IIa, instead type 0 are only the ∼13%. The LCs with flares are 129, that is the ∼30% of the total, as stated in previous works (Chincarini et al. 2010a). Moreover, 165 GRBs in our sample have known redshift. The short GRBs are 23, of which 19 have C-LCs and 12 have known redshift. A list of the short GRBs is in Table 2.2.

2.4 Results and Discussion

From the LC fitting, we calculated a group of quantities useful to describe quantitatively the X-ray emission: energies, slopes, timescales. We analyzed these parameters in two ways:

- For each parameter we studied its distribution (histogram) and we fitted

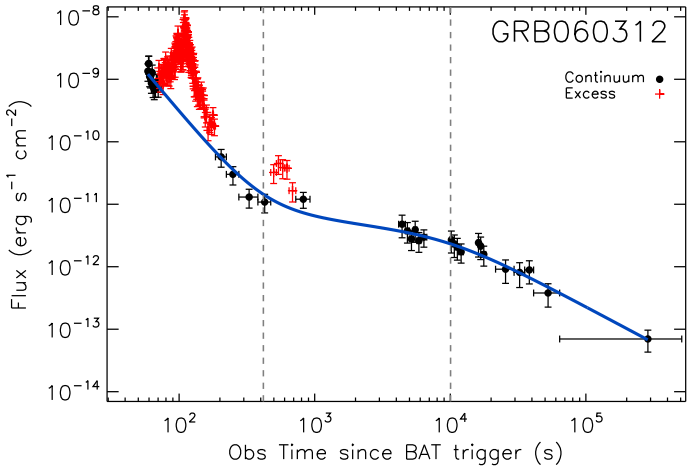

Figure 2.2: GRB 060312. *Black points*: data belonging to the identified continuum. *Red points*: the excesses automatically singled out by the program. *Blue solid line*: the model for the continuum part of the LC. *Dashed lines*: the break times. GRB060312 was classified as IICF.

it with a Gaussian[7] when possible. We distinguished between long and short GRBs to evidence differences and similarities. In order to account for the errors in the determination of each parameter, we generated 10^4 realizations of each distribution under the assumption that each element y is normally distributed around y^* with standard deviation σ_y (where y^* and σ_y stand for our best estimate of the parameter and associated uncertainty, respectively). This process established a distribution of 10^4 values for each histogram bin, which we used to define the 99% confidence intervals (*dashed gray area*). In Table 2.3 we report the list of the studied parameters with their mean (m), median (M), standard deviation (SD), skewness (SK) and Gaussian fit parameters (the mean μ, the standard deviation σ and the normalization N).

- We looked for the possible correlations between two or more parameters obtained by the LC fitting or collected from the literature (prompt emission parameters). Starting from a set of 44 parameters, we made a blind search of the possible 2-parameter correlations. The significance of the correlation was estimated by the R-index, the Spearman rank and the Kendall coefficient. The most significant correlations were fitted using the D'Agostini (2005) method, which takes into account the sample variance. When long and short GRBs occupy two different parts of the correlation plane, we made two fits: one considering the total number of short and long GRBs (colored band), and one only for long GRBs. The results are listed in Tab. 2.4.

[7]The Gaussian function: $y = N\, e^{-\frac{(x-\mu)^2}{2\sigma^2}}$, with $N = 1/(\sigma\sqrt{2\pi})$ the normalization, μ the mean, and σ the standard deviation.

Table 2.3: Characteristic quantities describing the parameter distributions (number of elements #, mean m, median M, standard deviation SD, skewness SK) and best-fitting values from a Gaussian fit to the distributions (mean μ, standard deviation σ, normalization$N$). Fluences (S) are given in 10^{-6} erg cm^{-2}, energies (E) in 10^{50} erg, fluxes (F) in 10^{-6} erg s^{-1} cm^{-2}, luminosities (L) in 10^{48} erg s^{-1}, times (t) in s, hydrogen column densities ($N_{\rm H}$) in 10^{22} cm^{-2}. Note that logarithmic (linear) units have been used in the upper (lower) half of the Table. When logarithmic units are used, the mean, median, standard deviation and skewness of the distribution of logarithmic values are reported. We refer to Appendix D for the exact definition of the parameters listed below.

	#	m	M	SD	SK	μ	σ	N
$\log(S_\gamma)$	386	0.17	0.18	0.61	−0.07	0.17 ± 0.05	0.60 ± 0.04	105.1 ± 7.7
$\log(T_{90})$	334	1.58	1.73	0.65	−1.18	1.67 ± 0.07	0.62 ± 0.06	93.9 ± 9.4
$\log(E_\gamma^{15-150})$	151	2.06	2.37	0.93	−1.12	2.26 ± 0.14	1.02 ± 0.1	$91.6 \pm 9.$
$\log(E_{\gamma,\rm iso})$	78	2.88	3.01	0.91	−0.89	3.01 ± 0.14	0.85 ± 0.12	38.9 ± 5.7
$\log(E_{\rm pk})$	78	2.64	2.71	0.52	−0.76	2.56 ± 0.1	0.47 ± 0.069	23.6 ± 4.7
$\log(L_{\rm pk,iso})$	85	2.43	2.51	1.00	−1.90	2.51 ± 0.19	0.91 ± 0.12	61.0 ± 9.3
$\log(T_{90}^{\rm RF})$	138	1.18	1.33	0.59	−0.65	1.26 ± 0.11	0.67 ± 0.09	53.8 ± 7.4
$\log(\rm N_{H,HG})$	161	21.6	21.8	1.21	−3.54	21.9 ± 0.1	0.62 ± 0.09	42.5 ± 7.3
$\log(S_{\rm X})$	316	−0.38	−0.42	0.62	0.23	-0.46 ± 0.05	0.57 ± 0.04	68.6 ± 5.3
$\log(S_{\rm X}^{\rm FL})$	115	−0.81	−0.76	0.82	−0.38	-0.76 ± 0.12	0.89 ± 0.12	51.3 ± 6.0
$\log(S_{1,\rm X})$	211	−0.90	−0.92	0.80	0.12	-0.89 ± 0.10	0.88 ± 0.06	97.2 ± 7.9
$\log(S_{2,\rm X})$	316	−0.58	−0.61	0.63	0.14	-0.57 ± 0.07	0.70 ± 0.06	102.2 ± 8.5
$\log(S_{1,\rm X}^{\rm FL})$	62	−0.75	−0.69	0.73	−0.38	-	-	-
$\log(S_{2,\rm X}^{\rm FL})$	71	−1.08	−0.98	0.90	0.03	-1.08 ± 0.17	0.95 ± 0.16	36.7 ± 5.6
$\log(E_{\rm X,iso})$	126	1.67	1.84	0.81	−0.67	1.82 ± 0.08	0.88 ± 0.08	31.1 ± 2.5
$\log(E_{\rm X}^{\rm FL})$	59	1.25	1.40	0.97	−0.64	-	-	-
$\log(E_{1,\rm X})$	86	1.00	1.04	0.92	−0.28	1.10 ± 0.11	0.94 ± 0.08	40.7 ± 3.6
$\log(E_{2,\rm X})$	126	1.45	1.63	0.92	−0.94	1.63 ± 0.11	0.82 ± 0.10	63.2 ± 7.0
$\log(E_{1,\rm X}^{\rm FL})$	35	1.13	1.38	1.00	−0.78	-	-	-
$\log(E_{2,\rm X}^{\rm FL})$	38	1.04	1.14	0.98	0.01	-	-	-
$\log(t_{\rm i})$	155	2.66	2.56	0.48	1.06	-	-	-
$\log(t_{\rm f})$	155	3.94	3.93	0.73	0.19	3.93 ± 0.14	0.8 ± 0.12	59.2 ± 8.9
$\log(F_{\rm i})$	155	−4.23	−4.26	0.83	−0.14	-4.18 ± 0.11	0.89 ± 0.12	61.1 ± 6.6
$\log(F_{\rm f})$	155	−5.01	−4.94	0.80	−0.12	-4.99 ± 0.11	0.80 ± 0.08	63.4 ± 6.9
$\log(t_{\rm i}^{\rm RF})$	62	2.13	2.03	0.62	1.27	-	-	-
$\log(t_{\rm f}^{\rm RF})$	62	3.58	3.48	0.74	0.29	3.53 ± 0.11	0.75 ± 0.09	23.0 ± 2.9
$\log(L_{\rm i})$	62	0.54	0.73	1.25	−1.07	0.79 ± 0.19	1.26 ± 0.16	46.6 ± 5.5
$\log(L_{\rm f})$	62	−0.47	−0.19	1.19	−1.19	0.04 ± 0.33	1.41 ± 0.29	38.2 ± 6.8
Γ	280	1.63	1.60	0.39	0.41	1.619 ± 0.043	0.389 ± 0.032	49.2 ± 4.8
$\alpha_{\rm st}$	213	3.96	3.56	2.34	3.95	3.22 ± 0.51	2.34 ± 0.35	238.0 ± 35.0
$\alpha_{\rm st}^{T90}$	195	3.15	2.71	1.73	1.78	-	-	-
$\alpha_{\rm sh}$	155	−0.16	0.18	1.23	−4.06	0.27 ± 0.14	0.52 ± 0.12	61.0 ± 13.0
$\alpha_{\rm n}$	204	1.59	1.38	1.04	8.30	1.34 ± 0.13	0.49 ± 0.11	93.0 ± 19.0

In the following Sections we consider only X-ray complete LCs, with the exception of Sec. 2.4.3.

2.4.1 Dispersion of X-ray LCs

We considered the 0.3-30 keV LCs calibrated in luminosity and we selected a sample of 79 long GRB C-LCs observed within a common rest frame time interval between 100 and 10^5 s and a group of 9 short GRB C-LCs observed within 100 and 10^4 s (Figure 2.3, top panels).

Long GRB LCs show a larger dispersion at $t \sim 100$ s than the end of the LCs ($t \sim 10^5$ s): this can be explained with the fact that the first part of the GRB X-ray emission is affected by the central engine activity and at the end they "forget" about the progenitor and the emission is probably influenced by the interaction of the ejecta with the external medium. This is also shown in the histograms in Figure 2.4, which represent the luminosity distribution at different times (100 s, 1000 s, 10 000 s). At $t^{\rm RF} \sim 100$ s, the standard deviation

Table 2.4: From left to right: X and Y parameters to be correlated (for each couple, the best fitting law reads: $\log(Y) = q + m\log(X)$. Best-fitting parameters as obtained accounting for the sample variance following the method by D'Agostini (2005): slope (m), normalization (q), intrinsic scatter (σ); errors are given at 95% confidence level. The last six columns list the value of the Spearman rank ρ, Kendall coefficient K and R-index r statistics and relative chance probability p of obtaining such correlations. For each parameter pair, values reported in the first line refer to the entire sample, while in the second line we restrict our analysis to the long GRB class. We refer to Appendix D for the exact definition of the parameters listed below.

X	Y	m	q	σ	ρ	$p(\rho)$	K	$p(K)$	r	$p(r)$
$E_{\rm X,iso}$	$E_{\rm X}^{\rm FL}$	1.07 ± 0.03	-4.1 ± 72.2	0.57 ± 0.01	0.70	3×10^{-10}	0.52	2×10^{-9}	0.79	$<10^{-10}$
		1.10 ± 0.07	-5.9 ± 198	0.58 ± 0.01	0.61	3×10^{-7}	0.45	6×10^{-7}	0.70	10^{-9}
$E_{\rm X,iso}$	$L_{\rm f}$	1.21 ± 0.06	-15.6 ± 169	0.85 ± 0.01	0.58	6×10^{-7}	0.45	2×10^{-7}	0.70	3×10^{-10}
		1.26 ± 0.08	-18.1 ± 206	0.85 ± 0.01	0.55	3×10^{-6}	0.43	8×10^{-7}	0.69	10^{-9}
$E_{\rm X,iso}$	$L_{\rm i}$	1.39 ± 0.06	-23.6 ± 172	0.83 ± 0.01	0.63	3×10^{-8}	0.49	2×10^{-8}	0.75	$<10^{-10}$
		1.37 ± 0.08	-22.8 ± 212	0.84 ± 0.02	0.60	3×10^{-7}	0.46	2×10^{-7}	0.72	10^{-10}
$t_{\rm f}^{\rm RF}$	$L_{\rm f}$	-1.23 ± 0.03	51.9 ± 0.46	0.77 ± 0.01	-0.80	$<10^{-10}$	-0.60	$<10^{-10}$	-0.77	$<10^{-10}$
		-1.24 ± 0.03	52.0 ± 0.45	0.73 ± 0.01	-0.82	$<10^{-10}$	-0.62	$<10^{-10}$	-0.78	$<10^{-10}$
$L_{\rm f}$	$E_{2,\rm X}$	0.52 ± 0.01	26.8 ± 11.8	0.47 ± 0.00	0.67	2×10^{-9}	0.51	5×10^{-9}	0.80	$<10^{-10}$
		0.50 ± 0.00	27.6 ± 10.8	0.43 ± 0.00	0.65	10^{-8}	0.50	2×10^{-8}	0.81	$<10^{-10}$
$E_{2,\rm X}$	$E_{1,\rm X}$	0.42 ± 0.02	29.1 ± 43.2	0.81 ± 0.01	0.42	4×10^{-5}	0.29	4×10^{-5}	0.45	6×10^{-6}
		$-$	$-$	$-$	0.28	6×10^{-3}	0.19	0.06	0.29	6×10^{-3}
$t_{\rm f}$	$F_{\rm f}$	-0.79 ± 0.01	-7.80 ± 0.09	0.45 ± 0.00	-0.69	$<10^{-10}$	-0.50	$<10^{-10}$	-0.74	$<10^{-10}$
		-0.79 ± 0.01	-7.78 ± 0.09	0.45 ± 0.00	-0.69	$<10^{-10}$	-0.50	$<10^{-10}$	-0.74	$<10^{-10}$
$E_{\gamma,\rm iso}$	$E_{\rm X,iso}$	0.79 ± 0.01	10.0 ± 20.6	0.39 ± 0.00	0.86	$<10^{-10}$	0.69	$<10^{-10}$	0.88	$<10^{-10}$
		0.67 ± 0.01	16.5 ± 18.8	0.29 ± 0.00	0.82	$<10^{-10}$	0.63	$<10^{-10}$	0.88	$<10^{-10}$
$E_{\gamma,\rm iso}$	$E_{\rm X}^{\rm FL}$	0.89 ± 0.05	3.85 ± 148	0.65 ± 0.01	0.64	8×10^{-5}	0.48	10^{-4}	0.74	3×10^{-6}
		0.93 ± 0.10	1.83 ± 287	0.62 ± 0.02	0.56	10^{-3}	0.41	10^{-3}	0.67	6×10^{-5}
$E_{\gamma,\rm iso}$	$E_{1,\rm X}$	0.67 ± 0.03	15.9 ± 91.3	0.81 ± 0.02	0.71	2×10^{-7}	0.56	2×10^{-7}	0.64	5×10^{-6}
		0.56 ± 0.04	21.6 ± 126	0.77 ± 0.02	0.62	5×10^{-5}	0.48	4×10^{-5}	0.54	5×10^{-4}
$E_{\gamma,\rm iso}$	$E_{2,\rm X}$	0.92 ± 0.01	2.96 ± 33.5	0.51 ± 0.01	0.76	$<10^{-10}$	0.59	$<10^{-10}$	0.85	$<10^{-10}$
		0.74 ± 0.01	12.6 ± 35.1	0.44 ± 0.00	0.67	10^{-8}	0.51	2×10^{-8}	0.81	$<10^{-10}$
$E_{\gamma,\rm iso}$	$L_{\rm f}$	1.06 ± 0.08	-8.86 ± 227	1.03 ± 0.04	0.54	9×10^{-4}	0.41	7×10^{-4}	0.70	8×10^{-6}
		1.05 ± 0.09	-8.43 ± 260	1.06 ± 0.04	0.50	3×10^{-3}	0.37	3×10^{-3}	0.68	2×10^{-5}
$E_{\rm pk}$	$E_{\rm X,iso}$	-	-	-	-	-	-	-	-	-
		0.98 ± 0.02	49.5 ± 0.15	0.37 ± 0.00	0.63	10^{-7}	0.46	5×10^{-7}	0.76	$<10^{-10}$
$L_{\rm pk}$	$E_{\rm X,iso}$	-	-	-	-	-	-			
		0.48 ± 0.01	27.0 ± 16.4	0.44 ± 0.00	0.58	2×10^{-7}	0.42	3×10^{-7}	0.74	$<10^{-10}$
$L_{\rm pk}$	$L_{\rm f}$	-	-	-	-	-	-			
		0.86 ± 0.03	2.35 ± 87.6	0.87 ± 0.02	0.50	10^{-3}	0.39	5×10^{-4}	0.76	7×10^{-8}
$L_{\rm pk}$	$E_{2,\rm X}$	-	-	-	-	-	-			
		0.60 ± 0.01	20.3 ± 15.9	0.43 ± 0.00	0.58	10^{-7}	0.42	3×10^{-7}	0.82	$<10^{-10}$
S_γ	$S_{\rm X}$	0.77 ± 0.01	-7.80 ± 0.09	0.45 ± 0.00	0.79	$<10^{-10}$	0.59	$<10^{-10}$	0.77	$<10^{-10}$
		0.82 ± 0.00	-1.58 ± 0.10	0.37 ± 0.00	0.78	$<10^{-10}$	0.58	$<10^{-10}$	0.78	$<10^{-10}$
$E_{\gamma,\rm iso}$	$L_{\rm X}^{\rm 11h}$	0.71 ± 0.01	8.53 ± 30.9	0.55 ± 0.01	0.66	3×10^{-10}	0.49	1×10^{-9}	0.77	$<10^{-10}$
		0.54 ± 0.01	17.5 ± 29.6	0.45 ± 0.00	0.55	2×10^{-6}	0.40	2×10^{-6}	0.70	$<10^{-10}$
$E_{\gamma,\rm iso}$	$L_{\rm X}^{\rm 10min}$	0.93 ± 0.01	-1.17 ± 0.01	0.45 ± 0.01	0.87	$<10^{-10}$	0.67	$<10^{-10}$	0.88	$<10^{-10}$
		0.78 ± 0.01	6.73 ± 32.6	0.40 ± 0.00	0.82	$<10^{-10}$	0.63	$<10^{-10}$	0.84	$<10^{-10}$

is roughly 0.75, then it grows until to reach the maximum dispersion (0.83) at $t^{RF} \sim 1000$ s. This is approximately the time when the plateau starts for type IIa and III LCs. Afterwards, the LC dispersion decreases until to reach a standard deviation of about 0.65 at $t^{\rm RF} \sim 10^5$ s.

To exclude the influence of peculiar LCs on our results, we randomly selected a sample of 55 LCs (out of the sample of 79 LCs) for 10^4 times and each time we calculate the median LC, the dispersion and the skewness (e.g. Wu 1986). From this procedure, we find that the dispersion is 0.74 ± 0.04, 0.84 ± 0.04, 0.65 ± 0.04 at $t^{\rm RF} = 10^2, 10^3, 10^5$ s, respectively. These results confirm that our previous dispersion values are not influenced by peculiar LCs. On the other hand, for short GRBs the dispersion increase with time. In addition, the median luminosity LC for short GRBs ($\sim t^{-1.3}$) is steeper than the

median luminosity LC for long GRBs ($\sim t^{-1}$). Short GRBs are less luminous on average respect to long GRBs by a factor $\sim 10-30$, even if the two samples overlap as shown in Figure 2.3. Short GRBs decay faster then long GRBs, so they are shifted toward lower luminosities than long GRBs as time goes by, as we can notice in the three histograms of Figure 2.4. This is true also if we consider GRBs from a restricted redshift range ($z < 1$, Figure 2.3).

The decay index of the median luminosity LC (~ -1) is in rough agreement with the standard afterglow predictions (Meszaros & Rees 1997; Sari et al. 1998).

The clustering of the LCs at late times is expected by the magnetar models (e.g. Dall'Osso et al. 2011), since after the phase of the energy injection, where the distribution is more spread, the LC decays as $t^{-(1+k)}$ (with $k = \epsilon_e$ and ϵ_e the fraction of the total energy that is transferred to the electrons), and the median luminosity distribution becomes narrower. In the accretion model (Kumar et al. 2008), after the end of the fallback of the envelope, the expected slope is $-2.7 < \alpha < -1.3$. Independently of the central engine nature, at late time the emission seems to be less beamed and the observer can see a large section of the jet.

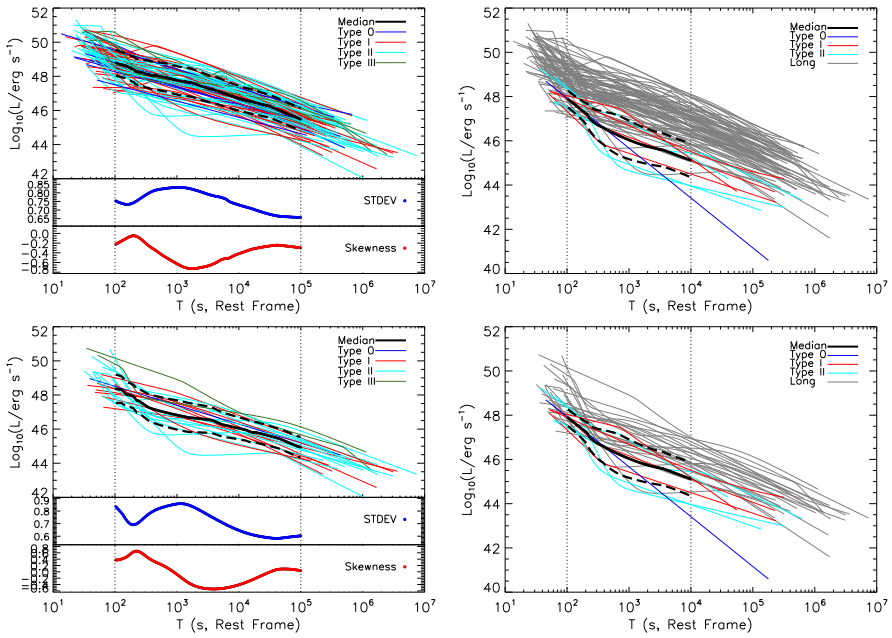

Figure 2.3: Luminosity C-LCs of GRBs of four sub-samples. *Top*: C-LCs of 79 long GRBs (*left*) and 9 short GRBs (*right*) with $t^{\rm RF}_{\rm min} < 300$ s and $t^{RF}_{max} > 10^5$ s for long GRBs and $t^{\rm RF}_{\rm min} < 300$ s and $t^{\rm RF}_{\rm max} > 10^4$ s for short GRBs. *Bottom*: as in the previous Figures, but only GRBs with $z < 1$ are plotted. *Black solid line*: the median logaritmic luminosity LC. *Dashed line*: 1σ dispersion. *Blue solid lines*: type 0 LCs. *Red solid lines*: type I LCs. *Light blue solid lines*: type II LCs. *Green solid lines*: type III LCs. *Gray solid lines*: long GRBs LCs.

2.4.2 Energetics

The fluence and the total energy

The fluences (erg cm^{-2}) were calculated in the observer-frame 0.3-10 keV band; for GRBs with known redshift, the energy (erg) was extracted in the 0.3-30 keV band.

The mean fluence for the X-ray continuum is $S_{\rm X} \approx 3.4 \times 10^{-7}$ erg cm^{-2} and for flares $S_{\rm X}^{\rm FL} \approx 1.7 \times 10^{-7}$ erg cm^{-2}, with a median $S_{\rm X}^{\rm FL}/S_{\rm X}$ equal 0.3 (mean = 0.98 and standard deviation = 3) (Figure 2.5). These values represent the population of GRBs with bright flares because our procedure does not allow us to identify small fluctuations as flares. The maximum ratio between the flares and continuum fluence has been observed for GRB 050502B (see also Falcone et al. 2006), where flares dominate the X-ray emission. Short GRBs follow the same fluence distribution of long GRBs, both for the observer frame and the rest frame band. The X-ray fluence is correlated with the γ-ray fluence in the BAT 15-150 keV band (Fig. 2.5): $S_{\rm X} \propto S_{\gamma}^{0.8}$, in agreement with Willingale et al. (2007) and Evans et al. (2007). Short GRBs lie in the low energy part of the plane $S_{\rm X} - S_{\gamma}$. The GRBs with maximum S_{γ} ($\sim 2 \times 10^{-6}$) are GRB 080508 and GRB 100816A. The short and long GRBs share the same trend, so short and long GRBs have the same efficiency (Zhang et al. 2007; Gehrels et al. 2008).

For the subsample of GRBs with known redshift, we calculated the X-ray

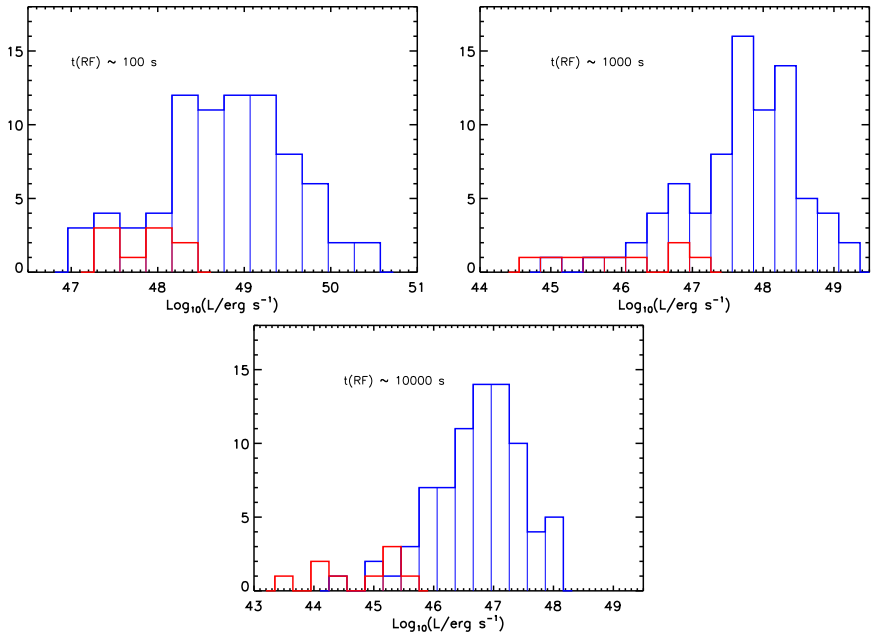

Figure 2.4: Histograms representing the luminosity distribution for the 79 long (*blue*) and 9 short (*red*) GRBs selected at three different rest frame times: 100 s, 1000 s, 10000 s. From left to right, a KS test gives 10^{-3}, 3×10^{-5}, 10^{-7} probability for the short and long GRBs to belong to the same parent distribution.

energy emitted in the 0.3-30 keV band. The $E_{X,iso}$ distribution peaks around 7×10^{51} erg, that is the 7% of $E_{\gamma,iso}$ (Figure 2.6). The most energetic event is GRB 080721 with $E_{X,iso} \sim 10^{53}$ ergWe calculated the evolution of $E_{X,iso}$ with z. We found that for $z > 2$ we are not sensitive to GRBs with $E_{X,iso} \lesssim 10^{51}$ erg and for $z < 1$ there is no evidence for an evolution of the upper bound of $E_{X,iso}$ with z.

The energy of flares

The X-ray energy of flares is $\sim 2 \times 10^{51}$ erg; the $E^{FL}_{X,iso}$ does not reach high energy values, maybe indicating the maximum limit of the energy budget, as for $E_{X,iso}$ (Figure 2.6). The total X-ray energy directly correlates with the total X-ray energy of flares, $E_{X,iso} \propto {E^{FL}_{X,iso}}^{1.07}$, so more energetic flares occur in more energetic GRBs in the X-ray band. Short GRBs follow the same relation of long GRBs, even if they are less energetic, as found also by Margutti et al. (2011a). The total X-ray energy correlates with the isotropic γ-ray emission, $E_{\gamma,iso} \simeq E^{0.8}_{X,iso}$ (Figure 2.6), as previously stated also by Willingale et al. (2007) with a smaller sample. Short GRBs are outlier of the relation calculated for long GRBs, because long and short GRBs have different $E_{X,iso}$

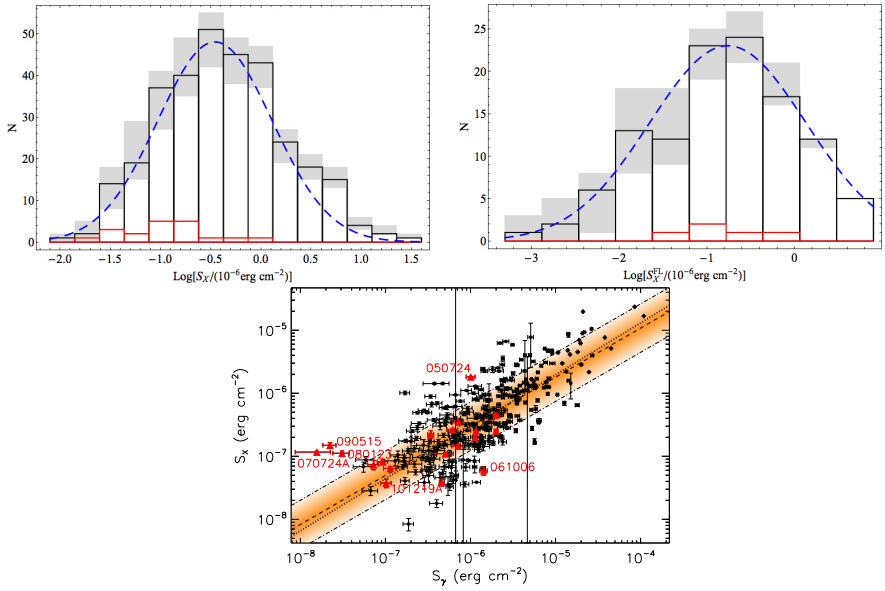

Figure 2.5: Fluences. *Top*: distributions of the 0.3-10 keV observer frame fluence of the X-ray continuum (S_X, *left*) and of X-ray flares (S^{FL}_X, *right*). *Black (red) solid line*: long (short) GRBs. *Dashed blue line*: best fitting normal distribution (Table 2.3). *Gray area*: 99% of the confidence level. *Bottom*: X-ray fluence (S_X)-γ-ray fluence in the BAT 15-150 keV band (S_γ) correlation. *Black points*: long GRBs. *Red triangles*: short GRBs. *Dashed line*: best-fitting power-law model for the entire sample (long plus short GRBs). *Dotted line*: best-fitting power-law model for long GRBs. The *colored* and *hatched* areas mark the 68% confidence region around the best fit for the total sample and long GRBs, respectively. Short GRBs and outliers are named.

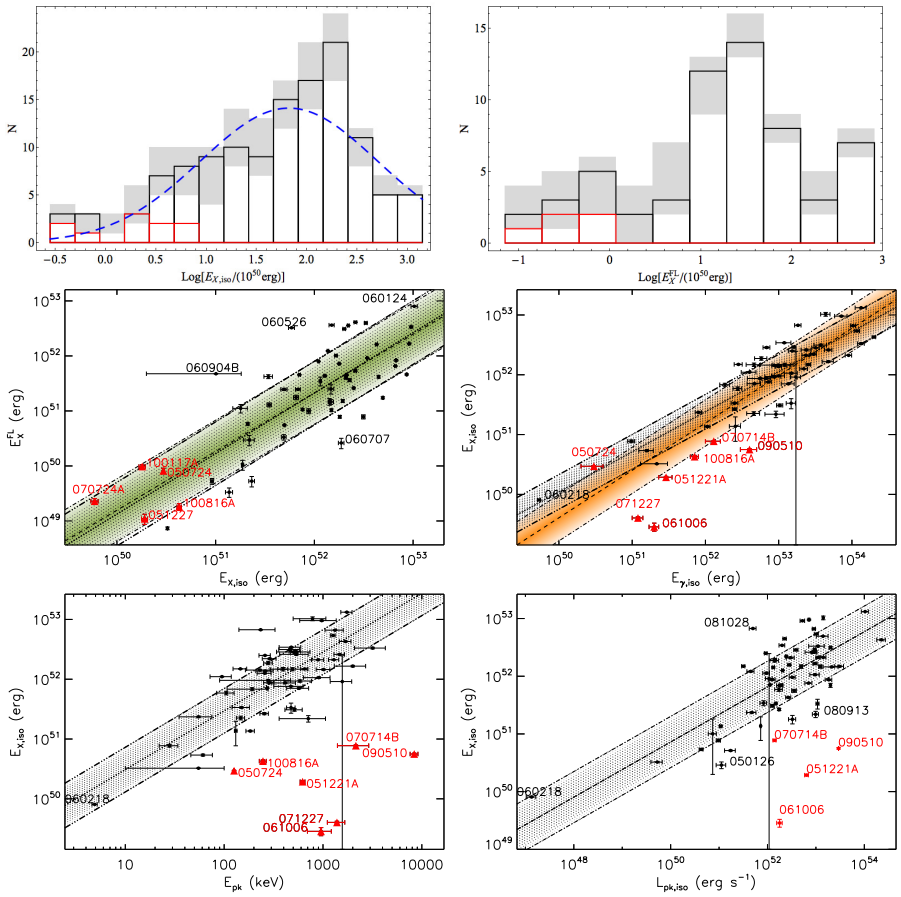

Figure 2.6: Energetics. *Top*: distribution of the X-ray energy in the rest frame 0.3-30 keV band for the continuum (*left*) and flares (*right*). *Center*: correlations of the X-ray total energy (0.3-30 keV, $E_{\rm X,iso}$) with the X-ray energy of flares ($E_{\rm X}^{\rm FL}$, *left*), and with the isotropic γ-ray energy ($E_{\gamma,\rm iso}$, *right*). *Bottom*: correlations of the X-ray total energy (0.3-30 keV, $E_{\rm X,iso}$) with the peak energy ($E_{\rm pk}$, *left*), and with the peak luminosity ($L_{\rm pk,iso}$, *right*). Color coding as in Figure 2.5.

distributions and short GRBs are less energetic than short GRBs ($E_{\rm X,iso}^{\rm long} \simeq 50 \times E_{\rm X,iso}^{short}$). The only exception is GRB 050724 (Barthelmy et al. 2005; Grupe et al. 2006), characterized by a very bright afterglow, with a powerful late time rebrightening (Bernardini et al. 2011; Malesani et al. 2007). X-ray flashes (XRFs) have the same low isotropic γ-ray budget, but stay on the same relation of long GRBs because have $E_{\rm X,iso}$ greater than long GBRs; this fact can be explained in terms of efficiency[8] to convert the γ-ray prompt emission energy into kinetic energy of the afterglow ($\eta_\gamma \propto E_\gamma/(E_\gamma+E_{\rm K})$): $\eta_\gamma^{\rm short} < \eta_\gamma^{\rm XRF}$. More details will be presented in Sec. 2.4.7, when we will discuss the 3-parameter correlation between $E_{\gamma,\rm iso}$, $E_{\rm X,iso}$ and $E_{\rm pk}$. In addition, there is a relation between $E_{\rm X,iso}$ and $E_{\rm pk}$ ($E_{\rm pk} \propto E_{\rm X,iso}^{0.98}$), where short and long GRBs occupy a different region of the plan, and between $E_{\rm X,iso}$ and $L_{\rm pk}$ ($E_{\rm X,iso} \propto L_{\rm pk}^{0.5}$,

[8] See Appendix C for details.

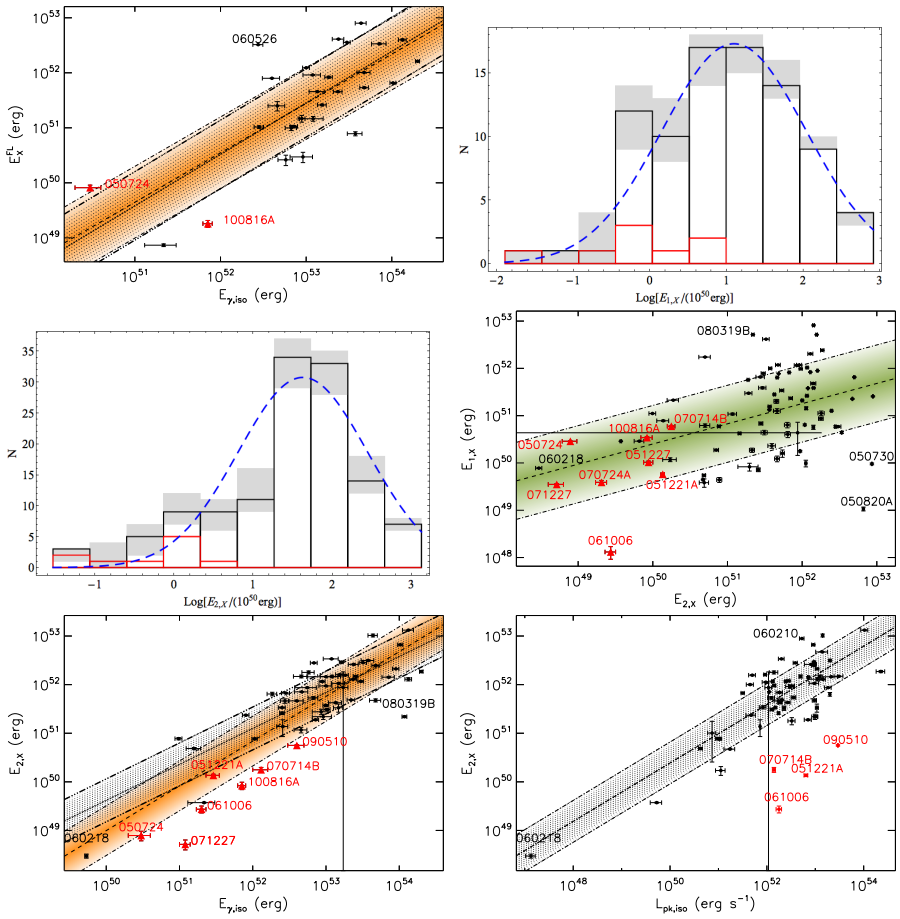

Figure 2.7: Energetics. *Top*: correlation between the isotropic γ-ray energy ($E_{\gamma,\mathrm{iso}}$) and the X-ray energy of flares ($E_{\mathrm{X}}^{\mathrm{FL}}$, *left*) and the distribution of first component energy (E_1, *right*). *Center*: distribution of the second component energy (E_2, *left*) and the correlation between the first (E_1) and second component (E_2) energies (*right*). *Bottom*: correlations of the second component energy (E_2) with the isotropic γ-ray energy ($E_{\gamma,\mathrm{iso}}$*left*) and with the peak luminosity ($L_{\mathrm{pk,iso}}$, *right*). Color coding as in Figure 2.5.

Figure 2.6). Also the X-ray energy of flares correlates moderately with the isotropic γ-ray emission ($E_{\gamma,\mathrm{iso}} \propto E_{\mathrm{X,iso}}^{\mathrm{FL}\ 0.89}$, with an intrinsic scatter of about 0.65; Figure 2.7); in fact in the low energy part of the the plane there is only the short GRB 050724, which leads the correlation.

The two components

The X-ray LCs can be divided in two phases, depending on the emission type and spectral evolution, the prompt emission and the afterglow (Willingale et al. 2007). The steep decay phase spectra evolve from hard to soft (Butler & Kocevski 2007a) and likely reflect the decay of the prompt emission (Tagliaferri et al. 2005a; Goad et al. 2006), in fact the E_{pk} crosses the XRT bandpass towards lower values with time and the transition between the prompt emission

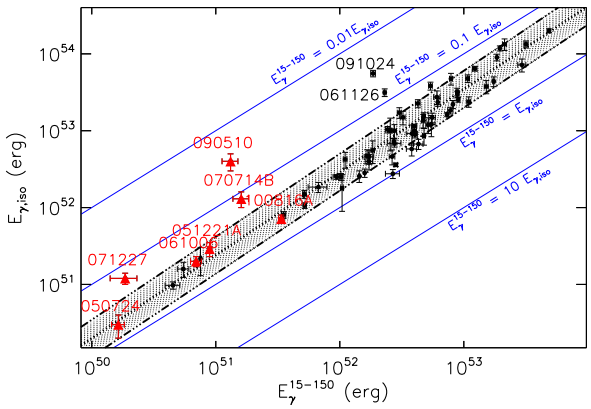

Figure 2.8: Energetics. Relation between the γ-ray energy in the BAT 15-150 keV band (observer frame, E_γ^{15-150}) and the isotropic γ-ray energy (rest frame, $E_{\gamma,\rm iso}$). Blue solid lines mark different $E_{\gamma,\rm iso}/E_\gamma^{15-150}$ ratios. Color coding as in Figure 2.5.

and steep decay flux is smooth. After the steep decay phase, the X-ray spectral index does not vary and sets to ∼2 (Liang et al. 2007): this corresponds to the flattening of the X-ray LC, which starts between 10^2 and 10^4 s after the trigger. Therefore, from these observational considerations, we decide to divided the LCs in two phases: the first component is the steep decay phase (strong spectral evolution) and the second component consists of the plateau and the normal decay phases (no spectral evolution). Hence, for the LC types picked out by our classification, following Fig. 2.1, the first ($E_{1,\rm X}$) and second ($E_{2,\rm X}$) components are:

- Type Ia: $E_{2,\rm X} = E_1 + E_2$.
- Type Ib: $E_{1,\rm X} = E_1$, $E_{2,\rm X} = E_2$.
- Type IIa: $E_{1,\rm X} = E_1$, $E_{2,\rm X} = E_2 + E_3$.
- Type IIb: $E_{1,\rm X} = E_1 + E_2$, $E_{2,\rm X} = E_3$.
- Type III: $E_{1,\rm X} = E_1 + E_2$, $E_{2,\rm X} = E_3 + E_4$.

From the first and second component energy distribution, we find that their peaks are: $E_{1,\rm X} \sim 1.1 \times 10^{51}$ erg and $E_{2,\rm X} \sim 4 \times 10^{51}$ erg (Figure 2.7). The energies do not exceed the value of 10^{53} erg, so this can be considered the limit of the energy budget for the two cases. The maximum limit of 10^{52} erg for the second component is predicted by Usov (1992) and Metzger et al. (2011) if this component is powered by the rotational energy of a newly born magnetar. The energies of the first and second component correlate: $E_{1,\rm X} \propto E_{2,\rm X}^{0.4}$ (Figure 2.7). The short GRBs stay in the low energy part of the $E_{1,\rm X}$-$E_{2,\rm X}$ plane. The energy of the two components correlate with $E_{\gamma,\rm iso}$ ($E_\gamma \propto E_{1,\rm X}^{0.67}$ and $E_\gamma \propto E_{2,\rm X}^{0.92}$), and E_2 with $L_{\rm pk,iso}$ (Figure 2.7).

In Figure 2.8 we show the relation between E_γ^{15-150} and $E_{\gamma,\rm iso}$, $E_{\gamma,\rm iso} = 10^{-3.7}(E_\gamma^{15-150})^{1.08\pm0.01}$ with $\sigma = 0.24$. Short GRBs are generally consistent with the long GRB scaling.

2.4.3 The luminosity

The rest frame X-ray luminosity ($L_{\rm X}^{\rm RF}$) correlates with the γ-ray prompt emission energy (Fig. 2.9). We calculated the rest frame luminosity for complete and truncated LCs, which have observed at 10 min and 11 hr after the trigger. The correlation scatter evolves with time, with $\sigma_{\rm 10min} = 0.45 \pm 0.01$ and $\sigma_{\rm 11hr} = 0.55 \pm 0.01$; this fact suggests that the influence of the prompt emission on the afterglow is getting less and less important as time progresses. Moreover, all short GRBs stay below the correlation calculated considering only long GRBs (i.e. gray band in Fig. 2.9), even if the relation has a high scatter ($\sigma_{\rm 10min}^{\rm long} = 0.40$ and $\sigma_{\rm 11h}^{\rm long} = 0.45$); the only exception is GRB 051212A. A different result was obtained by Nysewander et al. (2009b): in this case the gamma-ray fluences were however calculated into a much narrower energy band (15-150 keV) which makes a direct comparison difficult.

2.4.4 The plateau phase

The plateau or shallow decay phase is the part of the X-ray LC characterized by a mild slope and no spectral evolution in the X-ray band (Liang et al. 2007). According to our classification, the plateau can be found in Type IIa and III LCs, with $\alpha \equiv \alpha_2$, $t_{\rm i} \equiv t_{\rm b1}$, $t_{\rm f} \equiv t_{\rm b2}$, $E \equiv E_2$ and $\alpha \equiv \alpha_3$, $t_{\rm i} \equiv t_{\rm b2}$, $t_{\rm f} \equiv t_{\rm b3}$, $E \equiv E_3$ (Fig. 2.1), respectively. In the observer frame, the distribution peak of the end (begin) plateau phase is at about 10^4 s (10^3 s) since the trigger time and the flux in the same time interval has a peak at $\sim 10^{-11}$ (6×10^{-11}) erg cm^{-2} s^{-1}. These distributions are in accordance with those of Evans et al. (2009). The observer frame end plateau time and flux correlate, $t_{\rm f} \propto F_{\rm f}^{-0.79}$ with a scatter of 0.45. In the rest frame 0.3-30 keV band, the start plateau time is roughly 100 s and the end plateau time distribution peaks at about $10^{3.5}$ s, a time shorter than in the observer frame case. In a few cases, it reaches values of 40 ks, e.g. GRB 060614. The start and end plateau luminosity distributions peak at 6×10^{48} and 10^{48} erg s^{-1}, respectively. We confirm the correlation, $L_{\rm f} \propto t_{\rm f}^{\rm RF\ -1.2}$, previously found by Dainotti et al. (2008, 2010). In addition, luminosities correlate with X-ray

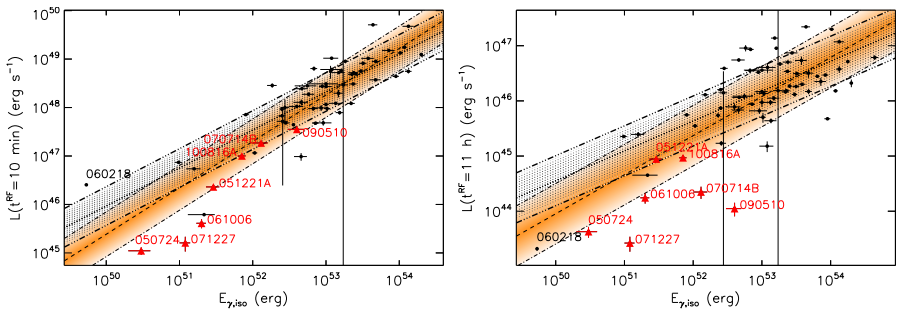

Figure 2.9: The luminosity. Relation between the isotropic γ-ray energy ($E_{\gamma,\rm iso}$) and the luminosity calculated at 10 min rest frame (*left*) and 11 hr (*right*). Color coding as in Figure 2.5.

energies: $E_{\rm X,iso} \propto L_{\rm i}^{1.4}$, $E_{\rm X,iso} \propto L_{\rm f}^{1.2}$ and $E_{\rm 2,X} \propto L_{\rm f}^{0.5}$ (see also Dainotti et al. 2011). As stated in Sec. 2.4.3, the isotropic prompt emission energy directly correlates with the X-ray luminosity at every time, so also the end plateau luminosity: $E_{\gamma,\rm iso} \propto L_{\rm f}^{1.06}$. Furthermore, $L_{\rm pk,iso} \propto L_{\rm f}^{0.8}$ for long GRBs.

Distributions and correlations involving the parameters characterizing the plateau phase are shown in Fig. 2.10-2.11.

There are at least two models that could explain the plateau properties listed above: the accretion model and the magnetar model.

The accretion model (Kumar et al. 2008) has difficulties to accommodate the long lasting plateaus ($t_{\rm f} \sim 40$ ks) and the fact that Type Ib LC plateaus are linked to Type Ia and II LC plateaus (Bernardini et al. 2012a). The accretion material must be ejected at a very large distance and/or a viscous time must be very long (Kumar et al. 2008; Bernardini et al. 2012a). For the Dainotti

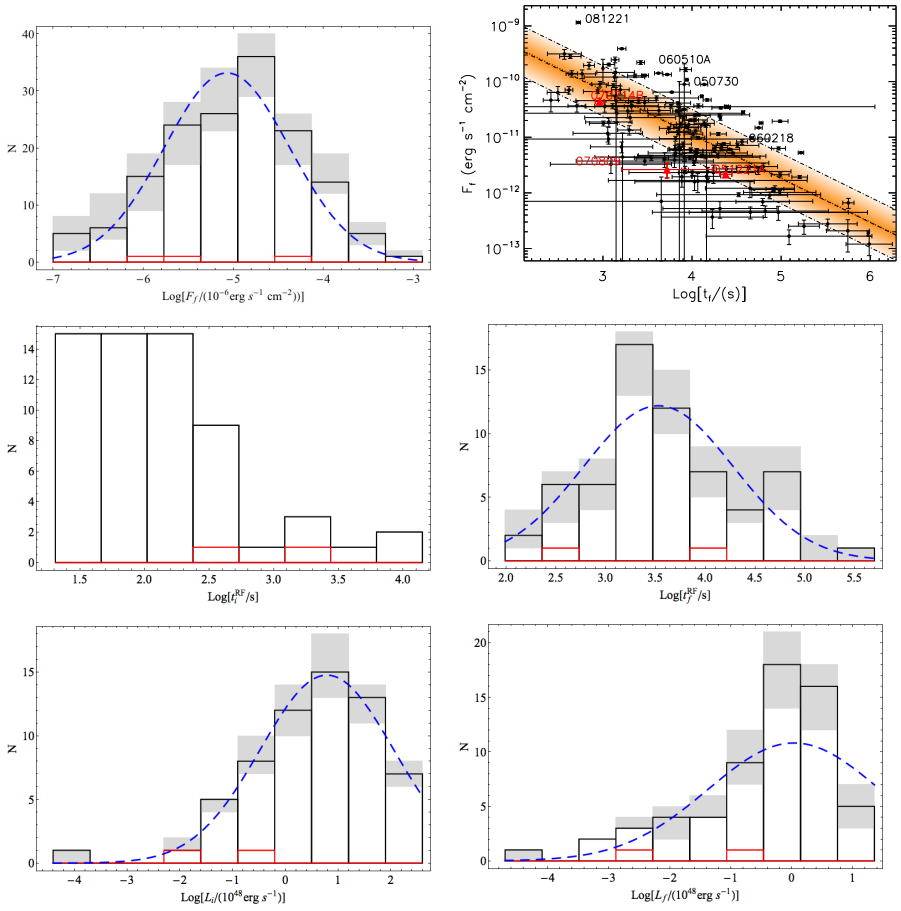

Figure 2.10: Plateau. *Top*: distribution of the end plateau fluence ($F_{\rm f}$, *left*) and correlation between the observer frame end plateau time ($t_{\rm f}$) and the end plateau fluence ($F_{\rm f}$, *right*). *Center*: distributions of the rest frame initial plateau time ($t_{\rm i}^{\rm RF}$, *left*) and the rest frame end plateau time ($t_{\rm f}^{\rm RF}$, *right*). *Bottom*: distributions of the rest frame initial plateau luminosity ($t_{\rm i}^{\rm RF}$, *left*) and the rest frame end plateau luminosity ($t_{\rm f}^{\rm RF}$, *right*). Color coding as in Figure 2.5.

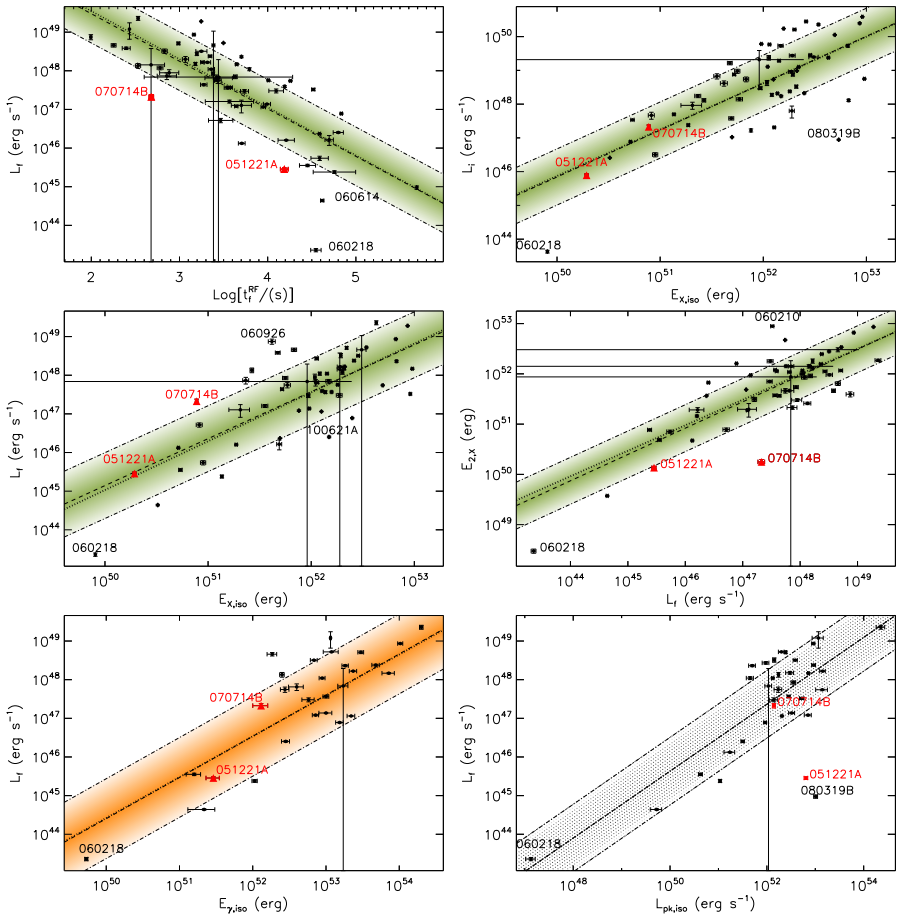

Figure 2.11: Plateau. *Top*: correlation between the rest frame end plateau time ($t_{\rm f}^{RF}$) and luminosity ($L_{\rm f}$, *left*) and the correlation between the isotropic X-ray energy ($E_{\rm X,iso}$) and the initial plateau luminosity ($L_{\rm i}$, *right*). *Center*: correlation of the end plateau luminosty ($L_{\rm f}$) with the isotropic X-ray energy ($E_{\rm X,iso}$, *left*) and the X-ray second component energy (E_2, *right*). *Bottom*: correlation of the end plateau luminosty ($L_{\rm f}$) with the isotropic γ-ray energy ($E_{\gamma,\rm iso}$, *left*) and the peak luminosity (E_2, *right*). Color coding as in Figure 2.5.

relation, a standard reservoir in fall back mass is needed (Cannizzo et al. 2011). The relation between the plateau and prompt emission energy is valid both for Type Ia and II LCs (Liang et al. 2007; Cui et al. 2010) and implies a self-similar structure of the progenitor, with a constant envelope-to-core mass ratio (∼0.02-0.03, Bernardini et al. 2012a).

For the magnetar scenario, a possible source of energy injection is the power emitted by a spinning-down newly-born magnetar (Dai & Lu 1998; Zhang & Mészáros 2001; Corsi & Mészáros 2009) that refreshes the forward shock. Bernardini et al. (2012a), using the model developed by Dall'Osso et al. (2011), fitted the plateaus and normal decay phases of a sample of 16 XRT LCs, excluding the flare contribution. In this scenario all the plateau properties are directly related to the central engine and, consequently, to the prompt

emission. This explains the connection between the plateau energy and the prompt emission energy. The basic information can be derived from two main quantities: the magnetic field B and the period P of the pulsar. In particular, they are all that is needed to explain the anticorrelation between the end plateau luminosity ($L_{\rm f}$) and time ($t_{\rm f}^{\rm RF}$) found by Dainotti et al. (2008, 2010). Starting from the distributions of B and P from the sample of Bernardini et al. (2012a), we obtained the normalization, the slope, and the scatter of the observed anticorrelation (Figure 2.12). These distributions are within the range of values expected for newly born, millisecond spinning magnetars (Duncan & Thompson 1992). Figure 2.12 (Bernardini et al. 2012a) shows the relation between $L_{\rm f}$ and $t_{\rm f}^{\rm RM}$ of type Ia light curves in the rest frame energy band corresponding to $z = 2.29$ (*red squares*), and we found that they follow the same luminosity-time anticorrelation and that they can be interpreted as the spindown luminosity of a millisecond pulsar for the same distribution of B and P as for type II. We added also Type Ib observations (*pink squares*) as a lower limit on the end of the injection phase and an upper limit on the luminosity. The possibility of having injection times up to 10^5 s, as observed in type Ib light curves, is allowed within reasonable values of the magnetic field and period. However, the upper limit on luminosity found for some type Ib is much lower than the expected one, unless we assume that the injection time is $\gtrsim 10^6$ s. We argued that a different beaming factor and/or efficiency in converting the spin-down power in X-rays may account for such type Ib light curves. The main constraints of the magnetar model is related to the energy budget. The maximum energy emitted in such a model is a few 10^{52} erg and limited by the maximum rotation energy attainable by a rotating neutron star (Usov 1992). The energy budget strongly depends on the uncertain estimate of the jet angle, however in a few cases the released energy may be high enough to challenge the model (Cenko et al. 2010).

2.4.5 LC temporal slopes

The X-ray LCs have a standard/canonical shape (Sec. 1.2.2), which consists in a rapid initial decay (*steep decay*), a quasi-constant or mild decay (*plateau* or *shallow decay*) and a final decay phase (*normal decay*). In our classification, this kind of LC is represented by Type IIa LC. We use the following classification to study and compare the LC slopes in the different phases:

- Steep decay: $\alpha_{\rm st} \equiv \alpha_1({\rm Ib, IIa})$; $\alpha_{\rm st} \equiv \alpha_2({\rm IIb, III})$.
- Shallow decay: $\alpha_{\rm sh} \equiv \alpha_2({\rm IIa})$; $\alpha_{\rm sh} \equiv \alpha_3({\rm III})$.
- Normal decay: $\alpha_{\rm n} \equiv \alpha_2({\rm Ia})$; $\alpha_{\rm n} \equiv \alpha_3({\rm IIa})$; $\alpha_{\rm n} \equiv \alpha_2({\rm III})$.

Since it is well known that at early times the estimation of the slopes depends on the initial time chosen as the zero time, we used as the beginning of the event both the trigger time and T_{90}. This will give an indication of the uncertainties of the calculation of the parameters at early times. The mean values obtained are $\alpha_{\rm st}(t_0 = t_{90}) = 3.15$ and $\alpha_{\rm st}(t_0 = 0) = 3.96$. T_{90} depends on

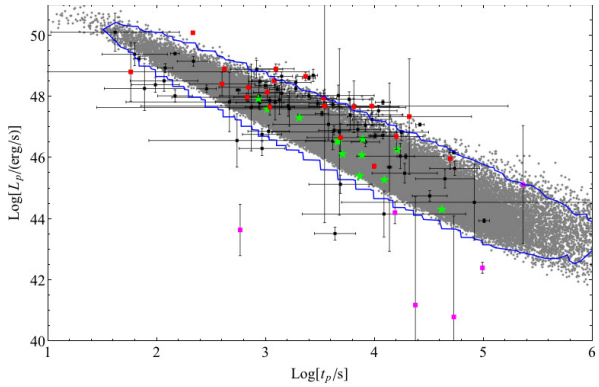

Figure 2.12: Plateau. End plateau luminosity ($L_\mathrm{p} \equiv L_\mathrm{f}$) vs. end plateau time ($t_\mathrm{p} \equiv t_\mathrm{f}$). *Black squares*: data of the sample of Dainotti et al. (2010). *Red squares*: type Ia LCs of the sample of Bernardini et al. (2012a). *Pink squares*: luminosity of the last observations in type Ib LCs of the sample of Bernardini et al. (2012a). *Gray dots*: the 100 000 simulations at the spin down time assuming that the magnetic field and the NS period are normally distributed around the mean values found for the Bernardini et al. (2012a) sample. *Blue line*: it delimitates the region that includes 99% of simulations. *Green stars*: the values found for the best fit of the Bernardini et al. (2012a) sample with the Dall'Osso et al. (2011) model.

the instrumental threshold and on the considered energy band, however it is the best estimation of the prompt emission phase duration. The shallow and normal decay slopes are less affected by the definition of the zero time, simply

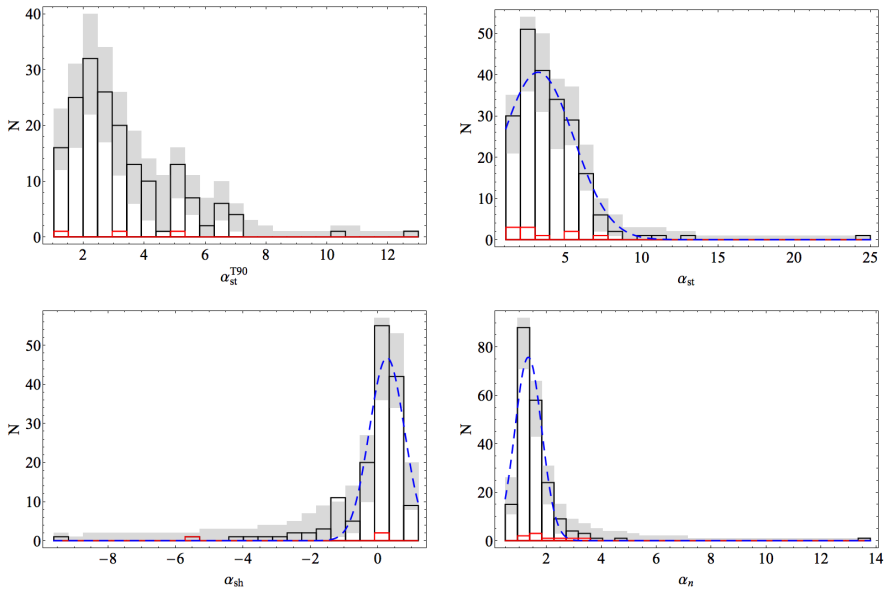

Figure 2.13: LC slopes. *Bottom*: distributions of steep decay slopes calculated considering $t_0 \equiv T_{90}$ ($\alpha_{\mathrm{st}}^{\mathrm{T90}}$, *left*) and $t_0 \equiv 0$ s (α_{st}, *right*). *Bottom*: distributions of the slopes of the plateau (α_{sh}, *left*) and of the normal decay (α_{n}, *right*). Color coding as in Figure 2.5.

because they are far from the prompt emission.

The shallow decay phase has a mean slope of about 0.3, in accordance with Evans et al. (2009) ($\alpha_{\rm n} \sim 0.2$, FWHM=0.79) and Racusin et al. (2009) ($\alpha_{\rm n} \sim 0.5$). Shallow decay slopes < -3 have large uncertainties, so they do not influence our analysis.

The normal decay phase slope has a mean value of about 1.3 and also in this case there is agreement with the results obtained by Evans et al. (2009) and Racusin et al. (2009).

From the three distributions, we note that $\sigma(\alpha_{\rm st}) > \sigma(\alpha_{\rm sh}) \gtrsim \sigma(\alpha_{\rm n})$: GRBs manifest their peculiarity at early times, and at late times they have a similar evolution, as seen by the luminosity dispersion in Sec. 2.4.1. Short GRBs have similar slopes as long GRBs during the steep, shallow and normal decay phases.

The distributions of the LC slopes are shown in Figure 2.13.

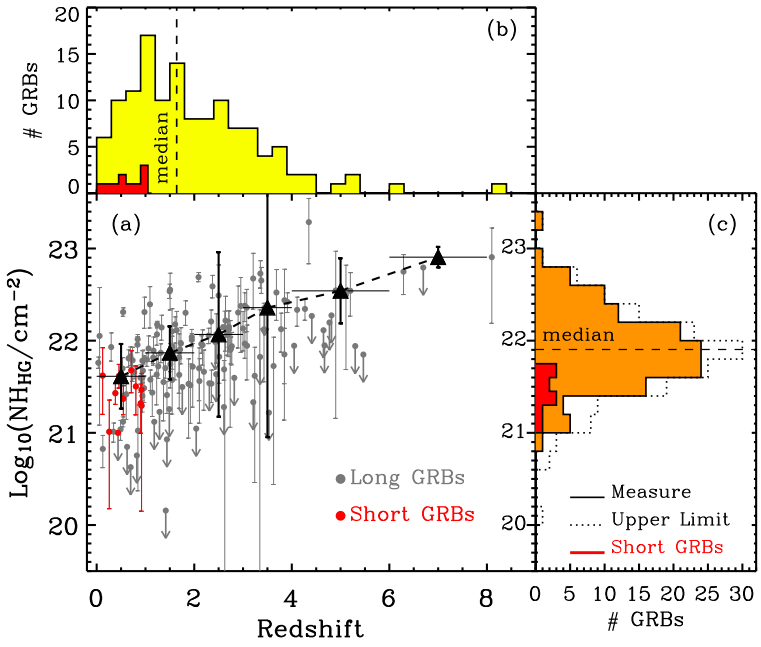

Figure 2.14: Hydrogen column density. *(a)*: intrinsic neutral hydrogen absorption vs. redshift for long and short GRBs (gray and red dots, respectively). 90% upper limits are marked with arrows. Median $N_{\rm H,HG}$ values in different redshift bins are indicated with filled triangles: for each bin, the error bars span the 1σ $N_{\rm H,HG}$ dispersion. *(b)*: redshift distribution of the sample of long (*yellow*) and short (*red*) GRBs. *(c)*: intrinsic neutral hydrogen distribution for long (*black line*) and short (*red line*) GRBs. The dashed histogram includes upper limits. The dashed line in panels *(a)* and *(b)* indicates the median value for the entire distributions ($\langle z \rangle = 1.82$, $\langle N_{\rm H,HG} \rangle = 10^{21.8}$ cm^{-2}).

2.4.6 The intrinsic hydrogen-equivalent absorption

We determined the equivalent column density $N_{\rm H,HG}$ fitting the spectra of GRBs with known redshift, using solar abundances. The mean value of the distribution of the measured $N_{\rm H,HG}$ is $10^{21.6}$ cm^{-2}, with $\mu(\log N_{\rm H,HG}\ {\rm cm}^{-2}) = 21.9 \pm 0.1$ and $\sigma = 0.6 \pm 0.1$; these results are in agreement with the value found by Campana et al. (2010, 2012), even if in our sample there are more GRBs with no evidence of intrinsic absorption and we found at low redshift ($z < 2$) an highly absorbed population ($N_{\rm H,HG} > 10^{22}$ cm^{-2}) (Figure 2.14).

We noted that $N_{\rm H,HG}$ increases with the redshift: this is only an apparent fact, since the sensitivity of XRT to detect X-ray absorption decreases with the increase of redshift and the sample is redshift selected[9].

Short GRBs have similar $N_{\rm H,HG}$ of long GRBs in the same redshift bin and their average absorption is $N_{\rm H,HG}^{\rm short} = 10^{21.4}$ cm^{-2}.

2.4.7 The 3-parameter correlation: $E_{\gamma,\rm iso}$ - $E_{\rm pk}$ - $E_{\rm X,iso}$

We used the statistical technique named the principal component analysis (PCA) to find patterns in our data (44 parameters) with the aim to "compress" the data by reducing the number of dimensions, without loss of information (see Appendix A and Jolliffe 2002 for details). Among all, we considered the group of 5 parameters $E_{\rm X,iso}$ (in the 0.3-10 keV band), $E_{\rm pk}$, $E_{\gamma,\rm iso}$, $L_{\rm pk}$ and T_{90} and we applied the PCA. In Table 2.5 we report the first of the three principal components (e.g. the directions with the greatest variance, PC) for these five parameters. In the first PC, each variable contributes in the same way, with the exception of $T_{90}^{\rm RF}$. The T_{90} is the parameter which dominates the second PC, instead the third PC is represented by $\hat{E}_{\rm X,iso}$ and $\hat{E}_{\rm pk}$. This suggests that, while $E_{\rm pk}$, $L_{\rm pk}$, $E_{\rm X,iso}$ and $E_{\gamma,\rm iso}$ are in some way physically related to one another, the duration of the γ-ray energy release represents an additional degree of freedom to the system.

Starting from these considerations we studied the relation between $E_{\rm pk}$, $E_{\rm X,iso}$ and $E_{\gamma,\rm iso}$. We considered only complete LCs and GRBs with $E_{\rm pk}$ and $E_{\gamma,\rm iso}$ and the $E_{\rm X,iso}$ calculated in the 0.3-10 keV energy band. Therefore, the sample is composed by 61 GRBs, with 7 GRBs (Table 2.6).

We calculated the relation between these three parameters considering the intrinsic scatter (D'Agostini 2005) and using Markov chain Monte Carlo techniques, generating 10^5 sample for every Markov chain according to the

[9] We would attribute a higher optical-to-X-ray absorption ratio at lower redshift if at high redshift the extinction curve is more quasar-like and at low redshift is similar to the extinction curve of the Milky Way.

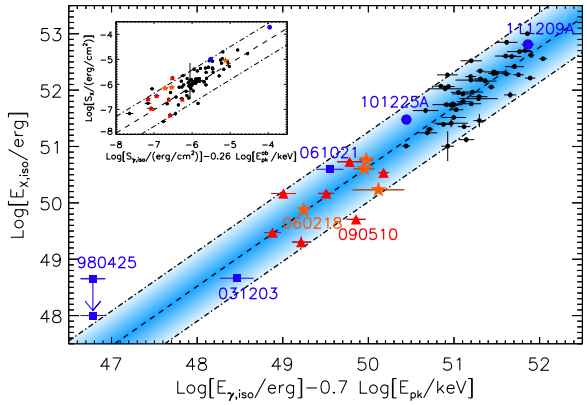

Figure 2.15: The 3-parameter correlation: $E_{\rm X,iso}$-$E_{\gamma,\rm iso}$-$E_{\rm pk}$, with $E_{\rm X,iso}$ computed in the 0.3-10 keV band. *Black points*: 54 long GRBs. *Red triangles*: 7 short GRBs. *Orange stars*: low-energetic GRBs (GRB 050416A, GRB 060218, GRB 060614, GRB 081007). *Blue squares*: outliers of the Amati relation, $E_{\rm pk} - E_{\gamma,\rm iso}$ (GRB 090425, GRB 031203, GRB 061021). *Blue circles*: GRB 101225A and GRB 111209A. *Black dashed line*: the best-fitting function $y = 1.6(x - 0.7z) - 2.36$. *Blue area*: the 2σ region. *Inset*: $S_{\rm X} - S_{\gamma,\rm iso} - E^{\rm ob}_{\rm pk}$ correlation for the sample of 71 long GRBs (*black points*) and 8 short GRBs (*red triangles*). Color coding as the main plot. The best fitting function is $y = 0.93(x - 0.26z) - 0.51$.

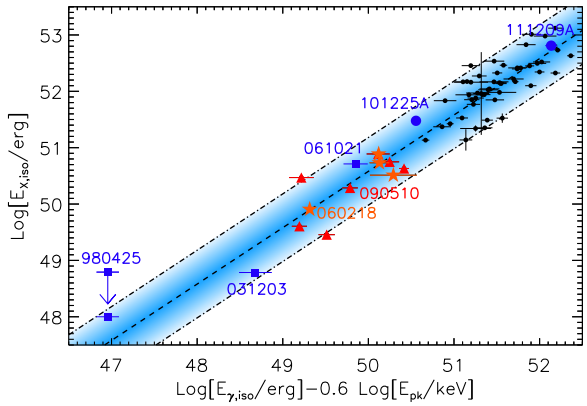

Figure 2.16: The 3-parameter correlation: $E_{\rm X,iso}$-$E_{\gamma,\rm iso}$-$E_{\rm pk}$, with $E_{\rm X,iso}$ calculated in the 0.3-30 keV band. Color coding as in Figure 2.5.

likehood function[10]. The relation that links together $E_{\rm pk}$, $E_{\rm X,iso}$ and $E_{\gamma,\rm iso}$ is

$$\log\left(\frac{E_{\rm X,iso}}{\rm erg}\right) = (1.06 \pm 0.06)\log\left(\frac{E_{\gamma,\rm iso}}{\rm erg}\right) - (0.74 \pm 0.10)\log\left(\frac{E_{\rm pk}}{\rm keV}\right) - (2.36 \pm 0.25), \quad (2.6)$$

with the scatter $\sigma_i = 0.31 \pm 0.03$ (Figure 2.15).

[10]In our analysis, we used JAGS (Just Another Gibbs Sampler), a program for the analysis of Bayesian hierarchical models using Markov Chain Monte Carlo simulation. More information can be found at http://mcmcjags.sourceforge.net/

Table 2.5: The three most significant PCs (85% of the total variance) projected upon $\hat{E}_{\gamma,\rm iso}$, $\hat{E}_{\rm pk}$, $\hat{L}_{\rm pk}$, $\hat{t}^{\rm RF}_{90}$ and $\hat{E}_{\rm X,iso}$.

	PC1	PC2	PC3
	40%	66%	85%
$\hat{E}_{\gamma,\rm iso}$	-0.561	0.141	0.171
$\hat{E}_{\rm pk}$	-0.448	-0.300	-0.630
$\hat{L}_{\rm pk}$	-0.502	-0.389	-
$\hat{t}^{\rm RF}_{90}$	-0.121	0.794	-0.512
$\hat{E}_{\rm X,iso}$	-0.466	0.331	0.588

Table 2.6: List of the 61 GRBs included in the sample. SGRBs are marked in boldface.

GRB name					
050401	050416A	050525A	**050724**	050820A	050904
050922C	051109A	**051221A**	060115	060124	060206
060218	060418	060526	060607A	060614	060707
060814	060908	060927	**061006**	061007	061121
070714B	071020	**071227**	080319B	080319C	080411
080413A	080413B	080605	080607	080721	080810
080913	080916A	080928	081007	081008	081028
081118	081222	090205	090418A	090423	090424
090510	090516	090618	090715B	090812	091018
091020	091029	091208B	100621A	100814A	**100816A**
100906A					

This correlation is very robust, because it spans over four order of magnitudes in $E_{\rm X,iso}$ and $E_{\rm pk}$ and six orders in $E_{\gamma,\rm iso}$ and it is valid both for short and long GRBs, even if short GRBs are outliers of 2-parameter correlations involving $E_{\gamma,\rm iso}$, $E_{\rm X,iso}$ and $E_{\rm pk}$. Therefore this correlation reflects some physical property in common to all GRBs.

We tested the 3-parameter correlation also in the observer frame, calculating the $S_{\rm X}$ fluence in the 0.3-10 keV band, the fluence S_γ in the 1-10^4 keV band and the peak energy in the observer frame ($E^{\rm ob}_{\rm pk}$). The sample is composed of 79 GRBs, with 8 short GRBs. The correlation is statistically significant also in the observer frame:

$$\log(S_{\rm X}) = (0.93 \pm 0.06)\log(S_\gamma) - (0.24 \pm 0.09)\log(E^{\rm ob}_{\rm pk}) - (0.51 \pm 0.04), \quad (2.7)$$

with $\sigma_i = 0.33 \pm 0.03$ (Figure 2.15, *inset*). In fact, this correlation is weakly dependent on the redshift, because $E_{\rm X} \propto E_{\rm pk}$ and a variation of the luminosity distance causes a shift along the best fitting direction.

To exclude that the correlation depends on the choice of a specific energy band in the calculation of $E_{\rm X,iso}$, we computed $E_{\rm X,iso}$ in a common rest frame

energy band 0.3-30 keV. We obtained the same result within uncertainties as in Eq. 2.6.

$$\log\left(\frac{E_{\rm X,iso}^{\rm RF,0.3-30}}{\rm erg}\right) = (1.00\pm0.06)\log\left(\frac{E_{\gamma,\rm iso}}{\rm erg}\right) - (0.60\pm0.10)\log\left(\frac{E_{\rm pk}}{\rm keV}\right) - (0.58\pm0.25), \quad (2.8)$$

with $\sigma_i = 0.30 \pm 0.03$ (Figure 2.16).

We tested also the influence of the interval time of the integration of $E_{\rm X,iso}$. The time interval over which the energy is calculated spans from 100 s to 10^6 s, giving a reliable estimate of the total X-ray energy. However, in most cases the time interval of the observation is an underestimate of the entire duration of the X-ray emission. To check the influence of the temporal interval, we extrapolated the X-ray LCs over a common interval from $t_{\rm start}^{\rm RF} = T_{90}$ to $t_{\rm end}^{\rm RF} = 10^7$ s and calculated the corresponding energy. The major difference is in the short GRB energy, since they have steeper luminosity LC than long GRBs. The new relation is consistent with Eq. 2.6 within uncertainties, and short GRBs are distributed in a narrower band.

The correlation does not include the energy emitted during the flaring activity, which is present in 40% of the GRBs of our sample. The energy content of flares is usually ∼3% of $E_{\gamma,\rm iso}$ but it can be as high as $E_{\gamma,\rm iso}$ for GRB 060526 and is ∼ 25% of their underlying continuum energy $E_{\rm X,iso}$. The inclusion of the flare energy into $E_{\rm X,iso}$ does not improve significantly the correlation scatter. This is not surprising since short GRBs, which are the most scattered population in the three-parameter correlation, have no bright flares (Margutti et al. 2011b) After a systematic analysis of all the flare properties (Chincarini et al. 2010a; Margutti et al. 2010b, 2011b; Bernardini et al. 2011), their origin remains elusive. Their observational properties point to a direct link with the prompt emission (as e.g. in the form of late-time activity of the central engine; Perna et al. 2006; Proga & Zhang 2006. However, they may also be produced by late-time dissipation within the outflow (see e.g. Giannios 2006). The association of the flare energy with either $E_{\gamma,\rm iso}$ or $E_{\rm X,iso}$ is not straightforward. Either way we note that even the extreme GRB 060526, for which $E_{\rm X}^{\rm FL}$-$E_{\gamma,\rm iso}$, is still consistent with the correlation at 2σ level.

We proved the robustness of the 3-parameter correlation considering peculiar GRBs, which have particular energy budgets or are outlier of the 2-parameter correlations:

- GRB 980425 and GRB 031203 are outliers of the Amati relation (Amati 2006; Ghisellini et al. 2006). We estimate the $E_{\rm X,iso}$ from the data present in literature and we found that GRB 031203 follows the correlation. GRB 980425 is associated to the SN 1998bw, so we must consider the SN energy release to estimate $E_{\rm X,iso}$. This GRB is a factor ∼10 over the correlation, but if we assume $E_{\gamma,\rm iso}$ as an upper limit over $E_{\rm X,iso}$, this GRB is consistent with the 3-paramter correlation.

- GRB 060218 is a long lasting GRB, with T_{90} ∼2100 s in the BAT energy band, with a very soft prompt emission spectrum and $E_{\rm pk}$ ∼5 keV. Computing $E_{\rm X,iso}$ starting from $t_{\rm start} = T_{90}$, this GRB follows the 3-parameter correlation within 2σ.

- GRB 090510 is a short GRB and it is the unique GRB in our sample observed at very high energies ($\gtrsim$ 1 GeV) by the *Fermi*-Large Area Telescope (LAT). It agrees with the 3-parameter correlation within 2σ, but it is an outlier of the other correlation involving the X-ray and γ-ray parameter, as well as the Amati relation. If we add the energy detected by *Fermi*-LAT to the X-ray energy or to $E_{\gamma,\rm iso}$, the GRB does not follow the 3-parameter correlation. Unfortunately, it is the only GRB observed both by *Swift* and *Fermi*-LAT and we cannot judge if it is a peculiar GRB or not.

- GRB 101225A is an unusual GRB because it has some characteristics which can be attributed to Galactic transients (Campana et al. 2011). In fact, it has an exceptionally long X-ray emission, followed by a bright X-ray transient with a hot thermal component and an unusual optical counterpart. If we assign to this GRB the redshift estimated by Thöne et al. (2011) from a possible SN component in the optical LC, $E_{\rm pk}$ from the Band spectrum and $E_\gamma^{15-150} - E_{\gamma,\rm iso}$ extrapolated from $E_{\rm pk} - E_{\gamma,\rm iso}$ relation, this possible GRB follow the 3-parameter correlation.

- GRB 111209A is a very long event. $E_{\gamma,\rm iso}$ and $E_{\rm pk}$ are estimated by Konus-Wind data and $E_{\rm X,iso}$ with the procedure presented in this Chapter. This GRB is in agreement with the 3-parameter correlation.

This 3-parameter correlation is followed by all types of GRBs, so it would not originate from ambient and progenitor properties, which are though different for long and short GRBs.

Short and low-energetic[11] GRBs are clustered in a zone of the plane with $E_{\rm X,iso} \lesssim 10^{51}$ erg, instead long GRBs have $E_{\rm X,iso} \gtrsim 10^{51}$ erg. If we consider the relation $E_{\gamma,\rm iso} - E_{\rm pk}$ (Amati et al. 2008), short GRBs do not follow the Amati relation valid for long GRBs. This fact could be influenced by the different X-ray energy of the two classes of objects (e.g. Zhang et al. 2012). Low energetic GRBs stay in the tail both of long and short GRBs (Figure 2.17, *left*).

We can rewrite Eq. 2.6 considering the ratio between the X-ray and γ-ray isotropic energies ($\epsilon \equiv E_{\rm X,iso}/E_{\gamma,\rm iso}$). To have a more accurate estimation we consider the X-ray energy in the common rest frame band 0.3-30 keV, $E_{\rm X,iso} \equiv E_{\rm X,iso}^{RF,0.3-30}$. Equation 2.6 becomes

$$\log(\epsilon) = -(0.58 \pm 0.40) \log\left(\frac{E_{\rm pk}}{\rm keV}\right) + (0.60 \pm 0.15) \qquad (2.9)$$

with $\sigma_i = 0.30 \pm 0.06$ (Figure 2.17, *right*); this is simply $\epsilon \propto E_{\rm pk}^{-0.6}$. ϵ is independent of the collimation, since the prompt and X-ray emissions have

[11] Low energetic GRBs have $E_{\gamma,\rm iso} \lesssim 10^{51}$ erg and $E_{\rm pk} \lesssim 50$ keV.

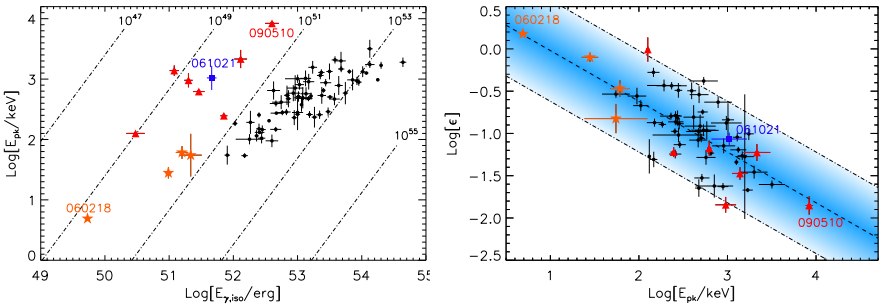

Figure 2.17: Different ways to write the 3-parameter correlation. *Left*: $E_{\rm X,iso}^{0.30-30} - E_{\gamma,\rm iso} - E_{\rm pk}$ correlation for the GRBs in our sample projected on the plane $E_{\gamma,\rm iso} - E_{\rm pk}$ plane. *Dashed-dotted lines*: different values of $E_{\rm X,iso}$. *Right*: $\epsilon \equiv E_{\rm X,iso}^{0.30-30}/E_{\gamma,\rm iso}$ vs. $E_{\rm pk}$. The best fitting function is $y = -(0.58 \pm 0.40)x + (0.60 \pm 0.15)$. Color coding as in Figure 2.15.

the same opening angle, and it is inversely proportional to the GRB efficiency (See Appendix C for details); hence GRBs with a high efficiency have low ϵ and the majority of the energy is emitted during the prompt emission. We note that short and long GRBs share the same area of the plane $\epsilon - E_{\rm pk}$, because they have a high efficiency, while low energetic GRBs form a separate group because of their low efficiency.

The correlations involving the prompt emission depend on the Lorentz factor of the ouflow Γ (Ghirlanda et al. 2012); in particular $E_{\rm pk}$ is directly proportional to Γ. Therefore, the physical parameter that rules this relation and the GRB efficiency could be the Lorentz factor: $\epsilon \propto \Gamma^{-\alpha}$. More efficient GRBs would have greater Lorentz factors and the majority of the energy is emitted during the prompt phase, while low efficiency GRBs would have small Γ and they do not emit all the initial energy during the prompt emission. Low energy GRBs are considered mildly relativistic (e.g. Ghisellini et al. 2007; Waxman et al. 2007), in fact we found that they have a low efficiency. An example of efficient GRB whit high Lorentz factor is GRB 090510 ($\Gamma \gtrsim 1000$, Racusin et al. 2011; $\Gamma \sim 800$, Ghisellini et al. 2010).

In the photospheric model (Rees & Mészáros 2005; Ryde et al. 2006), the peak energy corresponds to the thermal peak of the photospheric model, and it is related to the outflow properties, as the Lorentz factor. The energy is dissipated close to the photosphere because of the internal shocks, nuclear collisions or magnetic reconnection (Rees & Mészáros 2005). For the magnetic reconnection, $E_{\rm pk}$ is mainly determined by the bulk Lorentz factor (Giannios 2012).

For the magnetar model (Usov 1992; Metzger et al. 2011) the anti-correlation ϵ-$E_{\rm pk}$ rises from the fact that the magnetar rotational energy limits the energy budget, and less energy remains to power the following X-ray energy. The limited energy budget implies that if the prompt emission is more energetic, less energy is released after the main burst.

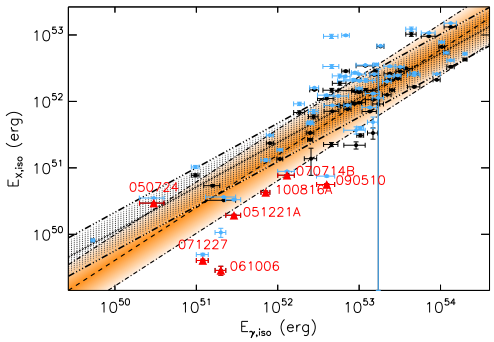

Figure 2.18: Temporal extrapolation effect on the $E_{\rm X,iso} - E_{\gamma,\rm iso}$ relation. *Light blue points*: $E_{\rm X,iso}$ values computed integrating the luminosity over a common rest frame time interval. Color coding as Figure 2.5.

2.4.8 Observational biases

We verified if some biases affect in the calculation of the parameters discussed above, in particular we focus on $E_{\rm X,iso}$. This energy is calculated integrating the X-ray LC between the XRT re-pointing time ($t_{\rm rep}$) and the end of the observations ($t_{\rm end}$), which are different from a GRB to another. Therefore, we estimated the lost energy at late times integrating until 10^7 s in the rest frame; in this way we overestimate the energy since the X-ray LCs can show a break at late times (Racusin et al. 2009). At the beginning we calculated the X-ray energy extrapolating backwards in time the X-ray LCs to the minimum rest frame *Swift* re-pointing time of the GRBs of our sample, 12.5 s. If $T_{90}^{\rm RF} > 12.5$ s, we used T_{90}^{RF} as the starting time, to avoid to extrapolate an unreal luminosity. Also in this case we overestimate the energy, as shown by the comparison with the *Swift*/BAT emission at the same rest frame. In Figure 2.18 the relation $E_{\gamma,\rm iso}$-corrected $E_{\rm X,iso}$ is shown (light blue dots). The relation for the long GRBs is not influenced by the correction. Short GRBs show a large difference between the two values of $E_{\rm X,iso}$ (up to a factor $\sim$9 for GRB 090510), but they remain a separate group respect long GRBs.

The different rest frame integration time intervals do not influence the validity of this correlation, and this can be confirmed also for the other correlations presented in this Chapter.

2.5 Conclusions

We performed a comprehensive statistical analysis of the X-ray LCs of GRBs detected between December 2004 and December 2010. The main characteristics of this analysis are:

- we calculated the properties of GRBs in a common rest-frame 0.3-30 keV energy band;
- we compared the characteristic of long and short GRBs;

- we made a cross-correlation between the prompt γ-ray properties and the X-ray LC properties.

For long GRBs we found that the X-ray energy release is about 7% of the γ-ray isotropic energy, and it is directly proportional to $E_{\gamma,\rm iso}$ and $E_{\rm pk}$. In addition, the maximum value of $E_{\rm X,iso}$ is 10^{53} erg (GRB 080721), and the X-ray energy is greater than 10^{51} for GRBs with a redshift greater than 2. This suggests that the budget of the emitted X-ray energy is limited. The X-ray luminosity calculated at different rest frame times between 100 and 10^5 s correlates with $E_{\gamma,\rm iso}$. The scatter of the correlation increases with time perhaps because the X-ray energy is more related to the prompt emission at early than late times; indeed the X-ray LCs in luminosity are more spread at the beginning of the observations than at late times.

Short and long GRBs represent two classes of GRBs with different energetics, environments and progenitors (see Chapter 1). In particular, the statistical analysis of GRBs in our sample shows that short and long GRBs have different energetics and luminosities:

- the median luminosity of short GRBs is a factor ∼10-30 lower than long GRBs, in the common rest frame time $10^2 - 10^4$ s;
- the median luminosity LC of short GRBs is steeper ($\propto t^{-1.3}$) than long GRBs ($\propto t^{-1}$);
- long GRB luminosity LCs are more clustered at late times than at the beginning; short GRBs do not show this trend;
- short GRBs are less energetic than long GRBs ($E^{\rm short}_{\rm X,iso} \sim 1/50 E^{\rm long}_{\rm X,iso}$), populating the low-energy tail of the $E_{\rm X,iso}$ distribution, and in particular they have a lower E_2;
- short GRBs stay below of the correlations $E_{\rm X,iso} - E_{\gamma,\rm iso}$, $E_{\rm X,iso} - E_{\rm pk}$, $L^{\rm 11h}_{\rm X} - E_{\gamma,\rm iso}$, and $L_{\rm f} - t^{\rm RF}_{\rm f}$ established for long GRBs[12];
- the X-ray plateaus are present more in long GRB LCs than in short GRB LCs;
- the mean hydrogen column density of short GRBs is lower than long GRBs ($N^{\rm short}_{\rm H,HG} \sim 10^{21.4}$ cm^{-2}, $N^{\rm long}_{\rm H,HG} \sim 10^{21.9}$ cm^{-2}), but there is no difference between short and long $N_{\rm H,HG}$ in a common redshift bin.

The 3-parameter correlation, which involves $E_{\gamma,\rm iso} - E_{\rm pk} - E_{\rm X,iso}$, is followed by long, short and low energy GRBs, even if they occupy a different region of the plane since short and low-energy GRBs have $E_{\rm X,iso} < 10^{51}$ erg and long GRBs have $E_{\rm X,iso} > 10^{51}$ erg. The existence of a common scaling for long and short GRBs implies that they have some characteristic in common, for example the properties of the outflow. Moreover, some low energetic GRBs (GRB 980425, GRB 031203, GRB 061021) that are outlier of the Amati

[12] In our sample there are only 2 short GRB LCs with the palteau.

relation ($E_{\gamma,\mathrm{iso}} - E_{\mathrm{pk}}$) are consistent with the 3-parameter correlation. This 3-parameter correlation can be re-written in a two parameter correlation in terms of efficiency ($\eta_\gamma \propto E_{\gamma,\mathrm{iso}}/E_{\mathrm{X,iso}}$) and peak energy: $\eta_\gamma \propto E_{pk}^{0.6}$. The outflow property that could explain this relation is the Lorentz factor.

3

The gamma-ray burst optical light-curve zoo

The *Swift* satellite opened a new era for the study and understanding of the phenomenon of GRBs. The rapid computation of the GRB position by *Swift*/BAT, refined with an accuracy of few arcseconds by *Swift*/XRT, and the instantaneous dissemination to the community via GCN[1] allow a growing number of robotic telescopes to promptly repoint to the source. Some examples are Robotic Optical Transient Search Experiment (ROTSE-III, Akerlof et al. 2003), Rapid Eye Mount telescope (REM, Zerbi et al. 2001; Chincarini et al. 2003), Gamma-Ray Burst Optical/Near-Infrared detector (GROND, Greiner et al. 2008), Liverpool (LT) and Faulkes telescopes (Gomboc et al. 2006), Télescopes à Action Rapide pour les Objets Transitoires (TAROT, Klotz et al. 2008b), etc.

Some generic features have been previously found in optical LCs. Optical and X-ray LCs are different at early times in the majority of cases (Melandri et al. 2008b; Rykoff et al. 2009; Oates et al. 2009, 2011). In particular, Oates et al. (2009, 2011) noted that the optical LCs can decay or rise before 500 s after the trigger in the observer frame, and they do not show a steep decay as the X-ray LCs; after 2000 s the optical and X-ray LCs have similar slopes. Panaitescu & Vestrand (2008, 2011) divided the optical LCs depending on their initial behavior (peaky or shallow). Peaks were associated to impulsive ejecta releases, while plateau phases to the energy released by a long-lived central engine. Chromatic and achromatic breaks have been found in the optical and X-ray LCs (Melandri et al. 2008b; Rykoff et al. 2009; Oates et al. 2009, 2011; Panaitescu & Vestrand 2011). Moreover, the brighter optical LCs decay faster (Oates et al. 2009, 2011, 2012). When optical and X-ray LCs do not share the same temporal decay, X-ray LCs have been found to decay faster (Oates et al. 2009, 2011; Panaitescu & Vestrand 2011). Only for some GRBs with shallow X-ray decay phases do we find a corresponding shallow decay in the optical (Rykoff et al. 2009; Li et al. 2012). Flares can occasionally appear in optical LCs and likely linked to the long term central engine activity (Li

[1] Gamma-ray Coordinates Network (GCN), http://gcn.gsfc.nasa.gov/gcn3_archive.html

et al. 2012).

Previous works mainly concentrated on data obtained by a single telescope (e.g. Melandri et al. 2008b; Klotz et al. 2009a; Cenko et al. 2009b; Oates et al. 2009, 2011; Rykoff et al. 2009) and only few authors compared the data from different instruments (e.g. Kann et al. 2010b, 2011; Li et al. 2012; Liang et al. 2012). For example, Kann et al. (2010b, 2011) focused on the classification of the optical LCs and the host galaxy extinction. Li et al. (2012) and Liang et al. (2012) concentrated on the optical LC shapes and particular features, as bumps, plateaus, late rebrightenings. Other works studied the dust extinction of the GRB host galaxies (e.g. Schady et al. 2012, 2010; Zafar et al. 2011) or the circumburst density profiles around GRB progenitors (Schulze et al. 2011).

In this Chapter we analyze a large sample of 68 GRBs with optical and X-ray observations and known redshift, detected between December 2004 and December 2010. Our starting sample includes 165 GRBs with known redshift presented by Margutti et al. 2013 (hereafter M13, see Chapter 2 for details). We collected the optical data from the literature and for 68 GRBs we obtained well sampled optical LCs, from different telescopes and instruments. For the comparison between the optical and X-ray observations, we used the X-ray data extracted and analyzed in M13. We focused on the relationship between the optical and X-ray emission, comparing their rest-frame temporal and spectroscopic properties and their energetics. In particular, we investigated the forward shock model and the synchrotron emission in the GRB afterglow. In Sect. 3.1 we detailed the sample selection criteria, the data selection and reduction, the procedure followed for fitting the optical LCs and of the spectral energy distributions (SEDs). The results of our analysis are presented in Sect. 3.2 and are discussed in Sect. 3.3. The main conclusions are drawn in Sect. 3.4. We adopted standard values of the cosmological parameters: $H_0 = 70$ km s^{-1} Mpc^{-1}, $\Omega_{\rm M}$=0.27, and Ω_Λ=0.73. For the temporal and spectral energy index, α and β, we use the convention $F_\nu(t,\nu) \propto t^{-\alpha}\nu^{-\beta}$. Errors are given at 1σ confidence level unless otherwise stated.

3.1 Sample selection and data analysis

We considered the 165 GRBs with known and secure redshift[2] observed by *Swift*/XRT between December 2004 and December 2010, presented in M13. Among these GRBs, we selected those with optical observations and with optical data available in the literature. We used only the data from refereed papers and with more than five data points per filter. In this way we obtained a subsample of 68 long GRBs (Table E.20, *Appendix*). This criterium automatically excluded short GRBs. Within these constraints we collected a large number of data coming from more then one hundred telescopes with different instruments and filters (Table E.20, *Appendix*). For these GRBs we analyzed

[2]From Margutti et al. (2013), we used only optical spectroscopic redshifts and photometric redshifts for which we can exclude sources of degeneracy. We listed the redshifts and luminosity distances of the GRBs of our sample in table5.dat at CDS, http://cdsweb.u-strasbg.fr/Abstract.html.

their energetics and luminosities and we calculated the spectral energy distributions in the optical/X-ray frequency range.

3.1.1 Optical data

Magnitudes have been converted into flux densities following standard practice. In the literature data are generally given in different photometric systems and based on the Vega or AB magnitude convention. The Vega system is defined as the system for which the magnitude of the Vega star is zero: $m-0 = -2.5\log f_\lambda + 2.5\log f_{\lambda,\mathrm{Vega}}$, with f_λ and $f_{\lambda,\mathrm{Vega}}$ in erg cm^{-2} s^{-1} Å^{-1}. In this case, the conversion formula used is $f_\lambda = f_{\lambda,Vega} 10^{-0.4\ m}$. The relation between flux density in frequency and wavelength units is $f_\nu = \lambda^2 f_\lambda / c$ with c the speed of light and λ the central wavelength of the considered filter. For the AB system the reference spectrum is flat in units of frequency density (erg cm^{-2} s^{-1} Hz^{-1}) and the system is defined by $m_{\mathrm{V}}^{\mathrm{Vega}} \equiv m_{\mathrm{V}}^{\mathrm{AB}} \equiv 0$ in the visual band; this occurs at 3631 Jy. So $m - m_{\mathrm{AB},0} = -2.5\log f_\nu - 2.5\log(3631 \times 10^{-23}) = -2.5\log f_\nu - (48.585 \pm 0.005)$, with f_ν in erg cm^{-2} s^{-1} Hz^{-1}. The conversion formula is $f_\nu = 10^{-0.4(m+48.585)}$. In various articles, the photometric system is not always specified, leading to mistakes in converting from magnitude to flux. For UVOT data the calibration has been provided by the UVOT team and we used their conversion factors (Poole et al. 2008). Some errors could occur when the photometric system is not specified, especially for the Gunn system or the standard Johnson system; for example, for the R filter, the Gunn conversion factor is twice as much the standard system conversion factor. On the other hand the IR filters used in literature are very similar. In this case, the choice of the photometric system does not influence noticeably the following analysis and we preferred to choose only standard systems listed in Table E.1 (*Appendix*).

For this analysis, we used only the LCs with more than five data points per filter and we excluded upper limits. This is the best compromise between statistics (in the sense that we do not discard too many GRBs) and reliability (robust fit and measurement of the energy). All the collected data will be available online.

For each filter we fitted the optical LCs with the same fit functions used for the X-ray data in M13. We chose these functional forms because they well represent the optical LC shapes and it makes it easier to compare optical with X-ray data. We used optical data not corrected for the reddening and the fit functions:

1. Single power-law:

$$F_\nu(t) = N\ t^{-\alpha}. \tag{3.1}$$

2. One or more smoothed broken power-laws:

$$F_\nu(t) = \sum_i N_i \left(\left(\frac{t}{t_{\mathrm{b},i}} \right)^{-\frac{\alpha_{1,i}}{s_i}} + \left(\frac{t}{t_{\mathrm{b},i}} \right)^{-\frac{\alpha_{2,i}}{s_i}} \right)^{s_i}. \tag{3.2}$$

3. Sum of power-law and smoothed broken power-law:

$$F_\nu(t) = N_1\, t^{-\alpha_1} + N_2 \left(\left(\frac{t}{t_\mathrm{b}} \right)^{-\frac{\alpha_2}{s}} + \left(\frac{t}{t_\mathrm{b}} \right)^{-\frac{\alpha_3}{s}} \right)^s . \tag{3.3}$$

where α is the power-law decay index, t_b the break time, s the smoothness parameter (always fixed to -0.3, -0.5 or -0.8) and N the normalization. The best fit parameters were determined using the IDL Levenberg-Marquard least-squares fit routine (MPFIT) supplied by Markwardt (2009)[3]. The best fitting function was chosen considering the χ^2 statistics. The best fitting parameters are reported on Tables E.2, E.4, E.6, E.15 (*Appendix*[4]). The best fit of the optical LCs and their residuals are shown in Figures E.1-E.7 (*Appendix*).

3.1.2 X-ray data

The X-ray spectra were extracted using the method presented in M13 (see also references therein). We fitted them using *Xspec* and the function `tbabs*ztbabs*pow`, which considers the hydrogen column density absorption of the Milky Way ($N_\mathrm{H,MW}$) and of the host galaxy ($N_\mathrm{H,host}$). The $N_\mathrm{H,MW}$ is calculated with the `nh` tool, which uses the weighted average value from Kalberla et al. (2005) map. The output data obtained from the X-ray spectrum are: $N_\mathrm{H,X,host}$ and X-ray photon index[5] (Γ_X) (Table E.11, *Appendix*[6]).

3.1.3 Optical/X-ray SEDs

For each GRB, we created the optical/X-ray SEDs at different epochs (Table E.14, *Appendix*). We chose the time intervals taking into account the shape of the X-ray and optical shapes: *a)* they belong to a determined phase of the X-ray LC, that is steep decay, plateau or normal decay, to avoid the X-ray LC breaks. In this way we have the SED both at early times (where the afterglow emission could be influenced by the prompt emission) and at late times (where the afterglow emission is very unlikely to be contaminated by the prompt emission); *b)* sometimes we perform the SEDs during X-ray and optical flares. For the optical data, we did not perform any extrapolation of the optical LC, so that if, for a given filter, no data are available, the filter is not included in the SED. For each filter with data in this time range, we calculated the flux density integrating the optical LC over the considered time interval.

We fitted the optical/X-ray SED accounting for absorption in the optical and X-ray ranges, both locally (i.e. in the GRB host galaxy) and arising from the MW:

[3] http://www.physics.wisc.edu/∼craigm/idl/fitting.html
[4] The complete and machine-readable form of the Table is at CDS (table1.dat).
[5] The spectral index β is related to the photon index Γ by $\Gamma = \beta + 1$.
[6] The complete and machine-readable form of the Table is at CDS (table4.dat).

- For the optical band we used the extinction laws given by Pei (1992) for the Milky Way (MW), Large Magellanic Cloud (LMC) and Small Magellanic Cloud (SMC)

$$\epsilon(\lambda) = \frac{A_\lambda}{A_B} = \sum_{i=1}^{6} \frac{a_i}{(\lambda/\lambda_i^{n_i}) + (\lambda_i/\lambda)^{n_i} + b_i}, \tag{3.4}$$

  i=1,2,3 indicates the parameters for the background far-ultraviolet and far-infrared extinctions, instead i=4,5,6 are the 2175 Å, 9.7 μm and 18 μm extincition terms. The values of these parameters for MW, LMC and SMC are listed in Pei (1992) (therein Table 4).

- For the X-ray data, we considered the model for the photoelectric cross section per HI-atom units for a given metallicity presented by Morrison & McCammon (1983), assuming solar metallicity.

Therefore, the function used to fit the optcal-X-ray SED is:

$$f_{SED} = \mathrm{f}_\nu(\nu) * \mathrm{X\_model} * \mathrm{optical\_model} \tag{3.5}$$

$$\mathrm{X\_model} = \mathrm{e}^{-\mathrm{NH_{MW}}\ \sigma_\nu - \mathrm{NH_{host}}\ \sigma_{\nu,(1+z)}}, \tag{3.6}$$

$$\mathrm{optical\_model} = 10^{C\,\epsilon_{\nu,MW} - C\,\epsilon_{\nu,(1+z)}}. \tag{3.7}$$

with $f_\nu(\nu)$ the fitting function, ν the frequency, $\beta_{op,X}$ the spectral index[5], σ the photoelectric cross section and z the redshift . ϵ_ν is the extinction curve function (Eq. 20 in Pei 1992) and corresponds to $\epsilon_\lambda = A_\lambda/A_B$ in frequency units. It depends on the type of galaxy chosen as model and A_λ and A_B are the extinctions in magnitudes at a wavelength λ and in the B band. C is a constant to convert the original formulae written for the U band in the V band: $C = \mathrm{E(B-V)_{MW}}/(2.5 * (-\epsilon_U + 1))$.

We first considered the case that the X-ray and the optical bands lie in the same spectral segment, hence the SED fitting function is the combination of the absorption laws presented above and a single power-law:

$$f_\nu(\nu) = f_0\ \nu_{\mathrm{obs}}^{-\beta_{\mathrm{op,X}}} \tag{3.8}$$

where ν_{obs} is the observed frequency, $\beta_{\mathrm{op,X}}$ the spectral index[5] and f_0 the normalization. From the input parameters $N_{\mathrm{H,MW}}$, $E(B-V)_{\mathrm{MW}}$[7] and z, we obtain $N_{\mathrm{H,op,X,host}}$, $E(B-V)_{\mathrm{host}}$ and the photon index $\beta_{\mathrm{op,X}}$.

Then, we examine the hypothesis that the cooling frequency is between the optical and the X-ray bands, and we fit the data using the absorption laws plus a broken-power law:

$$\begin{aligned} f_\nu(\nu) = {} & F_0(\nu_{\mathrm{obs}}^{-\beta_{\mathrm{op}}} step(\nu_{\mathrm{obs,BR}} - \nu_{\mathrm{obs}}) + \\ & + \nu_{\mathrm{obs}}^{-\beta_{\mathrm{X}}} \nu_{\mathrm{obs,BR}}^{\beta_{\mathrm{X}} - \beta_{\mathrm{op}}} step(\nu_{\mathrm{obs}} - \nu_{\mathrm{obs,BR}}) \end{aligned} \tag{3.9}$$

[7]The $E(B-V)$ values come from NASA/IPAC Extragalactic Database (NED) website (http://ned.ipac.caltech.edu/forms/calculator.html), which uses Schlegel et al. (1998) maps.

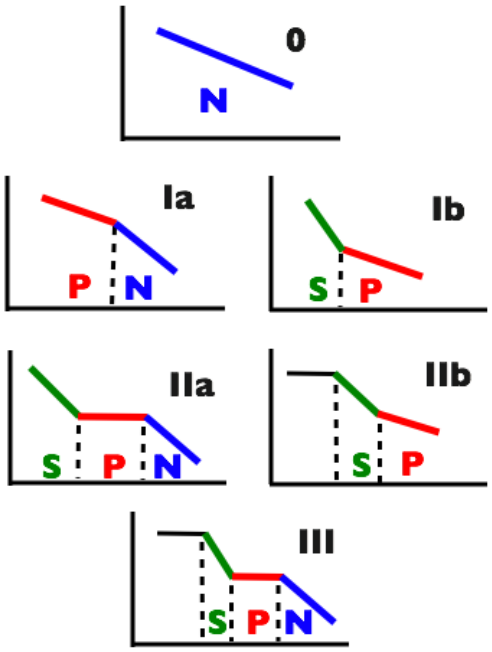

Figure 3.1: Cartoon representing the X-ray LCs types. For the X-ray LC shapes we used the code presented in M13 and in Chapter 2. From the prescription of Bernardini et al. (2012a) and M13, we denoted the different parts of the LCs as: *a)* steep decay (*S, green*): first segment of type Ib and IIa LCs; the second segment of type IIb and III LCs; *b)* plateau (*P, red*): the first segment of type Ia LCs; the second segment of type Ib and IIa LCs; the third segment of type IIb and III LCs; *c)* normal decay (*N, blue*): type 0 LCs; the second segment of type Ia LCs; the third segment of type IIa LCs; the forth segment of type III LCs.

with *step* the step function and $\nu_{\rm obs,BR}$ the observer frame break frequency between the optical and X-ray band. The fit is performed in two ways: with $\beta_{\rm op}$ let free to vary or fixed as $\beta_{\rm op} = \beta_{\rm X} - 0.5$, as predicted theorically by Sari et al. (1998) and empirically by Zafar et al. (2011). Letting $\beta_{\rm op}$ free to vary did not lead to reliable results. Therefore the best fit functions of the optical/X-ray SEDs may be a single power-law, a broken power-law with $\beta_{\rm op} = \beta_{\rm X} - 0.5$. To determine if the use of a broken power-law was required over a single power-law, we used an F-test probability <5% as the threshold. The results of this selection are presented in Table E.14 (*Appendix*) and Figures E.8-E.15. The fit parameters are listed in Tables E.7-E.10- E.18- E.19 (*Appendix*[8]). In Table E.13 (*Appendix*[9]) we listed the optical data used for the SEDs.

3.2 Results

3.2.1 Spectral parameter distributions

We considered the parameters obtained fitting the optical/X-ray SEDs (β, $N_{\rm H}$, $E(B-V)$, $\nu_{\rm BR}$) with a single power-law or a broken power-law, as selected in Sec. 3.1.3 (Table E.14, *Appendix*), and with a p-value[10] greater then 0.05. We eliminate the results which have errors greater than the data themself and we set to zero the data which are negative, but are consistent with 0 within uncertainties. In total, 78% of our fits have p-value¿0.05 and 33 GRBs have more than one SED with a p-value>0.05. For the steep decay SEDs, we obtained a good fit (p-value> 0.05) with a single power-law for 9/13 SEDs and with a broken power-law for 1/13. We could not fit 3 SEDs. Therefore, in the distribution we do not consider the parameters obtained with a broken power-law for the steep decay (i.e. $\nu_{\rm rest,BR}$, $\beta_{\rm op}$, $\beta_{\rm X}$, $N_{\rm H,BR}$).

For every distribution of the best-fitting values, we calculated the mean (m), the standard deviation (SD) and the median (M). When possible, we fitted the distributions with a Gaussian function obtaining the mean (μ) and the standard deviation (σ). All the results are listed in Table 3.1. In Figure 3.2 (*top panels*) we show the parameter distributions differentiating between the data obtained fitting the SEDs with a single-power law (*red*, "PL") or a broken-power law (*blue*, "BR") and in Figure 3.3 the distributions distiguishing the SED parameters extracted during the X-ray steep decay phase (*blue*, "S"), the plateau (*red*, "P") or the normal decay phase (*gray*, "N") (see Figure 3.1). We defined the X-ray LCs shapes as in M13 (Figure 3.1): "0" if there are no breaks, "Ia" or "Ib" if there is a break, "IIa" or "IIb" if there are two breaks and "III" if there are three breaks. The differentiation between model "Ia" and "Ib" depends of the smoothness parameter, $s < 0$ and $s > 0$, respectively. Type "IIa" is the canonical shape (e.g. Nousek et al. 2006, Zhang et al. 2006), while type "IIb" starts with a shallow phase followed by a steep decay and then a normal decay.

For the SEDs for which we were able to differentiate between the extinction laws used, we present in the bottom left panel of Figure 3.2, the distributions of host $E(B-V)$ for the MW, SMC and LMC.

The spectral index

The mean spectral slope computed fitting a single power-law is $\mu(\beta_{\rm op,X}) = 0.95\pm0.01$. This value is consistent with the spectral slope $\mu(\beta_{\rm X}) = 0.97\pm0.02$ obtained using a broken power-law; in fact the fit is largely weighted over the numerous X-ray data. The mean spectral slope of the optical part of the SED

[8]The complete and machine-readable forms of the Tables are at CDS (table2.dat, table3.dat).

[9]The complete and machine-readable form of the Table is at CDS (table6.dat).

[10]The p-value is a number between zero and one and it is the probability of obtaining a test statistic at least as extreme as the one that was actually observed, assuming that the null hypothesis is true.

Table 3.1: Characteristic quantities describing the parameter distributions (number of elements (#), mean (m), median (M), standard deviation (SD)) and best-fitting values from a Gaussian fit (mean (μ), standard deviation (σ)). The subscript "PL" indicates the values obtained by fitting the SED with a single power-law, instead "BR" indicates a broken power-law. "S" stands for steep decay, "P" for plateau and "N" for normal decay. The values of $E(B-V)$ depend on the extinction model law used to fit the SED: Milky Way (MW), Large Magellanic Cloud (LMC) and Small Magellanic Cloud (SMC).

Name	#	μ	σ	m	SD	M
$\beta_{\rm op,X}$	65	0.95±0.01	0.24±0.02	1.03	0.50	0.95
$\beta_{\rm X}$	34	0.97±0.02	0.18±0.02	0.99	0.22	0.95
$\beta_{\rm op}$	34	0.47±0.02	0.19±0.02	0.48	0.20	0.48
$\log(N_{\rm H,BR}/{\rm cm}^{-2})$	28	21.6±0.11	0.51±0.11	21.7	0.57	21.7
$\log(N_{\rm H,PL}/{\rm cm}^{-2})$	43	21.7±0.06	0.41±0.06	21.9	0.48	21.7
$E(B-V)_{\rm MW}$	30	0.19±0.02	0.14±0.02	11.1	59.1	0.22
$E(B-V)_{\rm LMC}$	14	-	-	0.20	0.16	0.18
$E(B-V)_{\rm SMC}$	25	-	-	0.20	0.29	0.10
$A_{\rm V,MW}$	30	0.56±0.10	0.42±0.11	34.2	182.	0.69
$A_{\rm V,LMC}$	14	-	-	0.63	0.51	0.57
$A_{\rm V,SMC}$	25	-	-	0.59	0.87	0.29
$\log(\nu_{\rm rest,BR}/{\rm Hz})$	28	-	-	16.20	0.98	16.1
$\log[(N_{\rm H}/{\rm cm}^{-2})/(A_{\rm V}/{\rm mag})]_{\rm MW}$	20	21.9±0.05	0.04±0.05	22.0	0.56	21.8
$\log[(N_{\rm H}/{\rm cm}^{-2})/(A_{\rm V}/{\rm mag})]_{\rm LMC}$	12	22.6±0.08	0.32±0.11	22.4	0.95	22.6
$\log[(N_{\rm H}/{\rm cm}^{-2})/(A_{\rm V}/{\rm mag})]_{\rm SMC}$	20	21.8±0.16	0.87±0.18	22.4	2.05	22.2
$\beta^{\rm S}_{\rm op,X}$	9	-	-	0.85	0.22	0.85
$\beta^{\rm P}_{\rm op,X}$	24	0.92±0.03	0.21±0.04	0.95	0.27	0.95
$\beta^{\rm N}_{\rm op,X}$	31	0.99±0.03	0.23±0.03	2.35	1.08	2.35
$\beta^{\rm P}_{\rm X}$	13	0.96±0.02	0.10±0.02	0.85	0.22	0.85
$\beta^{\rm N}_{\rm X}$	19	1.00±0.08	0.29±0.09	1.15	0.27	1.15
$\beta^{\rm P}_{\rm op}$	13	0.49±0.04	0.14±0.04	0.35	0.22	0.35
$\beta^{\rm N}_{\rm op}$	19	0.47±0.08	0.29±0.09	0.65	0.27	0.65
$\log(N^{\rm S}_{\rm H,PL}/{\rm cm}^{-2})$	6	-	-	22.2	0.63	22.2
$\log(N^{\rm P}_{\rm H,PL}/{\rm cm}^{-2})$	17	22.00±0.14	0.67±0.23	22.0	0.52	22.2
$\log(N^{\rm N}_{\rm H,PL}/{\rm cm}^{-2})$	19	21.70±0.04	0.30±0.04	22.2	0.86	22.2
$\log(N^{\rm P}_{\rm H,BR}/{\rm cm}^{-2})$	10	21.00±1.20	0.93±0.870	21.8	0.632	21.8
$\log(N^{\rm N}_{\rm H,BR}/{\rm cm}^{-2})$	17	21.90±0.05	0.23±0.04	21.8	0.86	21.8
$\log(\nu^{\rm P}_{\rm rest,BR}/{\rm Hz})$	14	-	-	16.80	1.08	16.80
$\log(\nu^{\rm N}_{\rm rest,BR}/{\rm Hz})$	16	-	-	16.20	1.08	16.20
$\log(L_{\rm R,500s}/({\rm erg\ s}^{-1}))$	64	45.90±0.06	0.83±0.06	46.00	3.72	45.90
$\log(L_{\rm R,1hr}/({\rm erg\ s}^{-1}))$	57	45.40±0.06	0.73±0.06	45.90	4.77	45.40
$\log(L_{\rm R,11hr}/({\rm erg\ s}^{-1}))$	40	44.50±0.08	0.74±0.08	45.70	7.44	44.50
$\log(L_{\rm R,1day}/({\rm erg\ s}^{-1}))$	32	44.20±0.11	0.83±0.13	44.20	0.68	44.20
$\log(E_{\rm R,920-1200s}/{\rm erg})$	46	49.50±0.07	0.72±0.07	50.20	5.86	49.40
$\log(E_{\rm R,tot}/{\rm erg})$	68	50.00±0.04	0.63±0.04	50.60	5.99	50.00
$\log(E_{\rm 1keV,920-1200s}/{\rm erg})$	52	48.50±0.06	0.73±0.06	48.40	0.72	48.40
$\log(E_{\rm 1keV,tot}/{\rm erg})$	126	49.50±0.03	0.77±0.03	49.30	0.81	49.40
$\log(E_{\rm 0.3-30,920-1200s}/{\rm erg})$	52	50.90±0.06	0.71±0.06	50.80	0.72	50.80
$\log(E_{\rm 0.3-30keV,tot}/{\rm erg})$	126	51.90±0.03	0.76±0.03	51.70	0.81	51.80

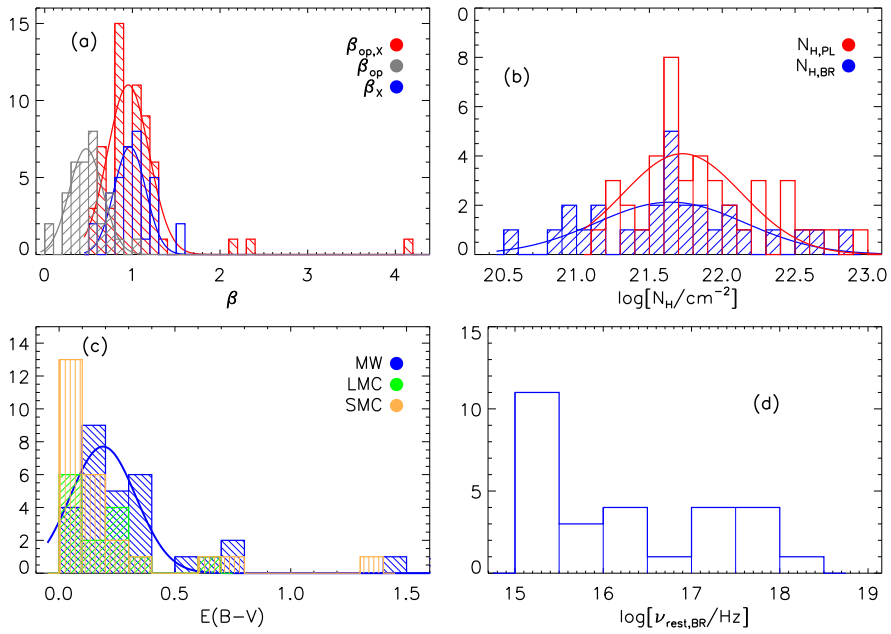

Figure 3.2: Parameter distributions. The color coding differentiates between different SED best fitting functions. *Top panels.Blue*: results obtained fitting the SEDs with a broken power-law and the relative Gaussian fit (*solid line*). *Red*: results obtained fitting the SEDs with a power-law and the relative Gaussian fit (*solid line*). *a)* The spectral indices (β) calculated fitting the SED with a single power-law ($\beta_{\rm op,X}$) and with a broken power-law ($\beta_{\rm op}$, *gray*, and $\beta_{\rm X}$). *b)* The hydrogen column density ($N_{\rm H}$). *Bottom panels. c)* The optical extinction ($E(B-V)$) distributions differentiating for the different extinction laws: MW (*blue*), LMC (*green*) and SMC (*orange*). *d)* The rest frame break frequency ($\nu_{\rm rest,BR}$) calculated fitting the SEDs with a broken-power law.

is $\mu(\beta_{\rm op}) = 0.47 \pm 0.02$, computed fixing $\beta_{\rm X} - \beta_{\rm op} = 0.5$, hence it is simply a rigid shift of the $\beta_{\rm X}$ distribution.

The distributions of β computed over the three different parts of the X-ray LCs (steep decay phase, plateau, normal decay phase) have the following mean values (Figure 3.3, *a, b, c*): *a)* $m(\beta^{\rm S}_{\rm op,X}) = 0.85$ (with $SD = 0.22$[11]), $\mu(\beta^{\rm P}_{\rm op,X}) = 0.92 \pm 0.03$, $\mu(\beta^{\rm N}_{\rm op,X}) = 0.99 \pm 0.03$. *b)* $\mu(\beta^{\rm P}_{\rm X}) = 0.96 \pm 0.02$, $\mu(\beta^{\rm N}_{\rm X}) = 1.00 \pm 0.08$. *c)* $\mu(\beta^{\rm P}_{\rm op}) = 0.49 \pm 0.04$, $\mu(\beta^{\rm N}_{\rm op}) = 0.47 \pm 0.08$. From these distributions we note that the mean spectral index during the plateau is smaller than during the normal decay phase, even though they are consistent within 2σ; in addition the normal decay spectral index distribution is broader than during the plateau. Therefore we tested the evolution of β for each GRB (Figure 3.4), with $\beta = \beta_{\rm op,X}$ or $\beta = \beta_{\rm X}$ depending of the fitting function used for each single SED (Table E.14, *Appendix*). In the majority of cases the spectrum gets softer (22 GRBs, *red lines*), and only for 10 GRBs it gets harder (*blue lines*). For 26 GRBs we have only one valid SED fit (*black dots*). If we examine these relationships in the rest frame (*Inset*), in particular only

[11] There are not sufficient data to fit a Gaussian over the distribution.

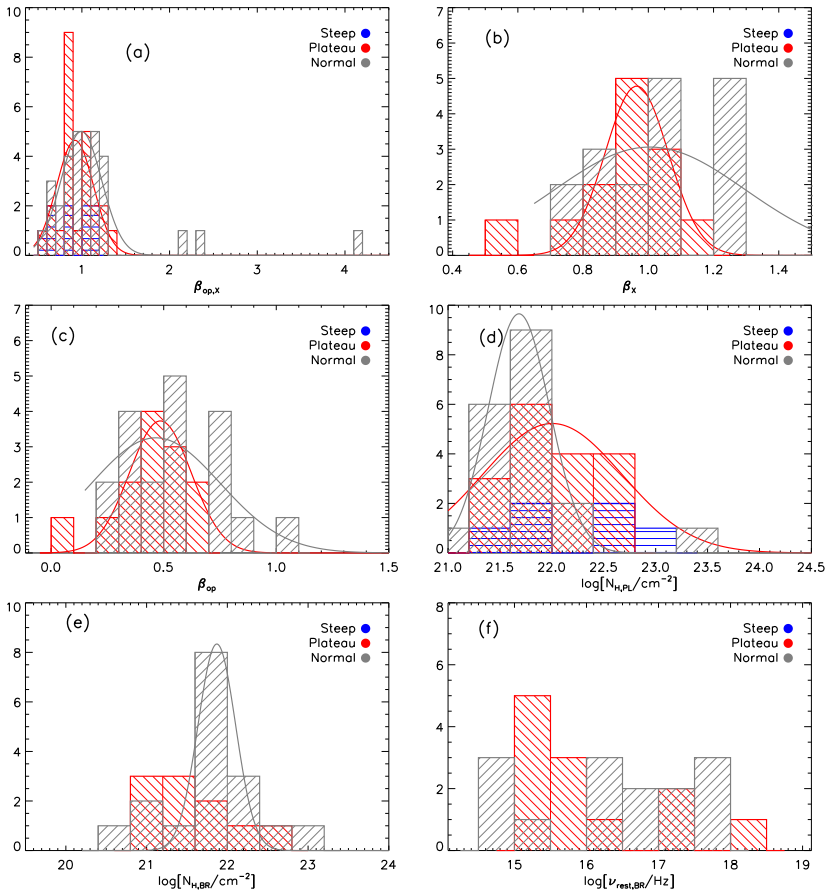

Figure 3.3: Parameter distributions considering the X-ray LC part of the SED. *Blue lines*: steep decay phase. *Red lines*: plateau. *Gray lines*: normal decay phase. *a)* $\beta_{\rm op,X}$: the spectral slopes calculated using a power-law as fitting function. *b)* $\beta_{\rm X}$ and *c)* $\beta_{\rm op}$: the broken power law spectral slopes for the X-ray and optical data, respectively. *d)* $N_{\rm H,PL}$ and *e)* $N_{\rm H,BR}$: the hydrogen column densities obtained using as SED fitting function a single power-law and a broken power-law, respectively. *f)* $\nu_{\rm rest,BR}$: the rest frame break frequency calculated fitting the SEDs with a broken-power law.

the plateau and normal decay data (*magenta dots* and *orange squares*, respectively) as we have few data for the steep decay phase (*light blue stars*) and the unclassified phase (*green triangles*), then the relationships do not change.

The hydrogen column density and the optical extinction

We calculated the hydrogen column density in two ways: by fitting the X-ray spectrum ($\rm N_{H,X}$) and by the optical/X-ray SED fit ($N_{\rm H,op,X}$). The $N_{\rm H}$ values found with the two methods are consistent, as shown in Figure 3.5 (*left*), even the low values of $N_{\rm H}$ ($< 10^{21}$ cm^{-2}) are consistent within two sigma.

We consider now only the hydrogen column densities calculated with the optical/X-ray SEDs ($N_{\rm H,op,X}$). The distributions of the hydrogen column densities of the host galaxies are consistent if calculated with the two fit functions:

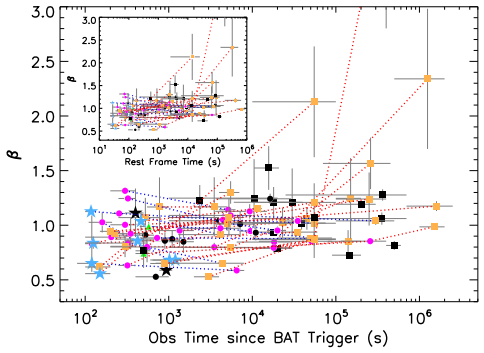

Figure 3.4: Evolution of β with time for individual GRBs. For every GRB we consider the "correct" spectral index as selected in Table E.14, hence β can be $\beta_{\rm op,X}$ or $\beta_{\rm X}$ depending on the chosen SED fitting function, a single power-law or a broken power-law. *Blue dotted lines*: the initial spectral slope is greater then the final spectral slope. *Red dotted lines*: the initial spectral slope is smaller then the final spectral slope. *Light blue stars*: steep decay data. *Magenta dots*: plateau data. *Orange squares*: normal decay data. *Black*: only one SED is available for these GRBs and precisely during the steep decay (*stars*), the plateau (*dots*) and normal decay (*squares*). *Inset*: the same as the principal plot, but in the rest frame.

$\mu(\log(N_{\rm H,PL}/{\rm cm}^{-2})) = 21.60 \pm 0.11$ and $\mu(\log(N_{\rm H,BR}/{\rm cm}^{-2})) = 21.70 \pm 0.06$ (Figure 3.2*b*). As shown by the distributions of $N_{\rm H}$ calculated in the different parts of the LCs (Figure 3.3*d,e*), this parameter does not evolve with time because it has similar mean value, within error, for the steep decay phase, the plateau and normal decay phase.

In Figure 3.2*c* we show the distributions of $E(B-V)$, differentiating between the best fitting extinction laws (MW, LMC, SMC). The mean values are: $\mu(E(B-V)_{\rm MW}) = 0.19 \pm 0.02$ mag, $m(E(B-V)_{\rm LMC}) = 0.20$ mag (SD=0.16), $m(E(B-V)_{\rm SMC}) = 0.20$ mag, which correspond to $\mu(A_{\rm V,MW}) = 0.56 \pm 0.10$ mag, $m(A_{\rm V,LMC}) = 0.63$ mag, $m(A_{\rm V,SMC}) = 0.59$ mag[12]. The mean $A_{\rm V,SMC}$ is in agreement with the value presented by Zafar et al. (2011).

The ratio between $N_{\rm H}$ and A_V is a measure of the gas-to-dust ratio (Figure 3.5, *right*). We considered the hydrogen column densities calculated with the optical/X-ray SEDs ($N_{\rm H,op,X}$) and, for different extinction laws, we obtained: $\mu(\log(N_{\rm H}/{\rm cm}^{-2})/(A_{\rm V}/{\rm mag}))_{\rm MW}) = 21.90 \pm 0.05$ (*blue*), $\mu(\log((N_{\rm H}/{\rm cm}^{-2})/(A_{\rm V}/{\rm mag}))_{\rm LMC}) = 22.60 \pm 0.08$ (*green*) and $\mu(\log((N_{\rm H}/{\rm cm}^{-2})/(A_{\rm V}/{\rm mag}))_{\rm SMC}) = 21.80 \pm 0.16$ (*orange*). We compared these results considering the $N_{\rm H}/A_{\rm V}$ values available in literature for the MW, LMC and SMC: $\log((N_{\rm H}/{\rm cm}^{-2})/(A_{\rm V}/{\rm mag}))_{\rm MW} = 21.27$ (Figure 3.5, *right*, *blue star*; Bohlin et al. 1978), $\log((N_{\rm H}/{\rm cm}^{-2})/(E(B-V)/{\rm mag}))_{\rm LMC} = 21.84$ (Weingartner & Draine 2001) and $\log((N_{\rm H}/{\rm cm}^{-2})/(E(B-V)/{\rm mag}))_{\rm SMC} = 22.19$ (Martin et al. 1989). To compare the Magellanic Clouds data of the $N_{\rm H}$ from the literature with our results, calculated assuming solar abundances, we converted the values from the literature considering a metallicity $Z = 0.26\ Z_\odot$ for the LMC and $Z = 0.14\ Z_\odot$ for the SMC (Draine 2003 and references therein). We obtained $\log((N_{\rm H}/{\rm cm}^{-2})/(A_{\rm V})/{\rm mag}))_{\rm LMC} =$

[12] $A_{\rm V} = R_{\rm V}\ E(B-V)$ with $R_{\rm V}^{\rm MW} = 3.08$, $R_{\rm V}^{\rm LMC} = 3.16$ and $R_{\rm V}^{\rm SMC} = 2.93$ (Pei 1992).

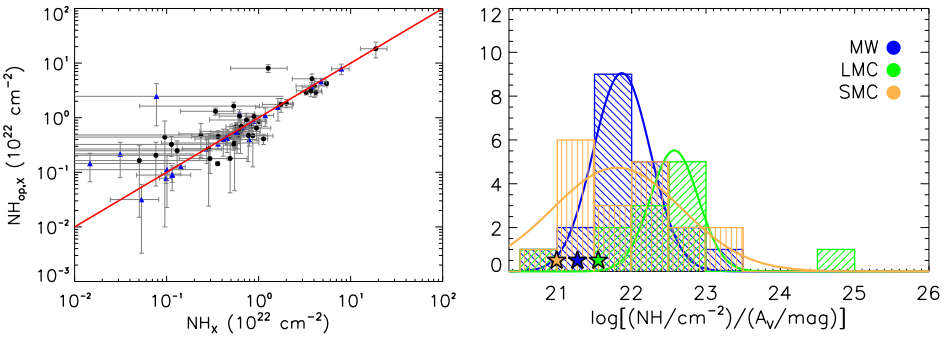

Figure 3.5: *Left*: Comparison between the $N_{\rm H}$ calculated from the X-ray spectrum ($N_{\rm H,X}$) and the optical/X-ray SED ($N_{\rm H,op,X}$). *Blue triangles* stand for the broken power-law fit function and *black dots* for the simple power-law. *Red line*: $N_{\rm H,X} = N_{\rm H,op,X}$. *Right:* distribution of $\log((N_{\rm H}/{\rm cm}^{-2})/({\rm A_V/mag}))$ considering the three different extinction laws used: MW (*blue*), LMC (*green*) and SMC (*orange*). *Stars*: reference values of the ratios $N_{\rm H}/A_{\rm V}$ from literature. *Blue star*: $\log((N_{\rm H}/{\rm cm}^{-2})/(A_{\rm V}/{\rm mag}))_{\rm MW} = 21.27$ (Bohlin et al. 1978). *Green star*: $\log((N_{\rm H}/{\rm cm}^{-2})/(A_{\rm V})/{\rm mag}))_{\rm LMC} = 21.55$ (assuming sub-solar abundances). *Orange star*: $\log((N_{\rm H}/{\rm cm}^{-2})/(A_{\rm V}/{\rm mag}))_{\rm SMC} = 20.99$ (assuming sub-solar abundances).

21.55 and $\log((N_{\rm H}/{\rm cm}^{-2})/(A_{\rm V}/{\rm mag}))_{\rm SMC} = 20.99$ (Figure 3.5, *right*, *green* and *orange stars*, respectively).

Our analysis shows that the gas-to-dust ratios of GRBs are larger than the values calculated for the MW, the LMC, and SMC assuming solar abundances (e.g. Schady et al. 2010, 2012).

The break frequency

The rest frame break frequency distribution has a peak around $\log(\nu_{\rm rest,BR}/{\rm Hz}) \sim 16$ (Figure 3.2*d*). The values are spread between the optical and the X-ray band frequencies and it is not possible to fit a Gaussian function to these data.

Since the majority of our data are at late times, they likely correspond to a slow cooling regime, for an homogeneous medium, when the break-frequency evolves as $t^{-1/2}$ (Sari et al. 1998), moving from the X-ray toward the optical frequencies. Since we cannot follow such changes on a single burst, we tested whether we could find any correlation between the mean time at which we measure the break frequency and the break frequency itself. If GRBs had similar behavior, the time and the break frequency would be correlated. Figure 3.6 shows that the peak at low frequencies is spread over a large time interval, and there is no evidence of correlation between time and frequency (Figure 3.6, *left*). This may be due above all to the dependence of the the break frequency from other parameters and in part to the uncertainties in its measurement and the fact we considered data from different GRBs.

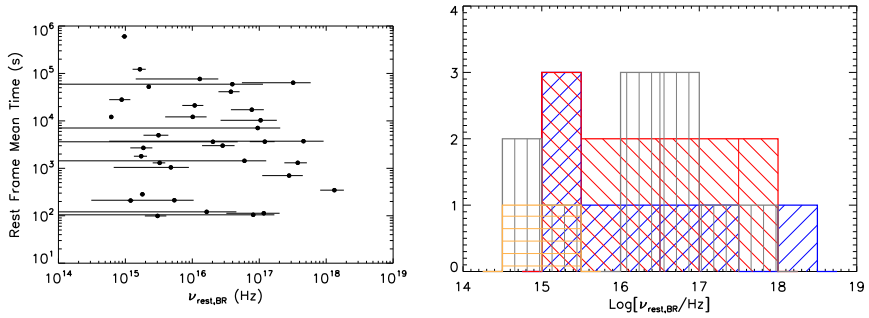

Figure 3.6: The break frequency. *Left*: break frequency ($\nu_{\rm rest,BR}$) vs. the mean time ($t_{\rm rest,m}$) of the interval in which the SED is calculated. *Right*: the distribution of the break frequencies. *Blue*: $t_{\rm rest,m} < 500$ s. *Red*: $500 < t_{\rm rest,m} < 10^4$ s. *Gray*: $10^4 < t_{\rm rest,m} < 10^5$ s. *Orange*: $t_{\rm rest,m} > 10^5$ s. The time intervals have been arbitrarily chosen.

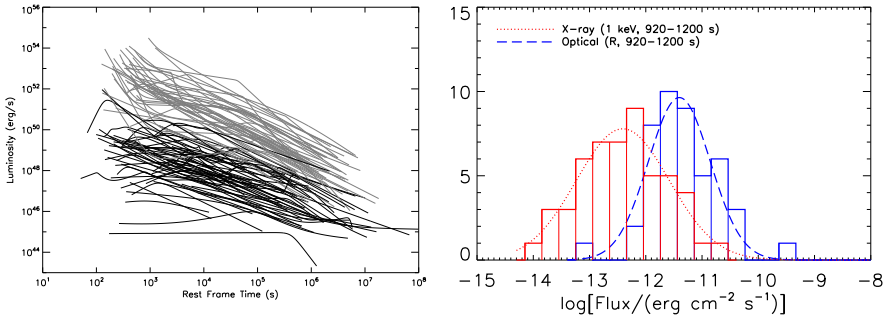

Figure 3.7: *Left*: X-ray (0.3-30 keV, *gray*) and optical (R band, *black*) LCs in the rest frame. *Right*: distribution of the X-ray (1 keV, *red, solid line*) and optical (R band, *blue, solid line*) fluence calculated in a common rest frame time interval (920-1200 s) for our sample and their distributions (*red, dotted line* and *blue, dashed line*, respectively).

3.2.2 Luminosity and energetics

In Figure 3.7 (*left*) the X-ray (1 keV, *gray lines*) and optical (R band) *black lines*) rest-frame LCs of the GRBs in our sample are plotted[13]. The optical LCs are underluminous with respect the X-ray LCs, even if some very luminous optical LCs overlap the subluminous X-ray LCs.

For the GRBs in our sample, we compared the optical (R band) and X-ray (at 1 keV) flux (Figure 3.7, *right*) in a common rest frame time interval (920-1200 s): the X-ray emission ($\log(\mu(F_{\rm op})/(\text{erg cm}^{-2}\text{ s}^{-1})) = -12.54$, $\sigma = 0.49$) is on average two orders of magnitude fainter than the optical ($\log(\mu(F_{\rm op})/(\text{erg cm}^{-2}\text{ s}^{-1})) = -10.41$, $\sigma = 0.34$).

The optical LCs can show an early time rise or a quasi-constant phase (or optical plateau), followed by a decay. Panaitescu & Vestrand (2011) claimed that there are some correlations involving the energies and luminosities calcu-

[13]The X-ray and optical data are k-corrected. Optical data are not corrected for Galactic and host galaxy absorption

Table 3.2: Two-parameter correlations involving optical luminosities and fluxes. From left to right: X and Y parameters to be correlated (the best fitting law reads: $\log(Y) = q + m\log(X)$); best-fitting parameters as obtained accounting for the sample variance (D'Agostini 2005): slope (m), normalization (q), intrinsic scatter (σ); errors are given at 95% c.l. The last three columns list the value of the Spearman rank (ρ), Kendall coefficient K and R-index r statistics.

X	Y	m	q	σ	ρ	K	R
$L \times t_{\rm rest}$	E_γ^{15-150}	0.65±0.03	-0.39±2.52	0.59±0.01	0.64	0.47	0.72
$L \times t_{\rm rest}$	$E_{\gamma,\rm iso}$	0.78±0.05	-4.42±4.99	0.58±0.03	0.72	-0.49	0.80
$t_{\rm rest,PL}$	$L_{\rm end,PL}$	-0.83±0.14	8.64±1.36	0.84±0.06	-0.66	-0.51	-0.65
$t_{\rm obs,PL}$	$L_{\rm end,PL}$	-0.77±0.18	8.81±2.35	0.90±0.07	-0.55	-0.41	-0.55
$t_{\rm rest,PK}$	$L_{\rm end,PK}$	-1.40±0.13	10.47±0.81	0.92±0.04	-0.79	-0.64	-0.77
$t_{\rm obs,PK}$	$L_{\rm end,PK}$	-1.32±0.20	10.86±0.75	1.08±0.06	-0.66	-0.48	-0.67
$t_{\rm obs,PL}$	$F_{\rm PL}$	-0.48±0.10	7.91±1.19	0.65±0.03	-0.39	-0.26	-0.53
$t_{\rm obs,PK}$	$F_{\rm PK}$	-0.93±0.08	9.86±0.72	0.69±0.02	-0.78	-0.62	-0.71

lated at the peak of the early time rise or at the end of the optical plateau, which are predicted by theoretical models. We tested the existence of these relations in the observer and the rest frames considering the GRBs with an optical LC with an initial peak and with an initial optical plateau (Table 3.3).

To compute the relations between two parameters, we used the best-fitting procedure which accounts for the sample variance (D'Agostini 2005). All results are listed in Table 3.2 and presented in Figures 3.8, 3.9 and 3.10.

We confirm the correlation between the optical energy ($L \times t_{\rm rest}$ with $L = L_{\rm end}, L_{\rm pk}$) and the isotropic gamma-ray energy[14] ($E_{\gamma,\rm iso}$, Amati et al. 2008) and the optical energy and the energy calculated in the BAT energy band[14] (E_γ^{15-150}) (Figure 3.8). However, the data are show a very broad distribution and for the $L \times t_{\rm rest}$ vs. $E_{\gamma,\rm iso}$ there are only 13 available data points.

There is a minor indication that the optical plateau end luminosities and the relative observer and rest frame times are correlated (Figure 3.9, *left*). The same occurs for the peak luminosities and the relative observer and rest frame times (Figure 3.9, *right*). Since there are few elements in our sample, the correlation is not reliable.

In the observer frame, the peak flux correlates with the peak time (Figure 3.10, *bottom*), but the optical plateau end fluxes and their times are not related (Figure 3.10, *top*). Also in this case there are few data: 19 GRBs for the peak relation and 14 for the plateau, and a few discrepant cases.

We also measured the optical luminosity distributions at 4 different rest frame times: 500 s, 1 hr, 11 hr and 1 day. The 11 hr is commonly chosen because reasonably the cooling frequency has not passed yet the optical band (Freedman & Waxman 2001; Piran et al. 2001), in addition 11 hr and 1 day are approximately the times at which several authors found a bimodal distribution[15] of the luminosities (Liang & Zhang 2006, Nardini et al. 2006, Kann et al. 2006, Nardini et al. 2008); we did not find a bimodal distribution in

[14] We used the values presented in M13.

[15] Possibly caused by a bimodality in the optical luminosity function or by the absorption of gray dust in a fraction of bursts (Nardini et al. 2008).

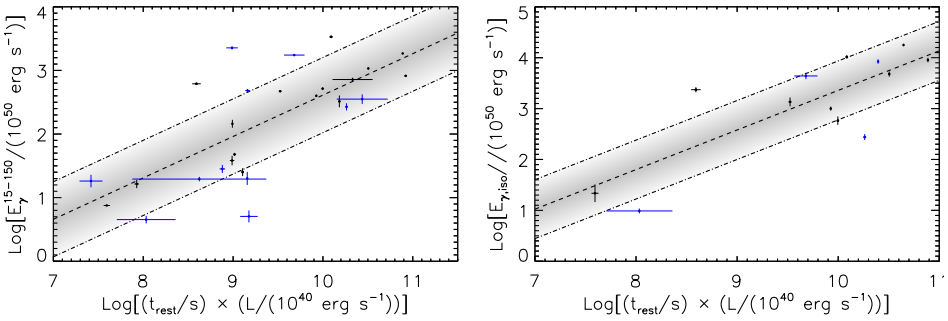

Figure 3.8: Relations between the optical energy (time×luminosity) of the optical plateau end (*blue dots*) and of the peak (*black dots*) and the 15-150 keV BAT energy (*left*) and the isotropic prompt emission energy (*right*). *Dashed line*: best fitting power-law model obtained accounting for the sample variance (D'Agostini 2005). *Gray area*: the 68% confidence region around the best fit. The results of the fit are in Table 3.2.

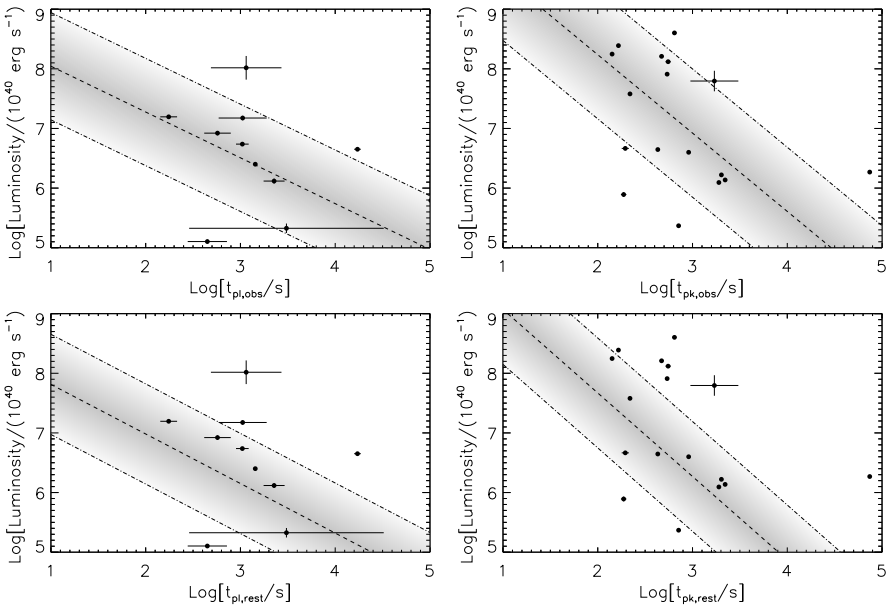

Figure 3.9: Relations between the optical luminosity of the end of the plateau (*left*) and of the peak (*right*) and the relative observer (*top*) and rest (*bottom*) frame time. *Dashed line*: best fitting power-law model obtained accounting for the sample variance (D'Agostini 2005). *Gray area*: the 68% confidence region around the best fit. The results of the fit are in Table 3.2.

our data, as asserted in recent studies (Melandri et al. 2008b; Oates et al. 2009, 2011; Kann et al. 2010b, 2011). The mean luminosity simply decreases with time (Figure 3.11): $\mu(\log(L_{500s}/\text{erg s}^{-1})) = 45.90 \pm 0.06$ (64 GRBs), $\mu(\log(L_{1hr}/\text{erg s}^{-1})) = 45.40 \pm 0.06$ (57 GRBs), $\mu(\log(L_{11hr}/\text{erg s}^{-1})) = 44.50 \pm 0.07$ (40 GRBs) and $\mu(\log(L_{1day}/\text{erg s}^{-1})) = 44.20 \pm 0.09$ (32 GRBs) (Table 3.1).

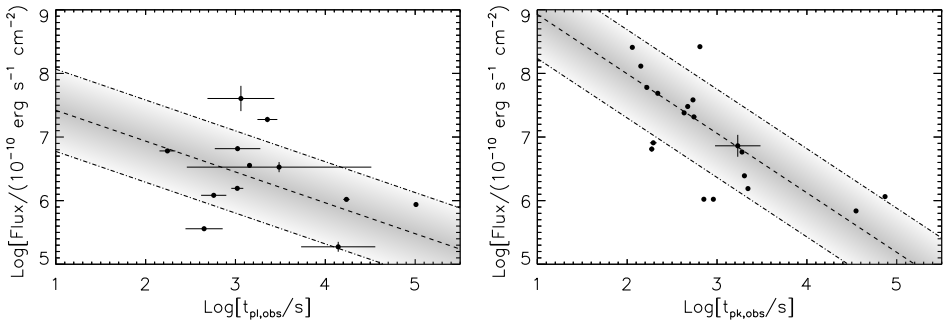

Figure 3.10: Relations between the optical flux and the observer time of the end of the plateau (*left*) and the peak (*right*). *Dashed line*: best fitting power-law model obtained accounting for the sample variance (D'Agostini 2005). *Gray area*: the 68% confidence region around the best fit. The results of the fit are in Table 3.2.

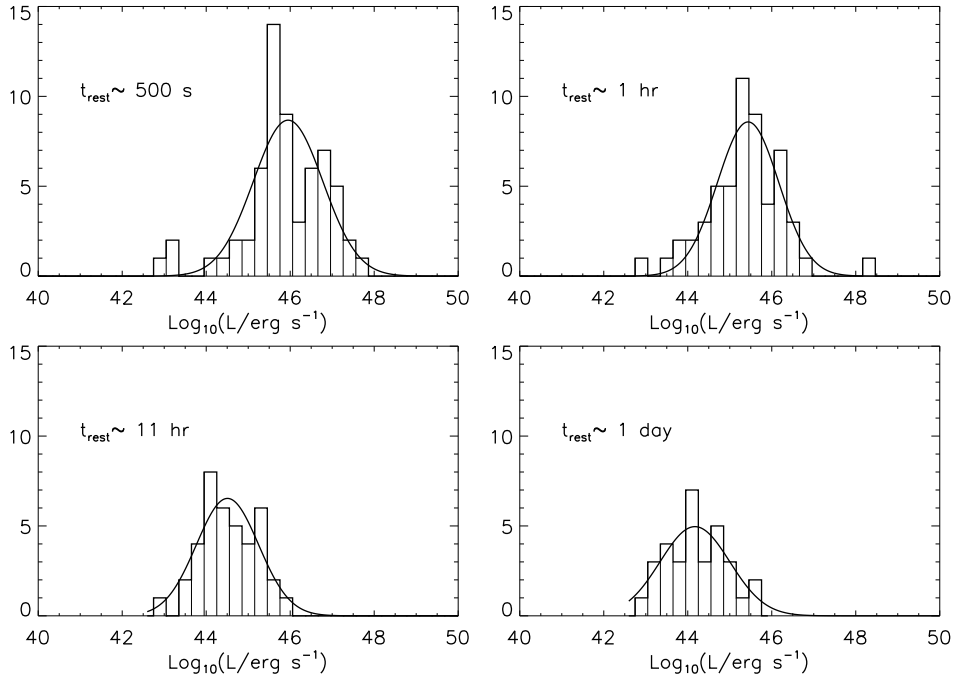

Figure 3.11: Distribution of the optical R luminosity calculated for four different rest frame times: 500 s, 1 hr, 11 hr, 1day. The black solid line corresponds to the Gaussian fit of the data. The results are listed in Table 3.1.

3.2.3 The optical LCs

The optical LCs show different and various shapes and features (Table 3.3; See also Li et al. 2012, their Figure 2). For each GRB, we selected the optical LC observed with the filter having the widest temporal coverage and with reliable fit (Tables E.2, E.4, E.6, *Appendix*[16]).

In general, they have a rising or constant part, which can occur at any

[16]The complete and machine-readable form of the Table is at CDS (table1.dat).

time. This happens for 53 GRBs in our sample. Only 10 GRBs show a simple power law trend and 5 GRBs have a LC with an initial decay and then an almost constant optical flux. The optical LCs with a single power-law decay have an initial time $\gtrsim$1000 s in the observer frame (GRB 050824, GRB 050908, GRB 060502A) or they are not well sampled (GRB 050904, GRB 051111, GRB 080721, GRB 091018). GRB 050401 and GRB 050922C show small variability in their optical LCs, even if their best fit function is a simple power-law. GRB 060912A has a well sampled optical LC, fitted with a single power-law. Of the five GRBs with an initial decay followed by almost constant flux, GRB 060908 and GRB 090424 show a shallow phase at late times ($\gtrsim 10^6$), which maybe due to the host galaxy. For GRB 061126, GRB 070529, and GRB 090102 the LC break occurs at $\sim 10^3 - 10^4$ s (observer frame). For these five GRBs the initial time of the optical observations is ∼100 s. Even if these GRBs do not show variable LCs, we did not know what happened before the beginning of the observations and they could have a very variable LC as GRB 080319B (Racusin et al. 2008).

There are 14 GRBs with an optical LC with an early peak (i.e. an initial rise followed by a decay) and 14 with a quasi-constant phase (i.e. *optical plateaus,* an initial quasi-constant phase followed by a decay). The optical plateaus and rises in the LCs are interpreted as the onset of the forward shock emission, when the blast wave decelerates: the peaked LCs correspond to an impulsive ejecta release, where all ejecta have the same Lorentz factor after the burst phase; the plateaus are caused by the energy injection in the forward shock due to an extended ejecta release, a wide distribution of the ejecta initial Lorentz factors or both (e.g. Panaitescu & Vestrand 2011; Oates et al. 2009) or the onset of the afterglow for the wind medium (e.g. Chevalier & Li 1999; Ghirlanda et al. 2012).

16 GRBs show a late time re-brightnening (i.e. at late times the LC displays a rise phase and then a decay phase with the same slope as before). The re-brightening may be related to the jet structure, and seem to be in accordance with the on-axis two-component jet model, with the re-brightening corresponding to the emergence of the slow component (e.g. Racusin et al. 2008; Liang et al. 2012).

For 3 GRBs there is a series of initial large bumps (i.e. more than one peak). GRB 060904B shows two bumps during the X-ray plateau and a shallow decay starting roughly at the beginning of the X-ray normal decay. The two optical peaks are not correlated with the high energy emission and the later optical bump is assumed to trace the onset of the forward shock (Rykoff et al. 2009). The optical LC of GRB 060906 has two bumps that coincide with the X-ray plateau. These bumps could be associated to a change of the circumburst density (Cenko et al. 2009b). The GRB 080928 optical LC was modeled by multiple energy injections into the forward shock, and not with the central engine, since the fluctuations have a long timescale (Rossi et al. 2011). The first peak is assumed to be the onset of the afterglow, while the following two bumps are produced by the central engine activity (Rossi et al. 2011).

In 5 optical LCs there are small bumps (i.e. small fluctuations over the

Table 3.3: Subdivision of the GRBs in our sample depending on the optical LC features. (a) At late times. (b) For the R_C observations.

An initial peak				
050730$^{(a)}$	050820A$^{(a)}$	060418	060605	060607A
060614$^{(a)}$	061007	061121	070318	070419A
070802$^{(a)}$	071025	071031	071112C	080603A
080710$^{(a)}$	080810	081008	081203A	
An initial shallow phase				
050408	050416A	060124	060210	060526
060729	070125	070208	070411	071010A
080330	090313	090426	090618	
A late time re-brightening				
050820A	060206	060526	060927	061121
071003	071010A	080310	080607	080913
081008	081029	091127	100418A	100901A
A series of initial large bumps				
060904B	060906	080928		
Small bumps				
050401$^{(b)}$	060607A	071025	071031	090313$^{(b)}$

power-law decay). The optical bumps could be related to the erratic late time central engine activity (Li et al. 2012).

The optical LCs have a complex behavior and during a well defined X-ray LC phase, the optical LC can rise and then decay, or vice versa. In particular[17]:

- Steep decay: 42% of the optical LCs rise, 32% decay, 16% are constant and 10% have a complex behavior (rise-decay, bumps).
- Plateau: 16% of the optical LCs rise, 47% decay, 8% are constant, 26% rise and decay and 4% have one or more bumps.
- Normal decay: 77% of the optical LCs decay and 23% rise and decay or have a more complex behavior.

The complexity of the LCs decreases as a function of time.

3.2.4 Comparison between the optical and X-ray LCs

For every GRB we compared the optical LC slopes with the contemporaneous X-ray LC slopes. For both the optical and the X-ray LCs, we considered only the continuum part of the LC, excluding small bumps and flares (see M13). As in the previous Section, for each GRB, we selected the optical LC observed with the filter having the widest temporal coverage and with reliable fit (Tables E.2, E.4, E.6, *Appendix*[18]); the X-ray LC parameters are

[17]The percentage refers to single LC parts, not to the total number of GRBs.
[18]The complete and machine-readable form of the Table is at CDS (table1.dat).

those derived in M13. From the synchrotron spectrum (Sari et al. 1998), if $\nu_c < \nu_{op} < \nu_X$, with ν_c the cooling frequency, the difference between the contemporaneous optical and X-ray slopes is $\Delta\alpha = 0$. If $\nu_{op} < \nu_c < \nu_X$, for the slow cooling regime, $\Delta\alpha = \pm 1/4$[19]. We subdivide our sample in three groups, depending if the pairs of the optical/X-ray slopes follow the relation $\Delta\alpha = 0, 1/4$ or not within 1σ[20] (Table 3.4 and Figure 3.12):

- Group A: all the pairs of slopes of the same GRB satisfy the relation $\Delta\alpha = 0, \pm 1/4$ (13 GRBs).
- Group B: some slopes of the same GRB satisfy the relation $\Delta\alpha = 0, \pm 1/4$ (27 GRBs).
- Group C: no slopes of the same GRB satisfy the relation $\Delta\alpha = 0, \pm 1/4$ (28 GRBs).

Some X-ray LCs show an initial steep decay; generally this is not present in the optical LCs, which display a rise, a plateau or a normal decay. The X-ray steep decay is well explained as the decay of the prompt emission and its slope value is particularly sensitive to the chosen zero time of the power-law decay, $t_0 \sim 0$ (e.g. the BAT trigger time) or $t_0 = t_{90}$ (for details see M13). For this reason, the steep decay phase is not considered in our classification.

We plot α_X vs. α_{op} for every GRB in Figure 3.13. About half α_X vs. α_{op} couples refers to the X-ray LC normal decay phase and half to the plateau. We noted that the GRBs in Group A and B have more complex LCs than the Group C GRBs, in fact most of the X-ray and optical LCs of Group A and B GRBs have Type IIa or III shapes. Therefore, when GRBs have LCs well sampled and with a good time coverage, hence with more complicated shapes, the X-ray and the optical LCs show a similar trend. When we have less data, we cannot compare some parts of the LCs and perhaps the observed slope is different from the real behavior of the LC.

The presence of the X-ray flares does not influence the relation between the X-ray and optical LCs, since in Group A there are 5/14 GRBs with flares (36%), in Group B 8/26 (31%) and in Group C 8/28 (29%). This is in agreement with the percentage found with other samples (Chincarini et al. 2010a; Margutti et al. 2013).

In the flowchart in Figure 3.14 we show the subdivision of the GRBs in our sample into the three groups. Below we describe in detail the characteristics of the GRBs subdivided into the three groups.

Group A. All the pairs of optical/X-ray slopes of the same GRB satisfy the relation $\alpha = 0, \pm 1/4$. The X-ray plateau and normal decay phase follows the optical slopes for 7 GRBs: GRB 080607, GRB 100901A, GRB 050416A, GRB 080310, GRB 080319B, GRB 100418A, and GRB 050824.

[19] This is valid in the slow cooling regime for the constant interstellar medium (ISM) and the wind case: for $\nu_m < \nu < \nu_c$, $\alpha_1 = 3(p-1)/4$, and for $\nu > \nu_c$, $\alpha_2 = (3p-2)/4$ in the ISM case, so $\alpha_1 - \alpha_2 = (3p - 3 - 3p + 2)/4 = -1/4$; for the wind case, for $\nu_m < \nu < \nu_c$, $\alpha_1 = (3p-1)/4$, and for $\nu > \nu_c$, $\alpha_2 = (3p-2)/4$, so $\alpha_1 - \alpha_2 = (3p - 1 - 3p + 2)/4 = 1/4$.

[20] A similar method was used by Panaitescu & Vestrand (2011) to classify coupled and decoupled LCs.

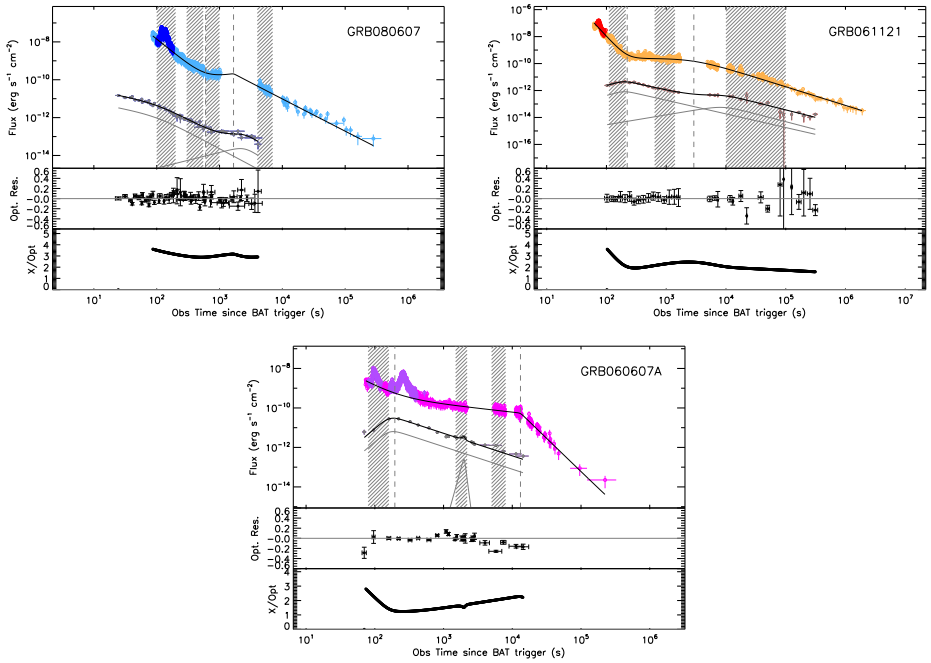

Figure 3.12: Comparison between optical and X-ray LCs, examples of the GRBs in each group. *Group A*: GRB 080607 (*blue/light blue*). *Group B*: GRB 061121 (*red/orange*). *Group C*: GRB 060607A (*purple/magenta*). For each Figure: *Top. Colored points*: X-ray data. The data in light color and bright color represent the continuum and the flaring portions, respectively, as calculated by M13. *Gray dashed lines*: X-ray break times. *Gray points*: optical data. *Black solid line*: fit to the data. *Gray solid lines*: components of the fit function used to fit the optical data. *Hashed gray boxes*: SED time intervals. *Middle.* Ratio between the optical data and their fit function. *Bottom.* Ratio between the fit to the X-ray continuum and the optical LC. See Figures E.1-E.7 (*Appendix*) for the other GRBs of our sample.

For six GRBs we can compare the optical and X-ray LCs only during the X-ray plateau or X-ray normal decay, because of the poor data. GRB 060912A, GRB 061007 and GRB 080913 have a Type 0 complete X-ray LC. GRB 060912A has a simple power-law optical LC. The GRB 061007 optical LC rises at early time, where there are no X-ray observations, and then follows the normal decay of the X-ray LC. Finally, the GRB 080913 optical LC traces the X-ray LC during the first and the last part for its optical LC. Unfortunately, there are no optical observations between 10^4 and 10^5 s. For GRB 080603A there are not observations before 10^4 s; GRB 050904 ($\alpha_{\rm op} - \alpha_{\rm X} = 0.25$) has a Type *Ib* X-ray LC, so there is only the normal decay; for GRB 080330 there are no observations after the plateau phase.

Group B. Some pairs of optical/X-ray slopes of the same GRB satisfy the relation $\alpha = 0, \pm 1/4$. This group can be subdivided into two classes depending on the LC shape: 6 GRBs have a similar shape for the X-ray and optical LCs, instead 21 GRBs have different shapes.

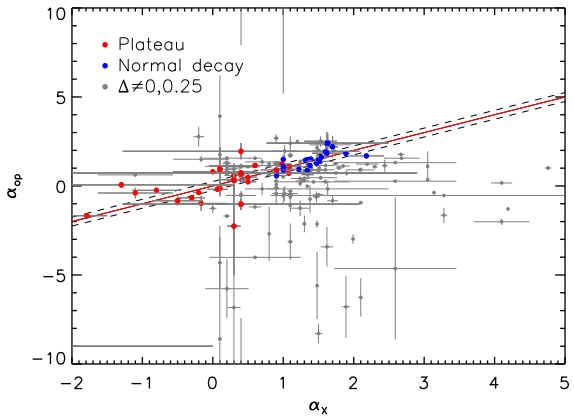

Figure 3.13: Comparison between the X-ray LC slope (α_X) and the optical one (α_{op}). *Red (blue) dots*: data for the plateau (normal decay) phase which are in accordance with the $\Delta\alpha = 0, 1/4$ relation whitin the 1σ errors. *Gray dots*: the data that do not follow the $\Delta\alpha = 0, 1/4$ relation. *Red solid line*: $\Delta\alpha = 0$. *Gray dashed lines*: $\Delta\alpha = \pm 1/4$.

Table 3.4: List of GRBs in the three groups.

GRB				
Group A (13 GRBs)				
050416A	050824	050904	060912A	061007
080310	080319B	080330	080603A	080607
080913	100418A	100901A		
Group B (27 GRBs)				
050319B	050401	050408	050525A	051109A
060124	060502A	060512	060526	060614
060904B	060908	061121	060729	070208
071003	071031	071010A	080413B	080710
080928	081008	081203A	090313	090618
091018	090926A			
Group C (28 GRBs)				
050730	050820A	050908	050922C	051111
060206	060210	060418	060605	060607A
060906	060927	061126	070125	070318
070411	070419A	070529	070802	071025
071031	071112C	080721	080810	081029
090102	090424	090426	091127	

GRBs with a similar optical/X-ray LC shapes are: GRB 051109, GRB 060526, GRB 071010A, GRB 060124, GRB 070208 and GRB 090618 where the optical and X-ray LC coincide during the X-ray plateau. In particular: the 060526 optical LC traces the X-ray LC at late time, even if the X-ray LC has few data points; the 090618 optical LC shows the presence of a SN at late

time (Dado & Dar 2010; Cano et al. 2011b), so at late time optical and X-ray LCs do not coincide.

We divided GRBs with different optical-X-ray LC shapes into four sub-groups: optical LC more complex than X-ray LC (5 GRBs), X-ray LC more complex than optical LC (5 GRBs), optical bumps (2 GRBs), peculiar cases (9 GRBs). In the first sub-group there are: GRB 050319B (coincidence during the X-ray plateau phase), GRB 061121 and GRB 050408 (coincidence during the X-ray normal decay phase); the GRB 080413B optical LC resembles the canonical X-ray shape and the first and last phases decay as the X-ray LC and the central part shows a plateau. The GRB 071031 normal decay has the same slope for the optical and X-ray LCs; we cannot conclude nothing sure about the emission mechanism during this phase, because SEDs are too uncertain. There are two bumps superimposed to this segment. In the second sub-group there are: GRB 050401 and GRB 060502A (correspondence during the X-ray plateau phase), GRB 060908, GRB 060614 and GRB 091018 (correspondence during the X-ray normal decay phase). In the third group (GRB 060904B, GRB 080928) there are the GRBs that show optical bumps in coincidence with the X-ray steep and plateau phase; the optical and X-ray LC coincide during the normal decay phase (after the optical bumps). In the fourth sub-group there are: GRB 050525A[21], GRB 060512, GRB 080710 and GRB 090313, which LCs coincide during the plateau phase; GRB 090926A, GRB 071003 and GRB 081008 and GRB 081203A which LCs agree during the normal decay. The slopes of GRB 060729 optical LC are similar to the slopes of the X-ray LC during the plateau and the normal decay, but there is an optical re-brightening coincident to the end of the X-ray plateau.

Group C. No pairs of optical/X-ray slopes of the same GRB satisfy the relation $\alpha = 0, \pm 1/4$. GRB 050730, GRB 060210, GRB 060605, GRB 060607A, GRB 070802, GRB 080810 have type IIa X-ray LC and Ia optical LC (four with X-ray flares); 070529 has type IIa X-ray LC and Ib optical LC. Nine GRBs have a simple power-law X-ray LC (6 truncated[22]): GRB 051111, GRB 061126, GRB 070125, GRB 070411, GRB 090102, GRB 090426, GRB 091127, GRB 070318, GRB 060206. Eight GRBs have a Type Ia X-ray LC (4 complete[22]): GRB 050908, GRB 060927, GRB 080721, GRB 081029, GRB 090424, GRB 050820A, GRB 050922C, GRB 071112C. Only two GRBs have Type Ib X-ray LC (GRB 060418, GRB 071025) and one GRB has Type IIb X-ray LC (GRB 070419B). GRB 060906 is observed in the optical band only during the X-ray plateau phase and it is not a regular shape, but there are optical bumps.

[21] In this case there is coincidence because the X-ray LC plateau slope has a relatively large error: $\alpha_{\rm X,PL} = 0.600 \pm 0.648$ and $\alpha_{\rm op} = 1.150 \pm 0.036$.

[22] As defined in M13, complete X-ray LCs correspond to those GRBs re-pointed by XRT at $t_{\rm rep}$ <300 s and for which we were able to follow the fading of the XRT flux down to a factor ∼5-10 from the background limit (or, equivalently, $t_{\rm end} \geq 4 \times 10^5$ s). The LCs which do not follow this criterium are classified as "truncated".

Figure 3.14: Subdivision of the GRB sample in different groups considering the optical-X-ray LC comparison. Colors follow the sample description done in the text.

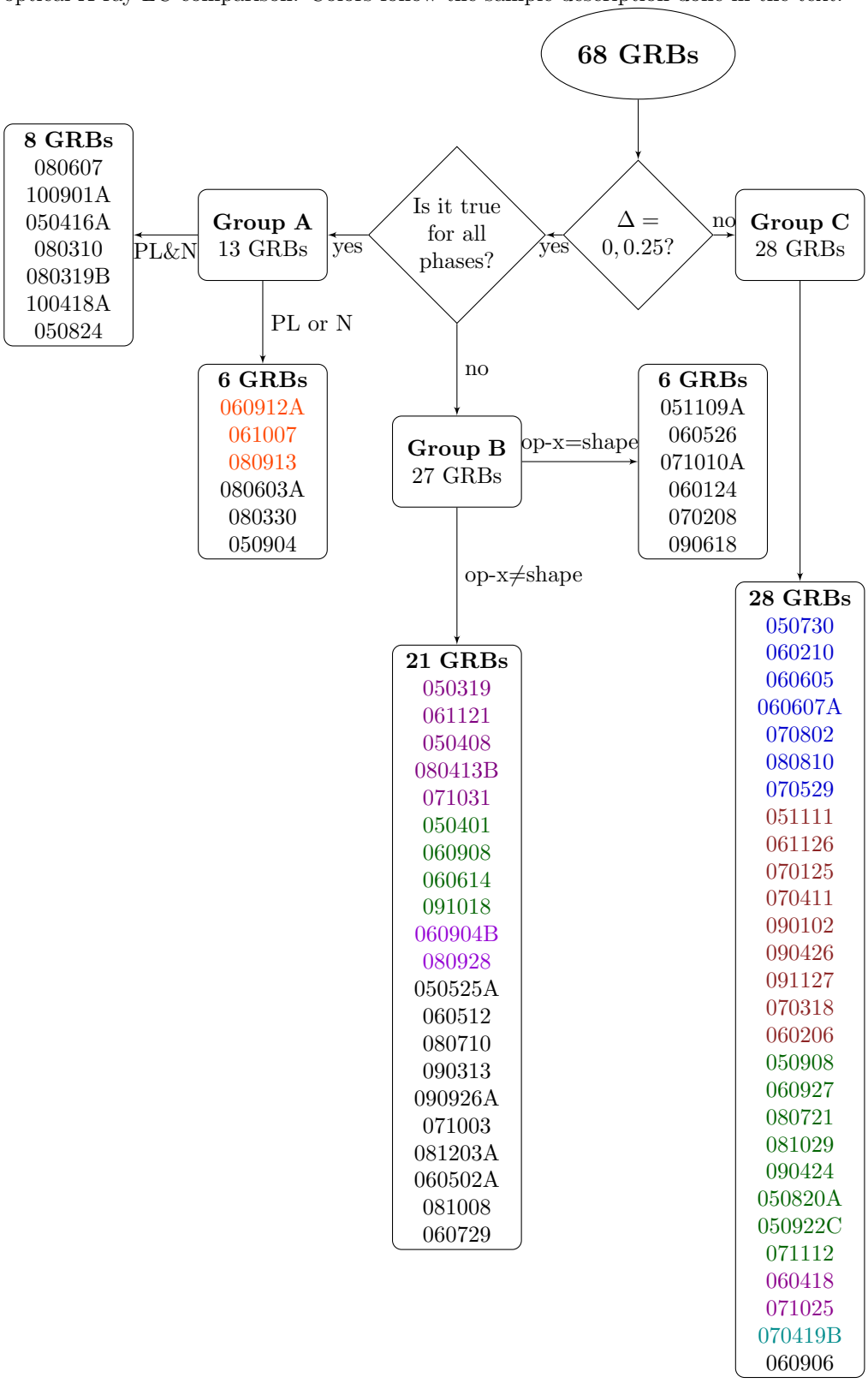

3.3 Discussion

In this Chapter we presented the analysis of a large and homogeneous data set, useful for the study of the GRB rest frame properties and for the comparison between the optical and X-ray emission.

The comparison between the X-ray and the optical LCs and SEDs gives us the possibility to investigate the nature of their emission mechanism and to verify if they have the same origin. For the internal-external shock model (Sari et al. 1998), the forward shock propagating into the external medium gives rise to the X-ray and optical emission. If the optical and the X-ray LCs have similar shape and slopes, they could be due to synchrotron emission and likely produced by the forward shock (e.g. Zhang et al. 2006). Indeed, the X-ray emission is largely influenced by the central engine activity: the steep decay is thought to be the tail of the prompt emission (Kumar & Panaitescu 2000) or it is direct emission from the central engine (Barniol Duran & Kumar 2009). The plateau reflects the effect of energy injection into the forward shock (e.g. Zhang et al. 2006). The optical LCs show various features: initial peaks or constant phases, which are the onset of the forward shock (e.g. Panaitescu & Vestrand 2011), late time re-brightenings, which may depend on the structure of the jet (e.g. Racusin et al. 2008), and small bumps linked to the central engine activity (Li et al. 2012).

Thanks to our sample of LCs and SEDs, we are able to discuss the similarities and differences of the optical and X-ray emission, comparing their LCs (Sect. 3.3.1). In Sect. 3.3.2 we consider the forward shock model and the closure relations (e.g. Sari et al. 1998; Zhang et al. 2006) and in Sect. 3.3.3 we present the radio/optical/X-ray SED of GRB 071003, which is well fitted by the synchrotron spectrum. Finally, we investigate the role of the optical emission in the three parameter correlation between $E_{\rm X,iso}$-$E_{\gamma,\rm iso}$-$E_{\rm pk}$ (M13, Bernardini et al. 2012b).

3.3.1 The LC phases

The steep decay phase, the plateau and the X-ray flares

The steep decay phase of the X-ray LCs is the tail of the prompt γ-ray emission (Kumar & Panaitescu 2000) or the prompt emission itself (Barniol Duran & Kumar 2009), since the X-ray flux is smoothly connected to the γ-ray emission (Tagliaferri et al. 2005b; Goad et al. 2006) and it is characterized by a strong hard-to-soft spectral evolution (Butler & Kocevski 2007b). The majority of the optical LCs in this phase rise (42%) or have a complex behavior, with the presence of bumps, peaks and plateaus (16%), so their slopes are different with respect to the X-ray steep decay slopes. In two cases out of the 32% of decaying optical LCs during this phase, the optical LC slope is similar to the X-ray one (e.g. GRB 080607, GRB 100901A). In some cases, there are X-ray flares superimposed to the steep decay, which are linked to the central engine activity (e.g. Zhang et al. 2006; Chincarini et al. 2010a).

The X-ray plateau is interpreted as an injection of energy into the forward

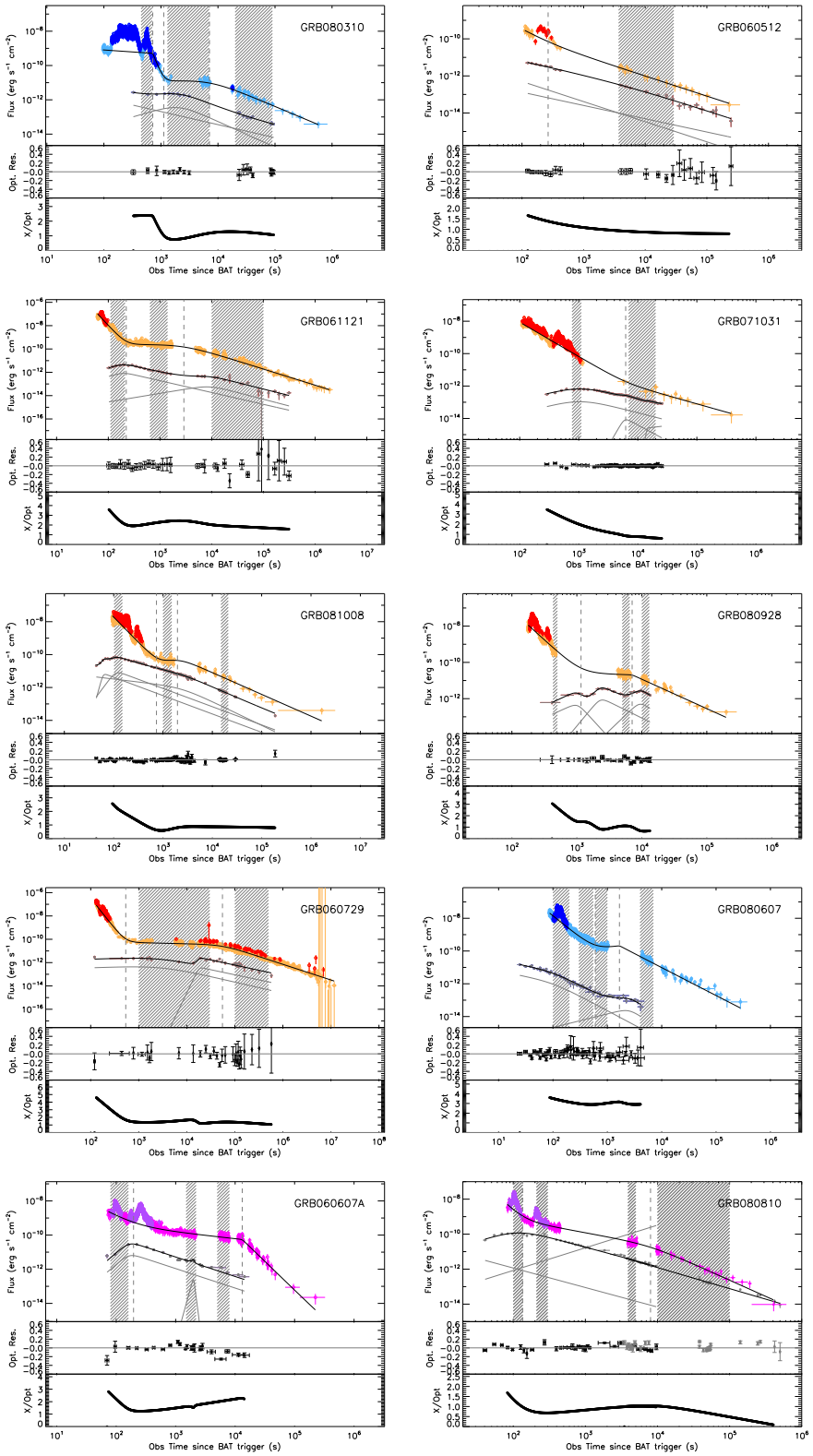

Figure 3.15: GRBs with X-ray flares during the steep decay phase and optical peak during or at the end of the X-ray steep decay. Color code as in Figure 3.12.

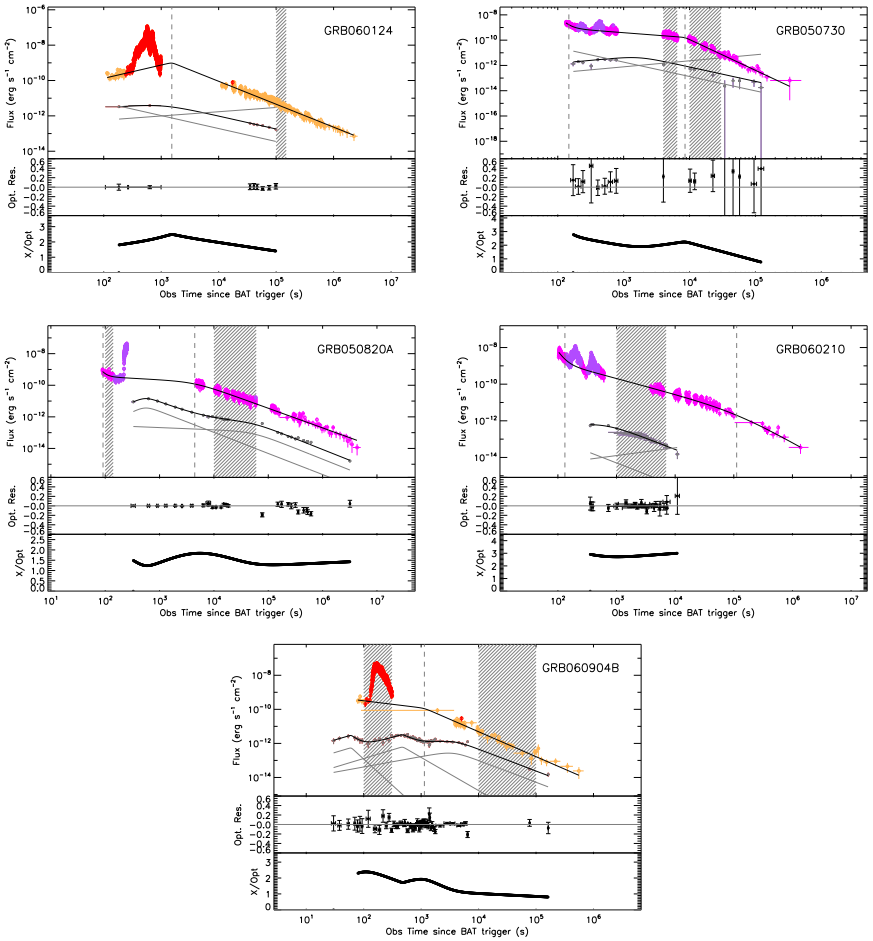

Figure 3.16: GRBs with X-ray flares during the plateau and optical peak during or at the end of the X-ray plateau. Color code as in Figure 3.12.

shock (e.g. Zhang et al. 2006) and agrees with this prediction since there is no significant spectral evolution (Bernardini et al. 2012a). The source of energy injection could be the power emitted by a spinning-down newly-born magnetar (Dai & Lu 1998; Zhang & Mészáros 2001; Corsi & Mészáros 2009) that refreshes the forward shock (Dall'Osso et al. 2011) or the fall-back and accretion of the stellar envelope on the central black hole (Kumar et al. 2008). During this phase the optical LCs behave in different ways and ∼46% of them rise or show peaks or bumps.

From the comparison of the X-ray and optical LCs, we noted that there is a relation between the occurrence of the X-ray flares and the peak time of the optical LCs (Figures 3.15-3.16-3.17). That is: when the flares are observed during the X-ray steep decay phase, the optical peak occurs early and before the beginning of the X-ray plateau, while in the case of no flares or late time flares, the optical peak occurs during the X-ray plateau.

The peak of the optical LC occurs during or at the end of the steep decay phase if there are X-ray flares in this phase, as in GRB 080310, GRB 060512,

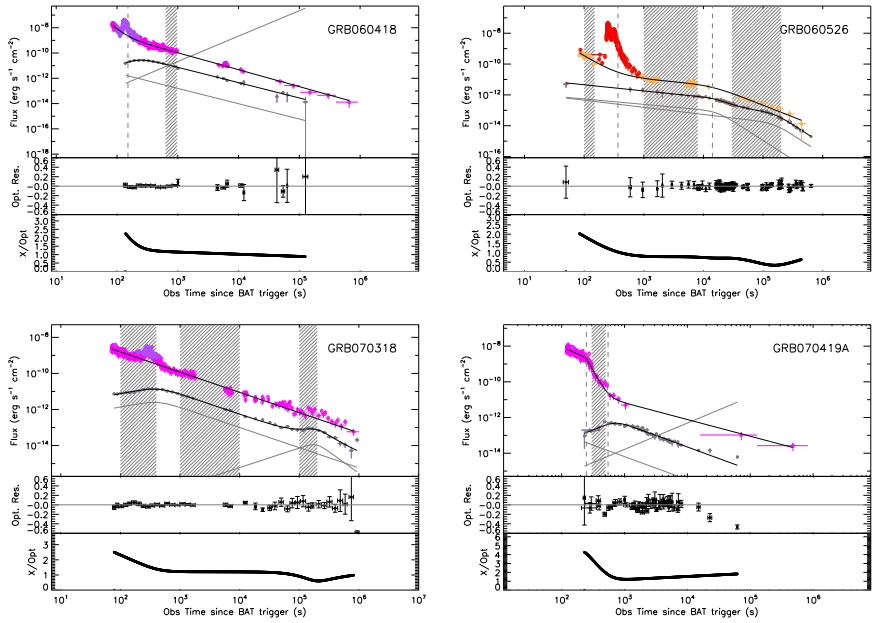

Figure 3.17: Particular cases. Color code as in Figure 3.12.

GRB 061121, GRB 071031, GRB 081008, GRB 080928, GRB 060729, GRB 080607, GRB 060607A, and GRB 080810.

The same occurs for the plateau phase: GRB 060124, GRB 050730, GRB 050820A, GRB 060210, GRB0 60904B, and GRB 060512.

In some cases is difficult to evaluate this relation between the X-ray flares and the optical LCs. For GRB 060418 the computation of the X-ray break time is influenced by the presence of a very bright X-ray flare (e.g. Margutti et al. 2010b for details). So if we consider a break time ∼200 s, the peak of the optical LC would be synchronous with the end of the steep decay phase and in this case it would be part of the group of GRBs with the break of the optical LC occurring during or at end of the steep decay. The GRB 060526 v filter data show a variability in correspondence of the X-ray flare, even if there is not a true break. GRB 070318 has a Type 0 X-ray LC with a superimposed flare which temporally corresponds to the optical peak. At late time it shows another optical re-brightening in correspondence to a small X-ray flux variation. GRB 070419A belongs to the 17/437 Type *IIb* GRBs with complete LCs (M13). The end of the X-ray steep decay corresponds to the peak of the optical LC even if there are no flares during the steep decay. Unlikely the X-ray LC is not well sampled after the steep decay phase.

If there are no flares, the optical break happens during the X-ray plateau. GRB 100418A and GRB 100901A simply follow the trend of the X-ray data. The GRB 060614 LCs are similar of those of GRB 100418A and GRB 100901A, but unlikely there are no data during the X-ray steep decay. For GRB 050319, GRB 081203A, GRB 060605, GRB 060906, GRB 070802 and GRB 071025 some data are lacking during the plateau and the steep decay is not well

sampled or has a small duration. GRB 071112C and GRB 080413B have Type Ia X-ray LC (M13) and so there is not a steep decay phase. GRB 081029 has no X-ray data before the optical peak. For GRB 091127 we have only late-time data ($t_{\rm start,X} \sim 5 \times 10^3$ s). The optical peak of GRB 051109A corresponds to the end time of the X-ray plateau, but there are no X-ray data during the plateau. GRB 050408, whose observations started 2000 s after the trigger, has a Type 0 LC and it shows an optical break at about 2×10^4 s, even if the X-ray LC does not show flux variations.

For GRB 050904, GRB 061007, GRB 080603A, GRB 050525A, GRB 080710, GRB 090313, GRB 090926A, GRB 070125, GRB 060729, GRB 080330, GRB 071003, GRB 071010A, GRB 070208, GRB 070411, and GRB 090426 the X-ray data are very poor.

The relation between the X-flares and the optical peaks and plateaus is displayed also in GRB 070110, GRB 080319A, GRB 081126, GRB 090812, and GRB 100906A studied by Li et al. (2012) and Liang et al. (2012).

The normal decay phase

The X-ray normal decay is present in the majority of the X-ray LCs of our sample (63/68). 77% of the optical LCs decay during the X-ray normal phase, but only the 62% have a similar slope. In addition, only few cases follow the closure relations.

23% of the optical LCs contemporaneous to the X-ray normal decay have a variable shape, with bumps and late time re-brightenings. Small bumps would represent the long time central engine activity (e.g. Li et al. 2012) and the late time re-brightenings the structure of the jet (e.g. Liang et al. 2012).

The normal decay phase of the X-ray LC and the contemporaneous optical emission can be considered afterglow emission, even if the central engine activity is revealed by the late time X-ray flares (e.g. Bernardini et al. 2011) and optical bumps and re-brightenings.

3.3.2 The closure relations

The standard fireball model predicts a link between the characteristic quantities of the spectrum and the LC of GRB afterglow (Sari et al. 1998). These relations are summarized in Zhang et al. (2006) (their Table 2). In our analysis we consider only the slow cooling regime, with a constant interstellar medium or a wind medium, with energy injection or not[23].

[23] In particular, we consider the following cases: *a)* $\alpha_{\rm op} - \alpha_{\rm X} = 0$: if there is no energy injection, $\alpha = (3\beta - 1)/2$; if there is energy injection, $\alpha = (q - 2 + (2+q)\beta)/2$. *b)* $\alpha_{\rm op} - \alpha_{\rm X} = -1/4$ corresponds to a constant density medium in the slow cooling regime with no energy injection, so $\alpha_{\rm op} = 3\beta_1/2$ and $\alpha_{\rm X} = (3\beta_2 - 1)/2$. *c)* $\alpha_{\rm op} - \alpha_{\rm X} = +1/4$ corresponds to a wind medium in the slow cooling regime, so $\alpha_{\rm op} = (3\beta_1 + 1)/2$ and $\alpha_X = (3\beta_2 - 1)/2$. *d)* $\alpha_{\rm op} - \alpha_{\rm X} = (q-2)/4$ corresponds to a constant density medium in the slow cooling regime with energy injection, so $\alpha_{\rm op} = (q-1) + (\beta_1/2)(2+q)$ and $\alpha_{\rm X} = ((q-2) + \beta(2+q))/2$. *e)* $\alpha_{\rm op} - \alpha_{\rm X} = (2-q)/4$ corresponds to a wind medium in the slow cooling regime with energy injection, so $\alpha_{\rm op} = (q + \beta_2(2+q)\beta)/2$ and $\alpha_{\rm X} = ((q-2) + \beta(2+q))/2$. In the energy injection case, we consider three values of q, 0, 0.3, 0.5, which depend on the strength of the

Only few GRBs of our sample obey to the closure relations. We define as α the value of the LC slope calculated fitting the LCs and $\tilde{\alpha}$ the LC slope expected by the closure relations, determined using the spectral indices computed with the SEDs. For Group A (defined in Sect. 3.2.4), the closure relations are valid in some GRBs only for the normal decay phase:

- GRB 080607: its optical/X-ray SED, extracted during the normal decay phase, is fitted with a broken power-law function and it follows the relation $\alpha_{\rm op} - \alpha_{\rm X} \sim 1/4$ because $\alpha_{\rm op} = 2.20 \pm 0.61$ and $\alpha_{\rm X} = 1.70 \pm 0.07$ (constant density medium in the slow cooling regime with no energy injection). Therefore $\tilde{\alpha}_{\rm op} = (3\beta_1 + 1)/2$ and $\tilde{\alpha}_{\rm X} = (3\beta_2 - 1)/2$. From the spectrum $\beta_{\rm op} = 0.80 \pm 0.10$ and $\beta_{\rm X} = 1.30 \pm 0.10$, then the expected slopes are $\tilde{\alpha}_{\rm op} = 1.70 \pm 0.15$ and $\tilde{\alpha}_{\rm X} = 1.45 \pm 0.15$.

- GRB 050416A: during the normal decay, the best fit of the SED is a broken power-law. $\alpha_{\rm op} = 0.86 \pm 0.15$ and $\alpha_{\rm X} = 0.90 \pm 0.04$ and $\alpha_{\rm op} - \alpha_{\rm X} \sim \pm 1/4$ within 2σ. This case is in agreement with a slow cooling regime, without energy injection, in a constant density medium (ISM): $\tilde{\alpha}_{\rm op} = 3\beta_{\rm op}/2 = 0.78 \pm 0.23$ and $\tilde{\alpha}_{\rm X} = (3\beta - 1)/2 = 1.03 \pm 0.21$.

- GRB 100418A: the best fitting function of the SED is a single power-law. $\alpha_{\rm op} = 1.38 \pm 0.07$, $\alpha_{\rm X} = 1.51 \pm 0.19$ and $\beta_{\rm op,X} = 1.19 \pm 0.02$. For the case of no energy injection, ISM or wind medium, with $\nu_{\rm c} < \nu_{\rm op} < \nu_{\rm X}$, the expected slopes are $\tilde{\alpha}_{\rm op} = \tilde{\alpha}_{\rm X} = (3\beta_{\rm op,X} - 1)/2 = 1.39 \pm 0.03$ in agreement, within errors, with our data.

For Group B, for the normal decay:

- GRB 071003: the X-ray LC has a simple power-law shape, instead the optical LC has an initial shallow decay and then a normal decay. For this last part, $\alpha_{\rm op} = 1.91 \pm 0.36$ and $\alpha_{\rm X} = 1.60 \pm 0.06$. The best fit of the SED is a simple power-law ($\beta_{\rm op,X} = 1.28 \pm 0.05$), so the expected $\tilde{\alpha} = 1.42 \pm 0.08$ for no energy injection, ISM or wind medium and $\nu_{\rm c} < \nu_{\rm op} < \nu_{\rm X}$. This is in agreement with the X-ray and the optical slopes within 2σ.

- GRB 080413B: for the normal decay phase, $\alpha_{\rm op} = 1.84 \pm 0.08$ and $\alpha_{\rm X} = 1.62 \pm 0.21$. The best fit of the SED is a broken power-law ($\nu_{\rm c} < \nu_{\rm op} < \nu_{\rm X}$). The expected X-ray slope is $\tilde{\alpha}_{\rm X} = 1.36 \pm 0.36$ for the no energy injection case and $\tilde{\alpha}_{\rm op} = 1.11 \pm 0.36$ for the slow cooling regime and $\tilde{\alpha}_{\rm op} = 1.61 \pm 0.36$ for the fast cooling regime. Therefore the normal decay observations are in agreement with a ISM medium, no energy injection and slow (2σ) or fast (1σ) cooling regime.

- GRB 080913: the X-ray LC is a simple power-law with $\alpha_{\rm X} = 1.00 \pm 0.06$. The optical LC shows a late time re-brightning, but at the beginning, between 600-1200 s after the trigger, $\alpha_{\rm op} = 0.98 \pm 0.04$. The best fit

injection.

of the SED is a simple power-law and it follows the closure relation in the case of ISM or wind medium, in the slow cooling regime and $\nu_{\rm m} < \nu_{\rm op} < \nu_{\rm X} < \nu_{\rm c}$; in fact $\tilde{\alpha}_{\rm op} = \tilde{\alpha}_{\rm X} = 0.98 \pm 0.06$ in the ISM case and $\tilde{\alpha}_{\rm op} = \tilde{\alpha}_{\rm X} = 1.06 \pm 0.05$ in the wind case.

- GRB080928: for the normal decay, $\alpha_{\rm op} = 2.38 \pm 0.65$ and $\alpha_{\rm X} = 1.62 \pm 0.09$. The best fit function is a power-law, hence there is one spectral index, $\beta_{\rm op,X} = 1.15 \pm 0.02$. The expected slope both for the X-ray and the optical LC is $\tilde{\alpha} = 1.69 \pm 0.02$ for the case of slow cooling, energy injection, wind medium and $\nu_{\rm m} < \nu_{\rm op} < \nu_{\rm X} < \nu_{\rm c}$. $\tilde{\alpha}$ is consistent with $\alpha_{\rm X}$ (1σ) and $\alpha_{\rm op}$ (2σ).

- GRB 081008: for the X-ray normal decay $\alpha_{\rm X} = 1.32 \pm 0.08$ and the corresponding optical slope is $\alpha_{\rm op} = 1.44 \pm 0.13$. The spectral index is $\beta_{\rm op,X} = 0.93 \pm 0.01$. In the case of no energy injection, ISM and $\nu_{\rm m} < \nu_{\rm op} < \nu_{\rm X} < \nu_{\rm c}$ the expected slope is $\tilde{\alpha} = 1.39 \pm 0.01$, which is in agreement with the optical and X-ray slopes of this GRB.

For Group B, for the plateau:

- GRB 060502A: $\alpha_{\rm op} = 0.50 \pm 0.05$ and $\alpha_{\rm X} = 0.45 \pm 0.13$. The best fit of the SED is a broken power-law, hence $\beta_{\rm op} = 0.51 \pm 0.12$ and $\beta_{\rm X} = 1.01 \pm 0.12$. For the case of energy injection, ISM and slow cooling regime, we obtain $\tilde{\alpha}_{\rm op} = 0.14 \pm 0.15$ and $\tilde{\alpha}_{\rm X} = 0.51 \pm 0.16$. These values are in agreement respectively with the optical slope (3σ) and the X-ray slope (1σ).

- GRB 060512: $\alpha_{\rm op} = 1.09 \pm 0.15$ and $\alpha_{\rm X} = 1.08 \pm 0.09$. The best fit of the SED is a single power-law ($\beta_{\rm op,X} = 1.24 \pm 0.05$). Therefore we obtain $\tilde{\alpha} = 1.05 \pm 0.06$, which is consistent of the optical and X-ray slopes. This result is obtained considering the energy injection, ISM, slow cooling regime and $\nu_{\rm m} < \nu_{\rm op} < \nu_{\rm X} < \nu_{\rm c}$.

- GRB 071031: $\alpha_{\rm op} = 0.93 \pm 0.03$ and $\alpha_{\rm X} = 1.02 \pm 0.18$. The best fit of the SED is a single power-law with $\beta_{\rm op,X} = 0.99 \pm 0.01$. The expected LC slope is $\tilde{\alpha} = 0.99 \pm 0.02$ for the no energy injection case and $\nu_{\rm c} < \nu_{\rm op} < \nu_{\rm X}$. This value agrees with the optical LC slope (2σ) and the X-ray slope (1σ).

The closure relations cannot explain the complexity of our data because they simply derive from the synchrotron emission equations. Actually, the dynamic of the fireball and its interaction with the external medium depend on the assumption of the microphysics parameters (ϵ_e, ϵ_B, which usually are fixed on the time), the medium density (constant density interstellar medium or wind) and other characteristc parameters describing the fireball (the radius, the Lorentz factor, the magnetic field). We conclude that in various cases the closure relations, as defined above, are not satisfied for $\sim$80% of the GRBs of our sample.

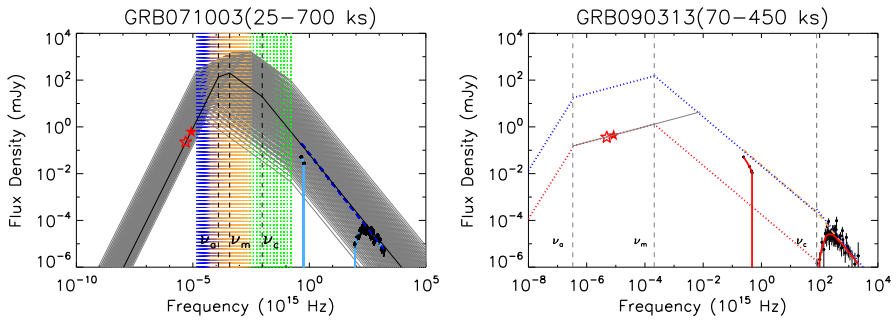

Figure 3.18: Radio/optical/X-ray SEDs. *Filled (empty) red star*: radio data (upper limit). *Black dots*: optical and X-ray data. *Upper panel*: GRB 071003. *Light blue solid line*: optical/X-ray SED. *Blue dashed line*: power-law which fits the data. *Black solid line*: radio/optical/X-ray SED fit function. *Black dashed line*: the absorption frequency (ν_a), the synchrotron frequency (ν_m) and the cooling frequency (ν_c). *Gray lines*: radio/optical/X-ray SED tests with relative absorption frequencies (*blue dashed lines*), synchrotron frequencies (*orange dashed lines*) and cooling frequencies (*green dashed lines*). *Lower panel*: GRB 090313. *Red solid line*: the optical/X-ray SED fit function. *Orange dashed line*: broken power-law which fits the data. *Blue dotted line*: radio/optical/X-ray SED calculated considering $\nu_{BR} = \nu_c$. *Red dotted line*: radio/optical/X-ray SED calculated using the same characteristic frequencies as the red dotted line, but considering the normalization for the radio data. *Gray dashed line*: the absorption frequency (ν_a), the synchrotron frequency (ν_m) and the cooling frequency (ν_c).

3.3.3 The broad band SEDs

From the GRB sample with radio data presented by Chandra & Frail (2012) we selected two GRBs (GRB 071003 and GRB 090313) which have radio observations contemporaneous with the optical/X-ray data presented here, in order to test the broadband behavior of the SEDs.

For GRB 071003 we calculated a set of illustrative radio/optical/X-ray SEDs starting from different values of the cooling frequency (ν_c) and the maximum flux ($F_{\nu,\max}$), as presented by Sari et al. (1998) for the slow cooling regime, because of the late time data[24] (25-700 ks in observer frame). The optical/X-ray SED is fitted with a simple power-law, so the cooling frequency is likely below the optical band. In this way we found a possible set of data which is consistent with the radio/optical/X-ray SED is: $\nu_a = 1.2 \times 10^{11}$ Hz, $\nu_m = 3.08 \times 10^{11}$ Hz, $\nu_c = 9.45 \times 10^{12}$ Hz and $F_{\nu,\max} = 198$ mJy (Figure 3.18). The total energy, calculated in the frequency interval $\nu = 10^7 - 10^{19}$

[24]For an adiabatic evolution, the equations that describe the emitted radiation are (Sari et al. 1998; Granot et al. 2000): $F_\nu = (\nu_a/\nu_m)^{1/3}(\nu/\nu_a)^2 F_{\nu,\max}$ for $\nu < \nu_a$; $F_\nu = (\nu/\nu_m)^{1/3} F_{\nu,\max}$ for $\nu_m > \nu$; $F_\nu = (\nu/\nu_m)^{-(p-1)/2} F_{\nu,\max}$ for $\nu_c > \nu > \nu_m$; $F_\nu = (\nu_c/\nu_m)^{-(p-1)/2}(\nu/\nu_c)^{-p/2} F_{\nu,\max}$ for $\nu > \nu_c$. The absorption frequency is $\nu_a = 0.247(4.24 \times 10^9)((p+2)/(3p+2))^{3/5}((p-1)^{8/5}/(p-2))\epsilon_e^{-1}\epsilon_B^{1/5}E_{52}^{1/5}n_1^{3/5}$ Hz; the synchrotron frequency $\nu_m = (5.7 \times 10^{14})\epsilon_B^{1/2}\epsilon_e^2 E_{52}^{1/2} t_d^{-3/2}$ Hz; the cooling frequency $\nu_c = (2.7 \times 10^{12})\epsilon_B^{-3/2} E_{52}^{-1/2} n_1^{-1} t_d^{-1/2}$ Hz; the maximum flux, which is the flux at ν_m, $F_{\nu,\max} = (1.1 \times 10^5)\epsilon_B^{1/2} E_{52} n_1^{1/2} D_{28}^{-2}$ μJy. t_d is the time in days, $E_{52} = E/10^{52}$ ergs, the density n_1 in cm^{-3}, the distance $D_{28} = D/10^{28}$ cm.

Hz, is 2.72×10^{52} erg. For the different parts of the spectrum, the energy is: $E_{10^7\mathrm{Hz}-\nu_\mathrm{a}} = 1.25 \times 10^{50}$ erg, $E_{\nu_\mathrm{a}-\nu_\mathrm{m}} = 9.56 \times 10^{50}$ erg, $E_{\nu_\mathrm{m}-\nu_\mathrm{c}} = 8.59 \times 10^{51}$ erg and $E_{\nu_\mathrm{c}-10^{19}Hz} = 1.76 \times 10^{52}$ erg.

This example shows that the synchrotron model can fit adeguately the GRB spectral properties at late time.

For GRB 090313 we know the cooling frequency, which is the break frequency calculated fitting the optical/X-ray SED with a broken power-law. At this time the data are unlikely to be influenced by the host galaxy, and we cannot reconstruct the radio/optical/X-ray SED, as shown in Figure 3.18.

3.3.4 The 3-parameter correlation

In M13 we found a 3-parameter correlation which we discussed in Bernardini et al. (2012b) and involves the isotropic energy emitted in the rest-frame 1-10^4 keV energy band during the prompt emission ($\mathrm{E}_{\gamma,iso}$), the peak of the prompt emission energy spectrum (E_{pk}) and the X-ray energy emitted in the 0.3-30 keV observed energy band ($\mathrm{E}_{X,iso}$). The X-ray energy was calculated in a specific energy band and we did not extrapolated the spectrum to smaller energies because we did not know the behavior of the spectrum at those energies. In this work we have presented the GRB spectra covering the energy band from the infrared to X-rays and we calculate the models that fit better the data. Using these models, for every GRB we calculate the ratio between the X-ray energy band (0.3-30 keV) and the total energy emitted from the IR to X-rays: $\sim$70% of the total energy is radiated in the X-rays. The mean value of the IR-optical-UV energy is $\lesssim$10%.

The correlation is not quantitatively modified by the inclusion of the optical energy. However, since the origin of the correlation is still unknown, it is not clear if the inclusion of the optical energy is conceptually necessary or not.

3.4 Conclusions

In this Chapter we performed a systematic analysis of a large sample of well monitored optical LCs (68 GRBs), obtained with different instruments, and we compared them with the X-ray emission. Since the GRBs of this sample have known redshift, we considered their rest frame properties. From this large sample of observations:

- for every GRB, we fitted the optical LCs collected from different instruments and the optical/X-ray SEDs at different times;
- we studied the distribution of the parameters computed from the SEDs, giving information about the medium and the spectrum, and we can assert that: *a)* there is a slight *softening* of the optical/X-ray spectrum with time; *b)* the gas-to-dust ratios (NH/A_V) of GRBs are larger than the values calculated for the MW, the LMC, and SMC assuming solar abundances (e.g. Schady et al. 2010, 2012); *c)* the break frequencies are spread between the optical and X-ray bands;

- for a given rest frame time range (920-12000 s), the optical flux in the R band is $\sim$2 orders of magnitude brighter than the X-ray flux in the 1 keV band;
- there is a correlation between the energy of the peak of the optical LCs and $E_{\gamma,iso}$ and E_{γ}^{15-150}, confirming the result of Panaitescu & Vestrand (2011)). The optical plateau end luminosity and rest frame time are correlated, and the same similarly the peak luminosity and the peak times are correlated (e.g. Panaitescu & Vestrand 2011);
- the optical LCs have a complex shape, with initial plateaus and peaks, bumps and late time re-brightenings. As time goes by the complexity of the LCs reduces and more and more of them just decay;
- only for 13 GRBs of our sample (Group A), all LC segments follow $\alpha_{\rm op} - \alpha_{\rm X} = 0, \pm 1/4$[25], in the other cases the X-ray and optical LCs show different shapes;
- the onset of the forward shock observed in the optical LCs could be linked to the presence of the X-ray flares. In fact when there are X-ray flares during the steep decay, the optical LC peak or end of the initial plateau occurs during or just at the end of the X-ray steep decay phase, while if there are no flares or they take place during the X-ray plateau, the optical peak or plateau end happens during the X-ray plateau;
- the forward shock model cannot explain all the features present in the optical and X-ray LCs, such as bumps, flares, re-brightenings, steep decays and plateaus, both at early and late time;
- the contribution of the optical energy to the 3-parameter correlation (M13, Bernardini et al. 2012b) is low, less than 10% of the total energy emitted from the IR and X-rays. Therefore the correlation is not quantitatively modified by the inclusion of the optical energy. However, since the origin of the correlation is still unknown, it is not clear if the inclusion of the optical energy is conceptually necessary or not.

From this study it clearly emerges that the complex shapes of the optical and X-ray LCs cannot be explained simply by the forward shock, although we can confirm that the synchrotron is a viable emission mechanism for GRBs at late times. Moreover, we show the importance of a systematic analysis of the multiwavelength observations of GRBs. To improve the knowledge of the physics of GRBs and their origin, very fast detectors and multi-wavelength observations are needed. In particular, we need an optical follow-up starting at least few seconds after the trigger, collecting homogeneous spectroscopic and photometric data (e.g. Chincarini et al. 2010b).

[25] We do not consider the steep decay, since during this phase the emission from the two bands clearly comes from different mechanisms or emitting regions.

4

Conclusions

The main subject of this thesis is the study of the X-ray and optical emission of GRBs.

We analyzed the XRT LCs of GRBs observed between December 2004 and December 2010, focusing on: the properties of GRBs in a common rest-frame 0.3-30 keV energy band, the characteristics of long and short GRBs, and the relation between the prompt γ-ray properties and the X-ray LC properties.

Short and long GRBs represent two classes of GRBs with different energetics, environments and progenitors. The X-ray isotropic energy of long GRBs is about 7% of the γ-ray isotropic energy, and it is directly proportional to $E_{\gamma,\rm iso}$ and $E_{\rm pk}$. Short GRBs are less energetic than long GBRs ($E^{\rm short}_{\rm X,iso} \sim 1/50 E^{\rm long}_{\rm X,iso}$), and their median luminosity is a factor $\sim$10-30 lower than long GRBs, in the common rest frame time $10^2 - 10^4$ s. Therefore, they stay below of the correlations $E_{\rm X,iso} - E_{\gamma,\rm iso}$, $E_{\rm X,iso} - E_{\rm pk}$, $L^{\rm 11h}_{\rm X} - E_{\gamma,\rm iso}$, and $L_{\rm f} - t^{\rm RF}_{\rm f}$ established for long GRBs.

Looking for new relations between the X-ray and prompt emission properties, we found a 3-parameter correlation which involves the isotropic X-ray energy ($E_{\gamma,\rm iso}$), the peak energy ($E_{\rm pk}$), and the prompt gamma-ray energy ($E_{\rm X,iso}$), which is followed by long, short, and low energy GRBs. These three groups of objects occupy a different region of the $E_{\rm X-ray} - E_{\gamma,\rm iso}$ vs. $E_{\rm pk}$ plane since short and low-energy GRBs have $E_{\rm X,iso} < 10^{51}$ erg and long GRBs have $E_{\rm X,iso} > 10^{51}$ erg. The existence of a common scaling for long and short GRBs implies that they have some characteristic in common, for example the properties of the outflow. Re-writing this relation in terms of efficiency ($\eta_\gamma \propto E_{\gamma,\rm iso}/E_{\rm X,iso}$) and peak energy, we obtain: $\eta_\gamma \propto E^{0.6}_{\rm pk}$. The outflow property that could explain this relation is the Lorentz factor.

To improve the study of the the relation between the prompt and the afterglow emission, we decided to include in our study also the optical data. Therefore, we performed a systematic analysis of a large sample of well monitored optical LCs (68 GRBs with known redshift), obtained with different instruments, and we compared them with the X-ray emission, considering their rest frame properties. For every GRB, we fitted the optical LCs collected from different instruments and the optical/X-ray SEDs at different times and we studied the distribution of the parameters computed from the SEDs. From the

analysis of their spectral properties we found that there is a slight *softening* of the optical/X-ray spectrum with time. From the study of their environmental properties, we establish that the gas-to-dust ratios ($NH/A_{\rm V}$) of GRBs are grater than the mean values calculated for the MW, LMC and SMC. For the energetics, in a given rest frame time range, the optical flux in the R band is $\sim$2 orders of magnitude brighter than the X-ray flux in the 1 keV band.

The temporal properties of the optical LCs are complex, since the optical LCs can show initial plateaus and peaks, bumps and late time re-brightenings. As time goes by the complexity of the LCs reduces and more and more of them just decay. Only for 13 GRBs of our sample (Group A), all LC segments follow $\alpha_{\rm op}-\alpha_{\rm X} = 0, \pm 1/4$, in the other cases the X-ray and optical LCs show different shapes. The forward shock model cannot explain all the features present in the optical and X-ray LCs, such as bumps, flares, re-brightenings, steep decays and plateaus, both at early and late time.

From our optical and X-ray LCs, we noted that the onset of the forward shock observed in the optical LCs could be linked to the presence of the X-ray flares. In fact when there are X-ray flares during the steep decay, the optical LC peak or end of the initial plateau occurs during or just at the end of the X-ray steep decay phase, while if there are no flares or they take place during the X-ray plateau, the optical peak or plateau end happens during the X-ray plateau.

The contribution of the optical energy to the 3-parameter correlation $E_{\rm X,iso}-E_{\gamma,\rm iso}-E_{\rm pk}$ is low, less than 10% of the total energy emitted from the IR and X-rays. Therefore the correlation is not quantitatively modified by the inclusion of the optical energy. However, since the origin of the correlation is still unknown, it is not clear if the inclusion of the optical energy is conceptually necessary or not.

From this study it clearly emerges that the complex shapes of the optical and X-ray LCs cannot be explained simply by the forward shock, although we can confirm that the synchrotron is a viable emission mechanism for GRBs at late times. Moreover, we show the importance of a systematic analysis of the multiwavelength observations of GRBs. To improve the knowledge of the physics of GRBs and their origin, very fast detectors and multi-wavelength observations are needed. In particular, we need an optical follow-up starting at least few seconds after the trigger, collecting homogeneous spectroscopic and photometric data (e.g. Chincarini et al. 2010b).

Appendices

Appendix A

Principal component analysis

The principal component analysis (PCA) is a statistical tool used in multivariate analysis and which identifies patterns in data, giving the possibility to reduce the starting set of interrelated parameters in a sub-set of uncorrelated quantities (Jolliffe 2002). This technique is used in various astronomy fields, for example when a large sample of spectra from a galaxy survey must be analyzed. For GRBs, PCA was used by Borgonovo & Björnsson (2006) to study the data obtain by BATSE for a sample of 197 long GRBs.
The main idea of PCA is based on the linear transformation of the data to a new coordinate system. The direction with the greatest variance is the first Principal Component (PC). In practice, given a sample of n observations of p variables

$$\mathbf{x} = (x_1, x_2, \ldots, x_p), \tag{A.1}$$

the first PC is the linear transformation

$$\mathbf{z_1} = \mathbf{a}_1^T \mathbf{x} = \sum_{i=1}^{n} a_{i,1} x_i, \tag{A.2}$$

where $\mathbf{a}_1 = (a_{11}, a_{21}, \ldots, a_{p1})$ corresponding to the eigenvector with the maximum variance ($var[z_1]$). In general, the k^{th} PC of a data sample is defined by the linear transformation

$$\mathbf{z_k} = \mathbf{a_k^T x}, \qquad k = 1, \ldots, p \tag{A.3}$$

$$\mathbf{a_k} = (a_{1k}, a_{2k}, \ldots, a_{pk}) \tag{A.4}$$

chosen with the maximum variance $var[z_k]$. The covariance ($cov[z_k, z_l]$, $k > l \geq 1$) is equal to zero and $\mathbf{a_k^T a_k} = 1$. The variance can be rewritten as

$$var[z_k] = \mathbf{a_k^T S a_k} = \lambda_k, \tag{A.5}$$

with $\mathbf{S}$ the covariance matrix and λ_k the maximum eigenvalue of $\mathbf{S}$. So the k^{th} largest eigenvalue of $\mathbf{S}$ is the variance of the k^{th} PC, which has the k^{th} greatest function of the variation in the sample.
In short, we calculate the eigenvector of the covariance matrix and we order

them starting from the eigenvector with the major eigenvalue to which with the lower eigenvalue. This corresponds to the diagonalization of the covariance matrix, where the eigenvectors are the PCs and the eigenvalues are the variances associated with each PC.

Appendix B

The synchrotron emission

We consider the simple case in which a spherical relativistic shock with radius $R(t)$ propagates in a interstellar medium (ISM) with constant density n and it evolves in an adiabatic way (Sari et al. 1998). The typical energy of photons in a fluid (Sari et al. 1996), calculated in the observer frame, is

$$h\nu(\gamma_e) = \Gamma\gamma_e^2 \frac{\hbar q_e B}{m_e c}, \tag{B.1}$$

where $\nu(\gamma_e)$ is the radiation frequency, Γ the Lorentz factor of the shock, γ_e, q_e and m_e the Lorentz factor, the charge and the mass of electrons, B the magnetic field strength. Therefore, the synchrotron frequency (for blue-shifted electrons) simply is

$$\nu(\gamma_e) = \Gamma\gamma_e^2 \frac{q_e B}{2\pi m_e c}. \tag{B.2}$$

We define $\epsilon_B = U_B/e = B^2/8\pi e$ as the ratio between the magnetic energy density and the total energy density behind the shock[1]. The total energy density behind the shock is $e = 4\Gamma^2 n m_p c^2$ (Eq. 4 in Sari et al. 1996), so the magnetic field is

$$B = (32\pi m_p \epsilon_B n)^{1/2} \Gamma c. \tag{B.3}$$

Now, we assume that electrons in the shock have a power law distribution of γ_e

$$N(\gamma_e)\mathrm{d}\gamma_e \propto \gamma_e^{-p}\mathrm{d}\gamma_e, \qquad \gamma_e \geq \gamma_m \tag{B.4}$$

with γ_m the minimum Lorentz factor and we define the parameter $\epsilon_e = U_e/e$ which is the ratio between the electrons energy density and the total energy

[1] ϵ_B and ϵ_e are two parameters difficult to estimate (Sari et al. 1996; Piran 1999). In fact we cannot know the exact distribution of the magnetic field and the particles momentum in a shocked shell. Moreover, we are not able to know what happens after the shock, the electrons and protons energy and if (or how) these parameters evolve during the burst. Usually, in the internal shock scenario, two assumptions are used: the energy is equally distributed between electrons, protons and magnetic fields (i.e. there is *equipartition*); these two quantities are constant during the bursts. In the external shocks, these parameters are defined in order to reproduce the afterglow spectra.

density dissipated in the shock[1]. These quantities are $e \cong \Gamma n m_p c^2$ and $U_e =< \gamma_e > n m_e c^2$, where $< \gamma_e >$ is the median electron Lorentz factor[2]

$$< \gamma_e > = \frac{\int_{\gamma_m}^{+\infty} N(\gamma_e)\gamma_e \mathrm{d}\gamma_e}{\int_{\gamma_m}^{+\infty} N(\gamma_e)\mathrm{d}\gamma_e} \tag{B.5}$$

$$= \frac{p-1}{p-2}\gamma_m. \tag{B.6}$$

The energy density is defined as $\epsilon_e e =< \gamma_e > n m_e c^2$, substituting Eq. B.5 and the definition of the total energy density, we obtain the minimum electron Lorentz factor

$$\gamma_m = \epsilon_e \left(\frac{p-2}{p-1}\right) \frac{m_p}{m_e}\Gamma. \tag{B.7}$$

We know that the synchrotron radiation is caused by electrons that are accelerated at relativistic velocity in a magnetic field.
The total force that acts over a particle of mass m and charge q is[3]

$$\bar{F} = q(\bar{E} + \bar{v} \times \bar{B}), \tag{B.8}$$

where $\bar{E}$ and $\bar{B}$ are the electric and magnetic fields, respectively. Considering that the particle is accelerated to relativistic velocity, the equations of motion are

$$\frac{d}{dt}(\gamma_e m \bar{v}) = \frac{q}{c}\bar{v} \times \bar{B} \tag{B.9}$$

$$\frac{d}{dt}(\gamma_e m c^2) = q\bar{v} \cdot \bar{E} = 0. \tag{B.10}$$

For the Eq. B.10 we assume that $\bar{v} \perp \bar{E}$ and it implies that $\gamma_e = constant$ or that $|\bar{v}| = constant$, so the Eq. B.10 becomes

$$\gamma_e m \frac{d\bar{v}}{dt} = \frac{q}{c}\bar{v} \times \bar{B}. \tag{B.11}$$

Considering the two velocity components, $\bar{v}_\parallel$ the component along the field and $\bar{v}_\perp$ the component in a plain normal to the field, we obtain

$$\frac{d\bar{v}_\parallel}{dt} = 0 \tag{B.12}$$

$$\frac{d\bar{v}_\perp}{dt} = \frac{q}{\gamma_e m c}\bar{v} \times \bar{B}. \tag{B.13}$$

Therefore, $\bar{v}_\parallel = constant$ and $\bar{v}_\perp = constant$, since $\bar{v} = constant$. The motion of the particle is helical (Fig. B.1), that is the composition of the circular motion and the uniform motion along the field. The frequency of the rotation is

$$\omega_B = \frac{qB}{\gamma_e m c}. \tag{B.14}$$

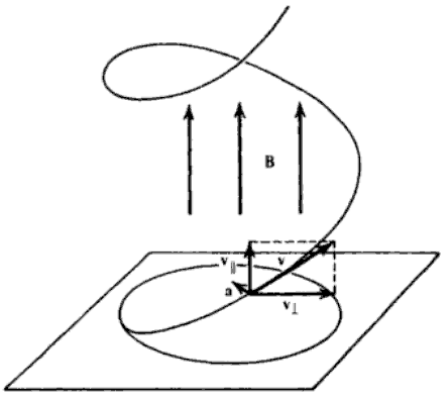

Figure B.1: Helical motion of a particle in a uniform magnetic field (Rybicki & Lightman 1979).

The total power emitted from a particle moving at relativistic speed is given by the Larmor formula, that is the radiation emitted for a dipole, and in the relativistic case it is

$$P = \frac{dW}{dt} = \frac{2q^2\bar{a}' \cdot \bar{a}'}{3c^3} \tag{B.15}$$

$$= \frac{2q^2}{3c^3}(a'_{\parallel} + a'^2_{\perp}) \tag{B.16}$$

where $a'_{\parallel} = \gamma_e^3 a_{\parallel}$ and $a'_{\perp} = \gamma_e^2 a_{\perp}$ and the ' that indicates the quantities calculated in an instantaneous rest frame of the particle (K'). Therefore

$$P = \frac{2q^2}{3c^3}\gamma_e^4(a_{\perp}^2 + \gamma_e^2 a_{\parallel}^2). \tag{B.17}$$

The acceleration is perpendicular to the velocity, so $a_{\perp} = \omega_B v_{\perp}$ and $a_{\perp} = 0$. The total power emitted is

$$P = \frac{2q^2}{3c^3}\gamma_e^4 \omega_B \bar{v}_{\perp}^2 \tag{B.18}$$

$$= \frac{2q^2}{3c^3}\gamma_e^4 \frac{q^2B^2}{\gamma_e^2 m^2 c^2} v_{\perp}^2 \tag{B.19}$$

$$= \frac{2}{3}\gamma_e^2 B^2 r_0^2 \beta_{\perp}^2 c, \tag{B.20}$$

with $\beta_{\perp} = \frac{v_{\perp}}{c}$ and $r_0 = \frac{q^2}{mc^2}$. It is necessary to average the formula B.20 over all angles for a given speed β to obtain an isotropic distribution of velocities

$$< \beta_{\perp}^2 >= \frac{\beta^2}{4\pi}\int \sin^2\alpha d\Omega = \frac{2\beta^2}{3}, \tag{B.21}$$

[2] p must be greater than 2 to avoid the divergence of the integral in Eq. B.5.

[3] For this general description I follow Rybicki & Lightman (1979).

with α the pitch angle, that is the angle between field and velocity.
Therefore,

$$P = (\frac{2}{3})^2 r_0^2 c\beta^2 \gamma_e^2 B^2 \quad \text{(B.22)}$$

$$= \frac{4}{3}\sigma_{Th} c\beta^2 \gamma_e^2 U_B, \quad \text{(B.23)}$$

with $\sigma_{Th} = \frac{8\pi r_0^2}{3}$, the Thomson cross section, and $U_B = \frac{B^2}{8\pi}$, the magnetic energy density[4].

Therefore, for a single electron in a magnetic field and randomly oriented, the radiation power is (Sari et al. 1998)

$$P(\gamma_e) = \frac{4\pi}{3}\sigma_{Th} c\Gamma^2 \gamma_e^2 \frac{B^2}{8\pi}, \quad \text{(B.24)}$$

with $\gamma_e \gg 1$. The peak spectral power is defined as $P_{\nu,max} \approx P(\gamma_e)/\nu_{\gamma_e}$, that is

$$P_{\nu,max} = \frac{m_e c^2 \sigma_{Th}}{3q_e}\Gamma B. \quad \text{(B.25)}$$

This definition is correct if electrons do not irradiate the majority of their energy (Sari et al. 1998); hence, $\gamma_e < \gamma_c$, with γ_c a critical value of the electron Lorentz factor derived by $P(\gamma_c)t = \Gamma\gamma_c m_e c^2$ and Eq. B.24:

$$\gamma_c = \frac{P(\gamma_c)t}{\Gamma m_e c^2}$$

$$= \frac{6\pi m_e c}{\sigma_{Th}\Gamma B^2 t}$$

$$= \frac{3m_e}{16\sigma_{Th} m_p c}\frac{1}{\Gamma^3 \epsilon_B n t}. \quad \text{(B.26)}$$

In a shock that evolves in a fully adiabatic way, its energy is constant and defined as (Blandford & McKee 1976; Eq. 1.3 in Sari 1997; Sari et al. 1998)

$$E = \frac{16}{17}\pi\Gamma^2 R^3 n m_p c^2. \quad \text{(B.27)}$$

If we simply consider $t \cong R/4\Gamma^2 c$ (Sari et al. 1998), we derive the expressions for the radius and the Lorentz factor of the shock in an adiabatic regime:

$$R(t) \cong \left(\frac{17Et}{4\pi m_p n c}\right)^{1/4} \quad \text{(B.28)}$$

$$\Gamma(t) \cong \left(\frac{17E}{1024\pi m_p n c^5 t^3}\right)^{1/8}. \quad \text{(B.29)}$$

[4]For an electron $\sigma_{Th} = 6.65 \times 10^{-25}$ cm^2, because its radius is $r_0 = \frac{e^2}{4\pi\epsilon_0 c^2 m_e} = 2.81\times^{-13}$ cm (e=1.60 C, m$_e$ = 9.1$\times$ MeV c^{-2}, $\epsilon_0 = 8.85 \times 10^{-12}$ C^2 m^{-2} N). The magnetic density for the terrestrial magnetic field is $U_\oplus = 1/32\pi$ G^2 ($B_\oplus = 0.5G$), instead for the Sun is $U_\odot = 1/8\pi$ G^2 ($B_\odot = 1G$).

Now, we have all the ingredients to derived three fundamental quantities for our discussion: the observed peak flux ($F_{\nu,max}$), the synchrotron frequency ($\nu_m \equiv \nu(\gamma_m)$) and the cooling frequency ($\nu_c \equiv \nu(\gamma_c)$). The observed peak flux is $F_{\nu,max} = N_e P_{\nu,max}/4\pi D^2$, with $N_e = 4\pi R^3 n/3$ the total number of swept-up electrons in the postshock fluid and D the distance of the source from the observer. Using Eq. B.25, B.3, B.28 and B.29, we obtain

$$F_{\nu,max} \propto \epsilon_B^{1/2} D^{-2} n^{1/2} E. \tag{B.30}$$

Substituting γ_e with γ_m in Eq. B.2 and using Eq. B.7, B.3, B.28 and B.29, we derive

$$\nu_m \propto E^{1/2} \epsilon_e^2 \epsilon_B^{1/2} n^{1/2} t^{3/2} \left(\frac{p-2}{p-1}\right). \tag{B.31}$$

Instead, substituting γ_e with γ_c in Eq. B.2 and using Eq. B.26, B.3, B.28 and B.29, we have

$$\nu_c \propto E^{-1/2} \epsilon_B^{-3/2} n^{-1} t^{-1/2}. \tag{B.32}$$

As said before, electrons have a power law distribution, cause to the first order Fermi acceleration (Longair 1994). The more energetic electrons obey to $\mathrm{d}E/\mathrm{d}t \propto \mathrm{d}\gamma/\mathrm{d}t$, then $N \propto \gamma^p$. Knowing that $\nu \propto \gamma^2$, we obtain $F_\nu \propto \nu^{-p/2}$. Less energetic electrons behave as single particles (Rybicki & Lightman 1979) and they cool less efficiently then more energetic electrons. In this case $F_\nu \propto \nu^{1/3}$. These two considerations are for both slow and fast cooling regimes. For the intermediate cases, the behavior of electrons is different in the two regimes: if $\nu_c < \nu < \nu_m$ (fast cooling regime), $F \propto \nu^{-p/2}$, instead if $\nu_m < \nu < \nu_c$ (slow cooling regime), $F_\nu \propto \nu^{-(p-1)/2}$. Therefore, the flux for an observer is (Sari et al. 1998):

- *Fast cooling* ($\gamma_m > \gamma_c$):

$$F_\nu = \begin{cases} \left(\frac{\nu}{\nu_c}\right)^{1/3} F_{\nu,max} & (\nu < \nu_c), \\ \left(\frac{\nu}{\nu_c}\right)^{-1/2} F_{\nu,max} & (\nu_c < \nu < \nu_m), \\ \left(\frac{\nu_m}{\nu_c}\right)^{-1/2} \left(\frac{\nu}{\nu_m}\right)^{-p/2} F_{\nu,max} & (\nu_m < \nu). \end{cases} \tag{B.33}$$

- *Slow cooling* ($\gamma_c > \gamma_m$):

$$F_\nu = \begin{cases} \left(\frac{\nu}{\nu_m}\right)^{1/3} F_{\nu,max} & (\nu < \nu_m), \\ \left(\frac{\nu}{\nu_m}\right)^{-(p-1)/2} F_{\nu,max} & (\nu_m < \nu < \nu_c), \\ \left(\frac{\nu_c}{\nu_m}\right)^{-(p-1)/2} \left(\frac{\nu}{\nu_c}\right)^{-p/2} F_{\nu,max} & (\nu_c < \nu). \end{cases} \tag{B.34}$$

Appendix C

The efficiency

In relation to the energetics of GRBs, it is important to consider their efficiency in converting the total initial energy in prompt γ-ray emission (Lloyd-Ronning & Zhang 2004; Fan & Piran 2006; Granot et al. 2006). The efficiency is defined as

$$\epsilon_\gamma = \frac{E_\gamma}{E_\gamma + E_{k,0}}, \tag{C.1}$$

where E_γ is the energy radiated in γ-rays and $E_{k,0}$ the initial kinetic energy, that is the percentage of the radiated energy. Many GRB light curves show a quasi-constant decay phase ("plateau") and this segment is generally interpreted as an additional injection of the energy into the outflow. In this case, the efficiency is

$$\epsilon_\gamma = \frac{E_\gamma}{E_\gamma + E_{k,0}} = \frac{f\ \tilde{\epsilon}_\gamma}{1 + (f-1)\tilde{\epsilon}_\gamma}, \tag{C.2}$$

where f is the parameter that takes into account of the energy injection (for example, for the energy injection at 10 h, $f = E_{k,10h}/E_{k,0}$, with $E_{k,10h}$ the kinetic energy at 10 h). $\tilde{\epsilon_\gamma}$ is the prompt efficiency without energy injection and it is defined as

$$\tilde{\epsilon_\gamma} = \frac{E_\gamma}{fE_{k,0} + E_\gamma} = \frac{E_\gamma}{E_{k,10h} + E_\gamma}. \tag{C.3}$$

In the standard fireball model (Sec. 1.3.1 and Appendix B), the fundamental equations of the flux and time dependent parameters are (Eq. B.30, B.31, B.32; Yost et al. 2003; Fan & Piran 2006):

$$F_{\nu,max} = 6.6\ mJy \left(\frac{1+z}{2}\right) D_{L,28.34} \epsilon_{B,-2}^{1/2} E_{k,53} n_0^{1/2}, \tag{C.4}$$

$$\nu_m = 7.6 \times 10^{11} Hz\ E_{k,53}^{1/2} \epsilon_{B,-2}^{1/2} \epsilon_{e,-1}^{2} C_p^2 \left(\frac{1+z}{2}\right)^{1/2} t_d^{-3/2}, \tag{C.5}$$

$$\nu_c = 1.4 \times 10^{15} Hz\ E_{k,53}^{-1/2} \epsilon_{B,-2}^{-3/2} n_0^{-1} \left(\frac{1+z}{2}\right)^{-1/2} t_d^{-1/2} \frac{1}{(1+Y)^2}. \tag{C.6}$$

$F_{\nu,max}$ is the observed peak flux at the distance D from the source, ν_m is the synchrotron frequency[1] and ν_c is the cooling frequency[2]. The quantities are expressed as

[1] The synchrotron frequency is $\nu(\gamma_e) = \Gamma \gamma_e^2 q_e B/(2\pi m_e c)$.

[2] $F_{\nu,max} = N_e P_{\nu,max}/4\pi D^2$ where $N_e 4\pi R^3 n/3$ is the total number of swept-up electrons in the post shock fluid, $P_{\nu,max} = m_e c^2 \sigma_{Th} \gamma B/(3q_e)$ is the peak spectral power. For details and Sari et al. (1998).

$Q_X = Q/10^X$in CGS units. z is the redshift, D_L is the luminosity distance, p is the power law index of the shocked electrons (in general[3], $p = 2.3$), E_k is the isotropic equivalent energy, ϵ_B is the magnetic energy fraction, ϵ_e is the electron energy fraction, $Cp = 13(p-2)/3(p-1)$, t_d is the observer time in day units. Sometimes an alternative mechanism is invoked in GRB models, the inverse Compton (IC): Y is the Compton parameter, that shows if the Compton cooling is efficient ($Y > 1$) or not ($Y < 1$). Here, $Y = (-1 + \sqrt{1 + 4(\epsilon_e/\epsilon_B)})/2$. If we consider the case for which the observed X-ray frequency (ν_X) is greater than ν_m and ν_c, it is known that for the standard fireball model (Eq. B.33; Sari et al. 1998) the observed flux is

$$\begin{aligned} F_\nu &= \left(\frac{\nu_m}{\nu_c}\right)^{-1/2} \left(\frac{\nu_X}{\nu_m}\right)^{-p/2} F_{\nu,max} \qquad \text{(C.7)} \\ &= 3.8\times10^{-4} mJy \left(\frac{1+z}{2}\right)^{(2+p)/4} D_{L,28.34}^{-2} \epsilon_{B,-2}^{(p-2)/4} \epsilon_{e,-1}^{p-1} E_{k,53}^{(p+2)/4} (1+Y)^{-1} t_d^{(2-3p)/4} \nu_{X,17}^{-p/2}. \end{aligned}$$

The observed flux in the XRT band ($[\nu_1, \nu_2] = [0.3, 10]$ keV) is done by

$$\begin{aligned} F &= \int_{\nu_1}^{\nu_2} F_\nu \, \mathrm{d}\nu_X \qquad \text{(C.8)} \\ &= 1.08\times10^{-12} erg\ s^{-1} cm^{-2} \left(\frac{1+z}{2}\right)^{(p+2)/4} D_{L,28.34}^{-2} \\ &\quad \times \epsilon_{B,-2}^{(p-2)/4} \epsilon_{e,-1}^{p-1} E_{k,53}^{(p+2)/4} (1+Y)^{-1} t_d^{(2-3p)/4}. \end{aligned}$$

So, the X-ray luminosity at 10 h (that is $t_d = 0.4$) is

$$\begin{aligned} L_X &= 4\pi D_L^2 F/(1+z) \qquad \text{(C.9)} \\ &= 9.98\times10^{45} erg\ s^{-1} cm^{-2} \left(\frac{1+z}{2}\right)^{(p+1)/4} \epsilon_{B,-2}^{(p-2)/4} \epsilon_{e,-1}^{p-1} (1+Y)^{-1} E_{k,53}^{(p+2)/4}, \end{aligned}$$

therefore

$$E_k = 1.02\times10^{53} \mathcal{R}\ L_{X,46}^{4/(p+2)} \left(\frac{1+z}{2}\right)^{(2-p)/(p+2)} \epsilon_{B,-2}^{-(p-2)/(p+2)} \epsilon_{e,-1}^{4(1-p)/(p+2)} (1+Y)^{4/(p+2)} \qquad \text{(C.10)}$$

with $\mathcal{R}$ a numerical factor that takes into account the energy radiation loss in a time interval and T_{90} is the duration of the burst[4]. The energy loss for the radiation process during the deceleration phase (Sari 1997) is $\mathrm{d}E/\mathrm{d}t = 4096\pi c^5 n m_p \Gamma^8 t^2 \epsilon_e$ with $\Gamma(t) = (1/4)(17E/\pi n m_p c^5 t^3)^{1/8}$, so we obtain[5]

$$\frac{\mathrm{d}E}{\mathrm{d}t} = \frac{17}{16}\frac{E}{t}\epsilon_e. \qquad \text{(C.11)}$$

Integrating this expression

$$\int_{E_{k,0}}^{E_{k,T}} \frac{\mathrm{d}E}{E} = \int_{T_{90}}^{T} \frac{17}{16}\epsilon_e \frac{\mathrm{d}t}{t}, \qquad \text{(C.12)}$$

[3]We have $N(\gamma_e) \sim \gamma_e^{-p}$ for $\gamma_e > \gamma_{e,min}$, $p > 2$ is required so that the energy does not diverge at large γ_e. $p \sim 2.2 - 2.3$ is derived from simulations and analytical considerations, starting from the particle acceleration in ultra-relativistic shocks (Vietri 2006).

[4]T_{90} is the time needed to accumulate from 5% to 95% of the counts in the 50keV - 300keV band (Piran 1999).

[5]Here the definition of $\Gamma(t)$ is different than Eq. B.29 because we are not in the adiabatic regime and so $t \cong R/16\Gamma^2 c$.

we obtain

$$\mathcal{R} = \frac{E_{k,T}}{E_{k,0}} = \left(\frac{T}{T_{90}}\right)^{(17/16)\epsilon_e} . \tag{C.13}$$

Since the aim of this discussion is to calculate the GRB efficiency, we calculate $E_{k,0}$ and $E_{k,10h}$, that appear in Eq. C.2 and C.3, putting in Eq. C.10 $\mathcal{R} = 1$ and $\mathcal{R} = (t_{10h}/T_{90})^{17\epsilon_e/16}$, respectively. If we know E_γ, we have the efficiency.

Appendix D

GRB XRT light-curves: glossary

This section provides the list of symbols used. As a general note: X-ray energies (fluences) were computed from the time of the *Swift*-XRT repointing up until the end of the observation; no temporal extrapolation was performed. The values reported assume isotropic emission. X-ray fluences and fluxes are reported in the 0.3-10 keV (observer-frame) energy band; energies, luminosities and intrinsic time scales are computed in the 0.3-30 keV (rest-frame) band.

- $\alpha_{\rm n}$: temporal slope of the normal decay phase. Type Ia: $\alpha_{\rm n} = \alpha_2$; type IIa: $\alpha_{\rm n} = \alpha_3$; type III: $\alpha_{\rm n} = \alpha_4$.
- $\alpha_{\rm st}$: temporal slope of the steep decay phase. Type Ib and IIa : $\alpha_{\rm st} = \alpha_1$; type IIb and III: $\alpha_{\rm st} = \alpha_2$ (see Fig. 2.1). The zero-time of the power-law decay is assumed to be the BAT trigger time (i. e. $t_0 = 0$).
- $\alpha_{\rm st}^{T90}$: temporal slope of the steep decay phase assuming $t_0 = T_{90}$.
- $\alpha_{\rm sh}$: temporal slope of the shallow decay (or plateau) phase. This corresponds to α_2 and α_3 for type IIa and type III light-curves, respectively.
- Γ_x: XRT 0.3-10 keV (observer frame) spectral photon index from this paper.
- $E_{\gamma,{\rm iso}}$: isotropic equivalent energy released during the prompt emission in the rest-frame $1 - 10^4$ keV energy band from Amati et al. (2008).
- $E_{\rm pk}$: rest-frame peak energy of the νF_ν spectrum during the prompt γ-ray emission from Amati et al. (2008).
- $F_{\rm f}$ ($L_{\rm f}$): flux (luminosity) at the end of the plateau (i.e. at $t = t_{\rm f}$).
- $F_{\rm i}$ ($L_{\rm i}$): flux (luminosity) at the beginning of the plateau (i.e. at $t = t_{\rm i}$).
- $L_{\rm pk,iso}$: $1 - 10^4$ keV (rest frame) isotropic peak luminosity during the prompt emission from Nava et al. (2008).
- $L_X^{11\rm h}$: luminosity at 11 hours rest-frame.
- $L_X^{10\rm min}$: luminosity at 10 min rest-frame.
- $\rm NH_{tot}$: total neutral hydrogen column density.
- $\rm NH_{HG}$: intrinsic neutral hydrogen column density at the redshift of the GRB.

- $S_{1,\mathrm{X}}$ ($E_{1,\mathrm{X}}$): fluence (energy) released during the first phase of the X-ray light-curve.Type Ib and IIa: $E_{1,\mathrm{X}} = E_1$; type IIb and III: $E_{1,\mathrm{X}} = E_1 + E_2$. Fluences follow the same definition scheme. E_1, E_2, E_3 and E_4 has been defined following Fig. 2.1.
- $S_{2,\mathrm{X}}$ ($E_{2,\mathrm{X}}$): fluence (energy) released during the second phase of the X-ray light-curve. Type Ia: $E_{2,\mathrm{X}} = E_1 + E_2$; type Ib: $E_{2,\mathrm{X}} = E_2$; type IIa: $E_{2,\mathrm{X}} = E_2 + E_3$; type IIb: $E_{2,\mathrm{X}} = E_3$; type III: $E_{2,\mathrm{X}} = E_2 + E_4$ (see Fig. 2.1). Same definition scheme for fluences.
- S_γ (E_γ^{15-150}): 15-150 keV (observer frame) fluence (energy) released during the prompt emission as calculated by Sakamoto et al. (2011).
- S_X ($E_{\mathrm{X,iso}}$): X-ray fluence (energy).
- S_X^FL (E_X^FL): X-ray fluence (energy) associated to flares. For each GRB, the total fluence (energy) released in X-rays reads: S_X^FL+S_X (E_X^FL+$E_{\mathrm{X,iso}}$).
- $S_{1,\mathrm{X}}^\mathrm{FL}$, $S_{2,\mathrm{X}}^\mathrm{FL}$ ($E_{1,\mathrm{X}}^\mathrm{FL}$, $E_{2,\mathrm{X}}^\mathrm{FL}$): X-ray fluence (energy) of flares superimposed on the first and second light-curve phase.
- t_f, t_f^RF, $t_\mathrm{f}^\mathrm{T90}$: end time of the plateau phase: observer frame, rest frame and in T_{90} units. This parameter corresponds to t_{b2} and t_{b3} for type IIa and type III light-curve, respectively.
- t_i, t_i^RF, $t_\mathrm{i}^\mathrm{T90}$: start time of the plateau phase: observer frame, rest frame and in T_{90} units. This parameter corresponds to t_{b1} and t_{b2} for type IIa and type III light-curve, respectively.
- Δt: plateau duration defined as $t_\mathrm{f} - t_\mathrm{i}$.
- T_{90}, T_{90}^RF: duration of the 15-150 keV prompt emission from Sakamoto et al. (2011), in the observer and in the rest-frame, respectively.

Appendix E

The optical light-curves: tables and figures

In this Section it is possible to retrieve:

- the factors to convert magnitudes into flux densities (Table E.1);
- the examples of the online tables of CDS: the optical LC fit parameters (from Tables E.2 to E.6); the parameters of the optical/X-ray SEDs fitted with a single power-law (Tables E.7- E.8) and with a broken power-law (Tables E.9, E.10); the X-ray spectrum fit parameters (Table E.11); redshifts and luminosity distances of the GRBs in our sample (Table E.12); the optical data used for the SEDs (Table E.13);
- the result of the F-test over the optical/X-ray SEDs to choose the better fit function (Table E.14);
- the result of the fit of the optical LCs plotted in Figures E.1-E.7 (Table E.13);
- the results of the fit of the SEDs. Only the SEDs selected in Table E.14 are presented (Tables E.18- E.19);
- the sample of the 165 GRBs with known redshift from which we started the data selection, with references to papers and GCNs where there are optical data (Table E.20);
- plots of the optical and X-ray LCs for the GRBs in our sample (Figures E.1-E.7);
- plots of the optical/X-ray SEDs (Figures E.8-E.15).

Table E.1: Conversion factors used to convert magnitude into flux density (Jy). Reference: (1) http://www.ipac.caltech.edu/2mass/releases/allsky/faq.html#jansky; (2) UVOT calibration files; (3) Fukugita et al. (1995); (4) http://svo.cab.inta-csic.es/; (5) Schneider et al. (1983).

Filter	λ_c (Å)	FWHM (Å)	F_0 (Jy)	Reference
J	12350	1620	1594	(1)
H	16620	2510	1024	(1)
KS	21590	2620	666.7	(1)
v	5468	769	3647	(2)
b	4392	975	4058	(2)
u	3465	785	1423	(2)
uvw1	2600	693	901	(2)
uvm2	2246	493	767	(2)
uvw2	1928	657	716	(2)
white	3850	2600	1732	(2)
U_J	3652	526	1890	(3)
B_J	4448	1008	4020	(3)
V_J	5505	827	3590	(3)
R_C	6588	1568	3020	(3)
I_C	8060	1542	2380	(3)
u'	3585	556	1568.5	(4)
g'	4858	1297	3965.9	(4)
r'	6290	1358	3162.0	(4)
i'	7706	1547	2602.0	(4)
z'	9222	1530	2244.7	(4)
g_{Gunn}	5200	1400	3730	(5)
r_{Gunn}	6700	1400	4490	(5)
i_{Gunn}	7900	1600	4760.	(5)
z_{Gunn}	9100	1300	4810	(5)
U_{Bessel}	3605.1	3031	1803.1	(4)
B_{Bessel}	4400.0	3701	4000.0	(4)
V_{Bessel}	5512.1	4733	3579.8	(4)
R_{Bessel}	6585.9	5504	2971.4	(4)
I_{Bessel}	8059.9	7042	2405.3	(4)

Table E.2: **GRB**: GRB name. **Fil**: filter name. **Fit**: fitting function. 0: $f(t) = N_1 t^{-\alpha_1}$; 1: $f(t) = N_1((t/t_{br,1})^{-\alpha_1/s_1} + (t/t_{br,2})^{-\alpha_2/s_1})^{s_1}$; 2: $f(t) = N_1((t/t_{br,1})^{-\alpha_1/s_1} + (t/t_{br,2})^{-\alpha_2/s_1})^{s_1} + N_2((t/t_{br,3})^{-\alpha_3/s_2} + (t/t_{br,4})^{-\alpha_4/s_2})^{s_2}$; 4: $f(t) = N_1((t/t_{br,1})^{-\alpha_1/s_1} + (t/t_{br,2})^{-\alpha_2/s_1})^{s_1} + N_2(t)^{-\alpha_3}$; 6: $f(t) = N_1((t/t_{br,1})^{-\alpha_1/s_1} + (t/t_{br,2})^{-\alpha_2/s_1})^{s_1} + N_2(t)^{-\alpha_3}$; 8: $f(t) = N_1((t/t_{br,1})^{-\alpha_1/s_1} + (t/t_{br,2})^{-\alpha_2/s_1})^{s_1} + N_2((t/t_{br,3})^{-\alpha_3/s_2} + (t/t_{br,4})^{-\alpha_4/s_2})^{s_2} + N_3((t/t_{br,5})^{-\alpha_5/s_3} + (t/t_{br,6})^{-\alpha_6/s_3})^{s_3}$; 9: $f(t) = N_1((t/t_{br,1})^{-\alpha_1/s_1} + (t/t_{br,2})^{-\alpha_2/s_1})^{s_1} + N_2((t/t_{br,3})^{-\alpha_3/s_2} + (t/t_{br,4})^{-\alpha_4/s_2})^{s_2} + N_3(t)^{-\alpha_5}$. **Ok**: '1' denotes the data used for the comparison with the X-ray data and plotted in Figures E.1-E.4 (*Online Material*). **Tmin (Tmax)**: initial (end) time of the observations in rest frame (s). $\mathbf{t_{br}}$, $\sigma(\mathbf{t_{br}})$: trigger times with relative errors (s). α, $\sigma(\alpha)$: slopes with relative errors. **s**: smoothness parameters. **N**, σ**N**: normalization with relative error (mJy). χ^2: chi-square. **DOF**: degree of freedom. **pval**: p_value. A "-9" indicates that the light-curve does not show such phase and the value of that parameter is therefore absent.This table is available in its entirety in a machine-readable form at the CDS (table1.dat, ReadMe). A portion is shown here for guidance.

GRB	Fil	Fit	ok	Tmin	Tmax	$t_{br,1}$	$\sigma(t_{br,1})$	$t_{br,2}$	$\sigma(t_{br,2})$
050319	b	0	0	243.0	28491.0	-9.0	-9.0	-9.0	-9.0
050319	v	0	0	259.1	767337.7	-9.0	-9.0	-9.0	-9.0
050319	BJ	0	0	5203.9	57196.8	-9.0	-9.0	-9.0	-9.0
050319	VJ	0	0	6944.0	400550.4	-9.0	-9.0	-9.0	-9.0
050319	RC	2	1	40.3	994118.4	157243.4	19520.9	482.5	30.1

Table E.3: Continued from Table E.2.

$t_{br,3}$	$\sigma(t_{br,3})$	$\alpha 1$	$\sigma(\alpha_1)$	α_2	$\sigma(\alpha_2)$	α_3	$\sigma(\alpha_3)$
-9.0	-9.0	7.040e-01	7.955e-02	-9.000e+00	-9.000e+00	-9.000e+00	-9.000e+00
-9.0	-9.0	6.618e-01	2.600e-02	-9.000e+00	-9.000e+00	-9.000e+00	-9.000e+00
-9.0	-9.0	4.112e-01	4.117e-02	-9.000e+00	-9.000e+00	-9.000e+00	-9.000e+00
-9.0	-9.0	6.905e-01	1.928e-02	-9.000e+00	-9.000e+00	-9.000e+00	-9.000e+00
-9.0	-9.0	4.457e-01	1.429e-02	1.559e+00	1.039e-01	2.520e+00	2.744e-01

Table E.4: Continued from Table E.3.

α_4	$\sigma(\alpha_4)$	α_5	α_5	$\sigma(\alpha_5)$	α_6
$\sigma(\alpha_6)$					
-9.000e+00	-9.000e+00	-9.000e+00	-9.000e+00	-9.000e+00	-9.000e+00
-9.000e+00	-9.000e+00	-9.000e+00	-9.000e+00	-9.000e+00	-9.000e+00
-9.000e+00	-9.000e+00	-9.000e+00	-9.000e+00	-9.000e+00	-9.000e+00
-9.000e+00	-9.000e+00	-9.000e+00	-9.000e+00	-9.000e+00	-9.000e+00
1.240e-01	7.844e-02	-9.000e+00	-9.000e+00	-9.000e+00	-9.000e+00

Table E.5: Continued from Table E.4.

s_1	s_2	s_3	N_1	$\sigma(N_1)$	N_2	$\sigma(N_2)$
-9.0	-9.0	-9.0	1.107515e-02	6.496899e-03	-9.000000e+00	-9.000000e+00
-9.0	-9.0	-9.0	1.747728e-02	3.708279e-03	-9.000000e+00	-9.000000e+00
-9.0	-9.0	-9.0	8.883478e-04	3.640030e-04	-9.000000e+00	-9.000000e+00
-9.0	-9.0	-9.0	2.510829e-02	4.822976e-03	-9.000000e+00	-9.000000e+00
-0.5	-0.5	-9.0	1.446221e-05	1.248363e-06	2.000459e-04	0.000000e+00

Table E.6: Continued from Table E.5.

N_3	$\sigma(N_3)$	χ^2	DOF	p_val
-9.000000e+00	-9.000000e+00	8.40	7.00	2.985e-01
-9.000000e+00	-9.000000e+00	37.76	19.00	6.367e-03
-9.000000e+00	-9.000000e+00	18.59	10.00	4.578e-02
-9.000000e+00	-9.000000e+00	85.86	18.00	7.473e-06
-9.000000e+00	-9.000000e+00	203.49	64.00	-3.484e-07

Table E.7: Parameters of the optical/X-ray SEDs fitted with a single power-law. **GRB**: GRB name. **Host**: the chosen extinction law; Milky Way (MW), Large Magellanic Cloud (LMC), Small Magellanic Cloud (SMC). **Part**: X-ray LC part considered; "S" steep decay, "P" plateau, "N" normal decay. $\beta_{\mathbf{op,X}}$, $\sigma(\beta_{\mathbf{op,X}})$: spectral index with error. **NH**, σ(**NH**): hydrogen column density with relative error (10^{22} cm^{-2}). **E(B-V)**, σ**(E(B-V))**: optical absorption with relative error (mag). **N**, σ**(N)**: normalization with error (mJy). $\chi^{\mathbf{2}}$: chi-square. **DOF**: degree of freedom. **pval**: p_value. $\mathbf{T_i}$, $\mathbf{T_f}$: initial (end) time of the interval of the SED in observer time (s). **ok**: "1" if the best fitting function is a power-law, otherwise "0". This table is available in its entirety in a machine-readable form at the CDS (table2.dat, ReadMe). A portion is shown here for guidance.

GRB	Host	Part	$\beta_{op,X}$	$\sigma(\beta_{op,X})$	NH	$\sigma(NH)$	E(B-V)	σ(E(B-V))	N	$\sigma(N)$
050319	MW	P	0.755	0.020	-0.269	0.184	0.082	0.019	0.215	0.025
050319	MW	N	0.945	0.026	-0.204	0.420	0.030	0.025	0.006	0.001
050401	MW	P	0.873	0.075	1.840	0.322	0.667	0.082	1.830	0.851
050408	SMC	N	0.679	0.016	0.632	0.337	0.247	0.007	0.012	0.000
050416A	LMC	P	0.627	0.015	0.307	0.086	0.232	0.041	0.054	0.005

Table E.8: Continued from Table E.7.

χ^2	DOF	pval	T_i	T_f	ok
9.976e+01	42	1.340e-06	300.	1500.	0
7.258e+01	10	3.190e-07	17000.	300000.	0
3.331e+01	146	1.000e+00	200.	2000.	1
2.273e+01	28	7.470e-01	20000.	40000.	0
2.702e+01	24	3.040e-01	700.	2000.	0

Table E.9: Parameters of the optical/X-ray SEDs fitted with a broken power-law. **GRB**: GRB name. **Host**: galaxy chosen as model to fit the SED; Milky Way (MW), Large Magellanic Cloud (LMC), Small Magellanic Cloud (SMC). **Part**: X-ray LC part considered; "S" steep decay, "P" plateau, "N" normal decay. $\beta_{\mathbf{op}}$, $\sigma(\beta_{\mathbf{op}})$: optical spectral index with error. $\beta_{\mathbf{X}}$, $\sigma(\beta_{\mathbf{X}})$: X-ray spectral index with error. ν, $\sigma(\nu)$: observer frame break frequency (10^{15} Hz). **NH**, σ(**NH**): hydrogen column density with relative error (10^{22} cm^{-2}). **E(B-V)**, σ**(E(B-V))**: optical absorption with relative error (mag). **N**, σ**(N)**: normalization with error (mJy). $\chi^{\mathbf{2}}$: chi-square. **DOF**: degree of freedom. **pval**: p_value. $\mathbf{T_i}$, $\mathbf{T_f}$: initial (end) time of the interval of the SED in observer time (s). **ok**: "1" if the best fitting function is a broken power-law, otherwise "0". This table is available in its entirety in a machine-readable form at the CDS (table3.dat, ReadMe). A portion is shown here for guidance.

GRB	Host	Part	β_{op}	$\sigma(\beta_{op})$	β_X	$\sigma(\beta_X)$	ν_{br}	$\sigma(\nu_{br})$	NH	σ(NH)
050319	MW	P	0.358	0.000	0.858	0.077	1.271	1.198	-0.030	0.283
050319	MW	N	0.607	0.000	1.107	0.045	0.545	0.118	0.114	0.437
050401	SMC	P	0.372	0.000	0.872	0.146	0.455	87.600	1.850	2.540
050408	LMC	N	0.342	0.000	1.210	0.310	22.350	26.190	1.560	0.690
050416A	SMC	P	0.619	0.000	0.951	0.156	339.900	131.310	0.398	0.097

Table E.10: Continued from Table E.9.

E(B-V)	σ(E(B-V))	N	$\sigma(N)$	χ^2	DOF	pval	T_i	T_f	ok
0.103	0.022	0.327	0.048	4.050e+01	40	4.467e-01	300.000	1500.000	1
0.165	0.034	0.021	0.005	4.050e+01	9	3.770e-05	17000.000	300000.000	1
0.462	10.500	2.700	263.000	2.050e+02	145	7.460e-04	200.000	2000.000	0
0.290	0.000	0.020	0.001	2.654e+01	27	4.885e-01	20000.000	40000.000	1
0.321	0.044	0.060	0.005	1.890e+01	23	7.059e-01	700.000	2000.000	1

Table E.11: Parameters of the fit of the X-ray spectrum. **GRB**: GRB name. **N**, σ(N): normalization with error (keV). β, $\sigma(\beta)$: spectral index. **NH**, σ**(NH)**: hydrogen column density with error (10^{22} cm^{-2}). $\mathbf{T_i}$, $\mathbf{T_f}$: initial (end) time of the interval of the SED in observer time (s). This table is available in its entirety in a machine-readable form at the CDS (table4.dat, ReadMe). A portion is shown here for guidance.

GRB	N	$\sigma(N)$	β	$\sigma(\beta)$	NH	σ(NH)	T_i	T_f
050319	0.365	0.170	0.857	0.077	-0.005	0.284	300.000	1500.000
050319	0.006	0.009	0.941	0.246	-0.310	0.823	17000.000	300000.000
050401	1.719	0.790	0.864	0.075	2.000	0.334	200.000	2000.000
050408	0.345	0.686	1.200	0.314	1.620	0.692	20000.000	40000.000
050416A	1.159	1.082	1.104	0.146	0.791	0.168	700.000	2000.000

Table E.12: Some useful information of GRBs in our sample. **GRB**: GRB name. **z**: redshift. **DL**: luminosity distance (Gpc). Redshifts and luminosity distances are from M13. This table is available in its entirety in a machine-readable form at the CDS (table5.dat, ReadMe). A portion is shown here for guidance.

GRB	z	DL
050319	3.240	28.369
050401	2.900	24.806
050408	1.236	8.644
050416A	0.653	3.913
050525A	0.606	3.567

Table E.13: Optical data used in the SED. **GRB**: GRB name. **Fil**: filter. λ_c: central wavelength of the filter ($\mathring{A}$). **FWHM**: full width half maximum of the filter ($\mathring{A}$). **F**, σ**(F)**: flux with error (mJy). This table is available in its entirety in a machine-readable form at the CDS (table6.dat, ReadMe). A portion is shown here for guidance.

GRB	Filter	λ_c	FWHM	F	σ(F)
050319	b	4392	975	1.029e-01	1.229e-02
050319	v	5468	769	2.144e-01	1.297e-02
050319	RC	6588	1568	2.184e-01	3.237e-03
050319	CR	6588	1568	2.901e-01	8.830e-03
050319	v	5468	769	8.072e-03	8.283e-04

Table E.14: Result of the F-test over the optical/X-ray SEDs. *GRB*: GRB name. h_{PL}: extinction curve type used to fit the data with a power-law. h_{BR}: host galaxy type used to fit the data with a broken power-law. *Part*: segment of the X-ray LC considered: S=steep decay, P=plateau, N=normal decay. t_{start} and t_{end}: initial and final time of the SED. χ^2_{PL}, DOF$_{PL}$, $p-val_{PL}$: χ^2, degree of freedom and p-value for the power-law fit function. χ^2_{BR}, DOF$_{BR}$, $p-val_{BR}$: χ^2, degree of freedom and p-value for the broken power-law fit function. *PROB*: the F-test probability computed for each SED to comapre the single and broken power-law. *PL* = power-law, *BR* = broken power-law: √ indicates the best fit model. ⋆ indicates the cases for which we decided that the simple power-law fits better the SED than the broken power-law fit, regardless of the F-test. (*a*) We could not perform the fit with a broken power-law function.

GRB	h_{PL}	h_{BR}	Part	t_{start}	t_{end}	χ^2_{PL}	DOF$_{PL}$	p-val$_{PL}$	χ^2_{BR}	DOF$_{BR}$	p-val$_{BR}$	PROB	PL	BR
050319	MW	MW	P	300	1500	99.76	42.	1.3e-06	40.50	40.	0.45	7.01e-20	-	√
050319	MW	MW	N	17e+03	300e+03	72.58	10.	3.2e-07	40.50	9.	3.8e-05	0.00342	-	√
050401	MW	SMC	P	200	2000	33.31	146.	1.0	205.00	145.	0.00075	-9.00	√	-
050408	SMC	SMC	N	20e+03	40e+03	22.73	28.	0.75	20.00	37.	0.83	0.00	-	√
050416A	LMC	SMC	P	700	2000	27.02	24.	0.30	18.90	23.	0.71	2.98e-07	-	√
050416A	SMC	MW	N	6000	40e+03	29.54	27.	0.34	22.40	26.	0.66	3.51e-07	-	√
050525A	SMC	SMC	N	6000	30e+03	49.56	29.	0.010	51.70	28.	0.0041	-9.00	√	-
050730	SMC	SMC	P	4000	6000	759.74	140.	-8.6e-07	16200.00	139.	-0.0036	-9.00	√	-
050730	SMC	LMC	N	10e+03	30e+03	206.32	119.	4.8e-07	117.00	118.	0.52	1.39e-82	-	√
050820A	MW	MW	P	100	140	10.76	67.	1.0	7810.00	66.	0.037	-9.00	√	-
050820A	LMC	SMC	N	10e+03	60e+03	202.66	225.	0.85	171.00	224.	1.0	2.06e-118	-	√
050824⋆	SMC	SMC	P	6500	30e+03	27.64	31.	0.64	20.07	29.	0.89	7.32e-06	√	-
050824	MW	LMC	N	500e+03	2000e+03	37.65	34.	0.31	1190.00	33.	0.0040	-9.00	√	-
050904	MW	MW	S	600	1800	46.06	55.	0.80	92.28	54.	0.00091	-9.00	√	-
050904	MW	MW	P	12e+03	90e+03	105.41	146.	0.99	105.00	145.	0.99	1.00	√	-
050908	MW	SMC	N	1000	20e+03	9.07	16.	0.91	479.00	15.	0.017	-9.00	√	-
050922C	MW	MW	P	200	400	10.59	38.	1.0	10.60	37.	1.0	-9.00	√	-
050922C	SMC	LMC	N	10e+03	80e+03	66.73	68.	0.52	44.00	67.	0.99	2.69e-34	-	√
051109A	MW	MW	N	10e+03	700e+03	77.08	100.	0.96	77.00	99.	0.95	1.00	√	-
051111	SMC	SMC	N	6000	30e+03	13.79	19.	0.80	11.80	18.	0.86	0.0113	-	√
060124	LMC	MW	N	100e+03	150e+03	45.85	26.	0.0095	101.00	25.	1.3e-06	-9.00	√	-
060206	MW	SMC	N	35e+03	1000e+03	41.47	19.	0.0021	70.70	18.	4.3e-06	-9.00	√	-
060210	MW	SMC	P	1000	7000	69.92	87.	0.91	69.50	86.	0.90	0.999	√	-
060418	SMC	SMC	P	630	970	235.11	33.	4.4e-07	199.00	32.	4.5e-07	1.42e-06	-	√
060502A	LMC	MW	P	3600	10700	24.60	25.	0.48	21.60	24.	0.60	0.00217	-	√
060512	SMC	MW	P	2000	30e+03	45.00	42.	0.35	923.00	41.	4.0e-05	-9.00	√	-
060526	MW	SMC	S	100	150	5.00	41.	1.0	40.80	40.	0.43	-9.00	√	-
060526	SMC	SMC	P	1000	8000	14.23	19.	0.77	757.00	18.	0.022	-9.00	√	-
060526	MW	MW	N	30e+03	200e+03	134.25	28.	9.9e-07	78.70	26.	1.3e-06	1.09e-07	-	√
060605	MW	MW	P	200	400	40.04	30.	0.10	212.00	29.	7.3e-07	-9.00	√	-
060605	MW	LMC	P	4000	6300	21.07	31.	0.91	38.50	30.	0.14	-9.00	√	-
060607A	MW	MW	S	80	160	12.42	51.	1.0	1640.00	50.	0.00034	-9.00	√	-
060607A	MW	LMC	P	1500	2200	112.55	47.	1.6e-07	114.00	46.	-4.2e-09	-9.00	√	-
060607A	MW	SMC	P	5000	8000	113.03	111.	0.43	80.60	110.	0.98	1.12e-60	-	√
060614	MW	MW	P	6000	30e+03	68.42	57.	0.14	52.30	56.	0.61	3.75e-21	-	√
060614	LMC	LMC	N	80e+03	200e+03	39.84	40.	0.48	36.00	39.	0.61	9.69e-06	-	√
060729	SMC	SMC	P	1000	10e+03	67.03	68.	0.51	53.90	67.	0.88	3.17e-24	-	√
060729	SMC	SMC	P	10e+03	30e+03	160.39	124.	0.015	167.00	123.	0.0049	-9.00	√	-

Table E.14: Continued.

GRB	h_{PL}	h_{BR}	Part	t_{start}	t_{end}	χ^2_{PL}	DOF_{PL}	p-val$_{PL}$	χ^2_{BR}	DOF_{BR}	p-val$_{BR}$	PROB	PL	BR
060729	SMC	SMC	N	100e+03	500e+03	206.59	192.	0.22	203.00	191.	0.26	1.60e-16	-	√
060904B	MW	MW	P	100	310	74.71	320.	1.0	76.00	319.	1.0	-9.00	√	-
060904B	MW	MW	N	10e+03	100e+03	42.60	65.	0.99	42.50	64.	0.98	1.00	√	-
060906	SMC	LMC	P	1000	6000	30.09	29.	0.41	28.78	28.	0.42	0.258	√	-
060906	SMC	SMC	P	7000	12000	12.62	20.	0.89	10.40	19.	0.94	0.00177	-	√
060908	SMC	MW	P	100	550	23.41	32.	0.86	3860.00	31.	0.17	-9.00	√	-
060908	SMC	MW	N	700	8000	26.43	33.	0.78	31.89	32.	0.47	-9.00	√	-
060912A	MW	MW	N	1300	7000	45.40	39.	0.22	45.30	38.	0.19	1.00	√	-
060912A	SMC	MW	N	250	800	38.04	55.	0.96	36.90	54.	0.96	0.0313	-	√
060927	MW	SMC	P	1000	2000	38.11	58.	0.98	60.87	57.	0.34	-9.00	√	-
061007	MW	MW	N	350	2000	713.51	309.	-1.9e-06	14800.00	308.	-1.9e-06	-9.00	√	-
061007	MW	MW	N	2200	75500	44.88	75.	1.0	37.20	74.	1.0	1.27e-25	-	√
061121	MW	MW	P	640	1400	80.72	77.	0.36	80.60	76.	0.34	1.00	√	-
061121	SMC	MW	S	110	210	27.52	117.	1.0	27.50	116.	1.0	1.00	√	-
061121[a]	LMC	-999.	P	10e+03	100e+03	168.09	132.	0.018	-999.00	-999.	-1.0e+03	-999.	√	-
061126	LMC	SMC	N	2000	4000	143.50	119.	0.063	148.00	118.	0.031	-9.00	√	-
061126	MW	LMC	N	10e+03	100e+03	71.77	76.	0.62	47.30	75.	0.99	6.19e-40	-	√
070125	MW	LMC	N	150e+03	300e+03	1275.52	48.	3.3e-05	64280.00	47.	0.40	-9.00	√	-
070208	MW	LMC	N	2300	2400	101.97	81.	0.058	93.50	80.	0.14	8.25e-17	-	√
070318⋆	MW	MW	N	100	200	16.11	52.	1.0	14.50	51.	1.0	2.48e-09	√	-
070318	MW	LMC	N	200	400	22.29	113.	1.0	22.20	100.	1.0	1.00	√	-
070318	MW	SMC	N	1000	10e+03	36.59	46.	0.84	1307.00	45.	-7.0e-05	-9.00	√	-
070318	MW	SMC	N	100e+03	200e+03	22.04	26.	0.69	22.00	25.	0.64	1.00	√	-
070411	MW	MW	N	550	1000	18.51	28.	0.91	2910.00	27.	0.15	-9.00	√	-
070411	MW	SMC	N	2000	5000	18.51	28.	0.91	18.50	27.	0.89	1.00	√	-
070419A	MW	MW	S	300	500	20.71	32.	0.94	365.00	31.	8.7e-07	-9.00	√	-
070529	MW	MW	P	200	900	17.00	21.	0.71	17.00	20.	0.65	-9.00	√	-
070529	MW	MW	N	10e+03	100e+03	8.00	18.	0.98	528.00	17.	-0.012	-9.00	√	-
070802	MW	SMC	P	2000	3000	28.67	13.	0.0073	115.00	12.	2.3e-05	-9.00	√	-
071003	MW	SMC	N	25e+03	700e+03	39.54	42.	0.58	358.00	41.	1.8e-08	-9.00	√	-
071010A	LMC	LMC	N	70e+03	220e+03	102.70	29.	8.5e-07	124.00	28.	8.5e-07	-9.00	√	-
071025	SMC	MW	P	250	390	40.15	107.	1.0	133.00	100.	0.039	-9.00	√	-
071025	MW	MW	P	3600	15e+03	101.58	65.	0.0025	50.60	64.	0.28	3.84e-41	-	√
071031	SMC	SMC	S	770	1100	100.38	78.	0.045	78.30	80.	0.44	0.00	-	√
071031	LMC	SMC	P	7000	20e+03	398.65	11.	-0.073	24290.00	10.	1.0	-9.00	√	-
071112C⋆	MW	LMC	P	400	1000	38.06	49.	0.87	36.10	48.	0.90	0.000583	√	-
080310⋆	SMC	MW	U	450	700	177.37	208.	0.94	93.80	207.	1.0	5.01e-175	√	-
080310	SMC	SMC	P	1300	7000	14.24	20.	0.82	14.20	19.	0.77	1.00	√	-
080310	SMC	SMC	N	20e+03	90e+03	29.79	25.	0.23	29.30	24.	0.21	0.986	√	-
080319B	MW	LMC	U	400	600	587.12	429.	-2.1e-06	341.00	428.	1.0	0.00	-	√
080319B	SMC	SMC	S	5000	20e+03	10033.85	210.	-1.3e-06	3492.00	209.	-1.3e-06	1.31e-210	-	√
080319B	SMC	SMC	P	115e+03	400e+03	108.47	84.	0.037	66.84	83.	0.90	6.08e-49	-	√
080319B	MW	MW	N	1000e+03	2000e+03	19.68	18.	0.35	16.10	17.	0.52	0.00425	-	√
080330	SMC	SMC	P	250	800	263.20	57.	-2.7e-07	69.80	56.	0.10	1.06e-46	-	√
080413B	SMC	SMC	P	200	500	146.49	63.	-3.2e-07	57.10	62.	0.65	2.75e-45	-	√
080413B	MW	MW	P	1000	2000	474.77	49.	-1.5e-07	126.00	48.	-1.4e-07	1.08e-38	-	√
080413B	MW	MW	N	100e+03	400e+03	89.23	41.	2.0e-05	33.60	40.	0.75	1.29e-26	-	√
080603A	SMC	SMC	N	10500	20900	51.41	55.	0.61	35.10	53.	0.97	9.29e-17	-	√
080607	LMC	SMC	S	100	200	228.45	318.	1.0	253.00	317.	1.0	-9.00	√	-

Table E.14: Continued.

GRB	h_{PL}	h_{BR}	Part	t_{start}	t_{end}	χ^2_{PL}	DOF_{PL}	p-val_{PL}	χ^2_{BR}	DOF_{BR}	p-val_{BR}	PROB	PL	BR
080607	MW	LMC	S	300	550	52.41	65.	0.87	231.93	64.	-3.4e-07	-9.00	√	-
080607	MW	SMC	P	600	1000	145.34	44.	-4.3e-08	230.00	43.	-3.7e-08	-9.00	√	-
080607	LMC	LMC	N	4000	7000	62.57	37.	0.0054	46.20	36.	0.12	3.91e-12	-	√
080710⋆	MW	MW	P	3200	5500	839.85	67.	-3.7e-07	721.00	66.	-3.6e-07	7.23e-19	√	-
080710	MW	MW	N	9000	11500	77.13	44.	0.0015	182.00	43.	-3.7e-08	-9.00	√	-
080721	LMC	MW	P	450	1000	70.33	272.	1.0	5227.00	271.	-1.7e-06	-9.00	√	-
080721	SMC	SMC	N	40e+03	60e+03	27.93	30.	0.57	47.95	29.	0.015	-9.00	√	-
080810⋆	LMC	MW	S	100	135	50.95	71.	0.96	31.40	70.	1.0	4.38e-39	√	-
080810	MW	MW	P	210	300	16.66	69.	1.0	4360.00	68.	-0.00090	-9.00	√	-
080810	MW	SMC	P	3900	5000	38.30	34.	0.28	38.30	33.	0.24	1.00	√	-
080810	MW	MW	N	10e+03	100e+03	22.07	24.	0.57	20.79	23.	0.59	0.206	√	-
080913	LMC	SMC	N	600	1200	20.33	35.	0.98	20.30	34.	0.97	1.00	√	-
080913	SMC	LMC	N	10e+03	100e+03	15.43	17.	0.56	17.40	15.	0.29	-9.00	√	-
080913	MW	SMC	N	100e+03	700e+03	6.86	14.	0.94	6.85	12.	0.87	1.00	√	-
080928	MW	MW	S	430	500	4.34	19.	1.0	4.12	18.	1.0	0.543	√	-
080928	SMC	SMC	P	5000	6500	78.75	25.	1.7e-06	75.60	24.	1.9e-06	0.501	√	-
080928(a)	SMC	-999.	N	10e+03	13e+03	80.40	78.	0.40	-999.00	-999.	-1.0e+03	-999.	√	-
081008⋆	SMC	LMC	S	102	150	253.00	129.	-7.9e-07	78.70	128.	1.0	7.23e-121	√	-
081008⋆	LMC	SMC	P	1000	1500	82.42	60.	0.029	78.60	59.	0.045	3.88e-05	√	-
081008	MW	SMC	N	15e+03	21e+03	5277.01	24.	0.29	5007.78	23.	0.27	0.307	√	-
081029	MW	LMC	P	3000	5000	4722.30	88.	0.00034	59600.00	87.	0.24	-9.00	-	√
081029	MW	MW	P	8000	18e+03	12394.42	34.	0.31	150000.00	33.	0.94	-9.00	-	√
081029⋆	MW	MW	N	20e+03	80e+03	164.57	70.	-3.9e-07	143.00	69.	-5.0e-09	4.36e-19	√	-
081203A	LMC	MW	P	250	400	40.98	90.	1.0	2470.00	89.	-2.6e-07	-9.00	√	-
081203A	MW	MW	P	4000	6000	48.71	46.	0.36	32.50	45.	0.92	1.11e-19	-	√
081203A	MW	SMC	N	15e+03	25e+03	29.01	27.	0.36	27.20	26.	0.40	0.0823	√	-
090102	MW	MW	N	400	600	12.21	52.	1.0	8.33	51.	1.0	1.24e-22	-	√
090102	MW	LMC	N	10e+03	11e+03	971.94	43.	5.8e-05	1440.00	42.	0.0013	-9.00	√	-
090313	LMC	MW	P	25e+03	45e+03	30.57	24.	0.17	32.36	23.	0.093	-9.00	√	-
090313	LMC	SMC	N	70e+03	450e+03	36.39	52.	0.95	33.10	51.	0.98	1.83e-08	-	√
090424	MW	MW	N	90e+03	200e+03	22.80	18.	0.20	25.36	17.	0.087	-9.00	√	-
090426	SMC	SMC	N	200	250	45.65	50.	0.65	45.80	49.	0.60	-9.00	√	-
090426	MW	MW	N	5000	5500	41.86	50.	0.79	41.80	49.	0.76	1.00	√	-
090618	SMC	-999.	N	150	250	113.04	446.	1.0	-999.00	-999.	-1.0e+03	-999.	√	-
090618	MW	LMC	P	6000	20e+03	677.70	258.	-1.6e-06	692.39	257.	-1.6e-06	-9.00	√	-
090618	MW	LMC	N	100e+03	200e+03	126.18	22.	2.5e-06	2487.29	21.	-0.69	-9.00	√	-
090618	SMC	MW	N	700e+03	2500e+03	12.25	12.	0.43	203.57	11.	0.0037	-9.00	√	-
090926A	MW	MW	N	50e+03	60e+03	30.67	38.	0.80	407.00	37.	1.6e-07	-9.00	√	-
090926A⋆	SMC	MW	N	75e+03	85e+03	320.61	33.	4.4e-07	292.00	32.	4.5e-07	0.000843	√	-
090926A	MW	SMC	N	160e+03	170e+03	442.39	15.	0.021	426.00	14.	0.022	0.877	√	-
090926A	SMC	SMC	N	300e+03	350e+03	76.41	12.	2.2e-05	75.60	11.	1.7e-05	1.00	√	-
091018	MW	MW	N	850	1200	191.36	26.	1.3e-06	172.00	25.	1.3e-06	0.00585	-	√
091018	SMC	SMC	N	12e+03	38e+03	404.72	28.	2.1e-05	211.95	26.	1.0e-06	6.79e-09	-	√
091127	SMC	MW	N	60e+03	100e+03	99.02	49.	3.1e-05	83.60	48.	0.0011	1.98e-12	-	√
091127	SMC	SMC	N	400e+03	600e+03	25.29	28.	0.61	20.40	27.	0.81	2.91e-06	-	√
100418A	SMC	SMC	N	100e+03	300e+03	10.30	18.	0.92	9.56	17.	0.92	0.290	√	-
100901A	SMC	SMC	S	4000	6000	77.42	26.	1.9e-06	512.00	25.	0.00051	-9.00	√	-
100901A	MW	SMC	P	10e+03	12e+03	67.80	56.	0.13	58.90	55.	0.33	2.16e-13	-	√
100901A	MW	SMC	N	50e+03	100e+03	120.78	53.	1.2e-07	73.40	52.	0.027	1.06e-26	-	√

Table E.15: **GRB**: GRB name. **Fil**: filter name. **Fit**: fitting function. 0: $f(t) = N_1 t^{-\alpha_1}$; 1: $f(t) = N_1((t/t_{br,1})^{-\alpha_1/s_1} + (t/t_{br,2})^{-\alpha_2/s_1})^{s_1}$; 2: $f(t) = N_1((t/t_{br,1})^{-\alpha_1/s_1} + (t/t_{br,2})^{-\alpha_2/s_1})^{s_1} + N_2((t/t_{br,3})^{-\alpha_3/s_2} + (t/t_{br,4})^{-\alpha_4/s_2})^{s_2}$; 4: $f(t) = N_1((t/t_{br,1})^{-\alpha_1/s_1} + (t/t_{br,2})^{-\alpha_2/s_1})^{s_1} + N_2(t)^{-\alpha_3}$; 6: $f(t) = N_1((t/t_{br,1})^{-\alpha_1/s_1} + (t/t_{br,2})^{-\alpha_2/s_1})^{s_1} + N_2(t)^{-\alpha_3}$; 8: $f(t) = N_1((t/t_{br,1})^{-\alpha_1/s_1} + (t/t_{br,2})^{-\alpha_2/s_1})^{s_1} + N_2((t/t_{br,3})^{-\alpha_3/s_2} + (t/t_{br,4})^{-\alpha_4/s_2})^{s_2} + N_3((t/t_{br,5})^{-\alpha_5/s_3} + (t/t_{br,6})^{-\alpha_6/s_3})^{s_3}$; 9: $f(t) = N_1((t/t_{br,1})^{-\alpha_1/s_1} + (t/t_{br,2})^{-\alpha_2/s_1})^{s_1} + N_2((t/t_{br,3})^{-\alpha_3/s_2} + (t/t_{br,4})^{-\alpha_4/s_2})^{s_2} + N_3(t)^{-\alpha_5}$. **Tmin (Tmax)**: initial (end) time of the observations in rest frame (s). $\mathbf{t_{br}}$, $\sigma(\mathbf{t_{br}})$: trigger times with relative errors (s). α, $\sigma(\alpha)$: slopes with relative errors. **s**: smoothness parameters. **N**, σ**N**: normalization with relative error (mJy). χ^2: chi-square. **DOF**: degree of freedom. **pval**: p_value.

GRB	Fil	Fit	Tmin	Tmax	t_{br1}	Δt_{br1}	t_{br2}	Δt_{br2}	α_1	$\Delta\alpha_1$	α_2	$\Delta\alpha_2$	α_3	$\Delta\alpha_3$	α_4	$\Delta\alpha_4$	s_1	s_2	N_1	ΔN_1	N_2	ΔN_2	χ^2	DOF	pval
050319	R_C	2	4.03e+01	9.94e+05	1.57e+05	1.95e+04	4.82e+02	3.01e+01	0.446	0.014	1.559	0.104	2.520	0.274	0.124	0.078	-0.5	-0.5	1.446e-05	1.248e-06	2.000e-04	0.000e+00	2.035e+02	64.	-3.484e-07
050401	CR	0	3.57e+01	1.12e+06	-	-	-	-	0.826	0.016							-	-	1.202e-02	2.114e-03	e+00	e+00	7.970e+00	14.	8.908e-01
050408	R_C	2	3.44e+03	2.62e+06	4.83e+04	1.15e+04	2.34e+06	0.00e+00	0.514	0.068	1.493	0.268	-0.538	0.451	11.120	5.908	-0.5	-0.5	5.643e-06	1.428e-06	1.434e-06	7.860e-07	1.658e+02	79.	-4.265e-07
050416A	I_C	1	2.16e+02	4.06e+05	1.39e+04	1.32e+04	-	-	0.859	0.147	0.232	0.082					-0.5	-	2.659e-05	1.271e-05	e+00	e+00	1.828e+01	8.	1.925e-02
050525A	v	4	6.65e+01	3.60e+04	3.00e+03	0.00e+00	-	-	-4.009	0.000	2.399	0.000	1.150	0.036			-0.5	-	8.404e-03	2.330e-03	3.192e+00	5.773e-01	3.209e+01	38.	7.386e-01
050730	v	1	1.71e+02	1.22e+05	1.70e+03	9.91e+02	-	-	1.138	0.340	-0.477	0.204					-0.5	-	1.029e-03	3.134e-04	e+00	e+00	4.760e+00	6.	5.749e-01
050820A	I_C	2	3.28e+02	3.18e+06	5.40e+02	2.07e+01	5.18e+04	7.66e+03	1.335	0.076	-1.691	0.105	0.140	0.162	1.369	0.032	-0.5	-0.5	5.101e-03	2.402e-04	1.205e-04	1.588e-05	6.062e+01	20.	7.563e-06
050824	R_C	0	6.35e+02	8.99e+06	-	-	-	-	0.593	0.004							-	-	7.888e-03	3.044e-04	e+00	e+00	2.544e+02	95.	-5.745e-07
050904	I_C	0	2.02e+02	9.44e+04	-	-	-	-	1.084	0.034							-	-	7.559e-01	2.631e-01	e+00	e+00	1.867e+01	4.	-3.858e-03
050908	R_C	0	3.10e+02	2.36e+04	-	-	-	-	0.653	0.036							-	-	5.627e-03	1.553e-03	e+00	e+00	9.960e+00	7.	1.909e-01
050922C	v	0	1.19e+02	3.84e+05	-	-	-	-	0.907	0.008							-	-	4.653e-01	2.509e-02	-	-	1.040e+02	21.	4.218e-06
051109A	R_C	1	2.20e+03	2.02e+07	5.33e+03	5.72e+03	-	-	0.412	0.193	0.932	0.070	-	-	-	-	-0.5	-	1.309e-04	9.492e-05	-	-	6.581e+01	24.	1.107e-05
051111	V_J	0	8.12e+01	3.08e+04	-	-	-	-	0.875	0.004	-	-	-	-	-	-	-	-	2.820e-01	7.887e-03	-	-	1.213e+02	12.	-8.833e-04
060124	v	1	1.83e+02	9.90e+04	1.06e+03	6.16e+02	-	-	-0.240	0.130	0.734	0.089	-	-	-	-	-0.5	-	9.280e-04	8.149e-05	-	-	1.440e+00	4.	8.364e-01
060206	v	4	6.05e+01	1.99e+06	4.91e+03	1.03e+03	-	-	-2.693	1.527	1.232	0.168	0.646	0.068	-	-	-0.5	-	3.561e-04	6.193e-05	8.908e-03	2.981e-03	2.490e+01	20.	2.052e-01
060210	R_C	1	3.56e+02	1.09e+04	5.73e+02	1.85e+02	-	-	-0.423	0.616	1.246	0.097	-	-	-	-	-0.8	-	2.113e-04	4.348e-05	-	-	2.258e+01	21.	3.670e-01
060418	v	1	1.37e+02	1.26e+05	2.19e+02	6.00e+00	-	-	1.212	0.014	-2.011	0.180	-	-	-	-	-0.8	-	8.475e-03	1.459e-04	-	-	2.006e+01	17.	2.712e-01
060502A	R_C	0	2.32e+03	1.04e+05	-	-	-	-	0.497	0.054	-	-	-	-	-	-	-	-	1.506e-03	7.133e-04	-	-	6.280e+00	7.	5.080e-01
060512	v	1	1.24e+02	2.47e+05	3.68e+03	1.03e+04	-	-	0.717	0.140	1.086	0.154	-	-	-	-	-0.5	-	8.867e-05	2.248e-04	-	-	1.117e+01	19.	9.179e-01
060526	R_C	2	4.96e+01	6.38e+05	1.72e+04	1.40e+03	1.56e+05	7.23e+03	0.352	0.113	2.489	0.306	0.463	0.115	2.527	0.053	-0.5	-0.5	8.889e-05	1.558e-05	1.505e-05	9.168e-07	1.362e+02	117.	1.079e-01
060605	CR	1	7.39e+01	6.32e+03	5.53e+02	3.50e+01	-	-	1.071	0.034	-0.534	0.068	-	-	-	-	-0.5	-	2.933e-03	8.467e-05	-	-	6.879e+01	50.	4.013e-02
060607A	r'	2	7.02e+01	1.44e+04	1.65e+02	2.60e+00	2.00e+03	0.00e+00	-2.981	0.266	1.141	0.012	-12.520	5.082	26.870	18.980	-0.5	-0.5	8.520e-03	1.350e-04	3.366e-04	7.456e-05	2.450e+02	18.	3.613e-06
060614	R_C	2	9.09e+02	1.28e+06	3.52e+04	1.63e+03	5.84e+04	1.17e+03	-0.374	0.042	2.771	0.564	-6.783	1.746	1.825	0.070	-0.5	-0.8	9.540e-05	4.844e-06	4.382e-05	1.284e-05	4.828e+03	42.	7.729e-02
060729	v	2	1.20e+02	5.77e+05	3.06e+03	7.23e+03	1.80e+04	1.18e+03	-0.143	0.440	0.950	1.225	-8.590	6.344	0.870	0.249	-0.8	-0.5	5.857e-04	4.630e-04	3.987e-04	1.129e-04	4.916e+01	21.	4.791e-04
060906	R_C	2	6.91e+02	1.37e+04	7.84e+02	2.50e+02	7.51e+03	1.35e+03	-2.255	2.755	0.957	0.324	-6.826	5.436	0.314	0.926	-0.8	-0.8	1.248e-04	1.864e-05	5.809e-05	3.065e-05	1.690e+00	13.	9.999e-01
060908	R_C	1	6.10e+01	3.43e+07	8.37e+05	2.85e+05	-	-	1.085	0.007	0.044	0.114	-	-	-	-	0.8	-	1.980e-07	7.060e-08	-	-	1.249e+02	58.	5.546e-07
060912A	white	0	2.15e+02	7.16e+03	-	-	-	-	1.168	0.033	-	-	-	-	-	-	-	-	1.967e-01	3.752e-02	-	-	1.364e+01	5.	1.830e-02
060927	R_C	1	1.26e+03	2.26e+04	1.53e+03	1.08e+02	-	-	-10.15	3.983	2.408	0.156	-	-	-	-	-0.5	-	3.387e-04	0.000e+00	-	-	1.640e+00	0.	1.000e+00
060927	clear	1	1.93e+01	1.47e+03	2.47e+02	1.34e+02	-	-	1.350	0.181	-0.165	0.346	-	-	-	-	0.5	-	2.429e-04	1.042e-04	-	-	1.341e+01	3.	-9.590e-03
061007	CR	1	2.97e+01	1.46e+04	6.29e+01	2.00e-01	-	-	-5.471	0.064	1.642	0.003	-	-	-	-	-0.7	-	1.067e+00	7.675e-03	-	-	1.341e+03	79.	-4.634e-07
061121	v	2	1.02e+02	3.13e+05	1.95e+02	1.70e+01	8.98e+03	2.31e+03	1.013	0.118	-1.263	0.270	1.152	0.103	- 0.736	0.786	-0.3	-0.5	9.926e-04	5.345e-05	7.843e-05	8.361e-06	2.348e+01	24.	4.918e-01
061126	R_C	1	9.68e+01	1.68e+05	4.14e+02	5.20e+01	-	-	1.765	0.044	0.797	0.014	-	-	-	-	0.8	-	4.209e-04	6.325e-05	-	-	3.203e+02	88.	-5.279e-07
070125	R_C	1	6.84e+04	2.32e+06	1.02e+05	1.39e+03	-	-	-0.492	0.072	2.003	0.020	-	-	-	-	-0.5	-	1.228e-04	1.595e-06	-	-	1.737e+03	134.	-8.264e-07
070208	R_B	1	1.59e+02	5.80e+03	4.47e+02	2.13e+02	-	-	-0.394	0.299	0.622	0.083	-	-	-	-	-0.5	-	5.112e-05	6.194e-06	-	-	9.060e+00	4.	5.938e-02
070318	v	2	7.85e+01	9.34e+05	4.30e+02	1.54e+01	1.94e+05	2.19e+04	-0.617	0.043	1.120	0.014	-1.080	0.385	2.404	0.411	-0.5	-0.5	3.392e-03	8.657e-05	1.481e-05	1.466e-06	5.593e+01	32.	5.527e-03

Table E.15: Continued.

GRB	Fil	Fit	Tmin	Tmax	$t_{\rm br1}$	$\Delta t_{\rm br1}$	$t_{\rm br2}$	$\Delta t_{\rm br2}$	α_1	$\Delta\alpha_1$	α_2	$\Delta\alpha_2$	α_3	$\Delta\alpha_3$	α_4	$\Delta\alpha_4$	s_1	s_2	N_1	ΔN_1	N_2	ΔN_2	χ^2	DOF	pval
070411	CR	1	5.22e+02	5.68e+03	1.05e+03	1.61e+02	-	-	-0.470	0.243	1.737	0.148	-	-	-	-	-0.8	-	2.716e-04	2.812e-05	-	-	6.083e+01	14.	1.155e-05
070419A	R_C	1	2.30e+02	6.24e+04	7.13e+02	3.03e+01	-	-	-1.473	0.168	1.291	0.031	-	-	-	-	-0.5	-	1.487e-04	4.974e-06	-	-	9.294e+01	53.	5.753e-04
070529	v	1	1.45e+02	2.55e+05	1.45e+03	6.22e+02	-	-	1.564	0.115	0.288	0.103	-	-	-	-	0.5	-	3.572e-05	1.921e-05	-	-	3.190e+01	21.	5.991e-02
070802	K_S	6	1.22e+03	8.89e+04	2.02e+03	6.12e+01	-	-	-5.773	1.655	1.103	0.135	0.231	0.091	-	-	-0.5	-	2.747e-04	2.161e-05	2.996e-04	2.713e-04	1.784e+01	14.	2.144e-01
071003	g_{Gu}	1	1.51e+03	6.05e+05	8.44e+04	4.40e+04	-	-	0.239	0.108	1.909	0.358	-	-	-	-	-0.5	-	3.498e-05	1.835e-05	-	-	1.388e+01	3.	-1.109e-02
071010A	K_S	2	1.53e+02	2.49e+05	2.27e+03	5.78e+02	8.07e+04	0.00e+00	0.071	0.095	2.243	0.477	0.060	0.000	2.312	0.000	-0.5	-0.5	1.959e-03	4.137e-04	4.037e-04	1.513e-05	1.032e+01	2.	-3.443e-02
071025	H	2	1.86e+02	8.41e+04	4.72e+02	2.31e+01	1.69e+03	7.68e+01	-2.140	0.227	1.175	0.040	-5.598	1.877	2.149	0.375	-0.8	-0.5	5.259e-03	1.201e-04	9.844e-04	8.004e-05	5.197e+01	37.	5.217e-02
071112C	I_C	1	1.32e+02	4.41e+04	1.88e+02	1.24e+01	-	-	1.014	0.038	-3.126	1.018	-	-	-	-	-0.5	-	9.149e-04	5.274e-05	-	-	2.600e+00	2.	2.585e-01
080310	R_C	4	3.28e+02	9.49e+04	2.01e+03	3.63e+02	-	-	-0.977	0.426	1.500	0.174	0.762	0.045	-	-	-0.8	-	6.033e-04	3.654e-05	3.993e-02	1.612e-02	1.788e+01	16.	3.309e-01
080319B	R_C	1	6.55e+01	6.12e+05	8.85e+02	1.66e+01	-	-	1.226	0.004	2.490	0.008	-	-	-	-	0.8	-	6.503e-03	2.217e-04	-	-	1.859e+03	257.	-1.591e-06
080330	r'	1	8.94e+01	1.17e+05	1.43e+03	4.11e+01	-	-	-0.182	0.018	1.148	0.006	-	-	-	-	-0.5	-	5.060e-04	1.155e-05	-	-	1.530e+02	48.	-1.307e-07
080413B	r'	4	7.65e+01	5.19e+06	1.46e+05	7.14e+03	-	-	0.071	0.033	1.845	0.075	0.838	0.032	-	-	-0.3	-	3.426e-05	1.878e-06	4.966e-02	8.598e-03	7.293e+01	51.	2.362e-02
080603A	R_C	1	1.05e+02	3.50e+05	2.21e+03	7.40e+01	-	-	-0.836	0.035	1.089	0.017	-	-	-	-	-0.8	-	2.694e-04	4.327e-06	-	-	1.826e+02	21.	2.281e-06
080607	R_C	2	2.45e+01	4.10e+03	9.99e+01	1.86e+01	2.50e+03	0.00e+00	0.652	0.086	1.767	0.094	-0.830	0.262	2.204	0.609	-0.5	-0.5	1.341e-03	3.095e-04	3.102e-05	1.996e-06	1.476e+02	49.	-1.796e-07
080710	g'	1	4.50e+02	9.91e+03	1.90e+03	1.01e+01	-	-	0.728	0.003	-1.189	0.012	-	-	-	-	-0.5	-	8.219e-04	1.125e-06	-	-	7.353e+02	46.	-6.314e-07
080721	white	0	1.64e+02	1.80e+05	-	-	-	-	1.250	0.013	-	-	-	-	-	-	-	-	1.494e+00	1.034e-01	-	-	1.797e+01	5.	3.077e-03
080810	R_C	0	3.47e+03	5.01e+05	-	-	-	-	1.203	0.015	-	-	-	-	-	-	-	-	1.742e+01	2.772e+00	-	-	1.347e+02	27.	1.553e-06
080810	clear	1	4.05e+01	9.64e+03	1.14e+02	2.80e+00	-	-	1.115	0.008	-1.295	0.050	-	-	-	-	-0.8	-	4.471e-02	6.801e-04	-	-	2.334e+02	28.	1.001e-06
080913	J	4	5.76e+02	8.70e+05	5.42e+04	4.45e+09	-	-	-9.486	1.e+03	0.897	0.102	0.976	0.035	-	-	-0.5	-	5.932e-06	4.358e-01	1.886e-02	4.553e-03	2.316e+01	10.	1.020e-02
081029	r'	4	5.21e+02	4.39e+05	8.23e+03	2.59e+01	-	-	-1.175	0.022	1.557	0.006	1.212	0.022	-	-	-0.1	-	4.300e-04	1.633e-06	1.036e+00	1.512e-01	9.885e+03	73.	-1.188e-02
081203A	R_C	1	2.35e+02	4.64e+04	6.45e+02	3.19e+01	-	-	1.694	0.023	-0.290	0.036	-	-	-	-	-0.5	-	3.726e-02	8.283e-04	-	-	3.239e+01	12.	1.225e-03
090102	R_C	1	4.38e+01	2.65e+05	2.34e+02	4.56e+01	-	-	1.900	0.118	0.995	0.012	-	-	-	-	0.8	-	7.023e-04	1.675e-04	-	-	6.287e+01	57.	2.764e-01
090313	J	1	6.00e+02	5.00e+05	1.15e+03	9.85e+02	-	-	-0.418	1.531	0.902	0.035	-	-	-	-	-0.5	-	5.708e-03	3.781e-03	-	-	2.057e+01	5.	9.946e-04
090424	R_C	1	2.50e+03	3.40e+06	3.61e+05	4.03e+04	-	-	0.826	0.010	-0.015	0.046	-	-	-	-	0.5	-	4.917e-06	3.184e-07	-	-	5.636e+01	20.	2.921e-05
090426	V_J	0	1.91e+03	1.07e+04	-	-	-	-	0.491	0.074	-	-	-	-	-	-	-	-	1.814e-03	1.119e-03	-	-	3.640e+00	9.	9.333e-01
090426	R_C	1	8.60e+01	1.51e+03	1.75e+02	3.57e+01	-	-	1.310	0.074	-0.098	0.163	-	-	-	-	-0.8	-	1.053e-03	1.385e-04	-	-	2.231e+01	29.	8.070e-01
090426	g'	1	4.47e+04	2.23e+05	9.04e+04	1.43e+04	-	-	2.679	0.222	0.269	0.345	-	-	-	-	0.5	-	9.504e-07	2.827e-07	-	-	3.510e+00	8.	8.983e-01
090618	R_C	2	3.20e+03	3.07e+07	1.52e+04	1.20e+03	1.12e+06	1.89e+05	0.575	0.024	1.311	0.014	-4.638	3.987	0.270	0.024	-0.5	-0.5	3.471e-04	2.631e-05	2.207e-06	1.039e-07	4.690e+02	153.	-9.456e-07
090618	CR	1	7.60e+01	7.33e+03	8.94e+01	3.00e+00	-	-	-1.178	0.303	0.799	0.009	-	-	-	-	-0.5	-	1.425e-02	2.259e-04	-	-	2.493e+02	4.	-6.328e-01
090926A	r'	1	7.32e+04	2.07e+06	7.41e+04	1.10e+02	-	-	1.491	0.007	-8.290	0.534	-	-	-	-	-0.5	-	1.637e-04	6.710e-07	-	-	6.713e+02	82.	-4.855e-07
091018	white	0	1.47e+02	5.76e+05	-	-	-	-	0.934	0.007	-	-	-	-	-	-	-	-	2.859e-01	1.280e-02	-	-	3.442e+01	13.	1.060e-03
091127	I_C	2	8.02e+03	8.82e+06	2.34e+04	3.64e+03	1.06e+06	6.58e+04	0.319	0.068	1.466	0.058	-2.129	0.470	0.441	0.037	-0.5	-0.5	4.271e-04	5.641e-05	5.669e-06	3.081e-07	4.562e+01	10.	1.314e-05
100418A	white	4	1.62e+02	2.98e+06	5.14e+04	3.89e+03	-	-	-0.670	0.098	1.384	0.072	0.169	0.028	-	-	-0.5	-	3.840e-05	1.692e-06	1.725e-05	6.576e-06	2.849e+01	9.	8.118e-04
100901A	R_C	4	1.03e+03	3.94e+05	2.73e+04	5.44e+02	-	-	-1.668	0.083	1.621	0.029	1.013	0.097	-	-	-0.5	-	6.687e-04	1.067e-05	4.154e-01	2.983e-01	2.866e+02	35.	2.140e-07

Table E.16: It continues from Table E.15.

GRB	Fil	Fit	Tmin	Tmax	$t_{\rm br1}$	$\Delta t_{\rm br1}$	$t_{\rm br2}$	$\Delta t_{\rm br2}$	$t_{\rm br3}$	$\Delta t_{\rm br3}$	α_1	$\Delta\alpha_1$	α_2	$\Delta\alpha_2$	α_3	$\Delta\alpha_3$	α_4	$\Delta\alpha_4$
060904B	CR	8	2.99e+01	1.63e+05	6.06e+01	1.05e+01	4.76e+02	2.24e+01	3.60e+03	4.34e+02	-1.006	0.824	3.078	2.452	-1.017	0.328	1.946	0.451
071031	g'	8	2.89e+02	2.57e+04	1.03e+03	4.13e+01	5.96e+03	1.21e+02	1.42e+04	2.87e+02	-0.941	0.038	0.929	0.033	-6.264	1.075	1.959	0.350
080928	CR	8	4.15e+02	1.34e+04	1.01e+03	7.46e+01	2.31e+03	1.20e+02	9.31e+03	5.84e+02	-1.637	0.417	3.919	2.297	1.763	0.438	-4.308	1.440
081008	r'	8	4.44e+01	1.88e+05	6.13e+01	2.60e+00	1.10e+02	8.00e+00	2.46e+03	5.44e+02	-10.850	3.668	1.116	2.481	-4.008	1.533	1.110	0.844

Table E.17: It continues from Table E.16.

α_5	$\Delta\alpha_5$	α_6	$\Delta\alpha_6$	s_1	s_2	s_3	N_1	ΔN_1	N_2	ΔN_2	N_3	ΔN_3	χ^2	DOF	pval
-0.610	0.318	1.279	0.065	-0.1	-0.1	-0.5	5.619e-04	1.667e-04	6.341e-04	7.152e-05	3.666e-04	1.800e-05	7.893e+01	45.	1.318e-03
-0.428	0.423	-22.900	12.870	-0.8	-0.5	-0.5	1.855e-04	8.037e-07	1.083e-05	9.570e-07	2.552e-06	4.396e-07	4.372e+02	63.	-3.516e-07
2.381	0.649	-3.416	1.108	-0.5	-0.5	-0.5	5.812e-04	7.380e-05	1.134e-03	9.466e-05	6.909e-04	7.496e-05	2.341e+01	10.	9.338e-03
0.356	0.076	1.443	0.134	-0.5	-0.5	-0.5	7.220e-03	1.321e-03	1.012e-02	7.053e-03	1.040e-03	3.077e-04	1.569e+02	79.	-3.544e-08

Table E.18: Parameters of the optical/X-ray SEDs fitted with a single power-law. **GRB**: GRB name. **Host**: the chosen extinction law; Milky Way (MW), Large Magellanic Cloud (LMC), Small Magellanic Cloud (SMC). **Part**: X-ray LC part considered; "S" steep decay, "P" plateau, "N" normal decay. $\beta_{\mathbf{op,X}}$, $\sigma(\beta_{\mathbf{op,X}})$: spectral index with error. **NH**, σ**(NH)**: hydrogen column density with relative error (10^{22} cm^{-2}). **E(B-V)**, σ**(E(B-V))**: optical absorption with relative error (mag). **N**, σ**(N)**: normalization with error (mJy). $\chi^{\mathbf{2}}$: chi-square. **DOF**: degree of freedom. **pval**: p_value. $\mathbf{T_i}$, $\mathbf{T_f}$: initial (end) time of the interval of the SED in observer time (s). **ok**: "1" if the best fitting function is a power-law, otherwise "0". This table is available in its entirety in a machine-readable form at the CDS (table2.dat, ReadMe).

GRB	Host	Part	$\beta_{op,X}$	$\sigma(\beta_{op,X})$	NH	$\sigma(NH)$	E(B-V)	σ(E(B-V))	N	$\sigma(N)$	χ^2	DOF	pval	T_i	T_f
050401	MW	P	0.873	0.075	1.840	0.322	0.667	0.082	1.830	0.851	3.331e+01	146	1.000e+00	200	2000
050525A	SMC	N	0.931	0.028	0.052	0.061	0.113	0.015	0.183	0.032	4.956e+01	29	1.010e-02	6000	30000
050730	SMC	P	0.796	0.004	2.380	0.257	0.184	0.001	1.600	0.022	7.597e+02	140	-8.640e-07	4000	6000
050820A	MW	P	0.831	0.258	0.178	0.573	0.367	0.270	1.940	3.040	1.076e+01	67	1.000e+00	100	140
050824	SMC	P	0.846	0.016	0.066	0.072	0.000	0.002	0.013	0.000	2.764e+01	31	6.400e-01	6500	30000
050824	MW	N	2.340	0.642	0.179	0.137	2.458	1.089	5.551	21.127	3.765e+01	34	3.057e-01	500000	2000000
050904	MW	S	0.682	0.019	-1.550	0.727	0.000	0.000	0.199	0.022	4.606e+01	55	7.990e-01	600	1800
050904	MW	P	0.853	0.018	1.750	0.497	0.347	0.021	0.119	0.013	1.054e+02	146	9.950e-01	12000	90000
050908	MW	N	1.248	0.357	0.612	1.030	0.381	0.353	0.085	0.177	9.072e+00	16	9.100e-01	1000	20000
050922C	MW	P	1.004	0.027	0.156	0.207	0.186	0.021	5.300	0.721	1.059e+01	38	1.000e+00	200	400
051109A	MW	N	1.061	0.056	0.851	0.204	0.399	0.056	0.040	0.014	7.708e+01	100	9.570e-01	10000	700000
060124	LMC	N	0.748	0.010	-0.231	0.306	0.023	0.006	0.018	0.001	4.585e+01	26	9.480e-03	100000	150000
060206	MW	N	1.659	0.049	4.130	0.876	-0.439	0.038	0.200	0.057	4.147e+01	19	2.090e-03	35000	1000000
060210	MW	P	1.041	0.024	2.910	0.302	0.652	0.023	1.600	0.234	6.992e+01	87	9.100e-01	1000	7000
060512	SMC	P	1.242	0.047	0.044	0.186	0.224	0.037	0.081	0.021	4.500e+01	42	3.470e-01	3700	29000
060526	MW	S	0.836	0.051	-0.109	0.881	0.106	0.021	0.995	0.269	5.003e+00	41	1.000e+00	100	150
060526	SMC	P	1.071	0.045	0.441	0.431	0.083	0.027	0.250	0.067	1.423e+01	19	7.700e-01	1000	8000
060605	MW	P	1.315	0.028	0.908	0.796	0.261	0.019	4.770	0.620	4.004e+01	30	1.040e-01	200	400
060605	MW	P	1.142	0.019	0.482	0.297	0.278	0.015	0.874	0.095	2.107e+01	31	9.100e-01	4000	6300
060607A	MW	S	0.651	0.010	0.344	0.298	0.078	0.007	3.620	0.144	1.242e+01	51	1.000e+00	80	160
060607A	MW	P	0.709	0.008	1.200	0.320	-0.000	-0.000	0.323	0.008	1.125e+02	47	1.560e-07	1500	2200
060729	SMC	P	0.881	0.006	0.038	0.011	0.073	0.003	0.270	0.009	1.604e+02	124	1.550e-02	10000	30000
060904B	MW	P	0.891	0.048	0.326	0.036	1.500	0.111	66.400	20.500	7.471e+01	320	1.000e+00	100	310
060904B	MW	N	1.209	0.175	0.104	0.114	0.744	0.624	0.075	0.082	4.260e+01	65	9.860e-01	10000	100000
060906	SMC	P	0.799	0.040	-1.790	1.460	0.046	0.024	0.039	0.009	3.009e+01	29	4.090e-01	1000	6000
060908	SMC	P	0.837	0.041	0.324	0.129	0.051	0.042	0.924	0.232	2.341e+01	32	8.650e-01	100	550
060908	SMC	N	0.652	0.007	-0.033	0.086	0.000	0.003	0.060	0.001	2.643e+01	33	7.840e-01	700	8000
060912A	MW	N	0.914	0.021	0.480	0.142	0.224	0.023	0.070	0.007	4.540e+01	39	2.230e-01	1300	7000
060927	MW	P	0.849	0.103	1.300	1.450	0.056	0.075	0.049	0.030	3.811e+01	58	9.800e-01	1000	2000
061007	MW	N	1.155	0.004	0.762	0.038	0.327	0.003	27.500	0.450	7.135e+02	309	-1.910e-06	350	2000
061121	MW	P	0.681	0.060	0.530	0.086	0.178	0.057	0.529	0.200	8.072e+01	77	3.640e-01	640	1400
061121	SMC	S	1.027	0.093	0.681	0.102	0.754	0.100	46.300	26.700	2.752e+01	117	1.000e+00	110	210
061121	LMC	P	0.681	0.022	0.333	0.038	0.252	0.028	0.053	0.007	1.681e+02	132	1.850e-02	10000	100000
061126	LMC	N	0.528	0.009	0.339	0.056	0.140	0.011	0.146	0.008	1.435e+02	119	6.260e-02	2000	4000
070125	SMC	N	1.126	0.015	-0.110	0.129	0.044	0.002	0.015	0.000	1.214e+03	48	-4.120e-05	150000	300000
070318	MW	N	0.618	0.012	1.070	0.206	-0.000	-0.000	1.210	0.023	1.611e+01	52	1.000e+00	100	200
070318	MW	N	0.807	0.099	0.456	0.058	0.212	0.140	4.050	2.500	2.229e+01	113	1.000e+00	200	400
070318	MW	N	0.797	0.006	0.683	0.084	-0.000	-0.000	0.184	0.002	3.659e+01	46	8.380e-01	1000	10000
070318	MW	N	1.246	0.369	0.561	0.341	0.461	0.528	0.066	0.152	2.204e+01	26	6.860e-01	100000	200000

Table E.18: Continued.

GRB	Host	Part	$\beta_{op,X}$	$\sigma(\beta_{op,X})$	NH	$\sigma(NH)$	E(B-V)	σ(E(B-V))	N	$\sigma(N)$	χ^2	DOF	pval	T_i	T_f
070411	MW	N	1.167	0.271	-1.380	2.640	0.327	0.300	0.672	1.160	1.851e+01	28	9.130e-01	550	1000
070411	MW	N	1.168	0.271	-1.430	2.640	0.567	0.300	0.678	1.170	1.851e+01	28	9.130e-01	2000	5000
070419A	MW	S	1.112	0.224	0.110	0.140	1.240	0.363	5.580	7.750	2.071e+01	32	9.380e-01	300	500
070529	MW	P	0.801	0.140	3.810	1.460	0.170	0.151	0.553	0.503	1.700e+01	21	7.110e-01	200	900
070529	MW	N	2.130	0.507	18.300	5.920	1.380	0.538	40.400	131.000	8.004e+00	18	9.790e-01	10000	100000
070802	MW	P	1.110	0.016	0.849	0.410	0.472	0.021	0.097	0.007	2.867e+01	13	7.290e-03	2000	3000
071003	MW	N	1.277	0.052	0.691	0.127	0.207	0.053	0.071	0.022	3.954e+01	42	5.790e-01	25000	700000
071010A	LMC	N	1.025	0.017	1.030	0.330	0.210	0.007	0.020	0.001	1.027e+02	29	8.470e-07	70000	220000
071025	SMC	P	0.632	0.014	5.160	1.170	0.145	0.017	1.660	0.132	4.015e+01	107	1.000e+00	250	390
071031	LMC	P	0.870	0.020	32.700	10.200	0.021	0.003	0.020	0.001	3.986e+02	11	-7.330e-02	7000	20000
071112C	MW	P	0.528	0.009	-0.030	0.037	0.000	-0.000	0.168	0.007	3.806e+01	49	8.710e-01	400	1000
080310	SMC	U	0.988	0.043	0.410	0.087	0.693	0.043	33.300	8.740	1.774e+02	208	9.390e-01	450	700
080310	SMC	P	0.972	0.038	0.505	0.283	0.087	0.036	0.273	0.062	1.424e+01	20	8.180e-01	1300	7000
080310	SMC	N	0.883	0.035	0.644	0.260	0.110	0.034	0.021	0.004	2.979e+01	25	2.320e-01	20000	90000
080607	LMC	S	0.557	0.007	4.230	0.158	0.375	0.006	11.500	0.477	2.284e+02	318	1.000e+00	100	200
080607	MW	S	0.857	0.009	2.920	0.418	0.613	0.008	3.200	0.129	5.241e+01	65	8.700e-01	300	550
080607	MW	P	0.835	0.007	3.410	0.465	0.580	0.007	1.290	0.049	1.453e+02	44	-4.310e-08	600	1000
080710	MW	P	0.932	0.006	0.564	0.108	0.061	0.002	0.429	0.005	8.398e+02	67	-3.670e-07	3200	5500
080710	MW	N	0.976	0.004	0.130	0.072	0.000	0.000	0.172	0.001	7.713e+01	44	1.480e-03	9000	11500
080721	LMC	P	0.884	0.008	1.050	0.125	0.254	0.004	16.000	0.741	7.033e+01	272	1.000e+00	450	1000
080721	SMC	N	0.875	0.023	-0.255	0.488	0.217	0.011	0.059	0.007	2.793e+01	30	5.740e-01	40000	60000
080810	LMC	S	1.125	0.013	8.040	1.320	0.285	0.006	180.000	10.300	5.095e+01	71	9.650e-01	100	135
080810	MW	P	1.108	0.017	0.908	0.297	0.170	0.013	22.900	1.950	1.666e+01	69	1.000e+00	210	300
080810	MW	P	1.050	0.033	0.267	0.243	0.173	0.032	1.070	0.208	3.830e+01	34	2.800e-01	3900	5000
080810	MW	N	1.018	0.019	0.465	0.339	0.100	0.017	0.049	0.005	2.207e+01	24	5.750e-01	10000	100000
080913	LMC	N	0.650	0.038	-0.023	2.080	0.100	0.031	0.026	0.006	2.033e+01	35	9.770e-01	600	1200
080913	SMC	N	0.869	0.169	2.610	4.500	0.078	0.202	0.001	0.001	1.543e+01	17	5.640e-01	10000	100000
080913	MW	N	4.192	1.390	-6.050	54.700	324.	216.	2.e+05	2.e+06	6.856e+00	14	9.400e-01	100000	700000
080928	MW	S	1.036	0.086	0.475	0.318	0.703	0.089	6.950	3.710	4.338e+00	19	1.000e+00	430	500
080928	SMC	P	0.949	0.018	-0.034	0.103	0.096	0.009	0.338	0.033	7.875e+01	25	1.740e-06	5000	6500
080928	SMC	N	1.152	0.017	0.452	0.125	0.157	0.009	0.561	0.048	8.040e+01	78	4.040e-01	10000	13000
081008	SMC	S	0.655	0.010	1.980	0.278	0.208	0.004	31.600	1.570	2.530e+02	129	-7.940e-07	102	150
081008	LMC	P	1.256	0.016	1.380	0.302	0.219	0.007	4.670	0.374	8.242e+01	60	2.900e-02	1000	1500
081008	MW	N	0.933	0.004	1.630	0.297	0.000	0.001	0.053	0.000	5.277e+03	24	2.930e-01	15000	21000
081029	MW	N	1.134	0.010	0.589	0.412	0.128	0.002	0.045	0.001	1.646e+02	70	-3.910e-07	20000	80000
081203A	LMC	P	1.245	0.010	1.310	0.191	-0.152	0.005	40.300	1.520	4.098e+01	90	1.000e+00	250	400
081203A	MW	N	0.952	0.036	0.164	0.149	0.000	0.038	0.055	0.012	2.901e+01	27	3.600e-01	15000	25000
090102	MW	N	0.579	0.006	0.387	0.107	0.148	0.004	0.027	0.001	9.719e+02	43	5.850e-05	10000	11000
090313	LMC	P	1.039	0.018	3.100	0.670	0.180	0.013	0.161	0.017	3.057e+01	24	1.660e-01	25000	45000
090424	MW	N	0.726	0.011	0.178	0.083	0.330	0.019	0.021	0.001	2.280e+01	18	1.980e-01	90000	200000
090426	SMC	N	0.928	0.012	-0.173	0.199	0.000	-0.000	0.248	0.003	4.565e+01	50	6.480e-01	200	250
090426	MW	N	1.072	0.173	0.095	0.350	0.243	0.171	0.072	0.075	4.186e+01	50	7.870e-01	5000	5500
090618	SMC	N	0.944	0.034	0.144	0.012	1.320	0.075	275.000	59.500	1.130e+02	446	1.000e+00	150	250
090618	MW	P	0.697	0.002	0.118	0.009	0.080	0.003	0.253	0.002	6.777e+02	258	-1.600e-06	6000	20000
090618	MW	N	0.790	0.009	0.130	0.064	0.112	0.009	0.016	0.000	1.262e+02	22	2.530e-06	100000	200000
090618	SMC	N	1.175	0.045	0.248	0.128	-0.524	0.108	0.006	0.002	1.225e+01	12	4.260e-01	700000	2500000
090926A	MW	N	1.071	0.025	-0.162	0.179	0.054	0.014	0.077	0.010	3.067e+01	38	7.950e-01	50000	60000
090926A	SMC	N	0.981	0.008	1.240	0.396	0.000	0.000	0.062	0.000	3.206e+02	33	4.380e-07	75000	85000
090926A	MW	N	1.068	0.013	0.163	0.958	0.011	0.003	0.023	0.001	4.424e+02	15	2.080e-02	160000	170000

Table E.18: Continued.

GRB	Host	Part	$\beta_{op,X}$	$\sigma(\beta_{op,X})$NH	$\sigma(NH)$	E(B-V)	σ(E(B-V))	N	$\sigma(N)$	χ^2	DOF	pval	T_i	T_f
090926A	SMC	N	1.002	0.029	1.460	0.032	0.003	0.011	0.001	7.641e+01	12	2.160e-05	300000	350000
100418A	SMC	N	1.192	0.023	0.149	0.245	0.009	0.034	0.002	1.030e+01	18	9.220e-01	100000	300000
100901A	SMC	S	0.750	0.009	-0.082	0.094	-0.000	-0.000	0.086	0.003	7.742e+01	26	1.860e-06	4000	6000

Table E.19: Parameters of the optical/X-ray SEDs fitted with a broken power-law. **GRB**: GRB name. **Host**: galaxy chosen as model to fit the SED; Milky Way (MW), Large Magellanic Cloud (LMC), Small Magellanic Cloud (SMC). **Part**: X-ray LC part considered; "S" steep decay, "P" plateau, "N" normal decay. $\beta_{\mathbf{op}}$: optical spectral index. $\beta_{\mathbf{X}}$, $\sigma(\beta_{\mathbf{X}})$: X-ray spectral index with error. ν, $\sigma(\nu)$: observer frame break frequency (10^{15} Hz). **NH**, σ(**NH**): hydrogen column density with relative error (10^{22} cm^{-2}). **E(B-V)**, σ(**E**($\mathbf{B-V}$)): optical absorption with relative error (mag). **N**, σ(**N**): normalization with error (mJy). $\chi^{\mathbf{2}}$: chi-square. **DOF**: degree of freedom. **pval**: p_value. $\mathbf{T_i}$, $\mathbf{T_f}$: initial (end) time of the interval of the SED in observer time (s). **ok**: "1" if the best fitting function is a broken power-law, otherwise "0". This table is available in its entirety in a machine-readable form at the CDS (table3.dat, ReadMe). A portion is shown here for guidance.

GRB	Host	Part	β_{op}	β_X	$\sigma(\beta_X)$	ν_{br}	$\sigma(\nu_{br})$	NH	σ(NH)$E(B-V)$	σ(E(B-V))	N	$\sigma(N)$	χ^2	DOF	pval	T_i	T_f	
050319	MW	P	0.358	0.858	0.077	1.271	1.198	-0.030	0.283	0.103	0.022	0.327	0.048	4.050e+01	40	4.467e-01	300	1500
050319	MW	N	0.607	1.107	0.045	0.545	0.118	0.114	0.437	0.165	0.034	0.021	0.005	4.050e+01	9	3.770e-05	17000	300000
050408	LMC	N	0.342	1.210	0.310	22.350	26.190	1.560	0.690	0.290	0.000	0.020	0.001	2.654e+01	27	4.885e-01	20000	40000
050416A	SMC	P	0.619	0.951	0.156	339.900	131.310	0.398	0.097	0.321	0.044	0.060	0.005	1.890e+01	23	7.059e-01	700	2000
050416A	MW	N	0.524	1.024	0.137	46.850	35.030	0.468	0.162	0.384	0.035	0.014	0.002	2.240e+01	26	6.642e-01	6000	40000
050730	LMC	N	0.288	0.788	0.022	0.372	-0.000	1.180	0.230	0.167	0.015	0.446	0.068	1.170e+02	118	5.180e-01	10000	30000
050820A	SMC	N	0.437	0.937	0.028	6.560	2.280	0.333	0.076	0.057	0.015	0.124	0.016	1.710e+02	224	9.960e-01	10000	60000
050922C	LMC	N	0.565	1.060	0.101	0.548	0.191	-0.080	0.194	0.064	0.059	0.044	0.022	4.400e+01	67	9.870e-01	10000	80000
051111	SMC	N	0.707	1.210	0.140	4.090	5.510	0.727	0.279	0.143	0.007	0.125	0.005	1.180e+01	18	8.580e-01	6000	30000
060418	SMC	P	0.437	0.937	0.009	0.180	0.016	0.846	0.130	-0.117	0.009	4.920	0.080	1.990e+02	32	4.512e-07	630	970
060502A	MW	P	0.506	1.010	0.117	12.100	13.500	0.472	0.218	0.359	0.062	0.094	0.033	2.160e+01	24	6.010e-01	3600	10700
060526	MW	N	0.729	1.229	0.035	0.545	0.079	2.500	1.170	-0.199	0.016	0.042	0.005	5.538e+01	27	1.030e-03	30000	200000
060607A	SMC	P	0.086	0.586	0.023	0.477	0.106	0.217	0.137	-0.043	0.010	0.188	0.012	8.060e+01	110	9.840e-01	5000	8000
060614	MW	P	0.295	0.794	0.043	0.865	0.349	-0.004	0.010	-0.044	0.035	0.064	0.007	5.230e+01	56	6.150e-01	6000	30000
060614	LMC	N	0.353	0.853	0.102	7.070	6.290	0.032	0.028	0.221	0.011	0.019	0.001	3.600e+01	39	6.090e-01	80000	200000
060729	SMC	P	0.589	1.090	0.069	15.500	7.860	0.093	0.027	0.115	0.011	0.291	0.029	5.390e+01	67	8.760e-01	1000	10000
060729	SMC	N	0.540	1.040	0.037	5.170	1.800	0.078	0.015	0.120	0.004	0.053	0.003	2.030e+02	191	2.620e-01	100000	500000
060906	SMC	P	0.447	0.947	0.037	0.446	0.095	2.460	1.750	0.095	0.015	0.138	0.021	1.040e+01	19	9.410e-01	7000	12000
060912A	MW	N	0.572	1.070	0.180	3.770	6.720	0.419	0.189	0.211	0.013	0.623	0.046	3.690e+01	54	9.630e-01	250	800
061007	MW	N	0.520	1.020	0.060	3.170	1.940	0.594	0.066	0.155	0.009	0.120	0.007	3.720e+01	74	1.000e+00	2200	75500
061126	LMC	N	0.375	0.875	0.062	24.200	12.400	0.671	0.101	0.057	0.034	0.012	0.002	4.730e+01	75	9.950e-01	10000	100000
070208	LMC	N	0.726	1.226	0.142	83.400	50.300	0.860	0.172	0.066	0.034	0.017	0.003	9.350e+01	80	1.430e-01	2300	2400
071025	MW	P	0.627	1.127	0.066	47.470	19.130	3.625	0.769	0.064	0.017	128.000	0.017	5.060e+01	64	2.800e-01	3600	15000
071031	SMC	S	0.088	0.588	0.014	0.545	0.046	-0.337	0.187	0.091	0.005	0.145	0.005	7.830e+01	80	4.380e-01	770	1100
080319B	LMC	U	0.241	0.741	0.027	0.599	0.212	0.127	0.016	0.097	0.001	49.700	0.296	3.410e+02	428	9.990e-01	400	600
080319B	SMC	S	0.344	0.844	0.032	3.890	1.198	0.161	0.020	0.018	0.001	0.254	0.001	3.492e+03	209	-1.293e-06	5000	20000
080319B	SMC	P	0.354	0.854	0.012	0.455	0.022	0.089	0.043	0.099	0.010	0.008	0.001	6.684e+01	83	9.000e-01	115000	400000
080319B	MW	N	0.485	0.985	0.024	0.389	0.037	0.046	0.108	0.147	0.019	0.001	0.000	1.610e+01	17	5.180e-01	1000000	2000000
080330	SMC	P	0.409	0.909	0.016	0.477	0.050	0.112	0.089	-0.088	0.005	0.487	0.013	6.980e+01	56	1.020e-01	250	800
080413B	SMC	P	0.423	0.923	0.142	37.700	27.300	0.269	0.124	0.000	-0.000	0.312	0.005	5.710e+01	62	6.540e-01	200	500
080413B	MW	P	0.315	0.815	0.081	13.900	8.090	0.270	0.083	0.003	0.002	0.127	0.001	1.260e+02	48	-1.370e-07	1000	2000
080413B	MW	N	0.740	1.240	0.243	9.410	17.600	0.407	0.210	0.020	0.005	0.011	0.000	3.360e+01	40	7.530e-01	100000	400000
080603A	SMC	N	0.742	1.524	0.200	108.749	108.613	1.097	0.404	0.211	0.289	0.067	0.018	3.510e+01	53	9.720e-01	10500	20900
080607	LMC	N	0.803	1.300	0.103	89.300	33.000	4.590	0.670	0.622	0.013	0.405	0.020	4.620e+01	36	1.180e-01	4000	7000
081029	LMC	P	0.503	1.003	0.008	0.312	0.008	-0.125	0.000	0.052	0.002	0.376	0.004	9.244e+01	86	2.980e-01	3000	5000
081029	LMC	P	0.602	1.102	0.007	0.346	0.003	0.334	0.000	0.057	0.001	0.368	0.003	2.100e+02	32	4.510e-07	8000	18000
081203A	MW	P	0.518	1.018	0.070	1.000	0.860	0.441	0.126	-0.000	-0.000	0.793	0.008	3.250e+01	45	9.180e-01	4000	6000
090102	MW	N	0.266	0.766	0.157	17.000	18.200	0.543	0.271	0.137	0.017	0.828	0.051	8.330e+00	51	1.000e+00	400	600

Table E.19: Continued.

GRB	Host	Part	β_{op}	β_X	$\sigma(\beta_X)$	ν_{br}	$\sigma(\nu_{br})$	NH	σ(NH)$E(B-V)$	σ(E(B-V))	N	$\sigma(N)$	χ^2	DOF	pval	T_i	T_f	
090313	SMC	N	1.066	1.566	0.236	78.600	65.100	7.860	1.720	0.127	0.011	0.023	0.002	3.310e+01	51	9.760e-01	70000	450000
091018	MW	N	0.375	0.875	0.027	0.865	0.108	0.059	0.081	0.113	0.016	0.985	0.108	1.720e+02	25	1.350e-06	850	1200
091018	SMC	N	0.509	1.310	0.171	16.163	11.610	0.421	0.131	0.101	0.006	0.058	0.003	2.119e+02	26	1.002e-06	12000	38000
091127	MW	N	0.198	0.698	0.005	0.225	0.013	0.065	0.020	0.000	-0.000	0.084	0.002	8.360e+01	48	1.120e-03	60000	100000
091127	SMC	N	0.315	0.815	0.040	0.404	0.090	0.145	0.078	0.067	0.064	0.005	0.001	2.040e+01	27	8.120e-01	400000	600000
100901A	SMC	P	0.432	0.932	0.071	0.455	0.165	0.129	0.140	0.071	0.062	0.189	0.060	5.890e+01	55	3.340e-01	10000	12000
100901A	SMC	N	0.866	1.360	0.072	166.000	37.400	0.267	0.081	-0.026	0.022	0.086	0.010	7.340e+01	52	2.710e-02	50000	100000

Table E.20: 165 GRBs with redshift from the beginning of Swift observations (December 2004) until now (December 2011). *GRB*: GRB name. (S) stands for short GRB. Boldface: radio sample from Chandra & Frail (2012). (1) Supernova. *Opt.*: × means that there are not sufficient data to analyse the optical light curve; √ indicates GRBs in our sample (69). *References Optical Data* and *Telescopes and Filters*: citations and names of telescopes between parenthesis mean that we do not use these data.

GRB	Opt.	XLC	z	References Optical Data	Telescopes[a] and Filters
050126	×	ICN	1.290		
050315	×	IICN	1.949		
050318	×	0UN	1.440	Still et al. (2005).	UVOT (u,v,b).
050319	√	IICN	3.240	Woźniak et al. (2005); Quimby et al. (2006); Mason et al. (2006); Kamble et al. (2007); Huang et al. (2007); George et al. (2006); Kann et al. (2010b).	RAPTOR(CR); ROTSE(CR); UVOT(v,b); SNT(B,V,R,I); Kiso and Lulin(B,V,R,I); Mt.Abu(J); MAO(R,B); RTT150(R); NOT(B,R,I,K_S); TNG(V,R,I).
050401	√	ICN	2.900	Watson et al. (2006a); Rykoff et al. (2005) De Pasquale et al. (2006); Kamble et al. (2009).	VLT(R,K); Subaru(R); NOT(R); D1.5(R); TNG(R); MAO(R); CTIO4m(H); UKIRT(J,H,K); ROTSE(CR) SSO(R); SNT(R); MAO(R); Loiano(R); TNG(R); SNT(V,R,I).
050408	√	0UN	1.236	Foley et al. (2006); de Ugarte Postigo et al. (2007); Kann et al. (2010b).	UVOT(v); Keck(V,I); Magellan(R,I); CTIO1.3m(I,J,V); PAIRITEL(J,H,K); REM(V,R,I,J); PROMPT(V); Kuiper(V,R,I); WIDGET(R); ART(R); Kiso(R); MITSuME(R); SNT(R); TLS(R); RTT150(R); SAO1m(R); Mercator(R); MAO(R,I); ARC(z'); D1.5(U,B,V); KPNO4m(U); BTA(B,V,R); CAHA3.5m(B); RTT150(R); TNG(U,B,V,R,I).
050416A	√	ICN	0.654	Soderberg et al. (2007); Holland et al. (2007); Kann et al. (2010b).	P60(IRz); P200(K); ATT2.3m(R); HST(AB); UVOT(u,v,b,uvw1,uvm2,uvw2); NOT(K); D1.5(RVBI); MAO(R,B); SMARTS(I,J).
050505	×	IUN	4.270	Hurkett et al. (2006).	BOOTES(R); TAROT(I); AAVSO(R); SARA(R); Keck(I,g); UKIRT(K); FTN(R,B,i').
050525A	√	IUN	0.606	Klotz et al. (2005b); Oates et al. (2009); Rykoff et al. (2009).	UVOT(v); TAROT(CR); ROTSE(CR).
050603	×	0UF	2.821	Grupe et al. (2006).	UVOT(v).
050724 (S)	×	IICF	0.258	Malesani et al. (2007)	VLT(I,R,V).
050730	√	IICF	3.967	Pandey et al. (2006); Oates et al. (2009); Perri et al. (2007); Klotz et al. (2005a).	OSN(B,V,R,I); LT(B,V,r',i'); CTIO1.3m(V,I,J,K); HTC(R); IAC80(I); UVOT(v); (UVOT(V,B)); TAROT(R).
050814	×	IICF	5.300		

Table E.20: Continued.

GRB	Opt.	XLC	z	References Optical Data	Telescopes[a] and Filters
050820A	√	IICF	2.612	Cenko et al. (2006); Vestrand et al. (2006); Kann et al. (2010b).	P60(R,I,g,z'); UVOT(u,v,b,uvw1); HET(R,I); HST(r',i',z'); RAPTOR(CR); RTT150(B,R,I); MAO(R); WIRO(J); UKIRT(J,H,K_S); TNG(J,H,K_S).
050824	√	IUN	0.830	Sollerman et al. (2007).	NOT(B,R,I); VLT(B,V,R,I); BOOTES(R); OSN(R,I); MDM1.3m(R); MDM2.4m(R); D1.5(R,I); MAO(R); CrAO(R); NTT(R); WHT(R).
050826	×	0UN	0.297		
050904	√	ICF	6.290	Tagliaferri et al. (2005a); Price et al. (2006); Haislip et al. (2006); Gou et al. (2007); Boër et al. (2006).	VLT(K_s,H,J,Z); TNG(J); INT(z); CAHA3.5m(I1,I2,R,V,J); BOOTES(R); P60(z',R,i'); PROMPT(CR,I); SOAR(J,K_s,Y); UKIRT(H,J,K,Z); IRTF(k'); Gemini-S(z',r',i').
050908	√	ICF	3.344	Cenko et al. (2009b); Durig et al. (2005); Dale et al. (2005).	P60(i,R,z).
050922C	√	ICN	2.19	Oates et al. (2009); Rykoff et al. (2009); Kann et al. (2010b).	UVOT(v); ROTSE(CR); MDM(B,R); D1.5(B,R,I); NOT(B,R,I); VLT(V,B,R); Terskol(R); INT(R); WHT(R).
051016B	×	IICN	0.936		
051109A	√	IICN	2.346	Oates et al. (2009); Rykoff et al. (2009); Yost et al. (2007b); Li (2005).	UVOT(v); ROTSE(CR); MDM1.3m(R).
051111	√	0UN	1.550	Guidorzi et al. (2007); Melandri et al. (2008b); Butler et al. (2006).	FNT(R,B,V,i'); KAIT(CR,V,I); Lulin(V,R,I,B).
051221A (S)	×	IICN	0.547	Soderberg et al. (2006); Boettcher & Joshi (2005).	Gemini-N(i',r',z'); MDM1.3m(R).
051227 (S)	×	ICN	0.710		
060115	×	ICF	3.530		
060124	√	ICF	2.296	Romano et al. (2006); Misra et al. (2007).	UVOT(v,b); SNT(B,V,R,I); HCT(V,R); INT(R).
060206	√	0CF	4.048	Oates et al. (2009); Woźniak et al. (2006); Monfardini et al. (2006); Curran et al. (2007b); Stanek et al. (2007); Kann et al. (2010b).	UVOT(v); RAPTOR(CR); LT(r',i',z'); NOT(R); INT(R); TNG(R); OSN(B,V,R,I); Asiago(R); FTN(R); MDM2.4m(R); MDM1.3m(R); SARA(R).
060210	√	IICF	3.910	Melandri et al. (2008b); Curran et al. (2007a); Stanek et al. (2007); Cenko et al. (2009b).	FTN(R,I,B); MDM2.4m(R); MDM1.3m(R); P60(R,i',z',gGu).
060218	×[(1)]	IIICN	0.033	Mirabal et al. (2006); Kocevski et al. (2007); Ferrero et al. (2006).	MDM2.4m(U,B,V,R,I); MDM1.3m(U,B,V,R,I); PAIRITEL(J,H,K_S); VLT(B,V,R,I); LT(B,V,R); KAIT(B,R,I).
060223A	×	0CF	4.410	Oates et al. (2009).	UVOT(v).
060418	√	ICF	1.489	Oates et al. (2009); Melandri et al. (2008b); Molinari et al. (2007); Kann et al. (2010b).	(UVOT(v)); LT(R); REM(z',H,J,K_S); REM(z',H,J,K_S); MAO(B,R,I); SMARTS(B,V,R,I,J,H,K_S).
060502A	√	IICN	1.510	Cenko et al. (2009b).	P60(R,i',z',gGu).
060510B	×	IICF	4.900	Melandri et al. (2008b).	LT(R)
060512	√	ICF	2.100	Oates et al. (2009); Melandri et al. (2008b); Kann et al. (2010b).	UVOT(V); LT(R); NOT(J).
060522	×	ICN	5.110	Thöne et al. (2010); Khamitov et al. (2007); Dai et al. (2007).	
060522	×	ICN	5.110		
060526	√	IICF	3.210	Thöne et al. (2010); Khamitov et al. (2007); Dai et al. (2007).	UVOT(uvw2,uvm2,uvw1,b,v,white); MAO(B,R); RTT150(B,V,R); NOT(B,R,I); Keck(g',R); TNG(V,R); MIRO(V,R,I); Loiano(V,R,I); D1.5(V,R,I); Watcher(R,CR); CrAO(R); TLS(R); VLT(R); ROTSE(CR); CTIO1.3m(I,J); PAIRITEL(J,H,K_S); HST(i').
060604	×	ICF	2.680		

Table E.20: Continued.

GRB	Opt.	XLC	z	References Optical Data	Telescopes[a] and Filters
060605	√	IICN	3.780	Ferrero et al. (2009); Oates et al. (2009); Rykoff et al. (2009).	UVOT(u,v,b,white,uvw1,uvm2,uvw2); ROTSE(CR).
060607A	√	IICF	3.082	Oates et al. (2009); Ziaeepour et al. (2008); Nysewander et al. (2009b); Molinari et al. (2007); Kann et al. (2010b).	UVOT(u,v,b,white,uvw1,uvm2,uvw2); PROMPT(g',r',i',B); REM(H); SMARTS(B,V,R,I,J,H,K).
060614	√	IICN	0.125	Yost et al. (2007a); Mangano et al. (2007); Cobb et al. (2006); Xu et al. (2009)Fynbo et al. (2006); Della Valle et al. (2006).	PROMPT(CR); UVOT(u,v,b,white,uvw1,uvm2,uvw2); CTIO1.3m(I,J); SSO40inch(R); Watcher(R); D1.5(R); VLT(R)
060707	×	ICN	3.430		UVOT(v)
060708	×	IICN	1.920	Oates et al. (2009).	LT(r'); CrAO(R); NOT(R); UVOT(v,b,u,white,uvw1); MAO(R,B).
060714	×	IIICF	2.711	Krimm et al. (2007); Melandri et al. (2006); Cobb (2006); Rumyantsev et al. (2006); Jakobsson et al. (2006a,b); Boyd & Marshall (2006); Asfandyarov et al. (2006).	ROTSE(CR); UVOT(u,v,b,uvw1,uvw2,uvm2); HST(AB,RC,IC); PROMPT(B,z); Gemini-S(R,z,g,I); CTIO4m(R).
060729	√	IICF	0.540	Rykoff et al. (2009); Grupe et al. (2007); Cano et al. (2011b).	
060814	×	IICF	0.840		ROTSE(CR); RTT150(R,B,V); MAO(R); SMARTS(V,J,K,I).
060904B	√	ICF	0.703	Rykoff et al. (2009); Kann et al. (2010b).	P60(R,i',g',z').
060906	√	IICN	3.685	Cenko et al. (2009b).	UVOT(u,b,white); SMARTS1.5m(B,V,R,I); REM(V,R,I); NOT(V); D1.5(R); TNG(R);UKIRT(J,H,K); P60(R,i',g',z').
060908	√	ICN	1.884	Covino et al. (2010); Cenko et al. (2009b).	TNT(CR,B,V); UVOT(u,v,b,uvw1,uvw2,uvm2,white); MDM(R,B); Skinakas(R).
060912A	√	0CN	0.937	Deng et al. (2009).	MASTER(CR); Skinakas(R).
060926	×	IICN	3.208	Lipunov et al. (2007); Stefanescu et al. (2006).	ROTSE(N); FTS(R,i); Kiso(R); NOT(R); WHT(B,V,R,I); VLT(R,K,J,I).
060927	√	ICN	5.467	Ruiz-Velasco et al. (2007).	
061006 (S)	×	ICN	0.438	D'Avanzo et al. (2009).	ROTSE(CR); FTS(R,B,V,i'); VLT(R); Magellan1(R); SMARTS(V,R,I,J,H,K_S).
061007	√	0CN	1.262	Melandri et al. (2008b); Rykoff et al. (2009); Mundell et al. (2007); Kann et al. (2010b).	UVOT(V).
061021	×	IICN	0.346	Oates et al. (2009).	
061110A	×	IICN	0.757		UVOT(v);Kanata(R); MITSuME(g,R,I); MDM2.4m(R); NMSU(I,R,V,B,U); UVOT(u,v,b,uvw1,uvw2,uvm2); FTN(R,i',B,V); TLS(R); SARA0.9m(R); SNT(R,I,V); HTC(R,B); MAO(R); OSN(I); LT(r',i'); INT(r',i',g'); Gemini-N(r',i',g')
061110B	×	0UN	3.440		
061121	√	IICF	1.314	Oates et al. (2009); Uehara et al. (2011); Ishimura et al. (2008); Halpern et al. (2006b,a); Halpern & Armstrong (2006b,a); Gomboc et al. (2008c).	
061222A	×	IICF	2.088		
061222B	×	0CN	3.355		
070110	×	IIICN	2.352	Troja et al. (2007).	UVOT(u,v,b,white).

Table E.20: Continued.

GRB	Opt.	XLC	z	References Optical Data	Telescopes[a] and Filters
070125	√	0UN	1.547	Updike et al. (2008b); Chandra et al. (2008); Kann et al. (2010b).	UVOT(u,b,v,uvw2,uvm2,uvw1); Bok(B,V,R); TNG(B,R); SARA(V); PROMPT(B,V,R,I); TNT(V,R); EST(V,R); MDM(V,R,I); KAIT(R); HTC(V); Kuiper(R); Loiano(R); PAIRITEL(J,H,K_S); SOAR(J,H,K_S); LBT(R); MMT(J); P60(R,i'); Gemini-N(r',i'); Keck(R,g'); SMARTS(B,V,R,I,J,H,K_S).
070208	√	ICN	1.165	Cenko et al. (2009b).	P60(R,i',z',g).
070306	×	IICN	1.496	Jaunsen et al. (2008).	WHT(J,K); VLT(J,K,R); NOT(I).
070318	√	0CF	0.836	Oates et al. (2009)	UVOT(v).
070411	√	0CN	2.954	Melandri et al. (2008b); Rykoff et al. (2007); Mikuz et al. (2007); Kann et al. (2007e).	LT(R); ROTSE(CR); Crni(R,B); TLS(CR).
070419A	√	IICN	0.970	Melandri et al. (2009); Cenko et al. (2009b).	LOTIS(R); KAIT(R,V,I); Kuiper(R,V); FTN(R); Lulin(R); Kiso(R,B); MAO(R); KPNO4m(R); FTN(B,i'); UKIRT(J,H,K); P60(R,i',g',r').
070506	×	0CN	2.310		
070529	√	IICN	2.500	Oates et al. (2009).	UVOT(v).
070611	×	0UN	2.040	Rykoff et al. (2009); Melady et al. (2007).	ROTSE(CR); Watcher(R).
070714B (S)	×	IICN	0.920	Graham et al. (2009); Melandri et al. (2008b).	LT(r,i); WHT(R); LT(r').
070721B	×	IICF	3.626		
070724A (S)	×	IUF	0.457		
070802	√	IICN	2.450	Elíasdóttir et al. (2009); Krühler et al. (2008).	VLT(z,I,R,V,B); GROND(g',r',i',z',J,H,K_S).
070810A	×	IUN	2.170		
071003	√	0UN	1.604	Perley et al. (2008b).	KAIT(CR,V,I); AEOS(CR); Keck(CR,g,R,V,u,k'); Gemini-S(g,i,R,z); P60(RC,i',z',gs).
071010A	√	IUN	0.980	Covino et al. (2008); Cenko et al. (2009b).	VLT(U,B,V,R); NOT(V); Keck(V,R); SNT(R); REM(J,H,K); GROND(J,H,K); NTT(J,K); Gemini-N(H,K); TNG(H); TAROT(CR); P60(R,i',z').
071010B	√	0UN	0.947	Wang et al. (2008); Oksanen et al. (2008); Kann et al. (2007a,b,c,d).	TAOS(R); Hankasalmi(CR,I,V); TLS1.34m(R).
071020	×	ICN	2.145	Cenko et al. (2009b)	P60(R,i',z')
071025	√	ICN	5.200	Perley et al. (2010).	PAIRITEL(J,H,K); REM(J,K,H,R,I); RAPTOR(clear); Lotis(R); Lick(R); MAGNUM(J,H,K,Y,R); Kuiper(V,R,I); NTT(J,H,K); GROND(J,H,K,g',i',r',z').
071031	√	ICF	2.692	Krühler et al. (2009b); Breeveld (2007).	GROND(g',r',i',z',J,H,K_S); UVOT(u,v,b,uvw2,uvm2,uvw1,white).
071031		ICF	2.692	Kann et al. (2010b).	SMARTS(B,V,R,I,J,H,K_S).
071112C	√	ICN	0.823	Yuan et al. (2007); Uehara et al. (2010); Dintinjana et al. (2007); Oates & Stratta (2007); Ishimura et al. (2007); Greco et al. (2007); Sposetti (2007); Minezaki et al. (2007)Greco et al. (2007); Sposetti (2007); Minezaki et al. (2007).	ROTSE(clear); Kanata(R,J,H,K_S); Crni(R); UVOT(u,v,b,uvw2,uvm2,uvw1,white); MITSuME(g',R,I); Loiano(R); AAVSO(clear); MAGNUM(R,I,J,H,K).
071117	×	0UN	1.331		
071122	×	0UF	1.140	Cenko et al. (2009b).	P60(i',z',R).
071227 (S)	×	IICN	0.383	D'Avanzo et al. (2009).	VLT(R).
080129	×	IUF	4.349	Greiner et al. (2009b); Perley & Bloom (2008);	(GROND); Gemini-S(R).

Table E.20: Continued.

GRB	Opt.	XLC	z	References Optical Data	Telescopes[a] and Filters
080210	×	IIUF	2.641	Klotz et al. (2009a).	TAROT.
080310	√	IIICF	2.430	Cenko et al. (2009b); Hoversten & Cummings (2008); Perley et al. (2008a); Yoshida et al. (2008b); Yuan et al. (2008); Kinugasa (2008); Wegner et al. (2008).	P60(R,i',g',z'); UVOT(u,v,b,uvw2,uvm2,uvw1,white); PAIRITEL(J,H,K_S; MITSuME(g',R,I); ROTSE(clear); GAO(R); LBT(r'); MDM2.4m(r').
080319B	√	IIICN	0.937	Cenko et al. (2009b); Woźniak et al. (2009); Pandey et al. (2009); Bloom et al. (2009); Swan et al. (2008); Hentunen et al. (2008); Novak (2008); Racusin et al. (2008).	P60(R,i',z'); RAPTOR(CR,R,I,V); IAC80(I,R,V); Mercator(r); MAO(R); IGO(R); NOT(R); SR-22(clear); ZT-8(RV); PAIRITEL(J,H,K_S); KAIT(clear,B,V,I); Nickel(B,V,R,I); Gemini-S -N(g',r',i',z'); ROTSE(clear); AAVSO(clear); Brno(R); Kharkiv(R); UVOT(u,v,b,uvw2,uvm2,uvw1,white); TORTORA(V); Pi(V); LT(r',i'); FNT(r',i',R,I); REM(R,I,J,H,K_S); HST(i',r'); VLT(J,K_S).
080319C	×	ICN	1.950	Cenko et al. (2009b); Williams & Milne (2008); Li & Filippenko (2008); Wren et al. (2008a); Holland & Pagani (2008).	P60(RC,i',z'); Lotis(R); KAIT(CR); RAPTOR(CR); UVOT(u,v,b,uvw2,uvm2,uvw1,white).
080330	√	IUN	1.510	Guidorzi et al. (2009).	LT(g',r',i'); FTN(r',i'); REM(R); NOT(R); TAROT(clear,R); UVOT(u,v,b,uvw2,uvm2,uvw1,white); GROND(g',r',i',z',J,H,K_S).
080411	×	ICN	1.030		
080413A	×	ICN	2.433	Klotz et al. (2008a); Oates & Marshall (2008); Cobb (2008a); Gomboc et al. (2008a).	TAROT(CR); UVOT(u,v,b,uvw2,uvm2,uvw1,white); CTIO1.3m(B,R,V,I,J,H,K_S); LT(R); FTS(R,I).
080413B	√	ICN	1.100	Filgas et al. (2011b); Oates & Stamatikos (2008); Gomboc et al. (2008b).	GROND(g',r',i',z',J,H,K_S); UVOT(u,v,b,uvw2,uvm2,uvw1,white); FTN(R,I).
080430	×	IICN	0.767	Andreev et al. (2008); Oksanen & Hentunen (2008); Thoene et al. (2008); Landsman & Guidorzi (2008); Khamitov et al. (2008); Terra et al. (2008).	Terskol(R); Hankasalmi(CR); NOT(U,B,V,R,I); UVOT(u,v,b,uvw2,uvm2,uvw1,white); RTT150(R,B); Loiano(R,I,V,B).
080520	×	ICN	1.545		
080603A	√	0UN	1.688	Guidorzi et al. (2011); Kuin & Mangano (2008a,b).	FTN(B,V,R,i'); LT(r',i'); KAIT(V,I,clear); TLS1.34m(R); AZT-11(I); Z1000(R); AZT-33IK(R); PAIRITEL(J,H,K_S); Keck(R,g'); Gemini-N(r'); UVOT(u,v,b,uvm2,uvw1).
080603B	×	IIUN	2.690		
080604	×	ICN	1.416		
080605	×	IUN	1.640	Rumyantsev & Pozanenko (2008b,a); Clemens et al. (2008a,b); Kuin et al. (2008); Kann et al. (2008); Yoshida et al. (2008a).	Z1000(R,I,V); GROND(r',i'); UVOT(u,v,b,uvw2,uvm2,uvw1,white); TLS1.34m(R,I); MITSuME(I,R).
080607	√	IICF	3.036	Perley et al. (2011).	PAIRITEL(J,H,K_S); KAIT(clear,I); ROTSE(clear); LOTIS(R); P60(R,i',z'); UKIRT(J,H,K_S).
080707	×	IICN	1.230		
080710	√	IUN	0.845	Krühler et al. (2009a); Landsman & Sbarufatti (2008).	GROND(g',r',i',z'.J,H,K_S); UVOT(u,v,b,uvw2,uvm2,uvw1,white).
080721	√	ICN	2.591	Starling et al. (2009).	UVOT(white,v); VLT(V,R,I); NOT(R); LT(r',i'); WHT(R).
080804	×	0CN	2.204	Guidorzi & Steele (2008); Kuin & Racusin (2008); Kruehler et al. (2008).	FTS(R); UVOT(u,v,b,uvw2,uvm2,uvw1,white); GROND(r').
080805	×	ICF	1.505		

Table E.20: Continued.

GRB	Opt.	XLC	z	References Optical Data	Telescopes[a] and Filters
080810	√	IICF	3.350	Page et al. (2009).	UVOT(v,b,white); ROTSE(clrear); NOT(R); OSN(I,R,V,B);D1.5(R); FTN(i',R); FTS(R); INT(i'); Kanata(V); LT(i',r').
080905A (S)	×	0CN	0.122	Rowlinson et al. (2010).	VLT(R); NOT(R).
080905B	×	IIUN	2.374		
080913	√	0CF	6.695	Greiner et al. (2009a).	GROND(g',r',i',z',J,H,K_S); VLT(z,I,B,V,R,J); NTT(J); Gemini-N(J); Subaru(J).
080916A	×	IICN	0.689		
080928	√	IICF	1.692	Rossi et al. (2011).	ROTSE(CR); UVOT(u,v,b,uvw2,uvm2,uvw1,white); GROND(g',r',i',z'.J,H,K_S).
081007	×	IICN	0.530	Smith et al. (2008); Wren et al. (2008b); Cobb (2008b); Brown & Baumgartner (2008).	FTN(R,I); RAPTOR(R); SMARTS(B,R,I); UVOT(u,v,b,uvw2,uvm2,uvw1,white).
081008	√	IICF	1.968	Kann et al. (2010b); Yuan et al. (2010).	SMARTS(B,V,R,I,J,H,K_S); ROTSE(r'); UVOT(b,v,uvw1,white); GROND(r',g',i',z',J,H,K_S).
081028	×	IIICF	3.038	Margutti et al. (2010a).	UVOT(u,v,b,uvw2,uvm2,uvw1,white); CrAO(R,I); GROND(g',r',i',z'.J,H,K_S); PAIRITEL(J,H,K_S); NOT(R).
081029	√	IUN	3.848	Holland et al. (2012); Nardini et al. (2011).	UVOT(u,v,b,uvw2,uvm2,uvw1,white); REM(H,J,R); ROTSE(CR); CTIO1.3m(B,V,R,I,J,H,K_S); GROND(g',r',i',z'.J,H,K_S).
081118	×	ICN	2.580		
081121	×	0CN	2.512	Loew et al. (2008); Oates (2008); Cobb (2008c).	GROND(g',r',i',z'.J,H,K_S); UVOT(u,v,b,uvw2,uvm2,uvw1,white); UVOT(u,v,b,uvw2,uvm2,uvw1,white); SMARTS(J,H,K_S,B,R,I).
081203A	√	IICN	2.100	de Pasquale & Parsons (2008); West et al. (2008); Mori et al. (2008); Isogai & Kawai (2008); Rumyantsev et al. (2008).	UVOT(u,v,b,uvw2,uvm2,uvw1,white); GORT(I,R); MITSuME(g',R,I); Murikabushi(g',R,I); AZT-11(V,R,I).
081222	×	ICN	2.770	Updike et al. (2008a); Melandri et al. (2008a); Breeveld & Grupe (2008); Breeveld et al. (2008); Kuroda et al. (2008).	GROND(g',r',i',z'.J,H,K_S); FTS(i',r'); UVOT(u,v,b,uvw2,uvm2,uvw1,white); MITSuME(g',R,I).
090102	√	0CN	1.547	Gendre et al. (2010).	P60(R); GROND(CR,g',i',z',H,J,K_S); TAROT(R); REM(R,H); IAC80(R); NOT(R).
090205	×	IICN	4.650	D'Avanzo et al. (2010).	VLT(R,I,J,H,K_S).
090313	√	IUN	3.375	Melandri et al. (2010); Klotz et al. (2009b); Nissinen (2009); Vaalsta et al. (2009); Perley (2009); Perley et al. (2009b); Updike et al. (2009c); Morgan et al. (2009a).	FTN(R,i'); FTS(R,i'); LT(r',i'); IAC80(R); CAHA1.23m(R); CAHA3.5m(J); NOT(J,K); OSN(I); MITSuME(I); TAROT(R); Gras-04(CR); Gemini-S(g',r',i',z'); CTIO1.3m(R,J); GROND(J,H,K_S); PAIRITEL(J,H,K_S).
090323	×	0UN	3.570	Cenko et al. (2011).	P60(r',i'); Gemini-S(i',r'); TNT(R); TLS(R); RTT150(R); FTS(i',R); Nickel(R); Shajn (R); NOT(R); Gemini-N(r').
090328	×	0UN	0.736	McBreen et al. (2010)	
090418A	×	IICN	1.608		
090423	×	ICF	8.100		

Table E.20: Continued.

GRB	Opt.	XLC	z	References Optical Data	Telescopes[a] and Filters
090424	√	ICN	0.544	Schady & Cannizzo (2009); Olivares et al. (2009); Nissinen & Hentunen (2009); Im et al. (2009); Mao et al. (2009a); Cobb (2009a); Kann et al. (2010b).	UVOT(u,v,b,uvw2,uvm2,uvw1,white); GROND(g',r',i',z'.J,H,K_S); XLT(CR); Lemmon1m(R); GMG(B,V,R,I); CTIO1.3m(I,J,H,K_S); CAHA1.23m(B,R,I); TLS(R); MAO(R); CAHA2.2m(I).
090426	√	0CN	2.609	Xin et al. (2011); Nicuesa Guelbenzu et al. (2011); Antonelli et al. (2009).	Lemmon1m(R); TNT(white,R,V); GROND(g',r',i',z'.J,H,K_S); TNG(B,V,R,I); LBT(g',r',i',z').
090510 (S)	×	ICN	0.903	X	
090516	×	IICF	4.109		
090519	×	ICN	3.850	X	
090529	×	IICN	2.625		
090618	√	IICN	0.540	Cano et al. (2011b); Li et al. (2009); Morgan et al. (2009b).	AZT-11(R); BOAO (V); BTA(B,R,i'); FTN(B,V,R,i'); Gemini-N(R,i'); HCT(R); INT(R); Lemmon1m(B,R); LT(R,i'); AZT-33IK(R); OAUV(V); CrAO(B,V,R); WHT(R,i'); Z1000(V,R); KAIT(CR); PAIRITEL(J,H,K_S).
090715B	×	0CF	3.000		
090726	×	0UN	2.710	Šimon et al. (2010).	Ondrejov(CR)
090809	×	ICF	2.737		
090812	×	ICF	2.452	Cenko (2009); Smith et al. (2009); Updike et al. (2009a); Schady & Stamatikos (2009); Wren et al. (2009); Cano et al. (2009a); Haislip et al. (2009a).	P60(r',i'); LT(r'); GROND(g',r',i',z'.J,H,K_S); UVOT(u,v,b,uvw2,uvm2,uvw1,white); RAPTOR(CR); FTS(i',r'); PROMPT(U,B,V,R,I); GORT(R,I).
090814A	×	ICN	0.696		
090902B	×	0UN	1.822	Pandey et al. (2010); Cenko et al. (2011); Haislip et al. (2009b).	ROTSE(R); LT(R,i'); Nickel(R); GROND(r'); NOT(I,R,V); UKIRT(J,H); WHT(J,K); UVOT(u); Gemini-N(r'); PROMPT(B,V,R,I).
090926A	√	0UN	2.106	Cenko et al. (2011); Rau et al. (2010).	UVOT(u,v); PTOMPT(B,V,R,I); SMARTS(I,J); Gemini-S(g',r',i'); GROND(g',r',i',z'.J,H,K_S).
090926B	×	IUN	1.240		
090927	×	IUN	1.370		
091003	×	0UN	0.897		
091018	√	ICN	0.971	Wiersema et al. (2012).	GROND(g',r',i',z'.J,H,K_S); UVOT(u,v,b,uvw2,uvm2,uvw1,white); FTS(R,i');
091020	×	IICN	1.710		
091024	×	IUN	1.092	Cano et al. (2009b); Henden et al. (2009); Updike et al. (2009b); Oates & Marshall (2009); Mao et al. (2009b); Rumyantsev et al. (2009).	FTN(R); SRO(R); LOTIS(R); UVOT(b,v,uvw1,uvw2); GMG(R); ZTE(R).
091029	×	IICF	2.752	Filgas et al. (2009); Lacluyze et al. (2009); Marshall & Grupe (2009); Cobb (2009b); Christie et al. (2009).	GROND(G',R',J); PROMPT(I); UVOT(u,v,b,uvw2,uvm2,uvw1,white); CTIO1.3m(I,J); Stardome(R).
091109A	×	IICN	3.076		
091127	√	0UN	0.490	Filgas et al. (2011a); Cobb et al. (2010); Klotz et al. (2009c).	GROND(g',r',i',z'.J,H); CTIO1.3m(B,V,R,I,J,H,K); UVOT(uvw1,uvm2,u); Gemini-S(I); TAROT(R).
091208B	×	IICN	1.063		
100117A (S)	×	0CF	0.920		
100219A	×	IICN	4.670		

Table E.20: Continued.

GRB	Opt.	XLC	z	References Optical Data	Telescopes[a] and Filters
100302A	×	IICF	4.813		
100316B	×	ICN	1.180		
100316D	×	ICN	0.059	Cano et al. (2011a).	FTS(B,V,R,i'); Gemini-S(B,R,i',z'); HST(F336W,V,i',F125W,F160W).
100418A	√	IICN	0.623	Marshall et al. (2011); Klose (2010); Siegel & Marshall (2010); Siegel et al. (2010); Klein et al. (2010); Morgan et al. (2010); Rumyantsev et al. (2010); Bikmaev et al. (2010a,b,c); Moody et al. (2010); Volnova et al. (2010).	UVOT(white,u,v,b,uvw2,uvm2,,uvw1); GROND(g',r',i',z',J); GROND(g',r',i',z',J); PAIRITEL(J,H,K_S); AZT-11(R); RTT150(R); BYUWMO(B,V,R); MAO(R).
100425A	×	IIICN	1.755		
100513A	×	ICF	4.772		
100621A	×	IICN	0.542		
100724A	×	0CN	1.288		
100814A	×	IICN	1.440		
100816A (S)	×	ICF	0.803		
100901A	√	IIICF	1.408	Gorbovskoy et al. (2012); Andreev et al. (2010a,b,c,e,d); Kuroda et al. (2010b,a,c); Hentunen et al. (2010); Sahu et al. (2010b,a); Pritchard & Immler (2010); Elenin et al. (2010a,b); Kann et al. (2010a,c); Yoshida et al. (2010); Sposetti & Immler (2010); Andreev et al. (2010e).	MARSTER; NOT; OSN; Mt.Terskol(R); MIT-SuME(g',R,I); THO(clear,R,B); HCT(R,I); UVOT(white,u,v,b,uvw2,uvm2,uvw1); ISON-NM(clear); TLS1.34m(R); Kanata(R); AAVSO(R); Z2000(B,V,rGu,gGu).
100906A	×	IICF	1.727	Gorbovskoy et al. (2012); Kuroda et al. (2010d); Siegel & Markwardt (2010); Kann et al. (2010d); Kelemen et al. (2010); Tkachenko et al. (2010).	MARSTER; NOT; OSN; MITSuME(g',R,I); UVOT(u,v,b,uvw2,uvm2,uvw1); TLS(R); Kolkony(R); RTT150(R).

(a) List of the telescopes acronyms:

- ***AAVSO**: American Association of Variable Star Observers (International High Energy Network).*
- ***AEOS**: 3.6-m US Air Force Advanced Electro-Optical System telescope.*
- ***ARC**: Astrophysical Research Consortium 3.5-m telescope at Apache Point Observatory.*
- ***ARIES**: Aryabhatta Research Institute of Observational Sciences (SNT and DFOT).*
- ***ART**: Automated Response Telescope.*
- ***Asiago**: 1.82-m telescope at Cima Ekar (Asiago).*
- ***ATT2.3m**: 2.3-m Advanced Tecnology Telescope at SSO.*
- ***AZT-8**: AZT-8 70 -cm Telescope at Kharkiv observatory .*
- ***AZT-11**: 1.25-cm telescope at CrAO.*
- ***AZT-33IK**: Russian IR telescope in Sayanskaya observatory.*
- ***Banon**: T50-Banon telescope of the Observatoire de Chante-Perdrix at Banon (France).*
- ***BOAO**: 15.5-cm telescope at Bohyunsan Optical Astronomy Observatory.*
- ***Bok**: 2.3-m Bok Telescope at Kitt Peak.*
- ***BOOTES**: Burst Observer and Optical Transient Exploring System.*
- ***BTA**: Big Telescope Alt-Azimuth at SAO.*
- ***Brno**: 40-cm Newtonian telescope.*
- ***BYUWMO**: 0.91m telescope at West Mountain Observatory (Brigham Young University).*
- ***CAHA**: telescope at Calar Alto Observatory: **CAHA3.5m**, **CAHA2.2m**, **CAHA1.3m**.*
- ***CrAO**: Crimean Astrophysical Observatory 2.6-m telescope; it corresponds to **Shajin**.*
- ***Crni**: Črni Vrh Observatory.*
- ***CTIO**: Cerro Tololo Inter-American Observatories. **CTIO4m**: 4-m Victor M. Blanco telescope. **CTIO1.3m**: 1.3-m (ex-2MASS) telescope.*
- ***D1.5**: Danish 1.54-m telescope.*
- ***DAO**: 16" Dolomiti Astronomical Observatory telescope.*
- ***DFOT**: Devasthal Fast Optical telescope at ARIES.*
- ***EST**: 1-m EOS telescope.*
- ***FTN**: Faulkes Telescope North.*
- ***FTS**: Faulkes Telescope South.*
- ***GAO**: 150-cm telescope at Gamma Astronomical Observatory.*
- ***Gemini-N**: Gemini North telescope.*

- ***Gemini-S***: *Gemini South telescope.*
- ***GMG***: *2.4m telescope at Gao-Mei-Gu.*
- ***GORT***: *14" Glast Optical Robotic Telescope at Hume observatory in California.*
- ***GRAS-04***: *Global-Rent-A-Scope telescope at Mayhill (AAVSO).*
- ***GRAS-005***: *Global-Rent-A-Scope telescope at New Mexico.*
- ***GRAS-17***: *Global-Rent-A-Scope CDK17 17" telescope.*
- ***GROND***: *Gamma-Ray Burst Optical/Near-Infrared detector.*
- ***Hankasalmi***: *0.4-m telescope at Hankasalmi Observatory.*
- ***HET***: *9.2-m Hobby-Eberly Telescope.*
- ***HST***: *Hubble Space Telescope.*
- ***HCT***: *2-m Himalayan Chandra Telescope.*
- ***IAC80***: *Instituto de Astrofísica de Canarias 0.8-m telescope.*
- ***IGO***: *IUCAA Girawali 2-m Optical telescope.*
- ***IUCAA***: *Inter-University Center for Astronomy and Astrophysics.*
- ***INT***: *Isaac Newton Telescope.*
- ***IRSF***: *IRSF 1.4-m telescope at SAAO (South Africa).*
- ***ISON-NM***: *0.45-m telescope at ISON-NM observatory.*
- ***KAIT***: *Katz Automatic Imaging Telescope.*
- ***Kanata***: *Kanata 1.5-m telescope.*
- ***Keck***: *Keck telescopes.*
- ***Kiso***: *Kiso Observatory (105-cm Schmidt telescope).*
- ***Konkoly***: *60/90-cm telescope a Kolnkoly observatory.*
- ***KPNO4m***: *Mayall 4-m telescope at Kitt Peak National Observatory.*
- ***Kuiper***: *Kuiper telescope.*
- ***LBT***: *Large Binocular Telescope.*
- ***Lemmon1m***: *Mt. Lemmon 1-m telescope.*
- ***Lick***: *3-m Shane telescope at Lick Observatory.*
- ***Lightbukets***: *0.61-m Lightbukets rental telescope in Rodeo (NM).*
- ***Loiano***: *1.52-m Cassini telescope at Loiano Astronomical Observatory.*
- ***LOTIS***: *Super-LOTIS (Livermore Optical Transient Imaging System)*
- ***LT***: *Liverpool Telescope.*
- ***Lulin***: *Lulin Observatory.*
- ***Magellan1***: *Magellan 1-Baade Telescope.*
- ***MAGNUM***: *Multicolor Active Galactic Nuclei Monitoring 2-m telescope on Haleakala.*

- ***MAO**: 1.5-m telescope at Maidanak Astronomical Observatory.*
- ***MASTER**: Mobile Astronomy System of Telescope Robots.*
- ***MDM**: Michigan-Dartmouth-MIT observatory. **MDM2.4m**: 2.4-m Hiltern telescope. **MDM1.3m**: Mc Graw-Hill telescope.*
- ***Meade-35**: telescope at Terskol.*
- ***Mercator**: 1.2-m Mercator telescope.*
- ***miniTAO**: 1-m miniTAO telescope at the University of Tokyo Atacama Observatory.*
- ***MIRO**: 1.2-m telescope of Mt. Abu InfraRed Observatory (India); it corresponds to **Mt.Abu**.*
- ***MITSuME**: Multicolor Imaging Telescopes for Survey and Monstrous Explosions.*
- ***Murikabushi**: 105-cm Murikabushi telescope (Japan).*
- ***MMT**: 6.5-m telescope at the Wipple Observatory on Mount Opkins in Arizona.*
- ***Mt.Abu**: 1.2 telescope of Physical Research Laboratory at Gurushikar (Mt. Abu/India). it corresponds to **MIRO**.*
- ***Nickel**: Lick 1-m Nickel telescope.*
- ***NMSU**: NMSU 1m telescope at the Apache Point Observatory.*
- ***NOT**: Noth Optical Telescope.*
- ***NTT**: New Technology Telescope.*
- ***OAUV**: 0.4-m OAUV telescope at the Observatorio Astronomico de Aras.*
- ***OHP**: T80 telescope of the Observatoire the Haute-Provence.*
- ***Ondrejov**: 500/1975-mm Newtonian telescope in Ondrejov.*
- ***OSN**: 1.5-m telescope at Observatorio de Sierra Nevada.*
- ***P60**: Palomar 60-Inch telescope.*
- ***P200**: Palomar 200-Inch telescope.*
- ***PAIRITEL**: Peters Authomated InfraRed Imaging TELescope.*
- ***PI**: Pi of the Sky.*
- ***PROMPT**: Panchromatic Robotic Optical Monitoring and Polarimetry Telescopes.*
- ***RAPTOR**: RAPid Telescope for Optical Response.*
- ***REM**: Rapid Eye Mount.*
- ***ROTSE**: Robotic Optical Transient Search Experiment.*
- ***RTT150**: Russian-Turkish 1.5-m Telescope.*
- ***SAO**: Special Astrophysical Observatory (1-m telescope Zeiss and 6-m BTA).*
- ***SARA**: Southeastern Association for Research in Astronomy. **SARA0.5m** and **SARA0.6m** telescopes.*

- ***Skinakas***: *1.3-m telescope at Skinakas Observatory.*
- ***SMARTS***: *Small and Moderate Aperture Research Telescope System (1.3-m telescope); it corresponds to* ***CTIO1.3m****.*
- ***SNT***: *Sunpurnanand Telescope at ARIES.*
- ***SR-22***: *0.22-m telescope.*
- ***SOAR***: *4.1-m SOuthern Astrophysical Research telescope.*
- ***SRO***: *Sonoita Research Observatory 35-cm telescope.*
- ***SSO***: *Siding Spring Observatory.* ***SSO40Inch*** *and* ***ATT2.3m****.*
- ***Stardome***: *Stardome 0.4-m telescope in Auckland (New Zealand).*
- ***Subaru***: *Subaru telescope.*
- ***T100***: *1-m telescope at TUBITAK National Observatory (Turkey).*
- ***T1M***: *T1M telescope at Observatoire du Pic du Midi.*
- ***TAOS (A,B,C,D)***: *Taiwanese-American Occultation Survey Telescopes.*
- ***TAROT***: *Télescopes à Action Rapide pour les Objects Transitoires.*
- ***Terskol***: *Zeiss-600 of Mt. (Pik) Terskol observatory.*
- ***THO***: *Taurus Hill Observatory.*
- ***TLS***: *Thüringer Landessternwarte Tauteburg.* ***TLS2m*** *and* ***TLS1.34m****.*
- ***TNG***: *Telescopio Nazionale Galileo.*
- ***TNT***: *0.8-m Tsinghua-NOAC Telescope.*
- ***TORTORA***: *camera mounted on REM telescope.*
- ***UKIRT***: *United Kingdom Infra-Red Telescope.*
- ***UVOT***: *Ultra-Violet/Optical Telescope on board Swift satellite.*
- ***VLT***: *Very Large Telescope.*
- ***Watcher***: *Watcher telescope.*
- ***WHT***: *4.2-m William Herchel Telescope.*
- ***WIDGET***: *WIDe-field camera for Gamma-ray bursts Early Timing.*
- ***WIRO***: *2.3m Wyoming Infrared Observatory telescope in Wyoming (USA).*
- ***XLT***: *0.35-m C14 XLT telescope at Taurus Hill Observatory.*
- ***Z1000***: *1-m Zeiss-telescope at CrAO.*
- ***Z2000***: *telescope at Mt. Terskol.*
- ***Zadko***: *1-m Zadko telescope.*
- ***ZTE***: *1.25-m ZTE telescope at the Crimean station of the Sternberg Astronomical Institute.*

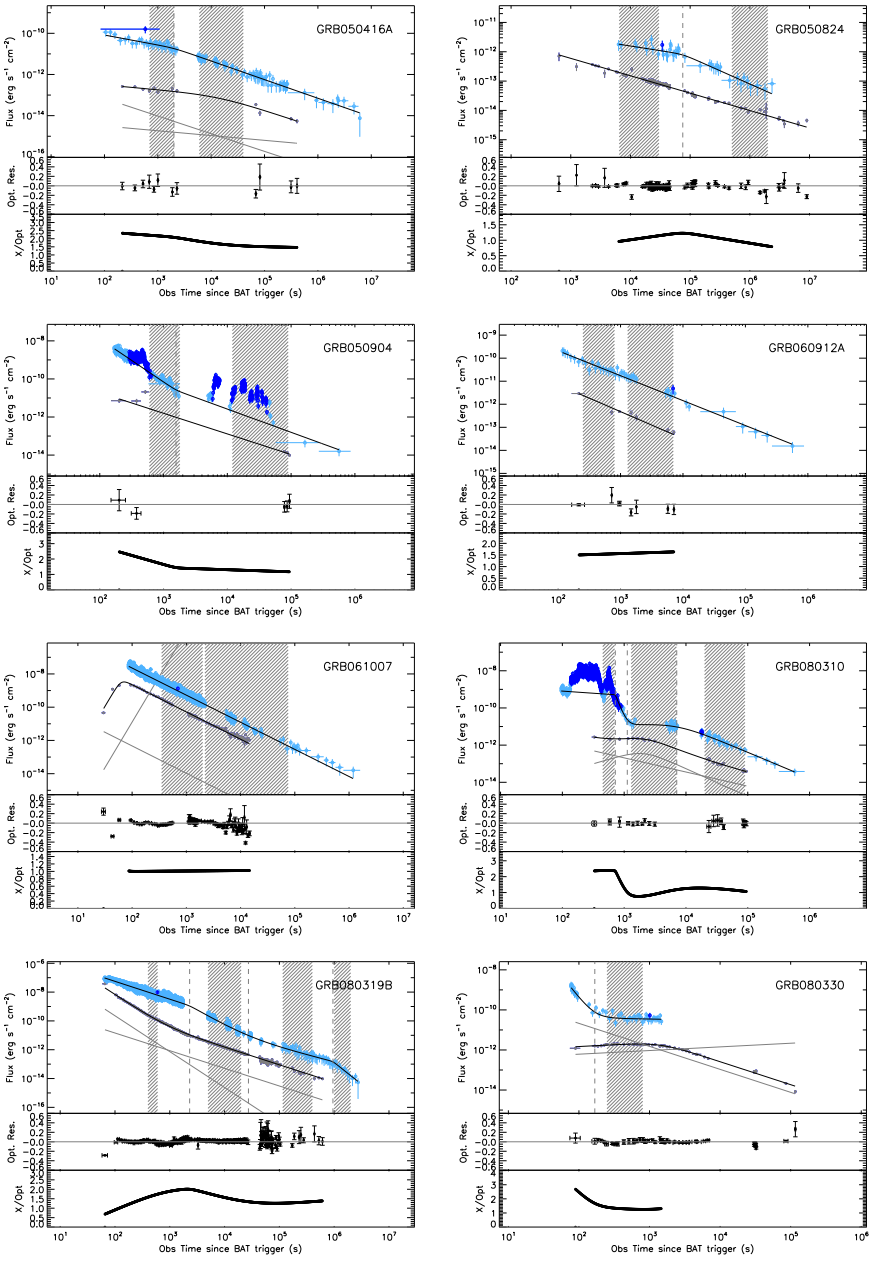

Figure E.1: Comparison between optical and X-ray LCs. *Top. Colored points*: X-ray data. Dark color represents the excesses and light colors the continuum, as calculated in M13. Group A: blue/lightblue. Group B: red/orange. Group C: purple/magenta. *Gray points*: optical data. Black solid line: fit of the data. *Gray solid line*: components of the fit function used to fit the optical data. *Middle.* Ratio between the optical data and their fit function. The points have different colors when the optical data comes from different filters. *Bottom.* Ratio between the X-ray flux and the optical flux. *Hashed gray boxes*: SED time intervals.

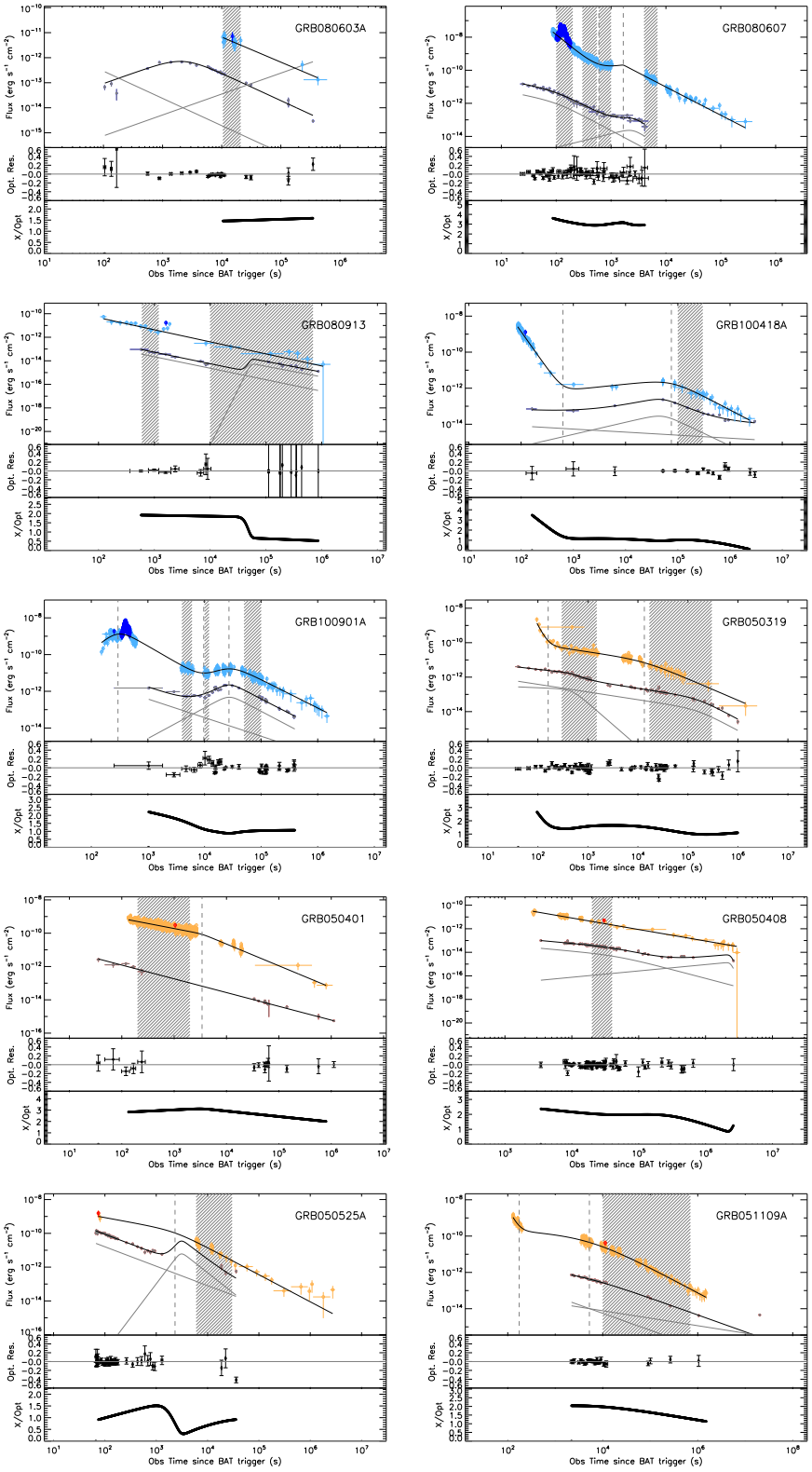

Figure E.2: Comparison between optical and X-ray LCs. Color coding as in Figure E.1.

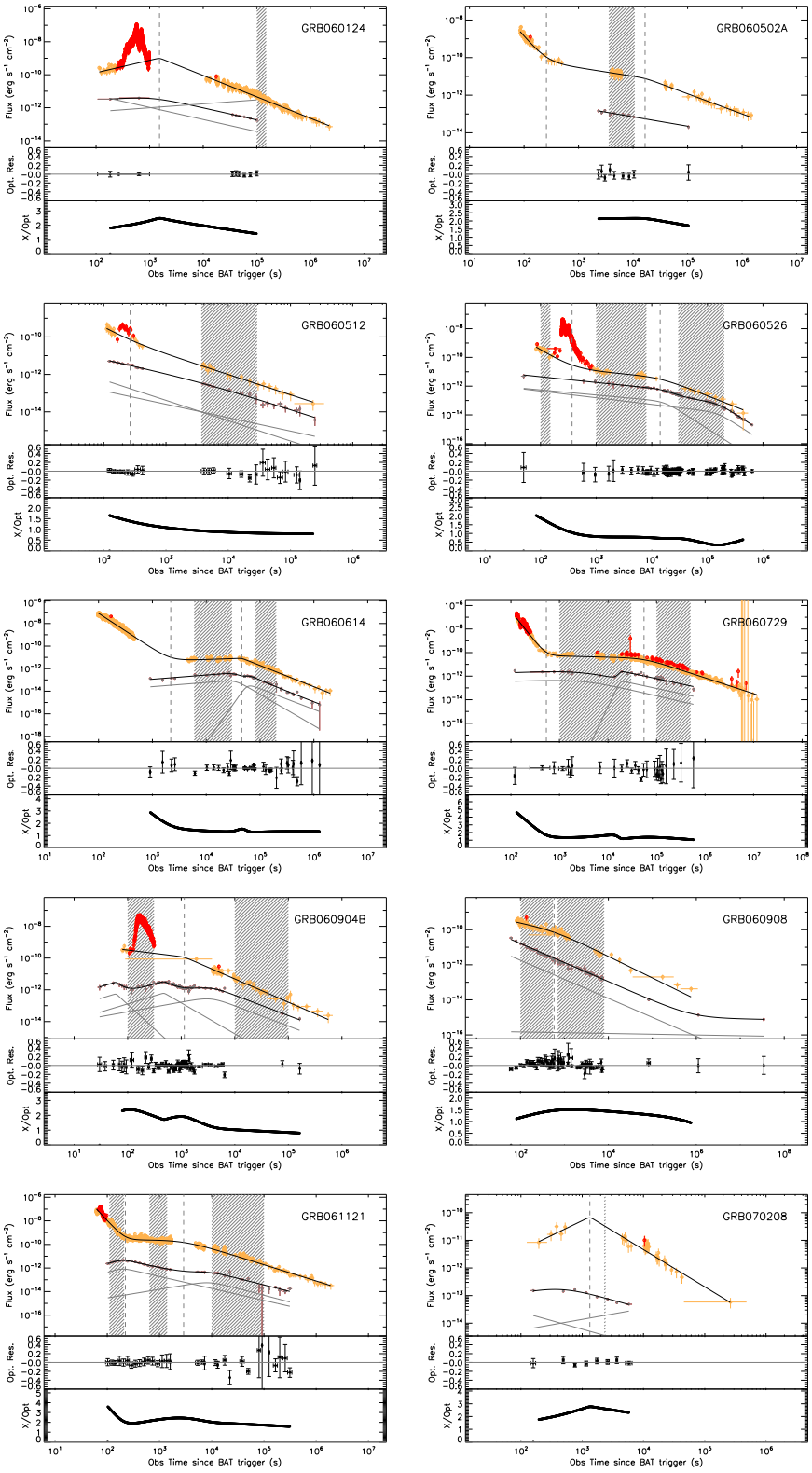

Figure E.3: Comparison between optical and X-ray LCs. Color coding as in Figure E.1.

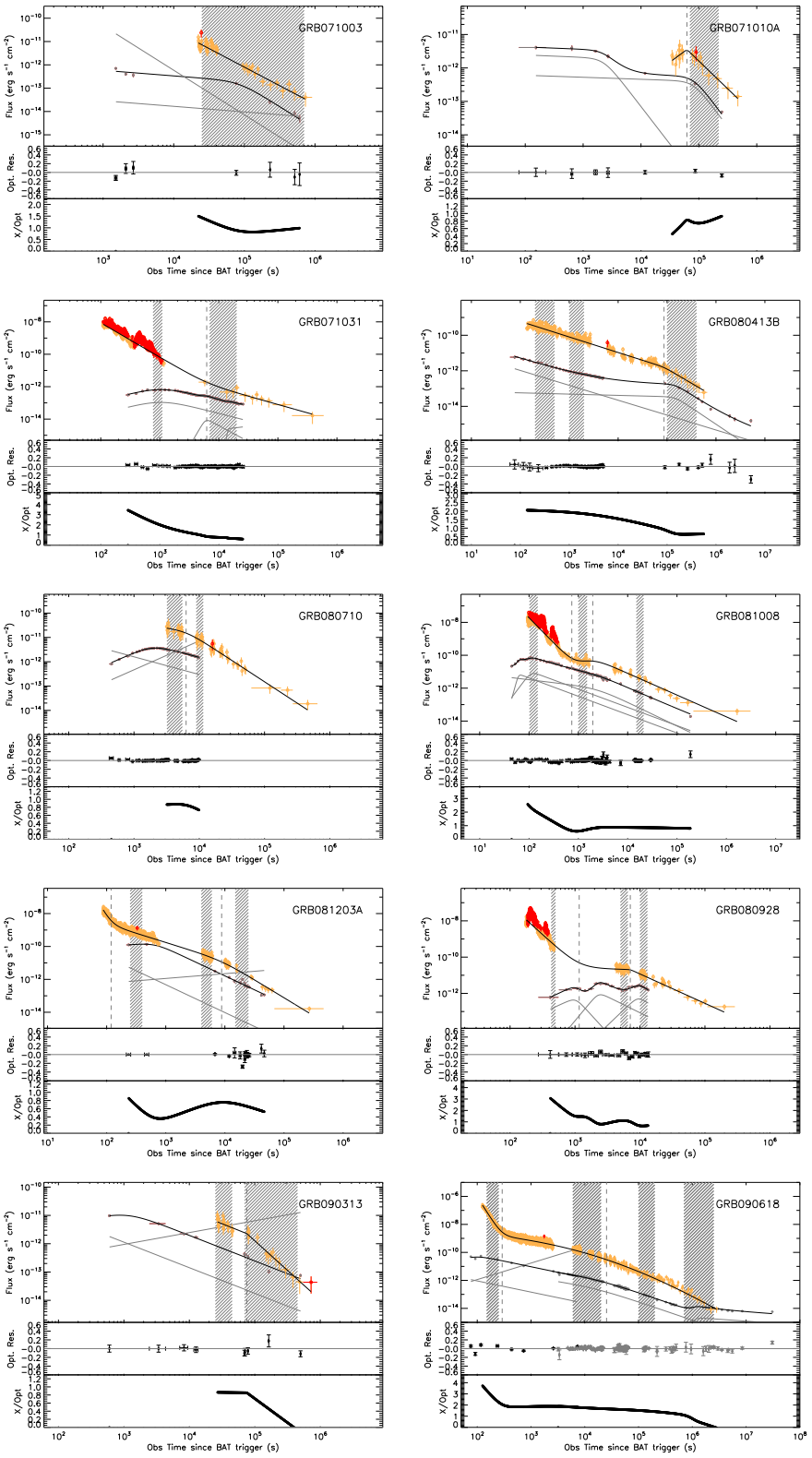

Figure E.4: Comparison between optical and X-ray LCs. Color coding as in Figure E.1.

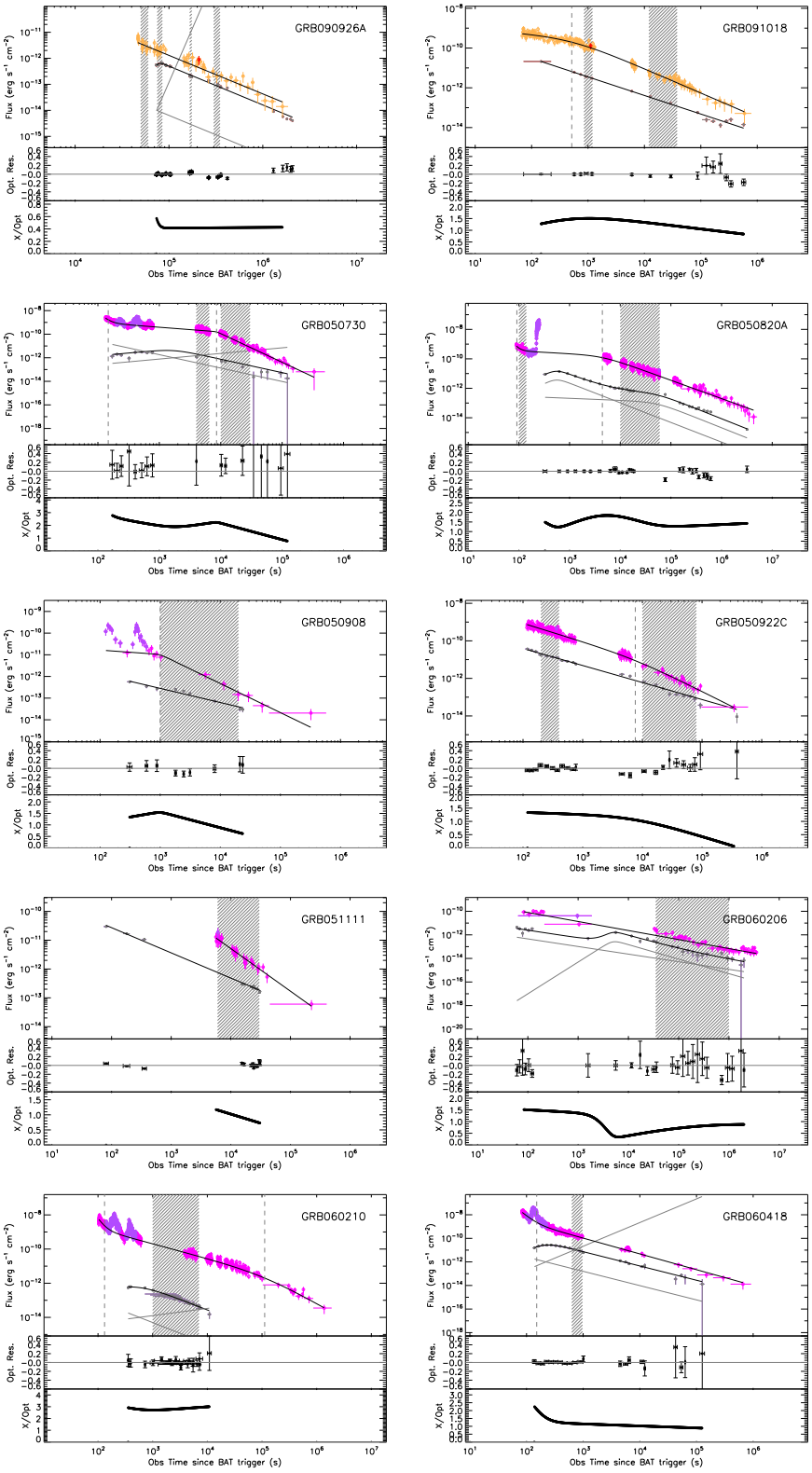

Figure E.5: Comparison between optical and X-ray LCs. Color coding as in Figure E.1.

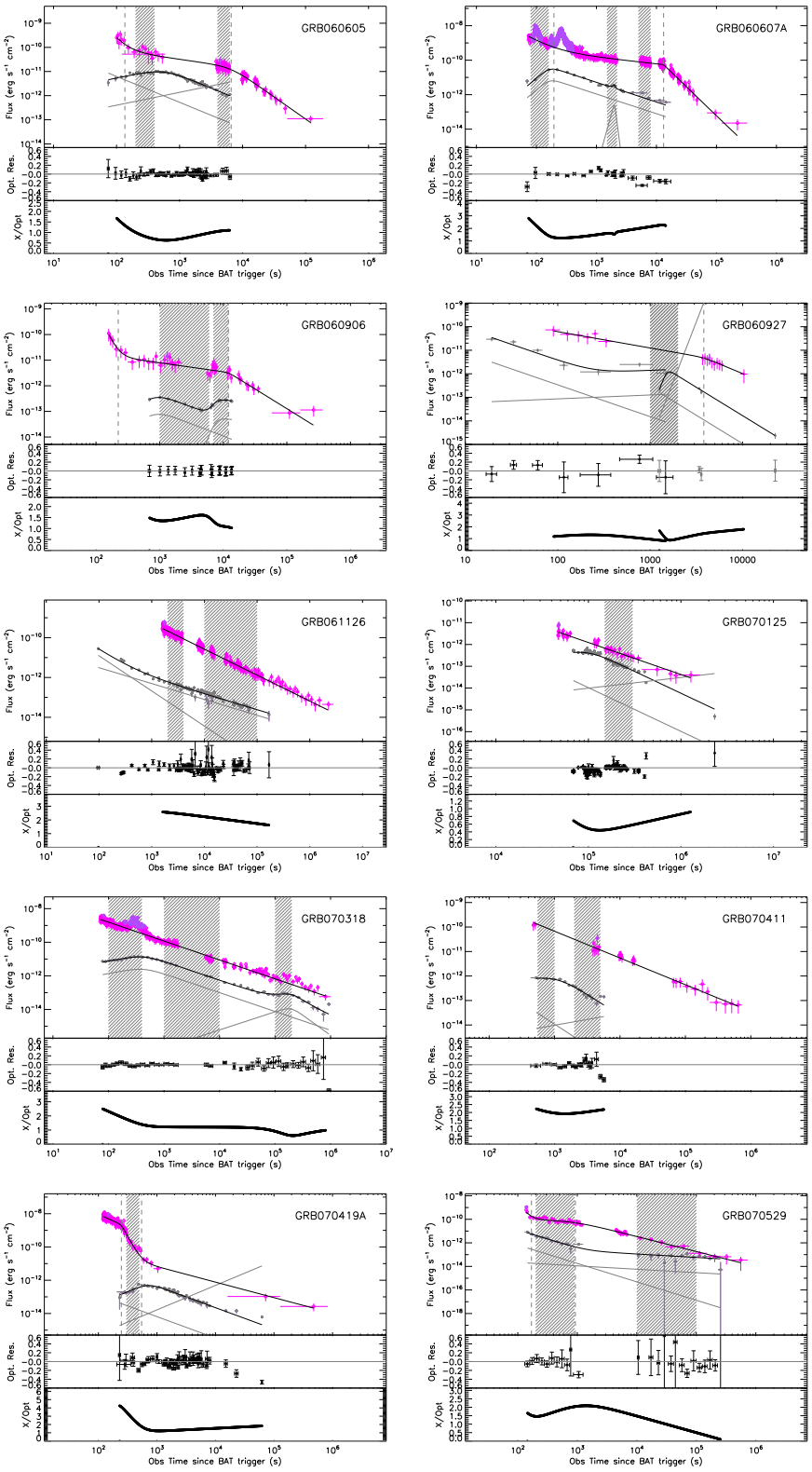

Figure E.6: Comparison between optical and X-ray LCs. Color coding as in Figure E.1.

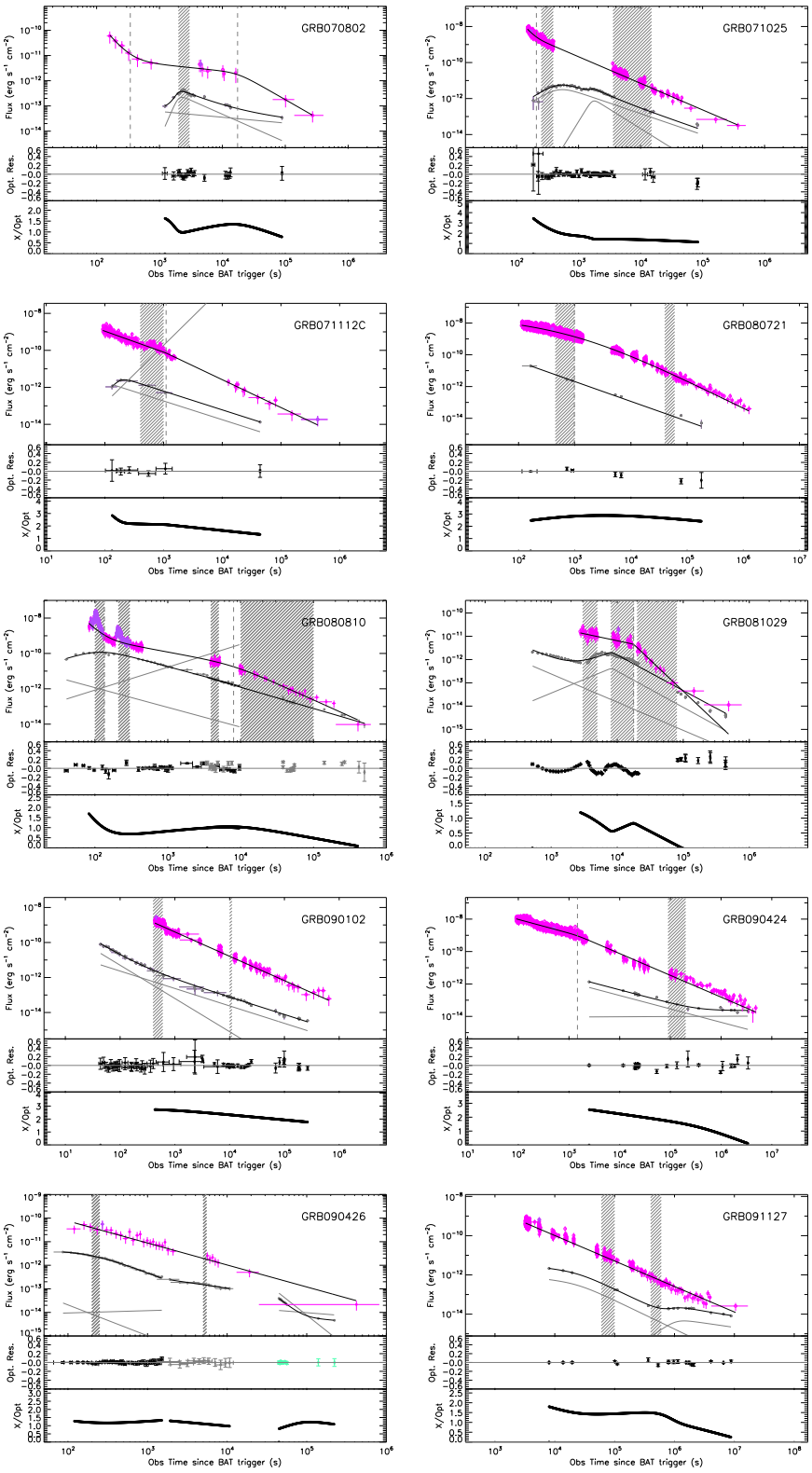

Figure E.7: Comparison between optical and X-ray LCs. Color coding as in Figure E.1.

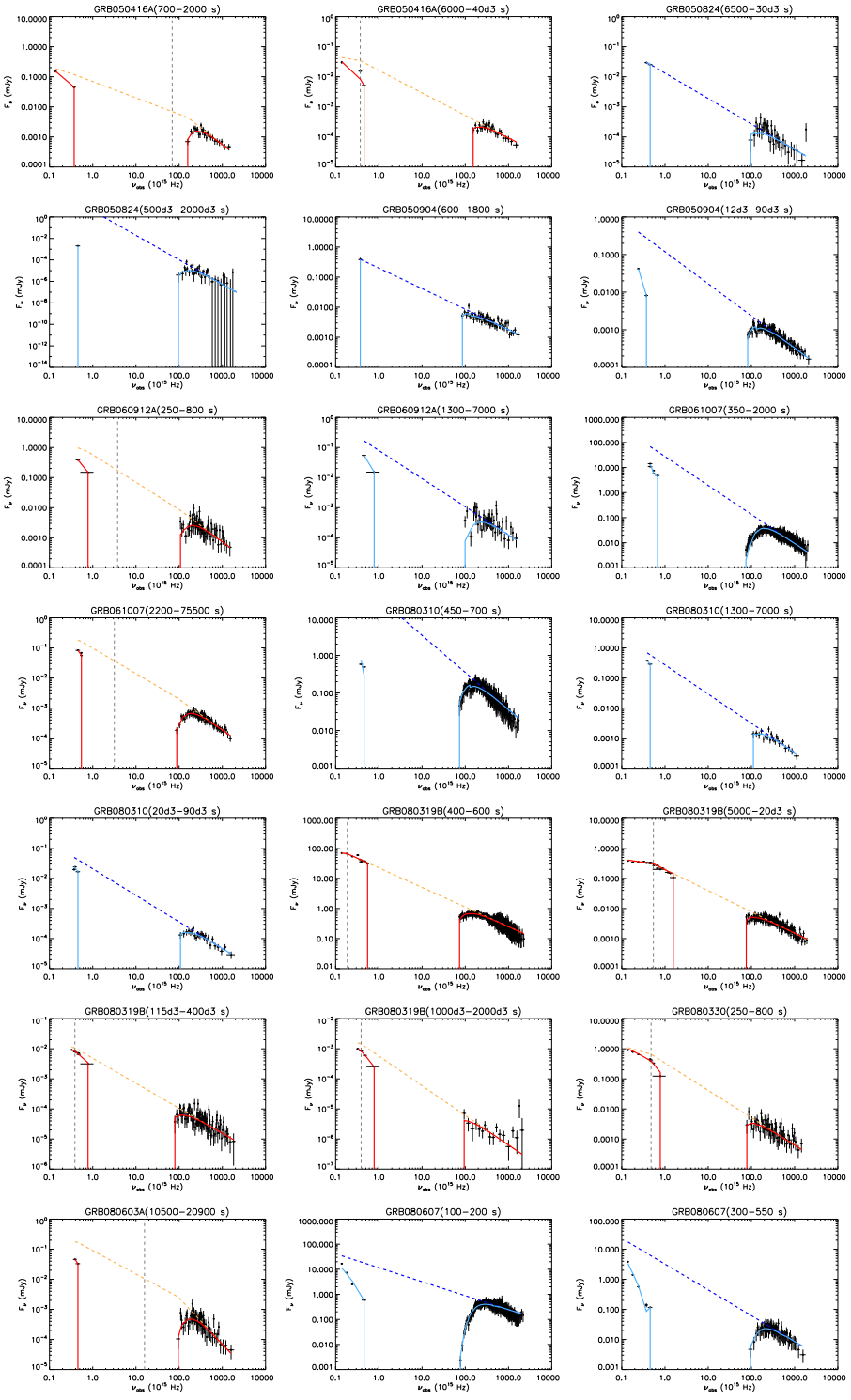

Figure E.8: Optical/X-ray SEDs for GRBs belonging to the Group A. *Solid line*: the fitting function. *Dotted line*: power-law (blue) or broken power-law (orange) fitting function. *Light blue/blue lines* stand for the power-law fitting functions. *Red/orange lines* correspond to the fitting function with the broken power-law. The decition between the two different laws follows Table E.14.

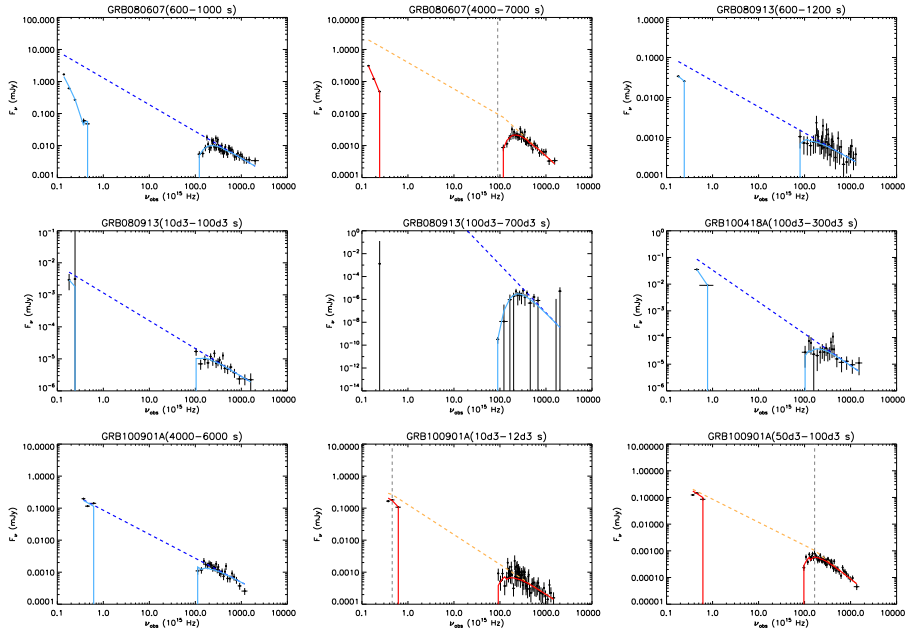

Figure E.9: Optical/X-ray SEDs for GRBs belonging to the Group A. Color coding as in Figure E.8.

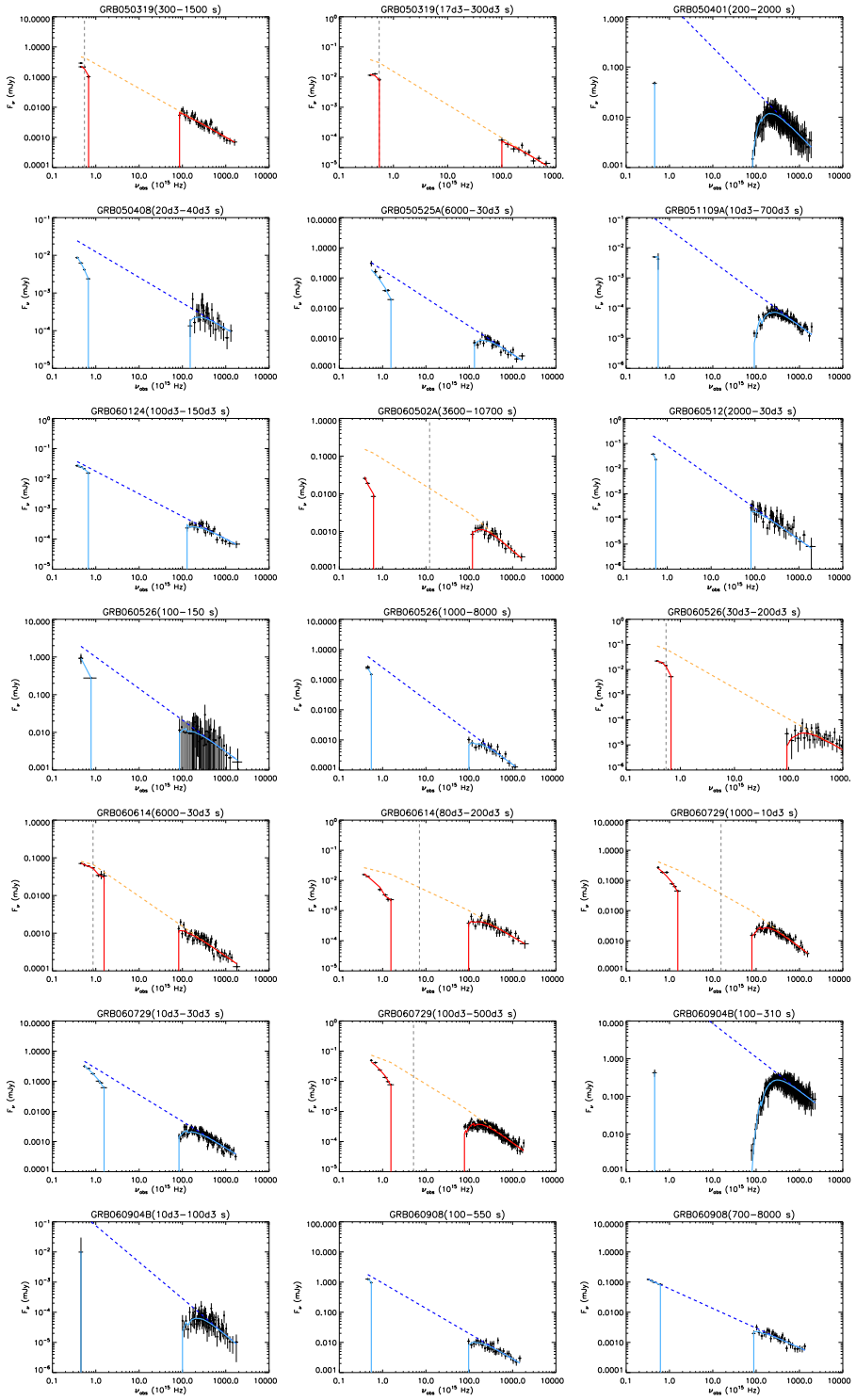

Figure E.10: Optical/X-ray SEDs for GRBs belonging to the Group B. Color coding as in Figure E.8.

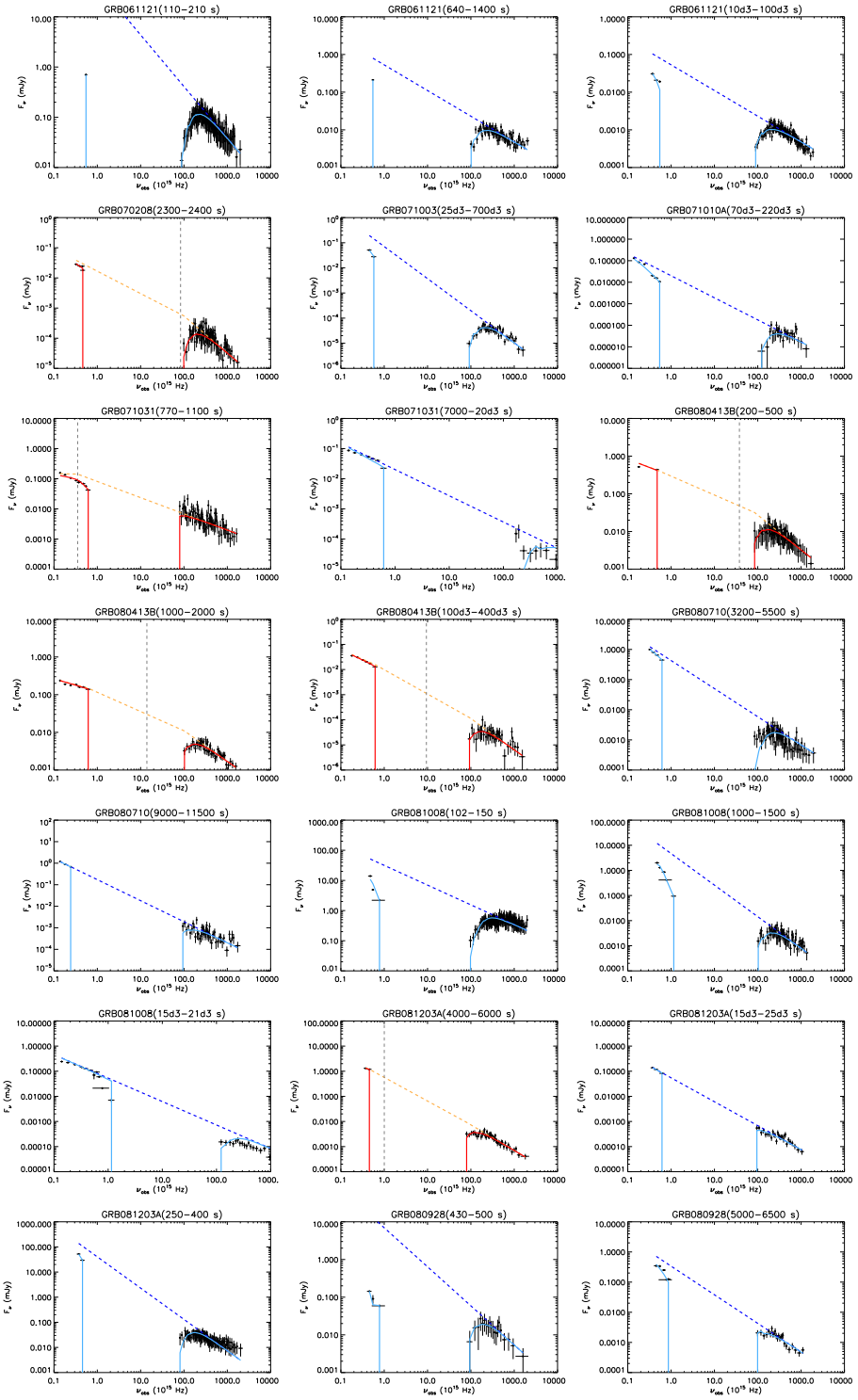

Figure E.11: Optical/X-ray SEDs for GRBs belonging to the Group B.Color coding as in Figure E.8.

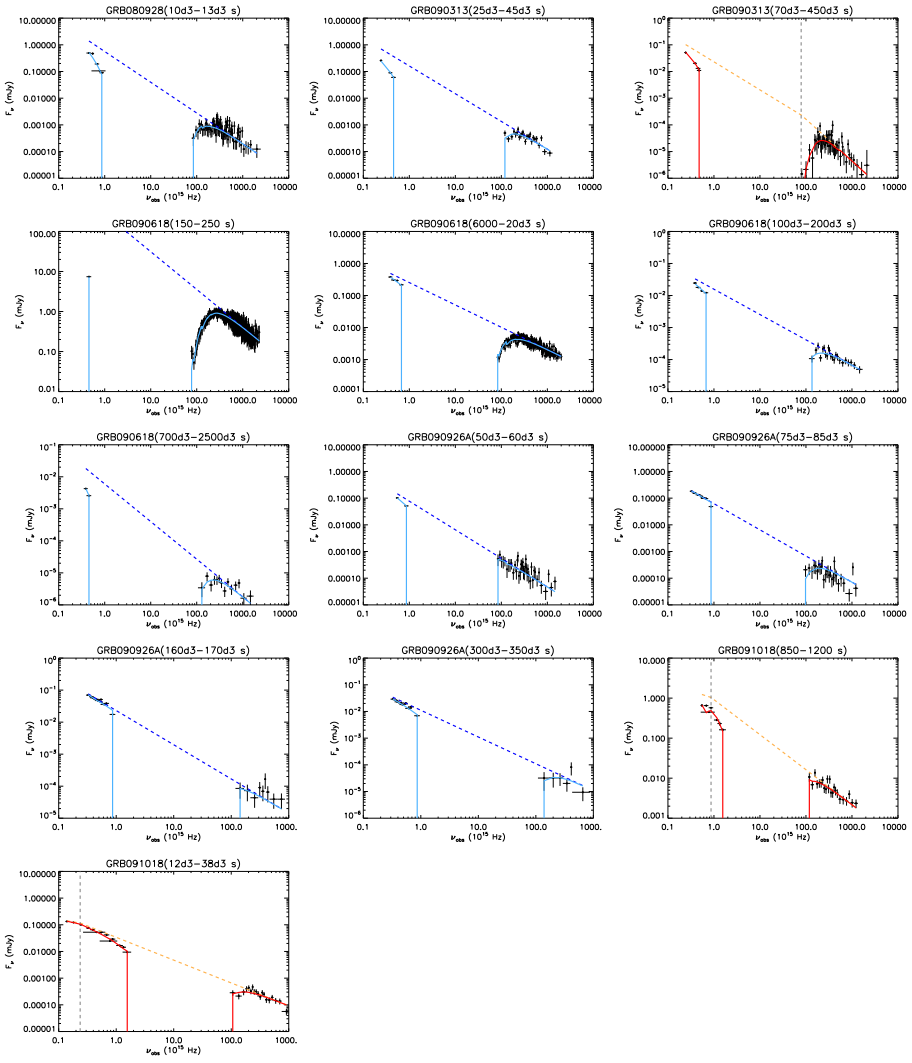

Figure E.12: Optical/X-ray SEDs for GRBs belonging to the Group B. Color coding as in Figure E.8.

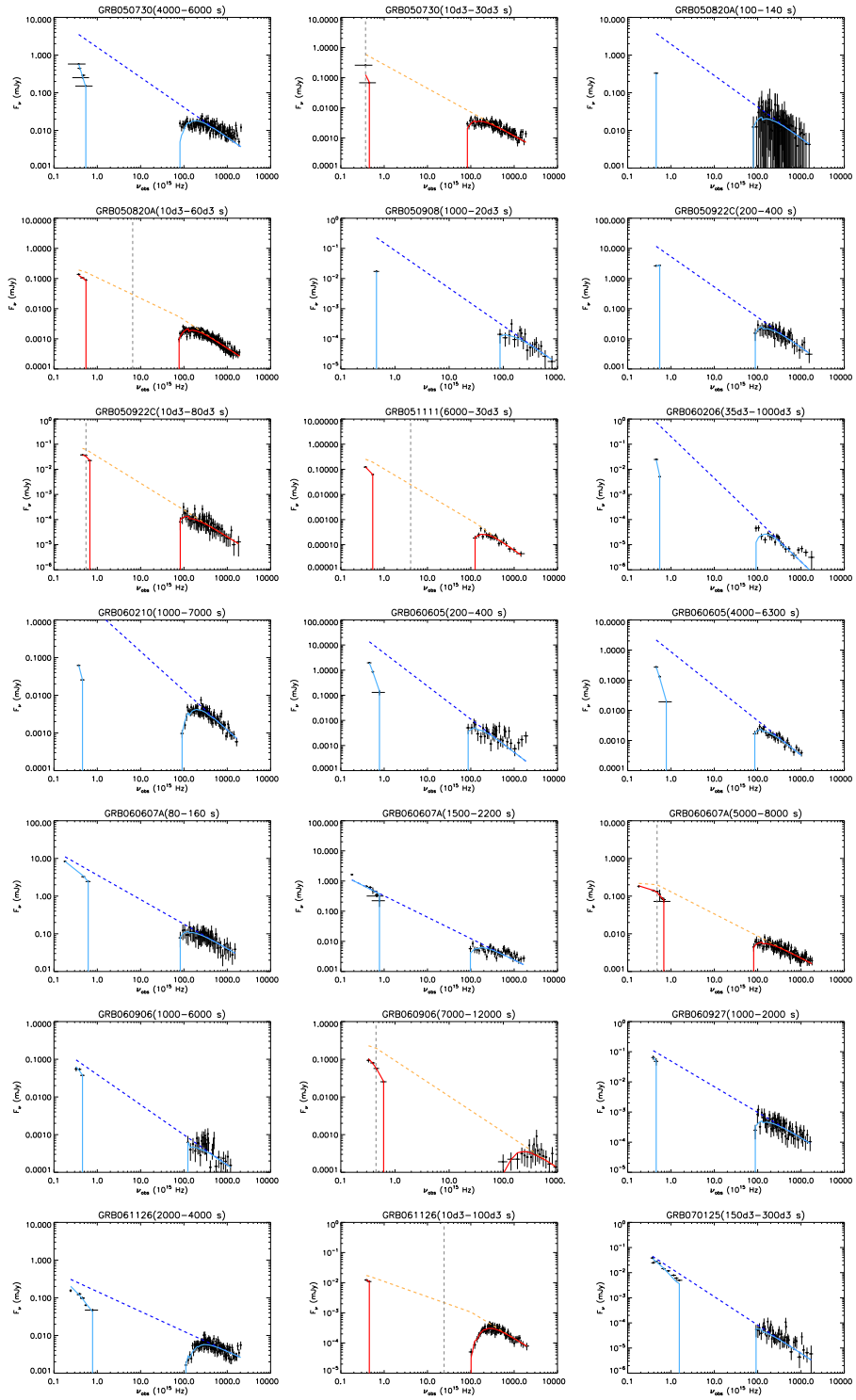

Figure E.13: Optical/X-ray SEDs for GRBs belonging to the Group C. Color coding as in Figure E.8.

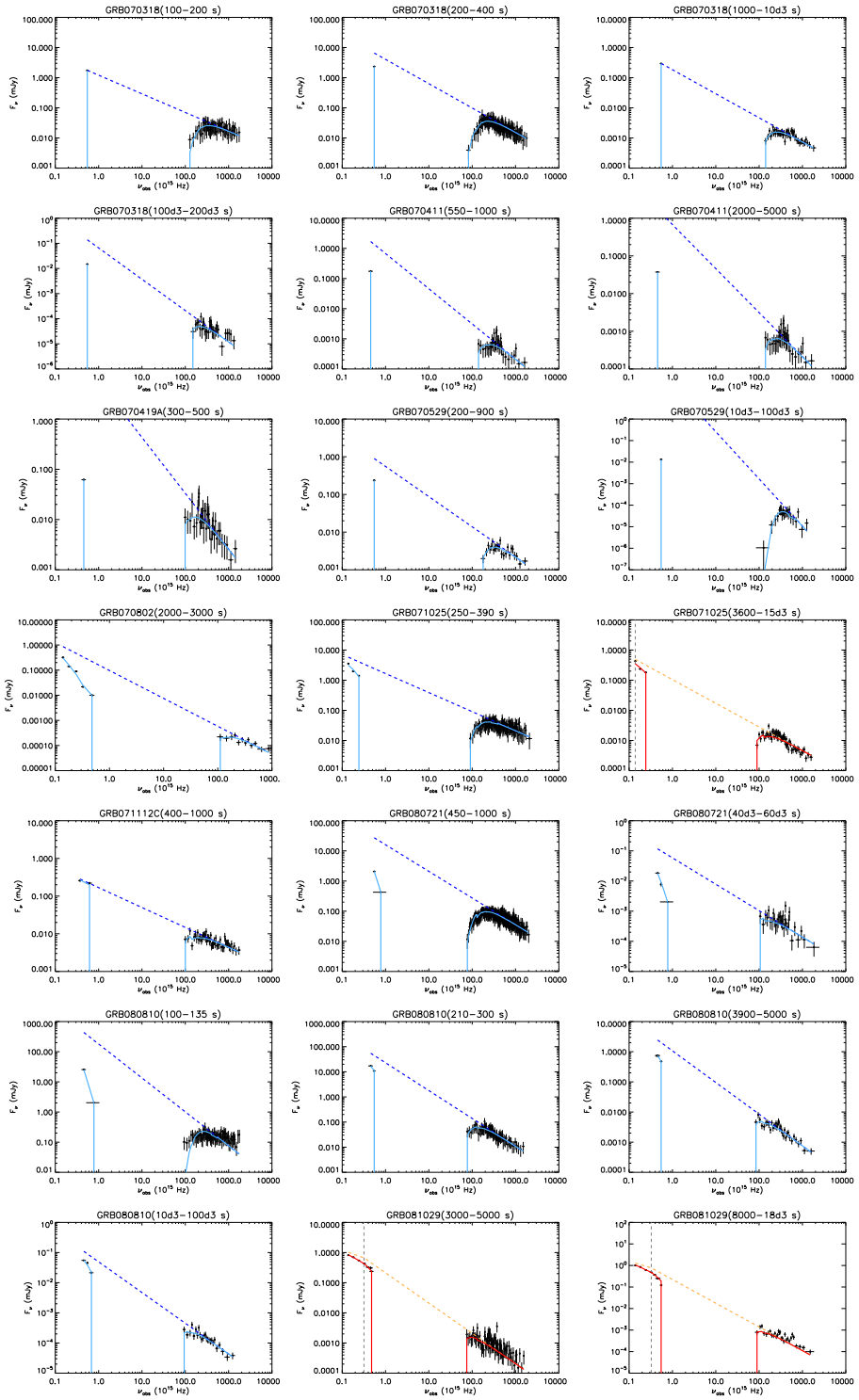

Figure E.14: Optical/X-ray SEDs for GRBs belonging to the Group C. Color coding as in Figure E.8.

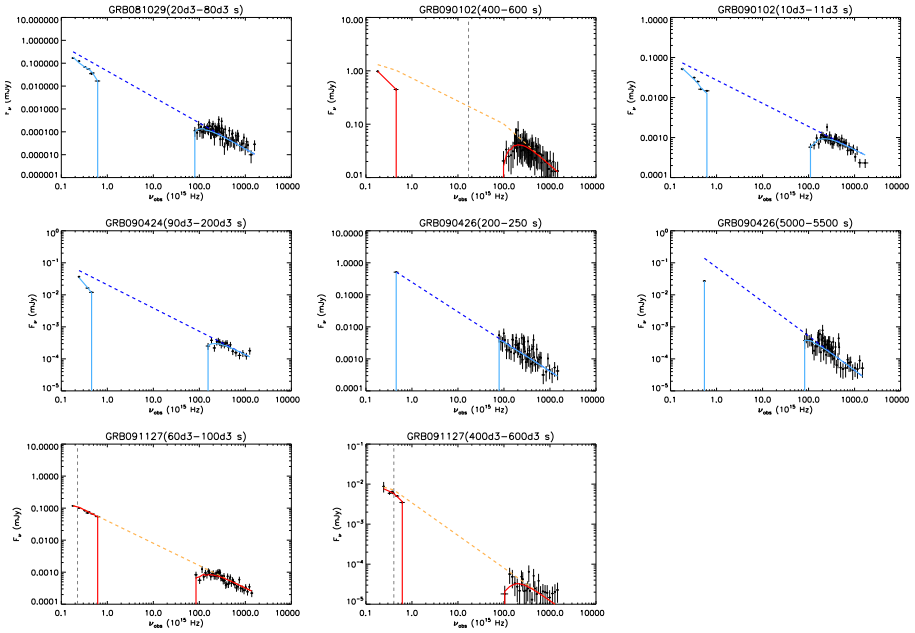

Figure E.15: Optical/X-ray SEDs for GRBs belonging to the Group C. Color coding as in Figure E.8.

Bibliography

Akerlof, C. W., Kehoe, R. L., McKay, T. A., et al. 2003, PASP, 115, 132

Amati, L. 2006, MNRAS, 372, 233

Amati, L., Frontera, F., & Guidorzi, C. 2009, A&A, 508, 173

Amati, L., Frontera, F., Tavani, M., et al. 2002, A&A, 390, 81

Amati, L., Guidorzi, C., Frontera, F., et al. 2008, MNRAS, 391, 577

Andreev, M., Sergeev, A., Babina, J., et al. 2008, GRB Coordinates Network, 7655, 1

Andreev, M., Sergeev, A., & Pozanenko, A. 2010a, GRB Coordinates Network, 11166, 1

Andreev, M., Sergeev, A., & Pozanenko, A. 2010b, GRB Coordinates Network, 11168, 1

Andreev, M., Sergeev, A., & Pozanenko, A. 2010c, GRB Coordinates Network, 11191, 1

Andreev, M., Sergeev, A., & Pozanenko, A. 2010d, GRB Coordinates Network, 11201, 1

Andreev, M., Sergeev, A., Pozanenko, A., et al. 2010e, GRB Coordinates Network, 11200, 1

Antonelli, L. A., D'Avanzo, P., Perna, R., et al. 2009, A&A, 507, L45

Asfandyarov, I., Pozanenko, A., & Ibrahimov, M. 2006, GRB Coordinates Network, 5434, 1

Band, D., Matteson, J., Ford, L., et al. 1993, ApJ, 413, 281

Barniol Duran, R. & Kumar, P. 2009, MNRAS, 395, 955

Barthelmy, S. D., Chincarini, G., Burrows, D. N., et al. 2005, Nature, 438, 994

Belczyński, K. & Kalogera, V. 2001, ApJ, 550, L183

Belczynski, K., Perna, R., Bulik, T., et al. 2006, ApJ, 648, 1110

Berger, E. 2011, NewAR, 55, 1

Berger, E., Cowie, L. L., Kulkarni, S. R., et al. 2003, ApJ, 588, 99

Bernardini, M. G., Margutti, R., Chincarini, G., Guidorzi, C., & Mao, J. 2011, A&A, 526, A27

Bernardini, M. G., Margutti, R., Mao, J., Zaninoni, E., & Chincarini, G. 2012a, A&A, 539, A3

Bernardini, M. G., Margutti, R., Zaninoni, E., & Chincarini, G. 2012b, MNRAS, 425, 1199

Bikmaev, I., Khamitov, I., Melnikov, S., et al. 2010a, GRB Coordinates Network, 10635, 1

Bikmaev, I., Khamitov, I., Melnikov, S., et al. 2010b, GRB Coordinates Network, 10643, 1

Bikmaev, I., Khamitov, I., Melnikov, S., et al. 2010c, GRB Coordinates Network, 10700, 1

Blandford, R. D. & McKee, C. F. 1976, Physics of Fluids, 19, 1130

Blandford, R. D. & Znajek, R. L. 1977, MNRAS, 179, 433

Bloom, J. S., Butler, N. R., & Perley, D. A. 2008, in American Institute of Physics Conference Series, Vol. 1000, American Institute of Physics Conference Series, ed. M. Galassi, D. Palmer, & E. Fenimore, 11–15

Bloom, J. S., Kulkarni, S. R., & Djorgovski, S. G. 2002, AJ, 123, 1111

Bloom, J. S., Perley, D. A., Li, W., et al. 2009, ApJ, 691, 723

Boër, M., Atteia, J. L., Damerdji, Y., et al. 2006, ApJ, 638, L71

Boettcher, M. & Joshi, M. 2005, GRB Coordinates Network, 4392, 1

Bohlin, R. C., Savage, B. D., & Drake, J. F. 1978, ApJ, 224, 132

Borgonovo, L. & Björnsson, C.-I. 2006, ApJ, 652, 1423

Boyd, P. T. & Marshall, F. E. 2006, GRB Coordinates Network, 5357, 1

Brainerd, J. J. 1994, in American Institute of Physics Conference Series, Vol. 307, Gamma-Ray Bursts, ed. G. J. Fishman, 346

Breeveld, A., Landsman, W., Kuin, P., & Grupe, D. 2008, GRB Coordinates Network, 8712, 1

Breeveld, A. A. 2007, GRB Coordinates Network, 7028, 1

Breeveld, A. A. & Grupe, D. 2008, GRB Coordinates Network, 8696, 1

Briggs, M. S., Band, D. L., Kippen, R. M., et al. 1999, ApJ, 524, 82

Bromm, V. & Loeb, A. 2002, ApJ, 575, 111

Brown, P. J. & Baumgartner, W. H. 2008, GRB Coordinates Network, 8340, 1

Burrows, D. N., Hill, J. E., Nousek, J. A., et al. 2005, Space Science Reviews, 120, 165

Butler, N. R. & Kocevski, D. 2007a, ApJ, 663, 407

Butler, N. R. & Kocevski, D. 2007b, ApJ, 668, 400

Butler, N. R., Li, W., Perley, D., et al. 2006, ApJ, 652, 1390

Campana, S., Lodato, G., D'Avanzo, P., et al. 2011, Nature, 480, 69

Campana, S., Salvaterra, R., Melandri, A., et al. 2012, MNRAS, 421, 1697

Campana, S., Thöne, C. C., de Ugarte Postigo, A., et al. 2010, MNRAS, 402, 2429

Cannizzo, J. K. & Gehrels, N. 2009, ApJ, 700, 1047

Cannizzo, J. K., Troja, E., & Gehrels, N. 2011, ApJ, 734, 35

Cano, Z., Bersier, D., Guidorzi, C., et al. 2011a, ApJ, 740, 41

Cano, Z., Bersier, D., Guidorzi, C., et al. 2011b, MNRAS, 413, 669

Cano, Z., Guidorzi, C., Mundell, C., et al. 2009a, GRB Coordinates Network, 9779, 1

Cano, Z., Guidorzi, C., Mundell, C. G., et al. 2009b, GRB Coordinates Network, 10066, 1

Castro Cerón, J. M., Michałowski, M. J., Hjorth, J., et al. 2010, ApJ, 721, 1919

Castro Cerón, J. M., Michałowski, M. J., Hjorth, J., et al. 2006, ApJ, 653, L85

Cenko, S. B. 2009, GRB Coordinates Network, 9769, 1

Cenko, S. B., Frail, D. A., Harrison, F. A., et al. 2011, ApJ, 732, 29

Cenko, S. B., Frail, D. A., Harrison, F. A., et al. 2010, ApJ, 711, 641

Cenko, S. B., Kasliwal, M., Harrison, F. A., et al. 2006, ApJ, 652, 490

Cenko, S. B., Kelemen, J., Harrison, F. A., et al. 2009a, ApJ, 693, 1484

Cenko, S. B., Kelemen, J., Harrison, F. A., et al. 2009b, ApJ, 693, 1484

Chandra, P., Cenko, S. B., Frail, D. A., et al. 2008, ApJ, 683, 924

Chandra, P. & Frail, D. A. 2012, ApJ, 746, 156

Chevalier, R. A. & Li, Z.-Y. 1999, ApJ, 520, L29

Chevalier, R. A. & Li, Z.-Y. 2000, ApJ, 536, 195

Chincarini, G., Mao, J., Margutti, R., et al. 2010a, MNRAS, 406, 2113

Chincarini, G., Moretti, A., Romano, P., et al. 2007, ApJ, 671, 1903

Chincarini, G., Zannoni, M., Covino, S., et al. 2010b, ArXiv e-prints

Chincarini, G., Zerbi, F., Antonelli, A., et al. 2003, The Messenger, 113, 40

Christensen, L., Hjorth, J., & Gorosabel, J. 2004, A&A, 425, 913

Christie, G. W., Dong, S., de Ugarte Postigo, A., & Natusch, T. 2009, GRB Coordinates Network, 10137, 1

Clemens, C., Kruehler, T., Greiner, J., et al. 2008a, GRB Coordinates Network, 7834, 1

Clemens, C., Kupcu Yoldas, A., Greiner, J., et al. 2008b, GRB Coordinates Network, 7851, 1

Cobb, B. E. 2006, GRB Coordinates Network, 5323, 1

Cobb, B. E. 2008a, GRB Coordinates Network, 7609, 1

Cobb, B. E. 2008b, GRB Coordinates Network, 8339, 1

Cobb, B. E. 2008c, GRB Coordinates Network, 8547, 1

Cobb, B. E. 2009a, GRB Coordinates Network, 9313, 1

Cobb, B. E. 2009b, GRB Coordinates Network, 10111, 1

Cobb, B. E., Bailyn, C. D., van Dokkum, P. G., & Natarajan, P. 2006, ApJ, 651, L85

Cobb, B. E., Bloom, J. S., Perley, D. A., et al. 2010, ApJ, 718, L150

Corsi, A. & Mészáros, P. 2009, ApJ, 702, 1171

Costa, E., Frontera, F., Heise, J., et al. 1997, Nature, 387, 783

Covino, S., Campana, S., Conciatore, M. L., et al. 2010, A&A, 521, A53

Covino, S., D'Avanzo, P., Klotz, A., et al. 2008, MNRAS, 388, 347

Cucchiara, A., Cenko, S. B., Bloom, J. S., et al. 2011a, ApJ, 743, 154

Cucchiara, A., Levan, A. J., Fox, D. B., et al. 2011b, ApJ, 736, 7

Cui, X.-H., Liang, E.-W., Lv, H.-J., Zhang, B.-B., & Xu, R.-X. 2010, MNRAS, 401, 1465

Curran, P. A., van der Horst, A. J., Beardmore, A. P., et al. 2007a, A&A, 467, 1049

Curran, P. A., van der Horst, A. J., Wijers, R. A. M. J., et al. 2007b, MNRAS, 381, L65

Dado, S. & Dar, A. 2010, ApJ, 708, L112

D'Agostini, G. 2005, ArXiv Physics e-prints

Dai, X., Halpern, J. P., Morgan, N. D., et al. 2007, ApJ, 658, 509

Dai, Z. G. & Lu, T. 1998, A&A, 333, L87

Dainotti, M. G., Cardone, V. F., & Capozziello, S. 2008, MNRAS, 391, L79

Dainotti, M. G., Ostrowski, M., & Willingale, R. 2011, MNRAS, 418, 2202

Dainotti, M. G., Willingale, R., Capozziello, S., Fabrizio Cardone, V., & Ostrowski, M. 2010, ApJ, 722, L215

Dale, D., Barlow, R., Paul, C., et al. 2005, GRB Coordinates Network, 3957, 1

Dall'Osso, S., Stratta, G., Guetta, D., et al. 2011, A&A, 526, A121

D'Avanzo, P., Malesani, D., Covino, S., et al. 2009, A&A, 498, 711

D'Avanzo, P., Perri, M., Fugazza, D., et al. 2010, A&A, 522, A20

De Pasquale, M., Beardmore, A. P., Barthelmy, S. D., et al. 2006, MNRAS, 365, 1031

de Pasquale, M. & Parsons, A. 2008, GRB Coordinates Network, 8603, 1

de Ugarte Postigo, A., Fatkhullin, T. A., Jóhannesson, G., et al. 2007, A&A, 462, L57

de Ugarte Postigo, A., Lundgren, A., Martín, S., et al. 2012, A&A, 538, A44

Della Valle, M., Chincarini, G., Panagia, N., et al. 2006, Nature, 444, 1050

Deng, J., Zheng, W., Zhai, M., et al. 2009, ArXiv e-prints

Dintinjana, B., Maticic, S., Mikuz, H., & Skvarc, J. 2007, GRB Coordinates Network, 7078, 1

Draine, B. T. 2003, ARA&A, 41, 241

Drenkhahn, G. & Spruit, H. C. 2002, A&A, 391, 1141

Duncan, R. C. & Thompson, C. 1992, ApJ, 392, L9

Durig, D. T., McLarty, N. P., & Manning, J. R. 2005, GRB Coordinates Network, 3950, 1

Eichler, D., Livio, M., Piran, T., & Schramm, D. N. 1989, Nature, 340, 126

Elenin, L., Molotov, I., & Pozanenko, A. 2010a, GRB Coordinates Network, 11184, 1

Elenin, L., Molotov, I., & Pozanenko, A. 2010b, GRB Coordinates Network, 11234, 1

Elíasdóttir, Á., Fynbo, J. P. U., Hjorth, J., et al. 2009, ApJ, 697, 1725

Evans, P. A., Beardmore, A. P., Page, K. L., et al. 2009, MNRAS, 397, 1177

Evans, P. A., Beardmore, A. P., Page, K. L., et al. 2007, A&A, 469, 379

Falcone, A. D., Burrows, D. N., Lazzati, D., et al. 2006, ApJ, 641, 1010

Falcone, A. D., Morris, D., Racusin, J., et al. 2007, ApJ, 671, 1921

Fan, Y. & Piran, T. 2006, MNRAS, 369, 197

Fenimore, E. E. & Ramirez-Ruiz, E. 2000, ArXiv Astrophysics e-prints

Ferrero, P., Kann, D. A., Zeh, A., et al. 2006, A&A, 457, 857

Ferrero, P., Klose, S., Kann, D. A., et al. 2009, A&A, 497, 729

Filgas, R., Greiner, J., Schady, P., et al. 2011a, A&A, 535, A57

Filgas, R., Krühler, T., Greiner, J., et al. 2011b, A&A, 526, A113

Filgas, R., Updike, A., & Greiner, J. 2009, GRB Coordinates Network, 10098, 1

Firmani, C., Ghisellini, G., Avila-Reese, V., & Ghirlanda, G. 2006, MNRAS, 370, 185

Foley, R. J., Perley, D. A., Pooley, D., et al. 2006, ApJ, 645, 450

Fong, W., Berger, E., & Fox, D. B. 2010, ApJ, 708, 9

Frail, D. A., Kulkarni, S. R., Nicastro, L., Feroci, M., & Taylor, G. B. 1997, Nature, 389, 261

Freedman, D. L. & Waxman, E. 2001, ApJ, 547, 922

Fruchter, A. S., Levan, A. J., Strolger, L., et al. 2006, Nature, 441, 463

Fruchter, A. S., Thorsett, S. E., Metzger, M. R., et al. 1999, ApJ, 519, L13

Fryer, C. L., Woosley, S. E., & Hartmann, D. H. 1999, ApJ, 526, 152

Fryer, C. L., Woosley, S. E., & Heger, A. 2001, ApJ, 550, 372

Fukugita, M., Shimasaku, K., & Ichikawa, T. 1995, PASP, 107, 945

Fynbo, J. P. U., Jakobsson, P., Möller, P., et al. 2003, A&A, 406, L63

Fynbo, J. P. U., Jakobsson, P., Prochaska, J. X., et al. 2009, ApJS, 185, 526

Fynbo, J. P. U., Prochaska, J. X., Sommer-Larsen, J., Dessauges-Zavadsky, M., & Møller, P. 2008, ApJ, 683, 321

Fynbo, J. P. U., Watson, D., Thöne, C. C., et al. 2006, Nature, 444, 1047

Fynbo, J. U., Gorosabel, J., Dall, T. H., et al. 2001, A&A, 373, 796

Gehrels, N., Barthelmy, S. D., Burrows, D. N., et al. 2008, ApJ, 689, 1161

Gehrels, N., Chincarini, G., Giommi, P., et al. 2004, ApJ, 611, 1005

Gendre, B., Klotz, A., Palazzi, E., et al. 2010, MNRAS, 405, 2372

George, K., Banerjee, D. P. K., Chandrasekhar, T., & Ashok, N. M. 2006, ApJ, 640, L13

Ghirlanda, G., Ghisellini, G., & Lazzati, D. 2004, ApJ, 616, 331

Ghirlanda, G., Nava, L., Ghisellini, G., et al. 2012, MNRAS, 420, 483

Ghisellini, G. & Celotti, A. 1999, ApJ, 511, L93

Ghisellini, G., Ghirlanda, G., Mereghetti, S., et al. 2006, MNRAS, 372, 1699

Ghisellini, G., Ghirlanda, G., Nava, L., & Celotti, A. 2010, MNRAS, 403, 926

Ghisellini, G., Ghirlanda, G., & Tavecchio, F. 2007, MNRAS, 382, L77

Ghisellini, G., Nardini, M., Ghirlanda, G., & Celotti, A. 2009, MNRAS, 393, 253

Giannios, D. 2006, A&A, 455, L5

Giannios, D. 2012, MNRAS, 422, 3092

Goad, M. R., Tagliaferri, G., Page, K. L., et al. 2006, A&A, 449, 89

Gomboc, A., Guidorzi, C., Melandri, A., et al. 2008a, GRB Coordinates Network, 7625, 1

Gomboc, A., Guidorzi, C., Melandri, A., et al. 2008b, GRB Coordinates Network, 7626, 1

Gomboc, A., Guidorzi, C., Mundell, C. G., et al. 2006, Nuovo Cimento B Serie, 121, 1303

Gomboc, A., Kobayashi, S., Guidorzi, C., et al. 2008c, ApJ, 687, 443

Goodman, J. 1986, ApJ, 308, L47

Gorbovskoy, E. S., Lipunova, G. V., Lipunov, V. M., et al. 2012, MNRAS, 421, 1874

Gou, L.-J., Fox, D. B., & Mészáros, P. 2007, ApJ, 668, 1083

Graham, J. F., Fruchter, A. S., Levan, A. J., et al. 2009, ApJ, 698, 1620

Granot, J., Königl, A., & Piran, T. 2006, MNRAS, 370, 1946

Granot, J., Piran, T., & Sari, R. 1999, ApJ, 513, 679

Granot, J., Piran, T., & Sari, R. 2000, ApJ, 534, L163

Greco, G., Terra, F., Bartolini, C., et al. 2007, GRB Coordinates Network, 7089, 1

Greiner, J., Bornemann, W., Clemens, C., et al. 2008, PASP, 120, 405

Greiner, J., Krühler, T., Fynbo, J. P. U., et al. 2009a, ApJ, 693, 1610

Greiner, J., Krühler, T., Klose, S., et al. 2011a, A&A, 526, A30

Greiner, J., Krühler, T., Klose, S., et al. 2011b, A&A, 526, A30

Greiner, J., Krühler, T., McBreen, S., et al. 2009b, ApJ, 693, 1912

Grindlay, J., Portegies Zwart, S., & McMillan, S. 2006, Nature Physics, 2, 116

Grupe, D., Brown, P. J., Cummings, J., et al. 2006, ApJ, 645, 464

Grupe, D., Gronwall, C., Wang, X.-Y., et al. 2007, ApJ, 662, 443

Guidorzi, C., Clemens, C., Kobayashi, S., et al. 2009, A&A, 499, 439

Guidorzi, C., Gomboc, A., Kobayashi, S., et al. 2007, A&A, 463, 539

Guidorzi, C., Kobayashi, S., Perley, D. A., et al. 2011, MNRAS, 417, 2124

Guidorzi, C. & Steele, I. 2008, GRB Coordinates Network, 8064, 1

Haislip, J., Reichart, D., Ivarsen, K., et al. 2009a, GRB Coordinates Network, 9999, 1

Haislip, J., Reichart, D., Ivarsen, K., et al. 2009b, GRB Coordinates Network, 9916, 1

Haislip, J. B., Nysewander, M. C., Reichart, D. E., et al. 2006, Nature, 440, 181

Halpern, J. & Armstrong, E. 2006a, GRB Coordinates Network, 5853, 1

Halpern, J. & Armstrong, E. 2006b, GRB Coordinates Network, 5851, 1

Halpern, J. P., Mirabal, N., & Armstrong, E. 2006a, GRB Coordinates Network, 5847, 1

Halpern, J. P., Mirabal, N., & Armstrong, E. 2006b, GRB Coordinates Network, 5840, 1

Henden, A., Gross, J., Denny, B., Terrell, D., & Cooney, W. 2009, GRB Coordinates Network, 10073, 1

Hentunen, V.-P., Nissinen, M., & Salmi, T. 2010, GRB Coordinates Network, 11173, 1

Hentunen, V.-P., Oksanen, A., & Kehusmaa, P. 2008, GRB Coordinates Network, 7484, 1

Hjorth, J., Malesani, D., Jakobsson, P., et al. 2012, ApJ, 756, 187

Holland, S. T., Boyd, P. T., Gorosabel, J., et al. 2007, AJ, 133, 122

Holland, S. T., De Pasquale, M., Mao, J., et al. 2012, ApJ, 745, 41

Holland, S. T. & Pagani, C. 2008, GRB Coordinates Network, 7497, 1

Hoversten, E. A. & Cummings, J. R. 2008, GRB Coordinates Network, 7398, 1

Huang, K. Y., Urata, Y., Kuo, P. H., et al. 2007, ApJ, 654, L25

Hurkett, C. P., Osborne, J. P., Page, K. L., et al. 2006, MNRAS, 368, 1101

Im, M., Jeon, Y., Park, W., et al. 2009, GRB Coordinates Network, 9275, 1

Ishimura, T., Kawai, N., Kotani, T., et al. 2008, in American Institute of Physics Conference Series, Vol. 1000, American Institute of Physics Conference Series, ed. M. Galassi, D. Palmer, & E. Fenimore, 261–264

Ishimura, T., Shimokawabe, T., Mori, Y., et al. 2007, GRB Coordinates Network, 7087, 1

Isogai, M. & Kawai, N. 2008, GRB Coordinates Network, 8629, 1

Jakobsson, P., Björnsson, G., Fynbo, J. P. U., et al. 2005, MNRAS, 362, 245

Jakobsson, P., Fynbo, J. P. U., Hjorth, J., et al. 2006a, GRB Coordinates Network, 5337, 1

Jakobsson, P., Fynbo, J. P. U., Tanvir, N., et al. 2006b, GRB Coordinates Network, 5355, 1

Jakobsson, P., Hjorth, J., Fynbo, J. P. U., et al. 2004, ApJ, 617, L21

Jakobsson, P., Hjorth, J., Malesani, D., et al. 2012, ApJ, 752, 62

Jakobsson, P., Levan, A., Fynbo, J. P. U., et al. 2006c, A&A, 447, 897

Jaunsen, A. O., Rol, E., Watson, D. J., et al. 2008, ApJ, 681, 453

Jolliffe, I. T. 2002, Principal component analysis (Berlin,Springer)

Kalberla, P. M. W., Burton, W. B., Hartmann, D., et al. 2005, A&A, 440, 775

Kamble, A., Misra, K., Bhattacharya, D., & Sagar, R. 2009, MNRAS, 394, 214

Kamble, A., Resmi, L., & Misra, K. 2007, ApJ, 664, L5

Kann, D. A., Hoegner, C., & Filgas, R. 2007a, GRB Coordinates Network, 6884, 1

Kann, D. A., Hoegner, C., & Filgas, R. 2007b, GRB Coordinates Network, 6918, 1

Kann, D. A., Klose, S., Laux, U., & Stecklum, B. 2010a, GRB Coordinates Network, 11187, 1

Kann, D. A., Klose, S., & Zeh, A. 2006, ApJ, 641, 993

Kann, D. A., Klose, S., Zhang, B., et al. 2011, ApJ, 734, 96

Kann, D. A., Klose, S., Zhang, B., et al. 2010b, ApJ, 720, 1513

Kann, D. A., Laux, U., & Ertel, S. 2008, GRB Coordinates Network, 7845, 1

Kann, D. A., Laux, U., & Filgas, R. 2007c, GRB Coordinates Network, 6923, 1

Kann, D. A., Laux, U., Filgas, R., et al. 2007d, GRB Coordinates Network, 6935, 1

Kann, D. A., Laux, U., Klose, S., et al. 2007e, GRB Coordinates Network, 6295, 1

Kann, D. A., Laux, U., & Stecklum, B. 2010c, GRB Coordinates Network, 11236, 1

Kann, D. A., Nicuesa Guelbenzu, A., Ludwig, F., & Stecklum, B. 2010d, GRB Coordinates Network, 11247, 1

Kelemen, J., Sarneczky, K., Kuli, Z., & Ujhelyi, B. 2010, GRB Coordinates Network, 11252, 1

Kelly, P. L., Kirshner, R. P., & Pahre, M. 2008, ApJ, 687, 1201

Khamitov, I., Bikmaev, I., Gumerov, R., et al. 2008, GRB Coordinates Network, 7661, 1

Khamitov, I. M., Burenin, R. A., Bikmaev, I. F., et al. 2007, Astronomy Letters, 33, 797

Kinugasa, K. 2008, GRB Coordinates Network, 7413, 1

Kistler, M. D., Yüksel, H., Beacom, J. F., Hopkins, A. M., & Wyithe, J. S. B. 2009, ApJ, 705, L104

Klebesadel, R. W., Strong, I. B., & Olson, R. A. 1973, ApJ, 182, L85

Klein, C. R., Morgan, A. N., Perley, D. A., & Bloom, J. S. 2010, GRB Coordinates Network, 10627, 1

Klose, S. 2010, GRB Coordinates Network, 10616, 1

Klose, S., Henden, A. A., Greiner, J., et al. 2003, ApJ, 592, 1025

Klose, S., Stecklum, B., Masetti, N., et al. 2000, ApJ, 545, 271

Klotz, A., Boer, M., & Atteia, J. L. 2005a, GRB Coordinates Network, 3720, 1

Klotz, A., Boer, M., & Atteia, J. L. 2008a, GRB Coordinates Network, 7595, 1

Klotz, A., Boër, M., Atteia, J. L., & Gendre, B. 2009a, AJ, 137, 4100

Klotz, A., Boër, M., Atteia, J. L., et al. 2005b, A&A, 439, L35

Klotz, A., Gendre, B., Boer, M., & Atteia, J. L. 2009b, GRB Coordinates Network, 8998, 1

Klotz, A., Gendre, B., Boer, M., & Atteia, J. L. 2009c, GRB Coordinates Network, 10200, 1

Klotz, A., Vachier, F., & Boër, M. 2008b, Astronomische Nachrichten, 329, 275

Kocevski, D., Modjaz, M., Bloom, J. S., et al. 2007, ApJ, 663, 1180

Kouveliotou, C., Meegan, C. A., Fishman, G. J., et al. 1993, ApJ, 413, L101

Krimm, H. A., Granot, J., Marshall, F. E., et al. 2007, ApJ, 665, 554

Kruehler, T., Schrey, F., Greiner, J., et al. 2008, GRB Coordinates Network, 8075, 1

Krühler, T., Greiner, J., Afonso, P., et al. 2009a, A&A, 508, 593

Krühler, T., Greiner, J., McBreen, S., et al. 2009b, ApJ, 697, 758

Krühler, T., Greiner, J., Schady, P., et al. 2011, A&A, 534, A108

Krühler, T., Küpcü Yoldaş, A., Greiner, J., et al. 2008, ApJ, 685, 376

Krühler, T., Malesani, D., Milvang-Jensen, B., et al. 2012, ApJ, 758, 46

Kuin, N. P. M. & Mangano, V. 2008a, GRB Coordinates Network, 7804, 1

Kuin, N. P. M. & Mangano, V. 2008b, GRB Coordinates Network, 7808, 1

Kuin, N. P. M. & Racusin, J. L. 2008, GRB Coordinates Network, 8069, 1

Kuin, N. P. M., Sbarufatti, B., Marshall, F., & Schady, P. 2008, GRB Coordinates Network, 7844, 1

Kumar, P., Narayan, R., & Johnson, J. L. 2008, MNRAS, 388, 1729

Kumar, P. & Panaitescu, A. 2000, ApJ, 541, L51

Kuroda, D., Yanagisawa, K., Shimizu, Y., et al. 2010a, GRB Coordinates Network, 11186, 1

Kuroda, D., Yanagisawa, K., Shimizu, Y., et al. 2010b, GRB Coordinates Network, 11172, 1

Kuroda, D., Yanagisawa, K., Shimizu, Y., et al. 2010c, GRB Coordinates Network, 11189, 1

Kuroda, D., Yanagisawa, K., Shimizu, Y., et al. 2010d, GRB Coordinates Network, 11241, 1

Kuroda, D., Yoshida, M., Yanagisawa, K., et al. 2008, GRB Coordinates Network, 8724, 1

Lacluyze, A., Reichart, D., Haislip, J., et al. 2009, GRB Coordinates Network, 10107, 1

Landsman, W. B. & Guidorzi, C. 2008, GRB Coordinates Network, 7660, 1

Landsman, W. B. & Sbarufatti, B. 2008, GRB Coordinates Network, 7965, 1

Lazzati, D. & Perna, R. 2003, MNRAS, 340, 694

Le Floc'h, E., Duc, P.-A., Mirabel, I. F., et al. 2003, A&A, 400, 499

Lee, W. H. & Ramirez-Ruiz, E. 2002, ApJ, 577, 893

Levinson, A. & Eichler, D. 2003, ApJ, 594, L19

Li, L., Liang, E.-W., Tang, Q.-W., et al. 2012, ApJ, 758, 27

Li, W. 2005, GRB Coordinates Network, 4240, 1

Li, W. & Filippenko, A. V. 2008, GRB Coordinates Network, 7475, 1

Li, W., Perley, D. A., & Filippenko, A. V. 2009, GRB Coordinates Network, 9517, 1

Liang, E., Racusin, J. L., Zhang, B., Zhang, B., & Burrows, D. N. 2008, ApJ, 675, 528

Liang, E. & Zhang, B. 2005, ApJ, 633, 611

Liang, E. & Zhang, B. 2006, MNRAS, 369, L37

Liang, E.-W., Li, L., Gao, H., et al. 2012, ArXiv e-prints

Liang, E.-W., Zhang, B.-B., & Zhang, B. 2007, ApJ, 670, 565

Lipunov, V. M., Kornilov, V. G., Krylov, A. V., et al. 2007, Astronomy Reports, 51, 1004

Lloyd-Ronning, N. M. & Zhang, B. 2004, ApJ, 613, 477

Loew, S., Kruehler, T., & Greiner, J. 2008, GRB Coordinates Network, 8540, 1

Longair, M. S. 1994, High energy astrophysics, Vol.1, Vol.2 (Cambridge, Cambridge University Press)

Lyutikov, M. 2006, New Journal of Physics, 8, 119

Lyutikov, M. 2009, ArXiv e-prints

Lyutikov, M. & Blackman, E. G. 2001, MNRAS, 321, 177

MacFadyen, A. I. & Woosley, S. E. 1999, ApJ, 524, 262

MacFadyen, A. I., Woosley, S. E., & Heger, A. 2001, ApJ, 550, 410

Malesani, D., Covino, S., D'Avanzo, P., et al. 2007, A&A, 473, 77

Mangano, V., Holland, S. T., Malesani, D., et al. 2007, A&A, 470, 105

Mao, J., Cha, G., & Bai, J. 2009a, GRB Coordinates Network, 9305, 1

Mao, J., Li, S., & Bai, J. 2009b, GRB Coordinates Network, 10092, 1

Margutti, R. 2009, PhD thesis (http://hdl.handle.net/10281/7465) (Milano Bicocca University)

Margutti, R., Bernardini, G., Barniol Duran, R., et al. 2011a, MNRAS, 410, 1064

Margutti, R., Chincarini, G., Granot, J., et al. 2011b, MNRAS, 417, 2144

Margutti, R., Genet, F., Granot, J., et al. 2010a, MNRAS, 402, 46

Margutti, R., Guidorzi, C., Chincarini, G., et al. 2010b, MNRAS, 406, 2149

Margutti, R., Zaninoni, E., Bernardini, M. G., et al. 2013, MNRAS, 428, 729

Markwardt, C. B. 2009, in Astronomical Society of the Pacific Conference Series, Vol. 411, Astronomical Data Analysis Software and Systems XVIII, ed. D. A. Bohlender, D. Durand, & P. Dowler, 251

Marshall, F. E., Antonelli, L. A., Burrows, D. N., et al. 2011, ApJ, 727, 132

Marshall, F. E. & Grupe, D. 2009, GRB Coordinates Network, 10108, 1

Martin, N., Maurice, E., & Lequeux, J. 1989, A&A, 215, 219

Mason, K. O., Blustin, A. J., Boyd, P., et al. 2006, ApJ, 639, 311

McBreen, S., Krühler, T., Rau, A., et al. 2010, A&A, 516, A71

Melady, G., French, J., Kubanek, P., & Jelinek, M. 2007, GRB Coordinates Network, 6528, 1

Melandri, A., Guidorzi, C., & Carter, D. 2008a, GRB Coordinates Network, 8699, 1

Melandri, A., Guidorzi, C., Kobayashi, S., et al. 2009, MNRAS, 395, 1941

Melandri, A., Kobayashi, S., Mundell, C. G., et al. 2010, ApJ, 723, 1331

Melandri, A., Mundell, C. G., Kobayashi, S., et al. 2008b, ApJ, 686, 1209

Melandri, A., Sbarufatti, B., D'Avanzo, P., et al. 2012, MNRAS, 421, 1265

Melandri, A., Tanvir, N., & Guidorzi, C. 2006, GRB Coordinates Network, 5322, 1

Mészáros, P. 2006, Reports on Progress in Physics, 69, 2259

Meszaros, P. & Rees, M. J. 1997, ApJ, 476, 232

Metzger, B. D. 2010, in Astronomical Society of the Pacific Conference Series, Vol. 432, New Horizons in Astronomy: Frank N. Bash Symposium 2009, ed. L. M. Stanford, J. D. Green, L. Hao, & Y. Mao, 81

Metzger, B. D., Giannios, D., Thompson, T. A., Bucciantini, N., & Quataert, E. 2011, MNRAS, 413, 2031

Metzger, M. R., Djorgovski, S. G., Kulkarni, S. R., et al. 1997, Nature, 387, 878

Michałowski, M. J., Kamble, A., Hjorth, J., et al. 2012, ApJ, 755, 85

Mikuz, H., Skvarc, J., & Dintinjana, B. 2007, GRB Coordinates Network, 6288, 1

Milvang-Jensen, B., Fynbo, J. P. U., Malesani, D., et al. 2012, ApJ, 756, 25

Minezaki, T., Price, P. A., Yoshii, Y., & Cowie, L. L. 2007, GRB Coordinates Network, 7135, 1

Mirabal, N., Halpern, J. P., An, D., Thorstensen, J. R., & Terndrup, D. M. 2006, ApJ, 643, L99

Misra, K., Bhattacharya, D., Sahu, D. K., et al. 2007, A&A, 464, 903

Molinari, E., Vergani, S. D., Malesani, D., et al. 2007, A&A, 469, L13

Monfardini, A., Kobayashi, S., Guidorzi, C., et al. 2006, ApJ, 648, 1125

Moody, J. W., Laney, D., Pearson, R., & Pace, C. 2010, GRB Coordinates Network, 10665, 1

Moré, J. 1977, in Numerical Analysis, vol. 630, ed. G. A. Watson (Berlin, Springer-Verlag)

Moré, J. & Wright, S. 1993, Optimization Software Guide, Frontiers in Applied Mathematics, vol. 14 (Philadelphia, PA: SIAM)

Morgan, A. N., Bloom, J. S., Perley, D. A., & Starr, D. 2009a, GRB Coordinates Network, 8995, 1

Morgan, A. N., Klein, C. R., & Bloom, J. S. 2009b, GRB Coordinates Network, 9563, 1

Morgan, A. N., Perley, D. A., Klein, C. R., & Bloom, J. S. 2010, GRB Coordinates Network, 10648, 1

Mori, Y. A., Nakajima, H., Shimokawabe, T., et al. 2008, GRB Coordinates Network, 8619, 1

Morrison, R. & McCammon, D. 1983, ApJ, 270, 119

Mundell, C. G., Melandri, A., Guidorzi, C., et al. 2007, ApJ, 660, 489

Nakar, E. 2007, Physics Reports, 442, 166

Narayan, R., Paczynski, B., & Piran, T. 1992, ApJ, 395, L83

Nardini, M., Ghisellini, G., & Ghirlanda, G. 2008, MNRAS, 383, 1049

Nardini, M., Ghisellini, G., Ghirlanda, G., & Celotti, A. 2010, MNRAS, 403, 1131

Nardini, M., Ghisellini, G., Ghirlanda, G., et al. 2006, A&A, 451, 821

Nardini, M., Greiner, J., Krühler, T., et al. 2011, A&A, 531, A39

Nava, L., Ghirlanda, G., Ghisellini, G., & Firmani, C. 2008, MNRAS, 391, 639

Nicuesa Guelbenzu, A., Klose, S., Rossi, A., et al. 2011, A&A, 531, L6

Nissinen, M. 2009, GRB Coordinates Network, 8993, 1

Nissinen, M. & Hentunen, V.-P. 2009, GRB Coordinates Network, 9246, 1

Norris, J. P., Gehrels, N., & Scargle, J. D. 2011, ApJ, 735, 23

Norris, J. P., Marani, G. F., & Bonnell, J. T. 2000, ApJ, 534, 248

Nousek, J. A., Kouveliotou, C., Grupe, D., et al. 2006, ApJ, 642, 389

Novak, R. 2008, GRB Coordinates Network, 7504, 1

Nysewander, M., Fruchter, A. S., & Pe'er, A. 2009a, ApJ, 701, 824

Nysewander, M., Reichart, D. E., Crain, J. A., et al. 2009b, ApJ, 693, 1417

Oates, S. R. 2008, GRB Coordinates Network, 8544, 1

Oates, S. R. & Marshall, F. E. 2008, GRB Coordinates Network, 7607, 1

Oates, S. R. & Marshall, F. E. 2009, GRB Coordinates Network, 10078, 1

Oates, S. R., Page, M. J., De Pasquale, M., et al. 2012, MNRAS, 426, L86

Oates, S. R., Page, M. J., Schady, P., et al. 2011, MNRAS, 412, 561

Oates, S. R., Page, M. J., Schady, P., et al. 2009, MNRAS, 395, 490

Oates, S. R. & Stamatikos, M. 2008, GRB Coordinates Network, 7611, 1

Oates, S. R. & Stratta, G. 2007, GRB Coordinates Network, 7080, 1

O'Brien, P. T., Willingale, R., Osborne, J., et al. 2006, ApJ, 647, 1213

Oksanen, A. & Hentunen, V.-P. 2008, GRB Coordinates Network, 7657, 1

Oksanen, A., Templeton, M., Henden, A. A., & Kann, D. A. 2008, Journal of the American Association of Variable Star Observers (JAAVSO), 36, 53

Olivares, F., Kupcu Yoldas, A., Greiner, J., & Yoldas, A. 2009, GRB Coordinates Network, 9245, 1

Paczynski, B. 1986, ApJ, 308, L43

Paczynski, B. 1998, ApJ, 494, L45

Page, K. L., Willingale, R., Bissaldi, E., et al. 2009, MNRAS, 400, 134

Panaitescu, A. & Kumar, P. 2001, ApJ, 560, L49

Panaitescu, A., Mészáros, P., Gehrels, N., Burrows, D., & Nousek, J. 2006, MNRAS, 366, 1357

Panaitescu, A. & Vestrand, W. T. 2008, MNRAS, 387, 497

Panaitescu, A. & Vestrand, W. T. 2011, MNRAS, 414, 3537

Pandey, S. B., Castro-Tirado, A. J., Jelínek, M., et al. 2009, A&A, 504, 45

Pandey, S. B., Castro-Tirado, A. J., McBreen, S., et al. 2006, A&A, 460, 415

Pandey, S. B., Swenson, C. A., Perley, D. A., et al. 2010, ApJ, 714, 799

Pei, Y. C. 1992, ApJ, 395, 130

Perley, D. A. 2009, GRB Coordinates Network, 8997, 1

Perley, D. A. & Bloom, J. S. 2008, GRB Coordinates Network, 7233, 1

Perley, D. A., Bloom, J. S., Klein, C. R., et al. 2010, MNRAS, 406, 2473

Perley, D. A., Bloom, J. S., & Li, W. 2008a, GRB Coordinates Network, 7406, 1

Perley, D. A., Cenko, S. B., Bloom, J. S., et al. 2009a, AJ, 138, 1690

Perley, D. A., Cenko, S. B., Bloom, J. S., Li, W., & Cobb, B. E. 2009b, GRB Coordinates Network, 9001, 1

Perley, D. A., Li, W., Chornock, R., et al. 2008b, ApJ, 688, 470

Perley, D. A., Morgan, A. N., Updike, A., et al. 2011, AJ, 141, 36

Perna, R., Armitage, P. J., & Zhang, B. 2006, ApJ, 636, L29

Perri, M., Guetta, D., Antonelli, L. A., et al. 2007, A&A, 471, 83

Piran, T. 1999, Physics Reports, 314, 575

Piran, T. 2004, Reviews of Modern Physics, 76, 1143

Piran, T., Kumar, P., Panaitescu, A., & Piro, L. 2001, ApJ, 560, L167

Piro, L., Garmire, G., Garcia, M., et al. 2000, Science, 290, 955

Poole, T. S., Breeveld, A. A., Page, M. J., et al. 2008, MNRAS, 383, 627

Price, P. A., Cowie, L. L., Minezaki, T., et al. 2006, ApJ, 645, 851

Pritchard, T. A. & Immler, S. 2010, GRB Coordinates Network, 11176, 1

Proga, D. & Zhang, B. 2006, MNRAS, 370, L61

Quimby, R. M., Rykoff, E. S., Yost, S. A., et al. 2006, ApJ, 640, 402

Racusin, J. L., Karpov, S. V., Sokolowski, M., et al. 2008, Nature, 455, 183

Racusin, J. L., Liang, E. W., Burrows, D. N., et al. 2009, ApJ, 698, 43

Racusin, J. L., Oates, S. R., Schady, P., et al. 2011, ApJ, 738, 138

Rau, A., Savaglio, S., Krühler, T., et al. 2010, ApJ, 720, 862

Rees, M. J. & Meszaros, P. 1992, MNRAS, 258, 41P

Rees, M. J. & Meszaros, P. 1994, ApJ, 430, L93

Rees, M. J. & Mészáros, P. 2005, ApJ, 628, 847

Reeves, J. N., Watson, D., Osborne, J. P., et al. 2002, Nature, 416, 512

Reichart, D. E. & Lamb, D. Q. 2001, in American Institute of Physics Conference Series, Vol. 586, 20th Texas Symposium on relativistic astrophysics, ed. J. C. Wheeler & H. Martel, 599–604

Rhoads, J. E. 1999, ApJ, 525, 737

Robertson, B. E. & Ellis, R. S. 2012, ApJ, 744, 95

Romano, P., Campana, S., Chincarini, G., et al. 2006, A&A, 456, 917

Rossi, A., Klose, S., Ferrero, P., et al. 2012, A&A, 545, A77

Rossi, A., Schulze, S., Klose, S., et al. 2011, A&A, 529, A142

Rosswog, S., Liebendörfer, M., Thielemann, F.-K., et al. 1999, A&A, 341, 499

Rosswog, S., Ramirez-Ruiz, E., & Davies, M. B. 2003, MNRAS, 345, 1077

Rowlinson, A., Wiersema, K., Levan, A. J., et al. 2010, MNRAS, 408, 383

Ruiz-Velasco, A. E., Swan, H., Troja, E., et al. 2007, ApJ, 669, 1

Rumyantsev, V., Antonyuk, K., Andreev, M., & Pozanenko, A. 2008, GRB Coordinates Network, 8645, 1

Rumyantsev, V., Biryukov, V., & Pozanenko, A. 2009, GRB Coordinates Network, 10116, 1

Rumyantsev, V., Pavlenko, E., & Pozanenko, A. 2006, GRB Coordinates Network, 5336, 1

Rumyantsev, V. & Pozanenko, A. 2008a, GRB Coordinates Network, 7857, 1

Rumyantsev, V. & Pozanenko, A. 2008b, GRB Coordinates Network, 7833, 1

Rumyantsev, V., Shakhovkoy, D., & Pozanenko, A. 2010, GRB Coordinates Network, 10634, 1

Rybicki, G. B. & Lightman, A. P. 1979, Radiative processes in astrophysics (New York, Wiley-Interscience)

Ryde, F., Björnsson, C.-I., Kaneko, Y., et al. 2006, ApJ, 652, 1400

Rykoff, E. S., Aharonian, F., Akerlof, C. W., et al. 2009, ApJ, 702, 489

Rykoff, E. S., Rujopakarn, W., Quimby, R., et al. 2007, GRB Coordinates Network, 6269, 1

Rykoff, E. S., Yost, S. A., Krimm, H. A., et al. 2005, ApJ, 631, L121

Sahu, D. K., Arora, S., Singh, N. S., & Kartha, S. S. 2010a, GRB Coordinates Network, 11197, 1

Sahu, D. K., Bhatt, B. C., & Arora, S. 2010b, GRB Coordinates Network, 11175, 1

Sakamoto, T., Barthelmy, S. D., Baumgartner, W. H., et al. 2011, ApJS, 195, 2

Salvaterra, R., Cerutti, A., Chincarini, G., et al. 2008, MNRAS, 388, L6

Salvaterra, R., Della Valle, M., Campana, S., et al. 2009, Nature, 461, 1258

Sari, R. 1997, ApJ, 489, L37

Sari, R., Narayan, R., & Piran, T. 1996, ApJ, 473, 204

Sari, R. & Piran, T. 1997, MNRAS, 287, 110

Sari, R., Piran, T., & Halpern, J. P. 1999, ApJ, 519, L17

Sari, R., Piran, T., & Narayan, R. 1998, ApJ, 497, L17

Savaglio, S. 2006, New Journal of Physics, 8, 195

Savaglio, S., Glazebrook, K., & Le Borgne, D. 2009, ApJ, 691, 182

Schady, P. & Cannizzo, J. K. 2009, GRB Coordinates Network, 9234, 1

Schady, P., Dwelly, T., Page, M. J., et al. 2012, A&A, 537, A15

Schady, P., Page, M. J., Oates, S. R., et al. 2010, MNRAS, 401, 2773

Schady, P. & Stamatikos, M. 2009, GRB Coordinates Network, 9774, 1

Schlegel, D. J., Finkbeiner, D. P., & Davis, M. 1998, ApJ, 500, 525

Schneider, D. P., Gunn, J. E., & Hoessel, J. G. 1983, ApJ, 264, 337

Schulze, S., Klose, S., Björnsson, G., et al. 2011, A&A, 526, A23

Shapley, A. E., Steidel, C. C., Pettini, M., & Adelberger, K. L. 2003, ApJ, 588, 65

Shemi, A. 1994, MNRAS, 269, 1112

Siegel, M. H. & Markwardt, C. B. 2010, GRB Coordinates Network, 11242, 1

Siegel, M. H. & Marshall, F. 2010, GRB Coordinates Network, 10625, 1

Siegel, M. H., Marshall, F. E., Holland, S. T., et al. 2010, GRB Coordinates Network, 10645, 1

Smith, R. J., Gomboc, A., Guidorzi, C., et al. 2009, GRB Coordinates Network, 9770, 1

Smith, R. J., Melandri, A., Steele, I. A., et al. 2008, GRB Coordinates Network, 8333, 1

Soderberg, A. M., Berger, E., Kasliwal, M., et al. 2006, ApJ, 650, 261

Soderberg, A. M., Nakar, E., Cenko, S. B., et al. 2007, ApJ, 661, 982

Sollerman, J., Fynbo, J. P. U., Gorosabel, J., et al. 2007, A&A, 466, 839

Sposetti, S. 2007, GRB Coordinates Network, 7090, 1

Sposetti, S. & Immler, S. 2010, GRB Coordinates Network, 11213, 1

Staley, T. D., Titterington, D. J., Fender, R. P., et al. 2012, MNRAS, 208

Stanek, K. Z., Dai, X., Prieto, J. L., et al. 2007, ApJ, 654, L21

Starling, R. L. C., Rol, E., van der Horst, A. J., et al. 2009, MNRAS, 400, 90

Stefanescu, A., Schrey, F., Duscha, S., et al. 2006, GRB Coordinates Network, 5623, 1

Still, M., Roming, P. W. A., Mason, K. O., et al. 2005, ApJ, 635, 1187

Svensson, K. M., Levan, A. J., Tanvir, N. R., et al. 2012, MNRAS, 421, 25

Swan, H., Yuan, F., & Rujopakarn, W. 2008, GRB Coordinates Network, 7470, 1

Tagliaferri, G., Antonelli, L. A., Chincarini, G., et al. 2005a, A&A, 443, L1

Tagliaferri, G., Goad, M., Chincarini, G., et al. 2005b, Nature, 436, 985

Tanvir, N. R., Fox, D. B., Levan, A. J., et al. 2009, Nature, 461, 1254

Tanvir, N. R., Levan, A. J., Rol, E., et al. 2008, MNRAS, 388, 1743

Terra, F., Munz, F., Greco, G., et al. 2008, GRB Coordinates Network, 8368, 1

Thoene, C. C., Fynbo, J. P. U., de Ugarte Postigo, A., et al. 2008, GRB Coordinates Network, 7658, 1

Thompson, T. A. 2008, in American Institute of Physics Conference Series, Vol. 1000, American Institute of Physics Conference Series, ed. M. Galassi, D. Palmer, & E. Fenimore, 399–404

Thompson, T. A., Chang, P., & Quataert, E. 2004, ApJ, 611, 380

Thöne, C. C., de Ugarte Postigo, A., Fryer, C. L., et al. 2011, Nature, 480, 72

Thöne, C. C., Kann, D. A., Jóhannesson, G., et al. 2010, A&A, 523, A70

Tkachenko, A., Khamitov, I., Burenin, R., et al. 2010, GRB Coordinates Network, 11254, 1

Totani, T. 1997, ApJ, 486, L71

Troja, E., Cusumano, G., O'Brien, P. T., et al. 2007, ApJ, 665, 599

Uehara, T., Uemura, M., Arai, A., et al. 2011, A&A, 526, A92

Uehara, T., Uemura, M., Kawabata, K. S., et al. 2010, A&A, 519, A56

Updike, A., Afonso, P., Clemens, C., & Greiner, J. 2008a, GRB Coordinates Network, 8693, 1

Updike, A., Rau, A., Kruehler, T., Olivares, F., & Greiner, J. 2009a, GRB Coordinates Network, 9773, 1

Updike, A. C., Haislip, J. B., Nysewander, M. C., et al. 2008b, ApJ, 685, 361

Updike, A. C., Hartmann, D. H., Milne, P. A., & Williams, G. G. 2009b, GRB Coordinates Network, 10074, 1

Updike, A. C., Klose, S., Clemens, C., & Greiner, J. 2009c, GRB Coordinates Network, 8983, 1

Usov, V. V. 1992, Nature, 357, 472

Šimon, V., Polášek, C., Jelínek, M., Hudec, R., & Trobl, J. Å. 2010, A&A, 510, A49

Vaalsta, T. P., Coward, D. M., Zadko, J., et al. 2009, GRB Coordinates Network, 8976, 1

van der Horst, A. J., Kamble, A., Wijers, R. A. M. J., et al. 2007, Royal Society of London Philosophical Transactions Series A, 365, 1241

van der Horst, A. J., Kouveliotou, C., Gehrels, N., et al. 2009, ApJ, 699, 1087

van Paradijs, J., Groot, P. J., Galama, T., et al. 1997, Nature, 386, 686

Vaughan, S., Willingale, R., O'Brien, P. T., et al. 2004, ApJ, 603, L5

Vestrand, W. T., Wren, J. A., Wozniak, P. R., et al. 2006, Nature, 442, 172

Vietri, M. 2006, Astrofisica delle alte energie (Bollati Boringhieri)

Virgili, F. J., Zhang, B., Nagamine, K., & Choi, J.-H. 2011, MNRAS, 417, 3025

Volnova, A., Msu, S., Ibrahimov, M., Karimov, R., & Pozanenko, A. 2010, GRB Coordinates Network, 10821, 1

Wang, J. H., Schwamb, M. E., Huang, K. Y., et al. 2008, ApJ, 679, L5

Watson, D., Fynbo, J. P. U., Ledoux, C., et al. 2006a, ApJ, 652, 1011

Watson, D., Hjorth, J., Levan, A., et al. 2004, ApJ, 605, L101

Watson, D., Vaughan, S. A., Willingale, R., et al. 2006b, ApJ, 636, 967

Waxman, E. 1997, ApJ, 485, L5

Waxman, E., Mészáros, P., & Campana, S. 2007, ApJ, 667, 351

Wegner, G., Garnavich, P., Prieto, J. L., & Stanek, K. Z. 2008, GRB Coordinates Network, 7423, 1

Weingartner, J. C. & Draine, B. T. 2001, ApJ, 548, 296

West, J. P., McLin, K., Brennan, T., et al. 2008, GRB Coordinates Network, 8617, 1

Wheeler, J. C., Yi, I., Höflich, P., & Wang, L. 2000, ApJ, 537, 810

Wiersema, K., Curran, P. A., Krühler, T., et al. 2012, MNRAS, 426, 2

Wijers, R. A. M. J. & Galama, T. J. 1999, ApJ, 523, 177

Williams, G. G. & Milne, P. A. 2008, GRB Coordinates Network, 7443, 1

Willingale, R., O'Brien, P. T., Osborne, J. P., et al. 2007, ApJ, 662, 1093

Woosley, S. E. 1993, ApJ, 405, 273

Woosley, S. E. & Bloom, J. S. 2006, ARA&A, 44, 507

Woosley, S. E., Zhang, W., & Heger, A. 2003, in American Institute of Physics Conference Series, Vol. 662, Gamma-Ray Burst and Afterglow Astronomy 2001: A Workshop Celebrating the First Year of the HETE Mission, ed. G. R. Ricker & R. K. Vanderspek, 185–192

Woźniak, P. R., Vestrand, W. T., Panaitescu, A. D., et al. 2009, ApJ, 691, 495

Woźniak, P. R., Vestrand, W. T., Wren, J. A., et al. 2005, ApJ, 627, L13

Woźniak, P. R., Vestrand, W. T., Wren, J. A., et al. 2006, ApJ, 642, L99

Wren, J., Vestrand, W. T., Wozniak, P. R., & Davis, H. 2008a, GRB Coordinates Network, 7477, 1

Wren, J., Vestrand, W. T., Wozniak, P. R., Davis, H., & Norman, B. 2008b, GRB Coordinates Network, 8337, 1

Wren, J., Vestrand, W. T., Wozniak, P. R., Davis, H., & Norman, B. 2009, GRB Coordinates Network, 9778, 1

Wu, C. 1986, The annals Statistics, 414, 1261

Xin, L.-P., Liang, E.-W., Wei, J.-Y., et al. 2011, MNRAS, 410, 27

Xu, D., Starling, R. L. C., Fynbo, J. P. U., et al. 2009, ApJ, 696, 971

Xu, M. & Huang, Y. F. 2012, A&A, 538, A134

Yonetoku, D., Murakami, T., Nakamura, T., et al. 2004, ApJ, 609, 935

Yoshida, M., Sasada, M., Komatsu, T., & Kawabata, K. S. 2010, GRB Coordinates Network, 11190, 1

Yoshida, M., Yanagisawa, K., Kuroda, D., et al. 2008a, GRB Coordinates Network, 7863, 1

Yoshida, M., Yanagisawa, K., Shimizu, Y., et al. 2008b, GRB Coordinates Network, 7410, 1

Yost, S. A., Aharonian, F., Akerlof, C. W., et al. 2007a, ApJ, 669, 1107

Yost, S. A., Harrison, F. A., Sari, R., & Frail, D. A. 2003, ApJ, 597, 459

Yost, S. A., Swan, H. F., Rykoff, E. S., et al. 2007b, ApJ, 657, 925

Yuan, F., Quimby, R., Swan, H., & Akerlof, C. 2008, GRB Coordinates Network, 7411, 1

Yuan, F., Rykoff, E. S., Rujopakarn, W., & Swan, H. 2007, GRB Coordinates Network, 7061, 1

Yuan, F., Schady, P., Racusin, J. L., et al. 2010, ApJ, 711, 870

Zafar, T., Watson, D., Fynbo, J. P. U., et al. 2011, A&A, 532, A143

Zerbi, R. M., Chincarini, G., Ghisellini, G., et al. 2001, Astronomische Nachrichten, 322, 275

Zhang, B. 2011, Comptes Rendus Physique, 12, 206

Zhang, B., Fan, Y. Z., Dyks, J., et al. 2006, ApJ, 642, 354

Zhang, B., Liang, E., Page, K. L., et al. 2007, ApJ, 655, 989

Zhang, B. & Mészáros, P. 2001, ApJ, 552, L35

Zhang, B. & Yan, H. 2011, ApJ, 726, 90

Zhang, F.-W., Shao, L., Yan, J.-Z., & Wei, D.-M. 2012, ApJ, 750, 88

Ziaeepour, H., Holland, S. T., Boyd, P. T., et al. 2008, MNRAS, 385, 453